Universitat Politècnica de Catalunya

Doctoral Thesis

A cold-atom approach to topological quantum matter across the energy scale

Author:
Daniel González Cuadra

Supervisor:
Prof. Dr. Maciej Lewenstein

Cosupervisor:
Dr. Alejandro Bermúdez

A thesis submitted in fulfillment of the requirements
for the degree of Doctor of Philosophy

Barcelona, October 2020

Acknowledgements

Being science a collective effort, I can't help but start thanking everyone I have worked with during these last four years: Alejandro, Alexandre, Andy, Apoorva, Erez, Fred, Ignacio, Kuba, Luca, Maciej, Monika, Pawel, Philipp, Przemek, Titas and Valentin. Their contributions made this thesis possible. Part of it is also theirs.

I would like to thank specially to my supervisors for their guidance, patience and trust. Maciej, who always let me do whatever I wanted, knowing I would anyway regret it, dziękuję. Alejandro, que más que un compañero ha sido un ejemplo y un amigo, gracias por enseñarme tanto, especialmente a disfrutar de este trabajo.

Thank you also to all the great professionals at ICFO working to make the life of a researcher easier. To the quantum optics theory group, and everyone else with whom I have shared discussions, worries, laughs and hangovers, it has been a pleasure. I finish this PhD with the satisfaction of carrying experiences and friends that made me grow in every aspect.

Gracias a Alex por todos los consejos. A Albert, Angelo y Gorka por resolver mil y una dudas. To Patrick, Joana and Salva for proofreading the thesis. A Isa por obligarme a que me preocupe por detalles de formato que no sabía si quiera que existían. Al futbolín de ICFO, que en paz descanse, por darme motivos para ir a trabajar cada día.

Gracias a Amelia, por haberme acompañado siempre, en los buenos momentos y en los no tan buenos. Si ha sido posible llegar al final ha sido gracias al cariño de la gente que me rodea, en especial a mi familia. Esta tesis se la quiero dedicar a mis padres, que llevan toda la vida creyendo en mi. Sin su apoyo no estaría ahora mismo escribiendo estas líneas.

Finally, I want to acknowledge every person that believes in science as a tool for human progress. This collective endeavor would not be possible without the help of many.

The projects developed under this PhD thesis have received funding from the European Union Horizon 2020 research and innovation programme under the Marie Skłodowska-Curie grant agreement No 665884, ERC AdG NOQIA, the Spanish Ministry MINECO and State Research Agency AEI (FIDEUA PID2019-106901GB-I00/10.13039 / 501100011033, SEVERO OCHOA No. SEV-2015-0522 and CEX2019-000910-S, FPI), European Social Fund, Fundació Cellex, Fundació Mir-Puig, Generalitat de Catalunya (AGAUR Grant No. 2017 SGR 1341, CERCA program, QuantumCAT _U16-011424, co-funded by ERDF Operational Program of Catalonia 2014-2020), MINECO-EU QUANTERA MAQS (funded by The State Research Agency (AEI) PCI2019-111828-2 / 10.13039/501100011033), and the National Science Centre, Poland-Symfonia Grant No. 2016/20/W/ST4/00314.

Abstract

The outstanding progress achieved in the last decades to isolate and manipulate individual quantum systems has revolutionized the way in which quantum many-body phenomena, appearing across Nature's different energy scales, can be investigated. By employing atomic systems such as ultracold atoms in optical lattices, an enormous range of paradigmatic models from condensed-matter and high-energy physics are being currently studied using table-top experiments, turning Feynman's idea of a quantum simulator into a reality.

Quantum simulators offer the possibility to gather information about complex quantum systems, which are either not accessible to experiments or whose properties can not be easily derived using standard analytical or numerical approaches. These synthetic quantum systems can be designed precisely such that they are described under the same models as natural systems, and their remarkable control allows to probe the relevant phenomena associated to them. Apart from their quantum simulation capabilities, atomic systems can also be employed to generate quantum matter with novel properties beyond those found in Nature, offering interesting prospects for quantum technological applications.

In this thesis, we investigate the possibilities that cold-atom systems present to address, in particular, quantum matter with non-trivial topological properties. Using mixtures of ultracold atoms, we analyze various quantum simulation strategies to access several many-body phenomena for which a satisfactory understanding is still lacking. Moreover, we show how such platforms display strongly-correlated topological effects beyond those found in natural systems.

We first focus on models inspired by condensed-matter physics. More precisely, we propose how lattices dynamics, similar to those described by phonons in solid crystals, can be implemented in an otherwise static optical lattice. By coupling the former to quantum matter using a mixture of bosonic atoms, we reproduce typical effects described by electronic systems, such as topological defects or charge fractionalization. We then extend these results and find novel features, from boson fractionalization to intertwined topological phases.

We then consider the quantum simulation of high-energy-physics problems. By using Bose-Fermi mixtures, we show how non-perturbative phenomena characteristic of non-abelian gauge theories, such as quark confinement, emerge in simpler models that are within the reach of current technology. Finally, we investigate how the interplay between gauge invariance and strong correlations gives rise to various mechanisms to prepare robust topological order in near-term quantum simulators.

In summary, our results show several connections between different areas of theoretical and experimental physics, and indicate how these can be harnessed further to advance our understanding of strongly-correlated quantum matter, as well as to utilize the latter for new technological applications.

Resumen

El enorme progreso llevado a cabo en las últimas decadas para aislar y manipular sistemas cuánticos individuales ha revolucionado la manera de investigar fenómenos cuánticos de muchos cuerpos, los cuales se presentan a diferentes escalas energéticas en la naturaleza. Actualmente, una gran variedad de modelos paradigmáticos en física de la materia condensada y de altas energías se estudian experimentalmente utilizando sistemas atómicos tales como átomos ultrafríos en retículos ópticos, llevando a la realidad la idea de simulador cuántico de Feynman.

Los simuladores cuánticos ofrecen la posibilidad de obtener información sobre otros sistemas cuánticos más complejos que, o bien no son accesibles experimentalmente, o cuyas propiedades no se pueden predecir fácilmente utilizando técnicas analíticas o numéricas usuales. Estos sistemas cuánticos sintéticos se pueden diseñar de tal manera que se encuentren descritos precisamente por los mismos modelos que los anteriores y, gracias a su notable control, permiten investigar los fenómenos más relevantes asociados a ellos. Aparte de su uso como simuladores cuánticos, estos sistemas atómicos se pueden utilizar para crear nuevos tipos de materia cuántica cuyas propiedades pueden ser diferentes de aquellas encontradas en la naturaleza, ofreciendo así aplicaciones interesantes en tecnología cuántica.

En esta tesis investigamos las posibilidades que los sistemas de átomos fríos ofrecen para obtener materia cuántica con propiedades topológicas no triviales. Analizamos, en particular, diferentes estrategias de simulación cuántica para acceder a varios fenómenos de muchos cuerpos que aún no se entienden de forma satisfactoria, utilizando para ello mezclas de átomos ultrafríos. Mostramos además como estas plataformas pueden dar lugar a efectos topológicos fuertemente correlacionados que van más allá de los encontrados hasta ahora en sistemas naturales.

Primero nos enfocamos en modelos inspirados por sistemas de materia condensada. En particular, proponemos como implementar retículos dinámicos, los cuales suelen ser estáticos en sitemas ópticos, de manera que podamos simular las partículas fonónicas que aparecen en sólidos cristalinos. Acoplamos estos últimos a materia cuántica utilizando una mezcla de átomos bosónicos, lo cual nos permite reproducir algunos de los efectos típicos que aparecen en sitemas electrónicos, tales como defectos topológicos o fraccionalización de la carga. Por último, extendemos estos resultados encontrando rasgos nuevos, desde la fraccionalización de bosones hasta fases topológicas entrelazadas.

Consideramos además simulaciones cuánticas para problemas en física de altas energías. Utilizando mezclas de átomos bosónicos y fermiónicos, mostramos como algunos fenómenos no perturbativos característicos de teorías gauge no abelianas, tales como el confinamiento de quarks, pueden aparecer en modelos más sencillos, los cuales están al alcance de la tecnología actual. Finalmente, investigamos como la interacción entre simetría gauge y correlaciones fuertes puede dar lugar a nuevos

mecanismos para genera orden topológico más robusto en simuladores cuánticos a corto plazo.

En resumen, nuestros resultados muestras varias conexiones entre diferentes areas de la física teórica y experimental, e indican como estas pueden ser exploradas para avanzar en el conocmiento de la materia cuántica fuertemente correlacionada, así como en las posibles aplicaciones tecnológicas de esta última.

Table of Contents

Introduction

Motivation

The last decades have witnessed an unprecedented progress in the degree with which quantum systems can be controlled experimentally. Within the field of atomic, molecular and optical (AMO) physics, in particular, several techniques, such as laser cooling and trapping [CT98, Phi98], are now routinely employed to isolate and manipulate quantum systems. Such degree of control has allowed to investigate fundamental properties of these systems at the level of single atoms and photons [LBMW03, RBH01], which has led to the Nobel prize in physics in 2012.

More recently, atomic experiments have moved into the many-body arena. Sparked by the observation of Bose-Einstein condensation (BEC) in cold and dilute atomic gases [AEM+95, DMA+95], quantum effects are now investigated at macroscopic scales using, among others, systems of neutral atoms [JZ05, BDZ08, LSA+07, BDN12, LSA17] and trapped ions [CZ95, LBMW03, BR12, LHN+11, PC04]. The use of optical lattices, in particular, has allowed access to regimes where, despite the difference in the characteristic energy scales, atoms behave similarly to electrons in crystalline solids [JBC+98, GME+02]. In both cases, the relevant dynamics are described by many-body lattice Hamiltonians, which in the former case can be engineered in great detail [Blo05]. These *synthetic* quantum systems can thus be employed to study the properties of materials that are less accessible in experiments, as it is the case for many solid-state systems. This approach realizes Feynman's vision of a *quantum simulator* [Fey82], a device that mimics the properties of other quantum systems, allowing to simulate the mathematical models that describe the latter in a much more efficient manner than what its classical counterparts could ever achieve [CZ12, BN09].

With this strategy in mind, cold-atom experiments are already exploring physical phenomena that fall beyond the capabilities of current analytical and numer-

ical methods [TCF+12]. One paradigmatic example of this trend involves the study of the Hubbard model [HF63] and its relation to high-T_c superconductivity [Eme87, ZR88, LNW06]. The exact mechanism behind this phenomenon remains unknown due to, among other reasons, the limitations of standard numerical approaches [LGS+90]. In this context, cold-atom quantum simulators can be designed to target the Hubbard model [HCZ+02, JSG+08], offering the possibility to explore the regimes of its phase diagram where other methods fail [MCJ+17].

An analogous approach can be employed as well to address open questions at much higher energies, in situations involving the interaction between fundamental particles and fields [PS95]. As in the condensed-matter case, the study of certain non-perturbative many-body effects in high-energy physics requires the use of numerical simulations, where similar limitations also appear [GL16]. A representative example of this situation can be found in the phenomenon of quark confinement, described by quantum chromodynamics (QCD) [KS03], which is still poorly understood despite many decades of research [Gre20]. Current experiments involving the collision of heavy-ions are trying to address such problems [BRvdS18], and alternative approaches that allow theoretical predictions to be compared with the experimental results are crucial at this stage. The use of ultracold atoms for this task is, however, more challenging compared to lower-energy situations. The reason behind this is the presence of local or *gauge* symmetries in QCD and other theories that form the standard model of particle physics [Sch14]. Since these symmetries are in general absent in the relevant low-energy description of atomic systems, bigger technical efforts are required to design quantum simulators capable of addressing high-energy phenomena [Wie13, ZCR15, DM16, BC19, BBC+20].

Despite these challenges, state-of-the-art experiments are starting to construct the basic building blocks required for this task [SGB+19, GSM+19, MZH+20, YSO+20]. Although a full-fledged quantum simulator capable of characterizing the phase diagram of QCD in $3+1$ dimensions is still a long-term goal, these *near-term* quantum simulators can already be employed to investigate simpler but still relevant models. The goal here is two fold. On the one hand, effects that are similar to those of interest can appear in simpler models whose simulations is less challenging. The interest in this strategy lies on the possibility to learn universal features that could also be present in more complicated models, by targeting only the relevant information and understanding which non-essential features could be safely disregarded. On the other hand, one could construct these simulators to generate novel quantum states of matter that, although inspired by those observed in natural systems, do not necessarily appear in them. Among other applications, such states could be helpful to design artificial materials with interesting properties [BAH17], or to be used as resources in quantum information and quantum computation technologies [JBC+99, JCZ+00].

Recently, the notion of topology has been identified as a paramount tool to deepen our understanding of quantum many-body systems [Kos17, Hal17], and it

lies nowadays at the center of quantum-simulation efforts [GBZ16], both from a fundamental and applied perspective. In quantum systems, topological properties refer to global characteristics that are robust against local perturbations [Nak03]. These properties have been found to be ubiquitous in the description of a plethora condensed-matter and high-energy phenomena, including several open problems such as high-T_c superconductivity [SF01] and quark confinement [Pol77, Hoo81]. The investigation of topological quantum matter using atomic systems exemplifies the dual role that synthetic matter plays in current research. Ultracold atoms in optical lattices have been used to study topological phases of matter [GJOS14, DGJbuO11]. One of the goals has been the simulation of strongly-correlated topological phases such as fractional quantum Hall states (FQHS) [Lau99], and to probe their properties in a controllable fashion [SDL05]. FQHS states, in particular, present *topological order*—whose low-energy properties can be described in terms of gauge theories [Sac18]—and anyonic excitations [Lau83], and their preparation would provide an important step towards, not only a better understanding of these strongly-correlated features, but also to build fault-tolerant quantum computers that are globally-protected against local errors [Kit03]. Beyond their role as quantum simulators, ultracold atoms are also addressing novel topological phases that do not have a counterpart in natural materials using, for instance, techniques such as Floquet engineering [WBÜ+20], as well as other topologically-ordered states [DYR+17].

In this thesis, we investigate topological quantum matter using cold-atomic systems following these two approaches. First, inspired by different condensed-matter and high-energy systems, we introduce models that, although do not exactly describe systems found in Nature, could allow the quantum simulation of relevant quantum many-body phenomena that are harder to access experimentally in the former. We propose implementation schemes for these models using mixtures of ultracold atoms in optical lattices, and study their properties using various analytical and numerical techniques. Second, we show how such atomic setups allow us to extend many of these phenomena beyond standard situations, as well as to uncover novel strongly-correlated topological effects.

Content

The thesis is organized as follows. We have divided the content into three different parts. The first two chapters in part I serve as a review that covers several background topics that we believe are useful to understand the subsequent parts of the thesis. An expert in the field might decide to skip these introductory chapters and jump directly to the results, returning to consult them whenever is required. The rest of the chapters include the main results of the thesis. Part II contains three chapters devoted to the study of strongly-correlated topological effects inspired by

condensed-matter phenomena. Part III contains two chapters focused on the study of high-energy physics in atomic systems. We now briefly summarize the contents of each chapter.

In chapter 1, we review the basic notions that are behind the description and classification of topological phenomena in quantum many-body systems. We focus, in particular, on topological defects and topological phases, and give examples from condensed-matter and high-energy physics where these effects play an important role.

In chapter 2, we review the two different but complementary approaches used in this thesis to investigate strongly-correlated systems: numerical methods based on tensor networks and quantum simulations using ultracold atoms in optical lattices.

In chapter 3, we describe how to implement a dynamical lattice using a mixture of ultracold bosonic atoms, allowing, on the one hand, to investigate several paradigmatic condensed-matter phenomena in greater detail, such as Peierls transitions and charge fractionalization induced by topological defects. On the other hand, we show how these effects, typical of fermion-phonon systems, also appear in the case of strongly-interacting bosonic matter.

In chapter 4, we show how synthetic quantum systems can present novel topological effects that have not been explored in natural materials. In particular, we extend the results from the previous chapter and find various intertwined topological phases, where long-ranger order coexists with non-trivial topological properties. We characterize several features that arise as a consequence of this interplay, such as emergent topological symmetry protection or fractional charge pumping.

In chapter 5, we conclude our investigation of strongly-correlated topological effect in systems with bosonic matter by studying in detail how topological defects arise in intertwined topological phases. We show how the latter give rise to the phenomenon of boson fractionalization, and how it could be detected in atomic experiments.

In chapter 6, we shift the focus and investigate the presence of high-energy phenomena in synthetic quantum matter, showing how questions associated with quark confinement can be addressed using an ultracold Bose-Fermi mixture. In particular, we propose a quantum simulation scheme for a simple lattice model where quark-like quasi-particles emerge and become deconfined due to the presence of topological defects. Moreover, we uncover a confinement-deconfinement phase transition that could be further studied in atomic experiments.

Finally, in chapter 7, we introduce a lattice gauge theory that could be implemented using near-term cold-atom quantum simulators, and show how the interplay between gauge symmetry and quantum correlations gives rise to new topological effects, including robust topological order and fermionic deconfinement.

List of publications

We finish this introduction presenting the publications on which this thesis is based, including both peer-reviewed articles as well as preprints. We also indicate which chapter corresponds to the content of each publication.

Peer-reviewed articles

1. [GCGDL18] D. González-Cuadra, P. R. Grzybowski, A. Dauphin, and M. Lewenstein. Strongly correlated bosons on a dynamical lattice. *Phys. Rev. Lett.* **121**, 090402 (2018). Chapter [3].

2. [GCDG+19] D. González-Cuadra, A. Dauphin, P. R. Grzybowski, P. Wójcik, M. Lewenstein, and A. Bermudez. Symmetry-breaking topological insulators in the $\mathbb{Z}_2$ Bose-Hubbard model. *Phys. Rev. B* **99**, 045139 (2019). Chapter [4].

3. [GCBG+19] D. González-Cuadra, A. Bermudez, P. R. Grzybowski, M. Lewenstein, and A. Dauphin. Intertwined topological phases induced by emergent symmetry protection. *Nat. Commun.* **10**, 2694 (2019). Chapter [4].

4. [GDG+19] D. González-Cuadra, A. Dauphin, P. R. Grzybowski, M. Lewenstein, and A. Bermudez. $\mathbb{Z}_n$ solitons in intertwined topological phases. *arXiv* 1908.02186 (2020). Accepted in *Phys. Rev. B*. Chapter [5].

5. [GCTLB20] D. González-Cuadra, L. Tagliacozzo, M. Lewenstein, and A. Bermudez. Robust topological order in fermionic $\mathbb{Z}_2$ gauge theories: from Aharonov-Bohm instability to soliton-induced deconfinement. *Phys. Rev. X* **10**, 041007 (2020). Chapter [7].

Preprints

6. [GDG+20] D. González-Cuadra, A. Dauphin, P. R. Grzybowski, M. Lewenstein, and A. Bermudez. Dynamical solitons and boson fractionalization in cold-atom topological insulators. *arXiv* 2003.10994 (2020). Submitted to *Phys. Rev. Lett.* Chapter [5].

7. [GCDA+20] D. González-Cuadra, A. Dauphin, M. Aidelsburger, M. Lewenstein, and A. Bermudez. The rotor Jackiw-Rebbi model: a cold-atom approach to chiral symmetry restoration and quark confinement. *arXiv* 2008.02045 (2020). Submitted to *Phys. Rev. X Quantum.* Chapter [6].

Part I

Preliminaries

Chapter 1

Topological quantum matter

In mathematics, the field of topology investigates the properties of certain objects, known as *topological spaces*, that do not change under continuous deformations [Nak03]. Topological spaces are sets equipped with a *topology*[1], one of the simplest mathematical structures that allows to define a notion of continuity[2]. One can classify topological spaces based on their global properties, also known as *topological invariants*, which are invariant under continuous maps, this is, they do not depend on the local details of the space. As we will see during this chapter, this classification can be further simplified by noting that, in many cases, these invariants carry an extra algebraic structure, such as a group structure. One can then use tools from abstract algebra to characterize topological spaces, a branch that is known as algebraic topology

Topological spaces can appear in the mathematical description of many different physical systems, as we will see. Topological phenomena are usually associated to certain robustness to local perturbations. In each situation, in order to understand these effects it is important first to identify the mathematical structure behind them that can give rise to non-trivial behavior, as well as the notion of continuity and its physical interpretation. The strength of this approach lies in the possibility to predict the behavior of a physical system without paying much attention to its local details, focusing instead on its global properties. In this first introductory

[1] More specifically, a topological space is a pair (X, τ), where X is a set and τ, the topology on X, is a collection of subsets of X, known as *open sets*, satisfying the following properties: (1) both the set X and the empty set belong to τ, (2) any finite or infinite union of elements of τ belongs to τ and (3) the intersection a finite number of elements of τ also belongs to τ. In the following, we denote the topological space by referring to the set X, keeping in mind that a certain topology is associated to it.

[2] A map $f\colon X \to Y$ between two topological spaces X and Y is continuous if for every open set $V \subseteq Y$, the inverse image $f^{-1}(V) = \{x \in X \mid f(x) \in V\}$ is an open subset of X. If f is a bijection and the inverse map f^{-1} is also continuous, f is called an *homeomorphism*.

chapter, we review the main examples where topology plays a role in the description of a physical system, focusing on those cases that are relevant to condensed-matter and high-energy physics. In Sec. 1.1, we consider the case of topological defects in ordered media, which can appear both in classical and quantum systems. In Sec. 1.2, we review the topological structure behind the description of quantum states, and how it can give rise to non-trivial observable effects arising from the interplay between topology and quantum statistics. Finally, in Sec. 1.3, we show how such structure brings about novel phases of matter, with important applications to different fields, ranging from material science to quantum computation.

Throughout this chapter, we introduce all the required mathematical concepts, where no prior knowledge on topology will be assumed. Although a full account on the mathematical details behind topological phenomena is beyond our scope, we will try at least to convey some basic notions to build an intuition on what is topological in topological physics. We refer the interested reader to more detailed references in due course.

1.1 Topological defects

Topological defects are arguable one of the most prominent examples where topology can be employed to predict the properties of a physical system. They refer to stable solutions of partial differential equations that can not be continuously connected to the vacuum—in a way that we will make more precise soon—caused by non-trivial topological properties in the boundary conditions of these equations. A prime example are solitons, wave packets that propagate in dispersive media without changing its shape due to non-linear effects [ZK65]. They are ubiquitous across different fields, ranging from hydrodynamics [SR44] and optics [HT73] to biology [Dav77]. Here we focus on topological defects in many-body systems, relevant both to condensed-matter and high-energy physics. In that context, the presence of defects is associated to the spontaneous breaking of certain symmetries [Mer79], emerging from the interactions among many microscopic degrees of freedom. We note that, although in the following we focus mostly on quantum states at $T = 0$, the theory of topological defects presented here is valid also for classical phases at finite temperatures. In that sense, we could regard topological defects as a classical phenomena—although quantum effects become relevant whenever defects interact with quantum matter, as we will see in chapter 5. This is in contrast to the case of topological phases, introduced in the next section, where non-trivial topology is found precisely in the structure of quantum states, and, therefore, no classical counterpart exists. In this section, we first review the notion of spontaneous symmetry breaking in quantum mechanics. We then classify topological defects based on the topological structure of the resulting ground-state manifold. We finish with some comments regarding the most common mechanisms to create defects in physical

systems.

1.1.1 Spontaneous symmetry breaking

In quantum mechanics, a system is said to be symmetric under a certain group of transformations $\mathcal{G}$[3] if the Hamiltonian that governs its dynamics, $\hat{H}(\boldsymbol{\lambda})$—where $\boldsymbol{\lambda} = (\lambda_1, \lambda_2, \dots)$ denotes possible external parameters—commutes with a set of unitary transformations,

$$[\hat{H}(\boldsymbol{\lambda}), \hat{U}_g] = 0, \tag{1.1}$$

where $\{\hat{U}_g\}_{g\in\mathcal{G}}$ forms a unitary representation of the symmetry group [Cor97]. In general, any state can be written as a superposition of states that transform according to irreducible representations of a group. This fact becomes very useful to characterize the eigenstates of a symmetric system, and has led, for instance, to a complete classification of elementary particles in the Standard Model [Sch14].

In condensed matter, the notion of symmetry [Gro96], together with emergence [And72], constitutes a driving force to understand the vast diversity of observed phenomena. On the one hand, emergence can account for the appearance of different collective behavior at macroscopic scales, starting from a collection of many individual particles that interact according to the same microscopic laws. On the other hand, symmetry can explain how, sometimes, this complexity can be tamed by understanding the underlying microscopic symmetries. According to Landau's paradigm [Lan37], even when the system's Hamiltonian respects a particular symmetry (1.1), its ground state $|\psi_{\text{g.s.}}(\boldsymbol{\lambda})\rangle$, defined up to a global phase, may not be invariant under a certain subgroup[4] of transformation, this is,

$$\hat{U}_g\,|\psi_{\text{g.s.}}(\boldsymbol{\lambda})\rangle \neq |\psi_{\text{g.s.}}(\boldsymbol{\lambda})\rangle \tag{1.2}$$

for at least one $g \in \mathcal{G}$. This situation is referred to as *spontaneous symmetry breaking* (SSB). For systems with a finite number constituents, the ground state always has the same symmetries as the corresponding Hamiltonian. For SSB to take place, therefore, an infinite number of degrees of freedom is required. This corresponds to the thermodynamic limit in condensed matter—where, in many situations, the low-energy physics can be described by an effective quantum field theory—and SSB allows us to explain many macroscopic phenomena, from magnetism to superconductivity [AS06]. The situation is analogous in high-energy physics, where SSB

[3] A group is a set $\mathcal{G}$ together with an operation $\cdot$ that takes two elements g_1 and g_2 from $\mathcal{G}$ to form a new element $g_1 \cdot g_2$, such that the following properties are fulfilled: (1) $g_1 \cdot g_2 \in \mathcal{G}$ $\forall g_1, g_2 \in \mathcal{G}$, (2) $g_1 \cdot (g_2 \cdot g_3) = (g_1 \cdot g_2) \cdot g_3$ $\forall g_1, g_2, g_3 \in \mathcal{G}$, (3) there exists a unique element $e \in \mathcal{G}$, called the identity, such that $e \cdot g_1 = g_1 \cdot e = g_1$ $\forall g_1 \in \mathcal{G}$ and (4) $\forall g_1 \in \mathcal{G}$ there exists an element $g_1^{-1} \in \mathcal{G}$, called the inverse of g_1, such that $g_1 \cdot g_1^{-1} = g_1^{-1} \cdot g_1 = e$.

[4] A subgroup $\mathcal{H}$ of a group $\mathcal{G}$, denoted $\mathcal{H} \leq \mathcal{G}$, is a subset of $\mathcal{G}$ that is also a group under the same group operation as $\mathcal{G}$.

accounts, for instance, for the separation between electromagnetic and weak interactions that took place shortly after the Big Bang [Wei67], or to the generation of mass in quantum chromodynamics [NJL61a, NJL61b].

In general, the symmetry does not have to be completely broken after SSB. In many situations, there is a residual symmetry group $\mathcal{H}$ represented by the set of transformations under which the ground state is still invariant,

$$\mathcal{H} = \{h \in \mathcal{G} \mid \hat{U}_h \left|\psi_{\text{g.s.}}\right\rangle = \left|\psi_{\text{g.s.}}\right\rangle\} \leq \mathcal{G}. \tag{1.3}$$

Note that, for $g \notin \mathcal{H}$, although $\left|\psi_{\text{g.s.}}(\boldsymbol{\lambda})\right\rangle$ and $\hat{U}_g \left|\psi_{\text{g.s.}}(\boldsymbol{\lambda})\right\rangle$ are different states (1.2), they have the same energy—since $\hat{U}_g$ commutes with the Hamiltonian (1.1). Therefore, symmetry-broken ground states are always degenerate. Take $\left|\psi_{\text{g.s.}}\right\rangle$ to be one of them. The set of degenerate ground states (GS) can be obtained by applying unitary transformations on it, $\mathsf{GS} \subset \{\hat{U}_g \left|\psi_{\text{g.s.}}\right\rangle\}_{g\in\mathcal{G}}$, requiring that the group element does not belong to the residual symmetry subgroup, $g \notin \mathcal{H}$. In particular, it is easy to show that the elements of GS are in a one-to-one correspondence with the elements of the quotient set

$$\mathcal{R} = \mathcal{G}/\mathcal{H}, \tag{1.4}$$

this is, the set of (left) cosets of $\mathcal{H}$ in $\mathcal{G}$, $g\mathcal{H} = \{gh : h \in \mathcal{H}\}$. The latter defines an equivalence relation in $\mathcal{G}$, and $\mathcal{G}/\mathcal{H}$ denotes to the set of equivalence classes. If $\mathcal{H}$ is a normal subgroup[5] of $\mathcal{G}$, the quotient set has also the structure of a group.

As an example, consider a scalar field theory with a non-linear potential, $V[\phi] = -m^2|\phi(x)|^2+\mu|\phi(x)|^4$, where $\phi(x)$ is a complex scalar field and the potential is symmetric under $U(1)$ transformations, $\phi(x) \to e^{i\alpha}\phi(x)$. This potential plays an important role in the Anderson-Higgs mechanism [And63, EB64, Hig64, GHK64], which is responsible of giving mass to the gauge bosons in the Standard model [Sch14]. In the classical limit, where no radiative corrections are included, the ground state corresponds to the field that minimizes the potential $V[\phi]$. For $m^2 < 0$, this occurs for $|\phi| \neq 0$, and the ground state spontaneously breaks the symmetry of the theory by spontaneously locking to a specific complex phase α (Fig. 1.1(a)). Since the symmetry is completely broken, $\mathcal{H}$ is trivial in this case and GS corresponds to $U(1)$ (1.4), and different ground states are connected through $U(1)$ transformations (Fig. 1.1(b)). Here $U(1)$ is an example of a *topological group*—this is, a group that has also the structure of a topological space such that both the group operation and the inverse operation are continuous—which in this case is homeomorphic to the circle, $U(1) \simeq S^1$.

In general, every symmetry group in quantum mechanics is a topological group. Moreover, the corresponding topological space can also be regarded as a *manifold*,

[5] A subgroup $\mathcal{N}$ of $\mathcal{G}$ is a normal subgroup if and only if $gng^{-1} \in \mathcal{N}$ $\forall g \in \mathcal{G}$ and $\forall n \in \mathcal{N}$.

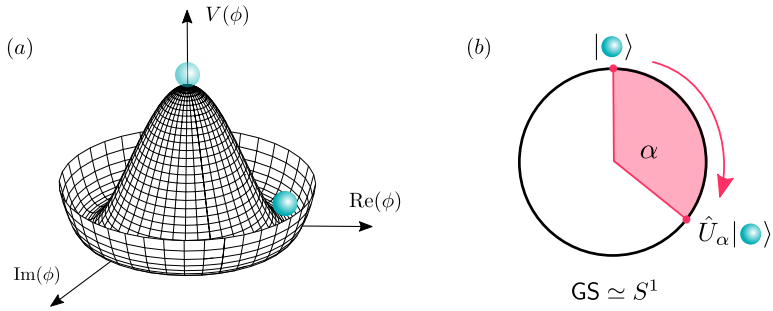

Fig. 1.1 Spontaneous symmetry breaking and ground state manifold: (a) The potential $V(\phi)$ is symmetric under $U(1)$ transformations in the field, $\phi \to e^{i\alpha}\phi$. For $m^2 > 0$, it has a minimum at $|\phi| = 0$, which has the same symmetry as the potential. At $m_c = 0$, this point becomes unstable and a new minimum appears at $|\phi| \neq 0$ for $m^2 < 0$, which is no longer symmetric. **(b)** The ground state is degenerate, as fields with the same amplitude and different complex phase have the same energy. Since the symmetry is completely broken, the ground state manifold GS is in a one-to-one correspondence with $U(1) \simeq S^1$ (1.4), inheriting its topological structure. Different states in GS are connected through $U(1)$ transformations.

this is, a topological space that is locally homeomorphic to the Euclidian space[6]. Continuous symmetries, such as $U(1)$, correspond to smooth manifolds[7], and are described by Lie groups. Discrete symmetries, on the other hand, are described by discrete groups, such as $\mathbb{Z}$ (the group of integers under addition), which is the symmetry group of translations in a crystal. The corresponding manifold is in this case a 0-dimensional manifold, this is, a discrete set of points equipped with the discrete topology[8]. In both cases, GS inherits the topological structure of the quotient set $\mathcal{R} = \mathcal{G}/\mathcal{H}$, which depends both on $\mathcal{G}$ and $\mathcal{H}$. In the following, we refer to the former as *ground state manifold*. It is precisely the non-trivial topological properties of GS as a topological space that gives rise to topological defects [Mer79], as we will see.

[6] More specifically, an n-dimensional manifold is a topological space for which each point is contained in an open set that is homeomorphic to an open set in $\mathbb{R}^n$

[7] A differentiable manifold is a manifold with an extra differentiable structure that allows one to do calculus on it. If this structure is such that derivatives, defined in a precise way, of all orders exists and are continuous then the manifold is called smooth. We refer the interested reader to Ref. [Nak03] for more details

[8] The discrete topology on X is defined by letting all subsets of X be open sets. X is a discrete topological space if it is equipped with this topology

1.1.2 Order parameter manifold

As we saw in the example above, SSB can occur as the microscopic parameters $\boldsymbol{\lambda}$ are modified across a critical point $\boldsymbol{\lambda}_c$. This leads to the so-called symmetry-breaking phase transitions, which can be characterized by *local order parameters*, and yields a classification of phases of matter in the Landau paradigm [AS06]. An order parameter is defined as the expectation value of certain observable $\mathcal{O}(\boldsymbol{\lambda}) = \langle\psi_{\text{g.s.}}(\boldsymbol{\lambda})|\,\hat{\mathcal{O}}\,|\psi_{\text{g.s.}}(\boldsymbol{\lambda})\rangle$ with the following properties: the observable $\hat{\mathcal{O}}$ is chosen in such a way that its eigenstates coincide with the inequivalent states of GS, having different non-zero eigenvalues, and has zero expectation value for symmetric states. The set of eigenvalues of $\mathcal{O}$ is thus also in a one-to-one correspondence with GS (1.4). In the following, we refer to this set of eigenvalues as the *order parameter manifold*, understanding that it has the same topological structure as GS, and we denote it by $\mathcal{R}$ in a slight abuse of notation.

We consider a medium to be *ordered* with respect to a certain symmetry if the corresponding order parameter takes a non-zero value, and *disordered* otherwise. Consider, for instance, the case of a superfluid phase, which can appears in systems of ultracold atoms [PS08], among others. This phase is characterized by the spontaneous breaking of the $U(1)$ symmetry associated to the conservation of the total number of particles. The ground state, therefore, does not possess a well defined particle number. The superfluid order parameter is defined as $\Psi = \langle\hat{\Psi}\rangle$, where $\hat{\Psi}$ corresponds to the annihilation operator in second quantization, and takes a non-zero value in the superfluid phase. As we discussed for the field theory example above, we have then $\mathcal{R} = S^1$, and the order parameter can be written as $\Psi = |\Psi|e^{i\varphi}$, where φ is referred to as the *superfluid phase* (Fig. 1.2(a)). Every value of φ, from 0 to 2π labels a degenerate ground state with the same energy.

For a general state, the local order parameter might vary in space. As we did for the superfluid order parameter, we can always decompose it as the product of two functions, $\mathcal{O}(x) = c(x)s(x)$, where c is a smooth function in the d-dimensional real space ($\mathbb{R}^d$) and s takes values in $\mathcal{R}$,

$$s\colon \mathbb{R}^d \to \mathcal{R}. \tag{1.5}$$

Each degenerate ground state is associated to a uniform function $s_r(x) = r\ \forall x \in \mathbb{R}^d$ Here we are interested in non-uniform functions where $s(x)$ is continuous everywhere except in regions of lower dimension $m < d$. Note that $\mathcal{O}(x)$ is not necessarily singular, as $c(x)$ can vanish in those regions. The singular regions of $s(x)$ are called *defects*, and the corresponding functions (1.5) are associated to certain solutions of a partial differential equation, such as the Schrödinger equation. This is particularly interesting whenever these solutions are close in energy to the ground state, as they can play a role due to the presence of quantum or thermal fluctuations. In the superfluid case, vortices are examples of point defects ($m = 0$), where the superfluid phase $\phi(x)$ becomes singular at the center of the vortex, while the amplitude van-

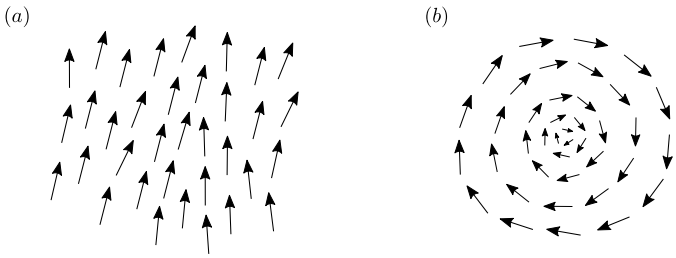

Fig. 1.2 Superfluid order parameter: The superfluid order parameter Ψ is represented in a plane using arrows, where the length and the angle of the arrow at a given point corresponds to the amplitude and phase of $\Psi(x)$. **(a)** Configuration without vortices, where the order parameter is perturbed only locally from one the uniform ground state configurations via Goldstone modes. **(b)** Vortex configuration with a singularity located at its core. Notice that the singularity in the phase can be avoided in the order parameter if the amplitude vanishes.

ishes to avoid the singularity in the full order parameter (Fig. 1.2(b)). Vortices are low-energy solutions of the Gross-Pitaevskii equation, which is a non-linear partial different equation for the order parameter $\Psi(x)$ obtained as a mean-field approximation of the Schrödinger equation. In this formulation, vortices are similar to other topological defects obtained in classical physics, such as in hydrodynamics or non-linear optics.

In the literature, the term vortex is used in general for $m = d - 2$ dimensional defect. Other standard notations include domain walls and monopoles, for $m = d - 1$ and $m = d - 3$, respectively. In high-energy physics, an instanton is a point defect in a $d = 4$ Euclidean spacetime, after a Wick rotation to imaginary time is performed. We note that there also exists a class of topological defects that do not require singularities, that some authors referred to as topological solitons [BRvW19]. We will not consider them here, however. In the following, we restrict the term soliton for point defects in $d = 1$.

1.1.3 Homotopy group and defect classification

An ordered medium is thus characterized by a map between two topological spaces, the d-dimensional real space and the quotient set (1.5). Given a broken symmetry, we are interested in classifying different configurations up to continuous transformations. The reason is that continuous deformations of the order parameter cost only a finite energy, and can be induced by local quantum and thermal fluctuations. Examples of excitations associated to these changes are Goldstone modes, which appear when a continuous symmetry is spontaneously broken, such as spin waves in the Heisenberg model [Sac11]. Topological defects, on the other hand, are a dif-

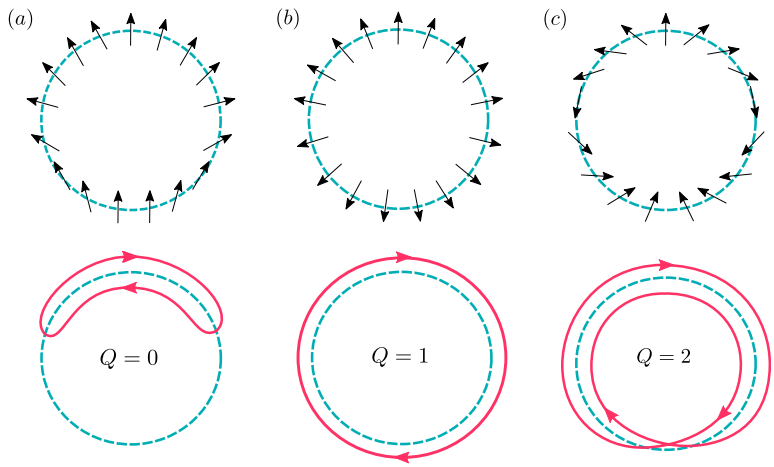

Fig. 1.3 Winding number: Superfluid vortices are classified by the first homotopy group $\pi_1(S^1) = \mathbb{Z}$ of inequivalent loops in the circle. In the figure, the dashed and solid lines corresponds to loops in $\mathbb{R}^2$ and S^1, respectively (f and g in the main text), and the arrows correspond to the values of the order parameter. **(a)** If there are no singularities, the loop in S^1 can be deformed continuously to a point. The order parameter configuration is thus trivial and has topological charge $Q = 0$. **(b)** and **(c)** correspond to vortex configurations with non-zero winding numbers, and topological charges $Q = 1$ and $Q = 2$, respectively.

ferent type of excitation, where an extensive amount of energy is usually required to remove them from the system. The latter is associated to a global change in the order parameter, making defects stable against local perturbations and thus topological.

We associated topological defects with the existence of singular maps. The latter cannot be continuously deformed into non-singular maps, such as the ones that characterize a ground state configuration. In algebraic topology, the mathematical structure that classifies inequivalent maps up to continuous transformations is the homotopy group [Nak03]. Before entering into more details, let us come back to our superfluid example and introduce the concept of a loop.

A loop in a topological space X is a continuous function $f\colon [0,1] \to X$ with $f(0) = f(1)$. If one thinks about a parameter $t \in [0,1]$ as a time variable, the loop traverses a closed contour in X, and $f(t)$ gives the position within the contour for a given time. Consider now a loop in a superfluid region, given by $g\colon [0,1] \to \mathbb{R}^2$. Since the function $s(x)$ (1.5) maps every point in $\mathbb{R}^2$ to a point in S^1, the composition $f(t) = s(g(t))$ can be viewed as a loop in the circle (Fig. 1.3). If $g(t)$ does not encircles any singularity in $s(\mathbb{R}^2)$, then $f(t)$ will not complete a turn

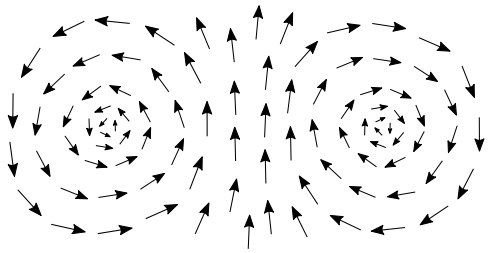

Fig. 1.4 $\mathbb{Z}$ **topological charge:** superfluid vortices are characterized by integer charges. Vortices can be combined forming new defects with a charge given by the sum of its parts. In the figure, two vortices with charge $Q = +1$ form a $Q = +2$ vortex.

around the circle and, therefore, can be continuously deformed into a point. This is not the case, however, if $g(t)$ encircles a vortex. These two situations are regarded as inequivalent.

Let us be a bit more precise now. Two loops f_1 and f_2 are said to be homotopic at $x_0 \in X$ if there exists a continuous function $F\colon [0,1] \times [0,1] \to X$ that interpolates between them, this is, if $F(0,x) = f_1(x)$ and $F(1,x) = f_2(x)$ $\forall x \in [0,1]$, and $F(t,0) = F(t,1) = x_0$ $\forall t \in [0,1]$. The latter defines an equivalence relation in the set of loops. The set of homotopy classes of loops in X with base point x_0 has a group structure, called the first homotopy group $\pi_1(\mathcal{R}, x_0)$, or *fundamental group*. The group operation is defined by "gluing together" loops, this is, the product of two loops f_1 and f_2 is a new loop f defined by traversing first f_1 and then f_2. Loops that are in the same equivalence class as the constant map are said to be homotopically trivial, and they correspond to the identity element. If $\mathcal{R}$ is abelian, the groups $\pi_1(\mathcal{R}, x_0)$ with different x_0 are all isomorphic to each other [Mer79].

The possible vortices that can appear in a superfluid phase are thus given by $\pi_1(S^1) = \mathbb{Z}$, the group of integers under addition. Each class is determined by the number of times the loop goes around the circle, which is also called the *winding number* of the loop—a notion that will appear again in the classification of topological phases. The group structure allows us to add topological defects. For example, two vortices with charges $+1$ can combine to form a vortex with charge $+2$ (Fig. 1.4).

One can define higher homotopy groups. In particular, $\pi_n(\mathcal{R}, x_0)$ is the set of equivalence classes of maps $f\colon [0,1]^n \to \mathcal{R}$, where two maps belong to the same class if they are homotopic to each other. Here $[0,1]^n$ denotes the hypercube in $\mathbb{R}^n$, and the homotopy relation generalizes straightforwardly from $n = 1$. In general, an m-dimensional defect in a d-dimensional medium is classified by the n-homotopy group $\pi_n(\mathcal{R}, x_0)$, where $n = d - m - 1$ [Mer79]. The equivalence class associated to the defect is called topological charge, which constitutes a conserved physical quantity for the defect, quantized up to local perturbations. In the case of S^1, every

homotopy group is trivial for $n > 1$, this is, it consists only on the identity element. Therefore, vortices are the only type of defects allowed in a two-dimensional superfluid. One example where non-trivial higher homotopy groups exists is the Heisenberg model. In the ferromagnetic phase, the $SU(2)$ does not break completely, since the ground state remains invariant under $U(1)$ transformations, and the order parameter manifold corresponds to the 2-sphere, $\mathcal{R} = SU(2)/U(1) \equiv S^2$. In three dimensions, monopoles are thus allowed, characterized by the second homotopy group $\pi_2(S^2) = \mathbb{Z}$.

So far we have given examples where the spontaneously broken symmetry is continuous and can be characterized by a Lie group, such as $U(1)$ or $SU(2)$. The theory of topological defects, however, can be applied to any symmetry group. As we have mentioned, discrete symmetry groups are 0-dimensional manifolds, a structure that is inherited by $\mathcal{R}$ after SSB. In that case, each path-connected component reduces to a point, and the n-homotopy group is always trivial for $n > 1$. The only non-trivial group is $n = 0$, which corresponds to the set of different components, and thus coincides with $\mathcal{R}$. Therefore, if $\mathcal{R}$ is discrete, only $d-1$-dimensional defects are allowed in the system. One example are domain walls in ferromagnetically-ordered spin systems [Sac11]. Along this thesis, specifically in chapters 5, 6 and 7, we will encounter examples of topological defects that arise after the spontaneous breaking of discrete symmetries.

1.1.4 Defects in physical systems

We finish this section with some comments regarding the presence of topological defects in physical systems. The example given so far, such as vortices in superfluids and domain walls in spin systems, correspond to condensed matter systems. However, as we mentioned at the beginning, topological defects are general solutions of the Schrödinger equation that describes many-body systems, associated to the spontaneous breaking of the system's symmetries. Therefore, they also appear in high-energy physics contexts. One example are instantons [VZNS82], point defects of non-abelian gauge theories in $3 + 1$-dimensional space-time, that are classified by the third homotopy group.

Other examples include domain walls and topological strings in cosmology, as analyzed by Kibble in Ref. [Kib76]. This work considers as well the production of topological defects when the system goes through a symmetry-breaking phase transition. The so-called Kibble-Zurek mechanism—extended by Zurek to condensed matter systems [Zur85]—relates the rate at which a system goes through a critical point with the density of defects that appear once it equilibrates in the symmetry-broken phase. For any finite velocity, the adiabatic theorem breaks down sufficiently close to the critical point, as the gap closes. The final state contains, therefore, a superposition of the instantaneous ground state and other excited states, including topological defects.

In general, although topologically non-trivial configurations can be close in energy to the trivial one, an infinite energy barrier separates both in the thermodynamic limit, since an extensive part of the system must be modified to connect both. As it occurs in the Kibble-Zurek mechanism, however, pairs of defects can be created from the vacuum with a finite energy cost, due to, for example, local quantum or thermal fluctuations. These defects can then separate and, if the system is sufficiently large, one can find regions around them that locally resemble non-trivial topological sectors. Finally, although in this section we only consider defects as excited states, in chapter 5 we will show how, in the presence of quantum matter, defects can also appear in the ground state of the system. In that case, defects are defined with respect to the ordered topologically-trivial vacuum that appears in the absence of matter.

1.2 The geometry of quantum states

As we mentioned above, there are many examples from classical physics where topological defects play an important role. There are, however, other topological phenomena that are specific to quantum systems. In this section, we review some of them by focusing on the non-trivial topological properties of the set of quantum states viewed as a topological space. We start the discussion by noting how the phase indeterminacy in quantum mechanics can give rise to non-trivial geometric phases in the evolution of a quantum state, such as the Aharonov-Bohm phase. We discuss the relevant concepts first from a physics perspective, associating them to specific examples. Finally, we will generalize these notions using the theory of fiber bundles, where the non-trivialities in the topological structure associated to interesting physical phenomena will become apparent.

1.2.1 The phase indeterminacy

The first postulate of quantum mechanics associates every quantum system to a separable complex Hilbert space $\mathcal{H}$. Quantum states, however, do not correspond to vectors in $\mathcal{H}$. Since the phase of a state can not be measured experimentally, two vectors $|\psi\rangle$ and $|\psi'\rangle$ that differ only by a phase factor, this is, $|\psi'\rangle = e^{i\varphi}|\psi\rangle$, should represent the same state. Therefore, to properly define quantum states one introduces first an equivalence relation $\sim$ in $\mathcal{H}' = \mathcal{H} \setminus \{0\}$. In particular, two vectors $u, v \in \mathcal{H}'$ are said to be equivalent, $u \sim v$, if $u = zv$ for any $z \in \mathbb{C} \setminus \{0\}$. The corresponding set of equivalence classes, also known as *rays*, forms a *projective Hilbert space* $P(\mathcal{H})$. Quantum states are then associated to the subspace of $P(\mathcal{H})$ formed by unit rays, this is, rays with norm one,

$$[|\psi\rangle] = \{e^{i\varphi}|\psi\rangle \mid \varphi \in \mathbb{R},\ \||\psi\rangle\| = 1\} \tag{1.6}$$

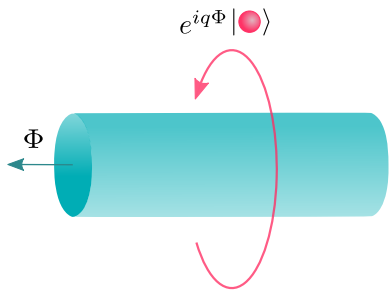

Fig. 1.5 Aharonov-Bohm effect: A particle moving around a closed loop that encircles a solenoid picks up a phase $\gamma = q\Phi$, where Φ is the flux that pierces the solenoid. This is true even if the particle is sufficiently far away a traverses a path where the magnetic field is zero everywhere.

which is itself a projective Hilbert space. This condition makes sure that measurable quantities, such as the expectation value of an observable $\hat{A}$, $\langle\psi|\,\hat{A}\,|\psi\rangle$, are independent of the representative of the class. In the following, we will use any $|\psi\rangle \in [|\psi\rangle]$ to denote the whole class.

The fact that quantum phases are not measurable does not mean that they can be neglected. For instance, the superposition state $\sum_n c_n\,|\psi_n\rangle$ is in general different from $\sum_n c_n e^{i\varphi_n}\,|\psi_n\rangle$, even if $|\psi_n\rangle = e^{i\varphi_n}\,|\psi_n\rangle\ \forall n$. In other words, the apparent redundancy in the description of quantum states have physical consequences. This property is reminiscent to the case of local symmetries in gauge theories. As we will see at the end of this section, the mathematical structure that lies behind is the same in both cases.

One of the earliest predictions of the non-trivial consequences of this phase indeterminacy was the Aharonov-Bohm effect [AB59], where the relation between phase indeterminacy and gauge invariance is already apparent. The effect consists on the accumulation of a phase shift when a charged particle travels in a region of space with a non-zero electromagnetic vector potential $\mathcal{A}(\mathbf{r})$, even if the magnetic field $\mathcal{B}(\mathbf{r}) = \nabla \times \mathcal{A}(\mathbf{r})$ is zero along the path. As an example, consider a particle moving sufficiently far from a solenoid (Fig. 1.5). In this situation, the magnetic field is non-zero only within the solenoid. Nevertheless, the particle accumulates a phase $\gamma = q\int_{\mathcal{C}} \mathrm{d}\mathbf{r}\cdot\mathcal{A}(\mathbf{r})$, where $\mathcal{C}$ corresponds to the path of the moving particle. If the latter is a closed curve around the solenoid, the accumulated phase can be written as $\gamma = \frac{q}{\hbar}\Phi$ using Stokes' theorem, where Φ is the magnetic flux piercing the solenoid. The Aharonov-Bohm effect can be measured in interference experiments [Cha60], showing the importance of gauge invariance in the description of electromagnetism. The gauge-dependent vector potential is thus not just a mathematical construct useful for computations, but a fundamental object with non-trivial physical consequences. We will now argue that the same is true for the

phase of a general quantum system.

1.2.2 Geometric phase

The Aharonov-Bohm phase can be regarded as a particular example of the more general notion of a *geometric phase*, also known as the Berry phase [Ber84]. As we will see, the term geometric refers here to the fact that, when such a phase manifests in a system, its properties will not depend on the dynamics of a certain process but on the geometric structure of the quantum state [XCN10]. To see this, let us consider a Hamiltonian $\hat{H}(\boldsymbol{\lambda}_t)$, where $\boldsymbol{\lambda}\colon [0,T] \to \mathcal{M}$ is a curve in the parameter space $\mathcal{M}$, parametrized by a time variable t in the interval $[0,T]$. In the following, we assume that $\mathcal{M}$ is a smooth manifold. At a given time t, the Hamiltonian can be diagonalized using an orthonormal basis $\{|n(\boldsymbol{\lambda}_t)\rangle\}_n$,

$$\hat{H}(\boldsymbol{\lambda}_t)\,|n(\boldsymbol{\lambda}_t)\rangle = \epsilon_n(\boldsymbol{\lambda}_t)\,|n(\boldsymbol{\lambda}_t)\rangle\,. \tag{1.7}$$

Let us prepare the system in the instantaneous ground state $|n(\boldsymbol{\lambda}_0)\rangle$ at $t=0$. According to the adiabatic approximation, if the rate of change in $\boldsymbol{\lambda}$ is sufficiently small, the time-evolved state $|\psi_n(T)\rangle$ at $t=T$ coincides, up to a phase, with the instantaneous ground state $|n(\boldsymbol{\lambda}_T)\rangle$,

$$|\psi_n(T)\rangle = e^{i\gamma_n(T)}\exp\left[-\frac{i}{\hbar}\int_0^T \mathrm{d}t\,\epsilon_n(\boldsymbol{\lambda}_t)\right]|n(\boldsymbol{\lambda}_T)\rangle\,, \tag{1.8}$$

where we wrote the possible phase difference as the sum between a phase γ_n, that we call the Berry phase, and the so-called dynamical phase. By plugging this expression into the Schrödinger equation, one can express the accumulated phase γ_n at time $t=T$ as a line integral

$$\gamma_n(T) = \int_{\mathcal{C}} \mathrm{d}\boldsymbol{\lambda}\cdot\mathcal{A}^n(\boldsymbol{\lambda}), \tag{1.9}$$

where

$$\mathcal{A}^n(\boldsymbol{\lambda}) = i\langle n(\boldsymbol{\lambda})|\,\partial_{\boldsymbol{\lambda}}\,|n(\boldsymbol{\lambda})\rangle \tag{1.10}$$

is a vector field called the *Berry connection*. Note that, although to calculate the phase $\gamma_n(T)$ we integrate the Berry connection along the curve $\boldsymbol{\lambda}(t)$ (1.9), the latter is defined in the whole parameter space $\mathcal{A}^n\colon \mathcal{M} \to \mathbb{R}^m$ (1.10). In a slight but standard abuse of notation, we use $\boldsymbol{\lambda}$ to denote both the curve in $\mathcal{M}$ as well as a general vector in this space.

Let us perform now a local phase transformation, $|n(\boldsymbol{\lambda})\rangle \to e^{i\theta(\boldsymbol{\lambda})}\,|n(\boldsymbol{\lambda})\rangle$, where $\theta(\boldsymbol{\lambda})$ varies in general with $\boldsymbol{\lambda}$, and we only require it to be smooth and single valued along the path. Since, as we have already pointed out, physically relevant quantities should be invariant under such transformation, the phase indeterminacy

in quantum mechanics can be regarded as a $U(1)$ gauge symmetry in the structure of quantum states. One can establish then a parallelism with electromagnetism, where the Berry connection plays a similar role to the vector potential. In particular, it transforms in a similar way

$$\mathcal{A}^n(\boldsymbol{\lambda}) \to \mathcal{A}^n(\boldsymbol{\lambda}) - \partial_{\boldsymbol{\lambda}}\theta(\boldsymbol{\lambda}). \tag{1.11}$$

The phase $\gamma_n(T)$ is not a gauge invariant quantity in general, with

$$\gamma_n(T) \to \gamma_n(T) - \theta(\boldsymbol{\lambda}_T) + \theta(\boldsymbol{\lambda}_0). \tag{1.12}$$

However, if the curve is closed, $\boldsymbol{\lambda}_0 = \boldsymbol{\lambda}_T$, we have $\theta(\boldsymbol{\lambda}_T) - \theta(\boldsymbol{\lambda}_0) = 0 \bmod 2\pi$, since $\theta(\boldsymbol{\lambda})$ is single valued. Therefore, $\gamma_n \bmod 2\pi$ is a gauge-invariant quantity for closed curves in the parameter space. This phase is called geometrical since it does not depend on the specific time evolution, but only on the geometric properties of the space $\mathcal{M}$—just as in the case of the Aharonov-Bohm effect described above. In his original paper [Ber84], Berry interpreted the Aharonov-Bohm phase as a Berry phase. In that case, the Berry connection turns out to be precisely the electromagnetic vector potential.

Following the parallelism with electromagnetism, we can use the connection $\mathcal{A}^n$ to define a *Berry curvature*

$$\Omega^n_{\mu\nu}(\boldsymbol{\lambda}) = \frac{\partial \mathcal{A}^n_\nu}{\partial \lambda^\mu} - \frac{\partial \mathcal{A}^n_\mu}{\partial \lambda^\nu} = i\left[\left\langle \frac{\partial n}{\partial \lambda^\mu}\middle|\frac{\partial n}{\partial \lambda^\nu}\right\rangle - \left\langle \frac{\partial n}{\partial \lambda^\nu}\middle|\frac{\partial n}{\partial \lambda^\mu}\right\rangle\right], \tag{1.13}$$

analogous to the magnetic field. The Berry curvature can also be written as

$$\Omega^n_{\mu\nu}(\boldsymbol{\lambda}) = i\sum_{m\neq n} \frac{\langle n|\,\partial\hat{H}/\partial\lambda^\mu\,|m\rangle\,\langle m|\,\partial\hat{H}/\partial\lambda^\nu\,|n\rangle - (\nu\leftrightarrow\mu)}{(\epsilon_n - \epsilon_m)^2}, \tag{1.14}$$

from which a local conservation law follows,

$$\sum_n \Omega^n_{\mu\nu}(\boldsymbol{\lambda}) = 0. \tag{1.15}$$

Using Stokes' theorem, we can write the Berry phase as an integral over the surface $\mathcal{S}$ enclosed by the path $\boldsymbol{\lambda}$,

$$\gamma_n = \int_{\mathcal{S}} \mathrm{d}\lambda^\mu \wedge \mathrm{d}\lambda^\nu \,\frac{1}{2}\Omega^n_{\mu\nu}(\boldsymbol{\lambda}). \tag{1.16}$$

Moreover, in the case of a three dimensional parameter space, we can define the *first Chern number* as the integral of the Berry curvature over a closed two-dimensional surface,

$$c_n = \frac{1}{2\pi}\oint_{\mathcal{S}} \mathrm{d}\boldsymbol{\lambda}\cdot\boldsymbol{\Omega}(\boldsymbol{\lambda}). \tag{1.17}$$

The first Chern number is quantized to integer values that depend on the singularities in $\boldsymbol{\Omega}(\boldsymbol{\lambda})$ enclosed by the surface $\mathcal{S}$. These singularities occur in general at degeneracy points (1.14), this is, whenever $\epsilon_n(\boldsymbol{\lambda}) = \epsilon_m(\boldsymbol{\lambda})$, for $n \neq m$.

To help illustrate these concepts, let us consider a two-level Hamiltonian, which can be written in the most general form as

$$\hat{H}^{\sigma}(h_0, \boldsymbol{h}) = h_0 \, \mathbb{I} + \boldsymbol{h} \cdot \hat{\boldsymbol{\sigma}}, \tag{1.18}$$

where $\boldsymbol{h} = (h_x, h_y, h_z) \in \mathbb{R}^3$ is a vector and $\hat{\boldsymbol{\sigma}} = (\hat{\sigma}^x, \hat{\sigma}^y, \hat{\sigma}^z)$, where σ^{μ} are Pauli matrices. In the following, we take $h_0 = 0$, since this term is just a shift in energy and does not change the eigenstates. For a parametrization of the form $\boldsymbol{h} = h\,(\sin\theta\cos\phi, \sin\theta\sin\phi, \cos\theta)$, where h, θ and ϕ are spherical coordinates, we can write the eigenstates of the Hamiltonian (1.18) as

$$|u_0(\theta,\phi)\rangle = \begin{pmatrix} \sin\frac{\theta}{2}\, e^{-i\phi} \\ -\cos\frac{\theta}{2} \end{pmatrix}, \quad |u_1(\theta,\phi)\rangle = \begin{pmatrix} \cos\frac{\theta}{2}\, e^{-i\phi} \\ \sin\frac{\theta}{2} \end{pmatrix}, \tag{1.19}$$

The corresponding energies are $\epsilon_0 = -h$ and $\epsilon_1 = h$. We can calculate the Berry curvatures using (1.13),

$$\Omega^0(\theta,\phi) = \frac{1}{2}\sin\theta, \quad \Omega^1(\theta,\phi) = -\frac{1}{2}\sin\theta, \tag{1.20}$$

which satisfies the conservation law (1.15). There is only one degeneracy point located at $h = 0$. If we compute now the surface integral of each curvature on a 2-sphere centered at the origin, and thus enclosing the degeneracy point, we obtain for the first Chern number the values $c_0 = 1$ and $c_1 = -1$ (1.17). In electromagnetism, the Berry connection given by (1.20) corresponds to the magnetic field generated by a monopole with a quantized charge given by the associated Chern number [Dir31]. In the next section, we will see how this simple example allows us to describe non-trivial topological phases of matter.

1.2.3 Fiber bundle theory

Before applying the previous concepts to the study of phases of matter, we finish this section with a brief sketch of the mathematical structures behind them. In particular, we introduce the notion of fiber bundles, and relate them to the structure of quantum states. By doing so, we will relate geometrical concepts such as connections and curvatures, dealing with the local structure of states, with topological invariants such as Chern or winding numbers, that characterize their global properties.

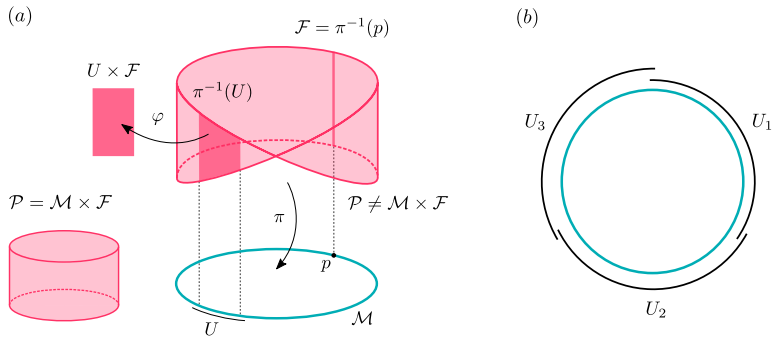

Fig. 1.6 Möbius strip as a non-trivial fiber bundle: (a) As opposed to the cylinder, the Möbius strip is an example of a $\mathcal{P}(S^1, \mathbb{R})$ non-trivial fiber bundle. In the figure, we represent the different elements composing the bundle. The fiber $\mathcal{F} = \mathbb{R}$ can be obtained from a point p in $\mathcal{M} = S^1$ by applying the inverse of the projection map π, $\mathcal{F} = \pi^{-1}(p)$. For each neighborhood U of S^1, $\pi^{-1}(U)$ is homeomorphic to $U \times \mathcal{F}$ through certain homeomorphism φ. Here we represent the real line as a finite interval for better visualization. The presence of a twist in the Möbius strip is an obstruction to define a global trivialization. **(a)** Example of a local trivialization for the Möbius strip, where the base manifold S^1 is expressed as the union of three open sets U_i.

Fiber bundles

A fiber bundle is a space that locally looks like a product space, but globally might not be so. More precisely, it is a structure composed by different elements, $(\mathcal{P}, \mathcal{M}, \pi, \mathcal{F})$, where $\mathcal{P}$, $\mathcal{M}$ and $\mathcal{F}$ are topological spaces called total space, base space and fiber, respectively. The map $\pi\colon \mathcal{P} \to \mathcal{M}$ is a continuous surjection called the projection map that satisfies the so-called *local triviality* condition: for every $x \in \mathcal{M}$ there is an open neighborhood $U \subset \mathcal{M}$ such that there exists a homeomorphism $\varphi\colon \pi^{-1}(U) \to U \times \mathcal{F}$, for which $\pi \circ \phi^{-1}(p) = p$ for every $p \in U$. A set $\{(U_i, \varphi_i)\}$ that fulfills this condition is called a *local trivialization* or *atlas* of the fiber bundle, and each pair (U_i, φ_i) is referred to as a *chart*. In general, a fiber bundle can be trivialized in many different ways. In the following, we will denote a fiber bundle with $\mathcal{P}(\mathcal{M}, \mathcal{F})$, keeping in mind that a local trivialization should be defined to fully characterize it.

A fiber bundle is said to be *trivial* if there exists a *global* trivialization, this is, a global homeomorphism $\varphi\colon \pi^{-1}(\mathcal{M}) = \mathcal{P} \to \mathcal{M} \times \mathcal{F}$, and *non-trivial* or *twisted* otherwise. In the former case, the bundle is homeomorphic to a direct product, $\mathcal{P} \simeq \mathcal{M} \times \mathcal{F}$. A simple example of a trivial bundle is given by the cylinder, with $\mathcal{P}(S^1, \mathbb{R}) \simeq S^1 \times \mathbb{R}$. A Möbius strip, on the other hand, is an example of a non-trivial bundle (Fig. 1.6(a)). Although in both cases the base space and fiber are the same, the latter is not globally equivalent to a product space since it contains

a twist. The Möbius strip is an example of a vector bundle, this is, a fiber bundle where the fiber has a vector space structure. In the following, we restrict ourselves to vector bundles, and assume that the space $\mathcal{M}$ is a smooth manifold. Most of the discussion, nevertheless, applies to more general fiber bundles.

The impossibility to define a global trivialization is in general called an *obstruction*. In the case of the Möbius strip, at least two neighborhoods are needed to completely defined the fiber bundle. Notice again that this can be done in different ways. Another simple example corresponds to fiber bundles of the form $\mathcal{P}(S^1, S^1)$. A trivial bundle corresponds in this case to the torus, where $\mathbb{T}^2 \simeq S^1 \times S^1$. The Klein bottle, on the other hand, contains a twist and can not be written globally as a product space.

Structure group, transition functions and sections

A fiber bundle is locally equivalent to a product space on each neighborhood U_i. Different neighborhoods can be connected in their overlapping regions $U_i \cap U_j$ through the maps

$$\varphi_i \varphi_j^{-1} \colon U_i \cap U_j \times \mathcal{F} \to \colon U_i \cap U_j \times \mathcal{F}. \tag{1.21}$$

These maps can be characterized in terms of a symmetry group $\mathcal{G}$, called the *structure group* or *gauge group* of the fiber bundle. In particular, $\mathcal{G}$ is a topological group acting continuously and faithfully on the fiber $\mathcal{F}$ from the left, this is, a group of homeomorphism on $\mathcal{F}$. A $\mathcal{G}$-atlas is an atlas where the functions (1.21) are given by

$$\varphi_i \varphi_j^{-1}(x, \xi) = (x, t_{ij}(x)\, \xi) \tag{1.22}$$

where $t_{ij} \colon U_i \cap U_j \to \mathcal{G}$ are continuous maps called *transition functions*, which completely characterize the degree of twisting of a fiber bundle.

Consider again the previous example, $\mathcal{P}(S^1, \mathbb{R})$, and, as a structure group, the general linear group $\mathrm{GL}(\mathbb{R})$. We choose the following three neighborhoods,

$$\begin{aligned} U_1 &= (0 - \epsilon, \pi/3 + \epsilon), \\ U_2 &= (\pi/3 - \epsilon, 2\pi/3 + \epsilon), \\ U_3 &= (2\pi/3 - \epsilon, 2\pi + \epsilon), \end{aligned} \tag{1.23}$$

for some $\epsilon > 0$ (Fig. 1.6(b)). In the case of the cylinder, we can define the transition functions $t_{12} = t_{23} = t_{31} = 1$, where $1 \colon \xi \to \xi$ is the identity in $\mathrm{GL}(\mathbb{R})$. For the Möbius strip we have $t_{12} = t_{23} = 1$ and $t_{31} = -1$, where $-1 \colon \xi \to -\xi$. The impossibility to define trivial transition functions everywhere is an obstruction of the fiber bundle.

Finally, another feature that characterizes non-trivial fiber bundles is the absence of *global sections*. A (local) *section*, also called *vector field* in the case of

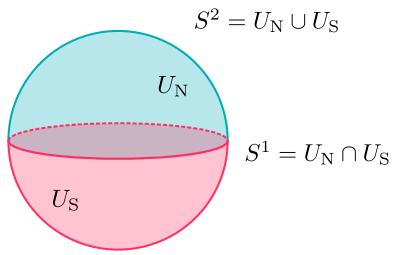

Fig. 1.7 Sphere bundle: local trivialization for the non-trivial principal fiber bundle $\mathcal{P}(S^2, U(1))$, formed by two open sets corresponding to the north and south hemispheres, $S^2 = U_\mathrm{N} \cup U_\mathrm{S}$. The transition function is defined on the intersection $S^1 = U_\mathrm{N} \cap U_\mathrm{S}$.

vector bundles, is a continuous map $f\colon U \to \mathcal{P}$ defined on a neighborhood $U \in \mathcal{M}$ such that $\pi(f(x)) = x\ \forall x \in U$. Global sections are sections defined over the whole space $\mathcal{M}$. While a global section clearly exists in the case of the cylinder, this is not true for the Möbius strip, where one always finds a discontinuity in S^1. Something similar occurs for tangent bundles on the n-sphere S^n, a result known as the hairy ball theorem [Nak03].

Two-level quantum system as a principal fiber bundle

Now that we have all the necessary ingredients, we can go back to the two-level system introduced in the previous section (1.18). It is easy to realize that the set of ground states $|u_0(\theta,\phi)\rangle$ is described by the vector bundle $\mathcal{P}(S^2, S^1)$, with an associated gauge group $\mathcal{G} = U(1)$. It is, in particular, a *principal fiber bundle*, since S^1 is a principal homogeneous space for $U(1)$[9]. We can then identify the fiber with the gauge group as a topological space, $S^1 \simeq U(1)$, and write $\mathcal{P}(S^2, U(1))$.

The states $|u_0(\theta,\phi)\rangle$ form a non-trivial bundle since we can not defined a global section on it. In other words, we can not find a global *gauge choice*, this is, a function $\varphi(\theta,\phi)$ that specifies the total phase of the state $|u_0(\theta,\phi)\rangle$, which is continuous and single valued everywhere in S^2. In Eq. (1.19) we wrote the states using a global gauge, but this choice is not single-valued. This is the reason why, if we follow the change in the phase of the state along a circle of fixed θ, we get a change of π after a full circle, which is just the Berry phase (1.9). A possible choice of a local gauge consist on fixing the phase of the state in each hemisphere of the sphere (Fig. 1.7). For example, we choose

$$|u_0^\mathrm{N}(\theta,\phi)\rangle = \begin{pmatrix} -\sin\frac{\theta}{2} \\ \cos\frac{\theta}{2}\, e^{i\phi} \end{pmatrix}, \quad |u_0^\mathrm{S}(\theta,\phi)\rangle = \begin{pmatrix} -\sin\frac{\theta}{2}\, e^{-i\phi} \\ \cos\frac{\theta}{2} \end{pmatrix}, \tag{1.24}$$

[9] A topological space $\mathcal{F}$ is a principal homogeneous space for a group $\mathcal{G}$ if $\mathcal{G}$ acts freely and transitively on $\mathcal{F}$, this is, if for every $\xi_1, \xi_2 \in \mathcal{F}$, there exists a unique $g \in \mathcal{G}$ such that $\xi_2 = \xi_1 \cdot g$, where $\cdot$ denotes the right action of $\mathcal{G}$ on $\mathcal{F}$.

In this case, there is just one transition function, which is given by

$$\begin{aligned} t_{\mathrm{NS}} \colon S^1 &\to U(1) \\ \phi &\to e^{-i\phi} \end{aligned} \tag{1.25}$$

where the intersection $U_{\mathrm{N}} \cap U_{\mathrm{S}} = S^1$ corresponds here to the equator of the sphere.

Regardless of the gauge choice, we will always find such a singularity when trying to define a global gauge. A gauge transformation just moves the singularity to a different point in the circle. In the language of fiber bundles, this corresponds to a transformation between sections, given in terms of transition functions defined by the gauge group acting on the fiber (1.22). The Berry phase, a gauge invariant quantity, will not change its value, and the same is true for the Chern number.

As we have mentioned before, the transition functions characterize completely a fiber bundler. A complete classification of the different principal vector bundles of the type $\mathcal{P}(S^2, U(1))$ reduces then to the topological classification of the possible transition functions $t_{\mathrm{NS}} \colon S^1 \to S^1$. As we saw in the last section, inequivalent loops in the circle form the first homotopy group $\pi_1(S^1) = \mathbb{Z}$, and the corresponding class for each loop is given by an integer winding number. Intuitively, the winding number characterizes the degree of twisting of the fiber bundle.

In this particular example, the winding number associated to Eq. (1.25) is one, which coincides with the first Chern number calculated from the Berry curvature (1.17). This connection is a particular case of the more general Chern-Gauss-Bonnet theorem, relating global topological invariants with the local geometric structure given by the curvature. Both connections and curvatures can be defined for general vector bundles, providing information on how to compare vector fields on different points of their base manifolds, a crucial requirement to define derivatives. The same is true for topological invariants. For example, higher Chern numbers can be defined to characterize the global structure of even-dimensional manifolds. They are particular examples of *characteristic classes*, which are used in algebraic topology to classify principal fiber bundles according to their degree of twisting. We will not review here the main tools from differential geometry that are necessary to classify general vector bundles, nor introduce the general Chern-Gauss-Bonnet theorem. We refer the interested reader to Ref. [Nak03] for further details. For the purpose of classifying phases of matter, specially in one and two dimensions, the definitions of the Berry connection and Berry curvature given in Sec. 1.2.2—specific to fibers describing quantum states—will suffice.

As a summary, we can say that quantum states are described by principal (complex) vector bundles with a $U(1)$ gauge group, $\mathcal{P}(\mathcal{M}, U(1))$ [Sim83], and they can be classified using topological invariants. The conservation law (1.15) implies that the bundle associated to the whole spectrum of a given Hamiltonian describing the system is trivial. As we have seen, however, subbundles associated to individual en-

ergy levels can be non-trivial.[10] Here we have defined the bundle of quantum states as eigenstates of a given Hamiltonian that depends on parameters from a manifold $\mathcal{M}$. However, we can be more general and take this manifold as the projective Hilbert space $\mathcal{M} = P(\mathcal{H})$, connecting with the definition given at the beginning of this section, such that quantum states are defined independently of any specific Hamiltonian. Finally, as we pointed out in the example of the Aharonov-Bohm effect and Dirac's monopoles, similar structures appear also in electromagnetism. In general, gauge theories are principal fiber bundles with a general gauge group $\mathcal{G}$, which corresponds to the symmetry group of the theory [WY75, DV80].

1.3 Topological phases

In this section, we show the non-trivial topological structure in the set of quantum states, described in the last section in terms of fiber bundles, can give rise to novel phases of matter known as *topological phases*. In Sec. 1.1, we mentioned how, according to Landau's paradigm, different phases can be classified according the different symmetries they break. More specifically, we consider here quantum phases defined as sets of quantum states that can be adiabatically connected to each other. According to Landau, these sets of states share the same symmetries, and they are separated in the phase diagram by phase transitions associated to the spontaneous breaking of a certain symmetry. Different topological phases, on the other hand, can have the same symmetries. They are instead characterized by topological invariants that take different values in different phases. These invariants, however, that depend on the topological structure of the quantum states, will not change within each phase, as long the gap does not close. We focus first on non-interacting topological phases, which are completely classified in terms of their corresponding Bloch bundle. We discuss some examples of topological insulators using simple models, where the most important concepts appear. Finally, we consider the role of interactions, where a full classification is still in progress, and we discuss both the case of symmetry-protected topological phases as well as topologically-ordered states.

1.3.1 Bloch bundle

In the last section we have seen examples where the non-trivial topological properties of the bundle $\mathcal{P}(\mathcal{M}, U(1))$ describing the ground state of a system have physical consequences. In particular, in the Aharonov-Bohm effect, where $\mathcal{M} = \mathbb{R}^3 \setminus \{0\}$, the system acquires a non-trivial phase that can be measured in an interference experiment. This occurs as the system travels in real space along a closed trajectory, which can be imposed by an external force. In general, however, $\mathcal{M}$ is not

[10] A bundle $\mathcal{P}'(\mathcal{M}, \mathcal{F})$ is a subbundle of $\mathcal{P}(\mathcal{M}, \mathcal{F})$ if $\mathcal{P}'$ is a subspace of $\mathcal{P}$ and $\pi' = \pi|_{\mathcal{P}'}$.

necessary a subspace of $\mathbb{R}^3$, but a general smooth manifold that labels the possible quantum states up to a phase, as we assumed throughout last section. Nevertheless, in the general case one can also find examples of physical observables that can be expressed in terms of integrals of a Berry connection or curvature over closed loops or surfaces in $\mathcal{M}$.

In condensed matter, this is the case for certain macroscopic observables such as the electric conductivity. For the case of non-interacting electrons in a crystal, $\mathcal{M}$ corresponds in particular to the manifold of possible quasi-momenta, this is, to the Brillouin zone. To see this, let us first consider the single-particle Hamiltonian of an electron in a periodic potential,

$$\hat{H} = \frac{\hat{p}^2}{2m} + \hat{V}(\mathbf{r}), \tag{1.26}$$

where $V(\mathbf{x}+\mathbf{a}) = V(\mathbf{r})$, and $\mathbf{a}$ is one of the Bravais lattice unit vectors. Using Bloch's theorem [AM76], we can express the eigenstates of this Hamiltonian for periodic boundary conditions as *Bloch states*,

$$|\psi_{n\boldsymbol{q}}(\mathbf{r})\rangle = e^{i\boldsymbol{q}\cdot\mathbf{r}}\,|u_{n\boldsymbol{q}}(\mathbf{r})\rangle\,, \tag{1.27}$$

where $|u_{n\boldsymbol{q}}(\mathbf{r}+\mathbf{a})\rangle = |u_{n\boldsymbol{q}}(\mathbf{r})\rangle$ has the same periodicity as the potential. Here $\boldsymbol{q} \in$ B.Z. is the *quasi-momentum*, the possible values of which are given by the Brillouin zone, which has the structure of a d-dimensional torus, B.Z. $\simeq \mathbb{T}^d$. The number N of different bands, each one labeled by n, depends on the unit cell of the crystal, in particular the number of sublattices, as well as on other internal quantum numbers such as the spin of the electron. For example, a system of spinfull fermions on a bipartite lattice, such as an hexagonal one, possess four different bands in the tight-binding approximation [AM76].

Each Bloch band given by $|u_{n\boldsymbol{q}}(\mathbf{r})\rangle$ for a fixed n can be described by a fiber bundle over the Brillouin zone. This is clear if we first consider the *Bloch Hamiltonian* by applying the unitary transformation (1.26),

$$\hat{H}(\boldsymbol{q}) = e^{-i\boldsymbol{q}\cdot\mathbf{r}}\hat{H}e^{i\boldsymbol{q}\cdot\mathbf{r}}. \tag{1.28}$$

We can now interpret the quasi-momentum as an external parameter for the $N\times N$ Bloch Hamiltonian $\hat{H}(\boldsymbol{q})$. The quantum states $|u_{n\boldsymbol{q}}(\mathbf{r})\rangle$, which are now the eigenstates of (1.28), form a principal vector bundle on the B.Z., given by $\mathcal{P}(\mathbb{T}^d, U(1))$, called the *Bloch bundle*. Therefore, one expects that the topological properties of the Bloch bundle have consequences on measurable physical quantities.

Zak phase

As a first example, consider an electric field E applied to a one-dimensional crystal. An electron originally described by a Bloch state will adiabatically evolve with a

quasi-momentum given by $q(t) = q(0) - eEt$. The electric field causes then a periodic motion of q in the Brillouin zone, B.Z. $\simeq S^1$, called Bloch oscillation. We can calculate the Berry phase accumulated after one period,

$$\gamma_n = \int_{\text{B.Z.}} \mathrm{d}q \, \langle u_n(q)| \, i\partial_q \, |u_n(q)\rangle \tag{1.29}$$

which is usually referred to as *Zak phase* in this context, and is quantized to values 0 or π in the presence of chiral or inversion symmetry [Zak89]. If the Bloch bundle is non-trivial the electron will acquire a non-zero Zak phase.

Quantized particle transport

Another example where a physical quantity is given in terms of a topological invariant is the adiabatic transport of particles in a 1D chain under a periodic perturbation, also known as *Thouless pumping*. As first shown by Thouless [Tho83], if the system remains gapped at all times during the evolution, the transported charge after one period is quantized, and its value depends on the Chern number of an extended 2D system. To see this, let us first write the velocity operator in terms of the Bloch Hamiltonian

$$\hat{v}(q,t) = e^{-iqx}\hat{v}(t)e^{iqx} = \partial_q \hat{H}(q,t) \tag{1.30}$$

where the velocity is calculated in the Heisenberg picture, $\hat{v}(t) \equiv \partial_t \hat{x}(t) = i[\hat{H}, \hat{x}(t)]$, and the Hamiltonian is periodic in time $\hat{H}(t) = \hat{H}(t+T)$.

If the periodic modulation is slow enough, at a given time the eigenstates of the Hamiltonian are Bloch states of the form $e^{iqx}\,|u_n(q,t)\rangle$. In the rotated frame, the expectation value of the velocity can be expressed as

$$v(q,t) = \langle u_n(q,t)| \, \hat{v}(q,t) \, |u_n(q,t)\rangle = \partial_q \epsilon_n(q,t) - \Omega^n(q,t), \tag{1.31}$$

where $\Omega^n(q,t)$ is the Berry curvature defined over a $\mathbb{T}^2$ manifold, where q and t are regarded as external parameters. This second term in (1.31) is obtained by considering first-order corrections to the adiabatic theorem and using Eq. (1.14). The total current is obtained by considering all occupied states, this is, by integrating over the B.Z. and summing over the n_0 filled bands,

$$j(t) = -\sum_{n \le n_0} \int_{\text{B.Z.}} \mathrm{d}q \, v(q,t) = -\sum_{n \le n_0} \int_{\text{B.Z.}} \mathrm{d}q \, \Omega^n(q,t) \tag{1.32}$$

where the zeroth-order term vanishes due to the periodicity of the B.Z., and the current is defined with a conventional minus sign due to the negative charge of the

electrons. The total charge transported during a period can now be expressed as a sum of Chern numbers corresponding to each filled band,

$$\Delta n = \int_0^T \mathrm{d}t\, j(t) = -\sum_{n \leq n_0} c_n \tag{1.33}$$

Therefore, if the extended 2D system obtained by considering time as a quasi-momentum in a second dimension is described by a non-trivial Bloch bundle, the charge transported in the 1D system will be quantized to non-zero integer values. Although here we considered a non-interacting system, the relation (1.33) holds in the presence of interactions as long as the gap remains open during the evolution.

Integer quantum Hall effect

As a last example we consider the *integer quantum Hall effect* (IQHE), a transport phenomena that, similar to the Thouless pumping described above, is quantized in terms of topological invariants [Lau81]. The IQHE was discovered experimentally by von Klitzing in 1980 using a metal-oxide-semiconductor field effect transistor (MOSFET) [KDP80]. In this type of systems, the electrons are confined to a two-dimensional plane and, if a perpendicular magnetic field is applied, a transverse current can be measured. This is the so-called *classical Hall effect* and the Hall, or transverse, conductivity σ_{H} corresponds to the off-diagonal element of the conductivity tensor,

$$j_y = \sigma_{\mathrm{H}} E_x \tag{1.34}$$

where j_y is the current in the transverse direction, proportional to the applied electric field E_x, resulting from a longitudinal bias potential. According to the classical theory, the Hall conductivity is inversely proportional to the applied magnetic field,

$$\sigma_{\mathrm{H}} = \frac{1}{R_{\mathrm{H}} B}, \tag{1.35}$$

where the Hall constant R_{H} depends on the specific properties of the material, such as the carrier's density. In contrast, at low temperatures, and for strong-enough magnetic fields, the Hall conductivity is quantized in terms of a combination of fundamental constants, and do not depend on the details of the sample nor on the possible presence of disorder or imperfections,

$$\sigma_{\mathrm{H}} = \frac{e^2}{h} N, \tag{1.36}$$

with $N \in \mathbb{Z}$.

Soon after its experimental discovery, the robust quantization present in the IQHE was explained theoretically [TKNdN82]. In particular, using linear response

theory, it can be shown how the transverse conductivity can be expressed in terms of a Berry curvature,

$$\sigma_{\mathrm{H}} = \frac{e^2}{h} \sum_{n \leq n_0} i \int_{\mathrm{B.Z.}} \frac{\mathrm{d}^2 q}{2\pi} \left[\left\langle \frac{\partial u_n}{\partial q_x} \middle| \frac{\partial u_n}{\partial q_y} \right\rangle - \left\langle \frac{\partial u_n}{\partial q_y} \middle| \frac{\partial u_n}{\partial q_x} \right\rangle \right] \tag{1.37}$$

After integrating over the B.Z. one obtains the Hall conductivity as a sum of Chern numbers over filled bands, each one corresponding to a Bloch bundle $\mathcal{P}(\mathbb{T}^2, U(1))$,

$$\sigma_{\mathrm{H}} = \frac{e^2}{h} \sum_{n \leq n_0} c_n. \tag{1.38}$$

1.3.2 Topological insulators

The IQHE is arguably the first manifestation of a topologically non-trivial phase of matter. Although we described this effect in the presence of a magnetic field, we will see below that it can also occur in the absence of it. Similarly to the Aharonov-Bohm effect, which is a specific example of the more general notion of a geometrical phase, the deeper origin of the IQHE is not the interaction with an electromagnetic field, but the non-trivial topological structure of the corresponding quantum states. This was first realized by Haldane in 1988 [Hal88], when he introduced a model that shows similar properties as quantum Hall systems without any net magnetic field, a behavior known as the *quantum anomalous Hall effect* (QAHE). The Haldane model provides thus the first example of a *topological insulator* [HK10, QZ11], a phase of matter with non-trivial topological properties. Above we gave some examples of physical observables that can be written in terms of topological invariants. Since these are protected against continuous transformations, this is, those that do not close the gap, they can be used to classify different phases of matter separated by phase transitions where the gap closes.

Two-band Bloch Hamiltonian

Let us first consider the case of a system with two bands, which is described by a two-dimensional Bloch Hamiltonian $\hat{H}(\boldsymbol{q})$. We can always write this Hamiltonian in terms of Pauli matrices using Eq. (1.18),

$$\hat{H}(\boldsymbol{q}) = \boldsymbol{h}(\boldsymbol{q}) \cdot \hat{\boldsymbol{\sigma}} = \hat{H}^{\sigma}(\boldsymbol{h}(\boldsymbol{q})) \tag{1.39}$$

This implies, in particular, that the Bloch bundle associated to each energy band can be written as a *pullback*[11] of the sphere bundle by the continuous map $\boldsymbol{h}\colon \mathbb{T}^n \to$

[11] Consider a fiber bundle $\mathcal{P}(\mathcal{M}, \mathcal{F})$ and $\pi\colon \mathcal{P} \to \mathcal{M}$ its projection map. A continuous map $f\colon \mathcal{M}' \to \mathcal{M}$ from a topological space $\mathcal{M}'$ to the base space $\mathcal{M}$ defines a new fiber bundle $f^*\mathcal{P}$

S^2. In the last section, we saw how the sphere bundle describing the eigenstates of a two-level Hamiltonian is not trivial. In particular, since the sphere encloses a singularity at $\boldsymbol{h} = 0$, the ground state has a Chern number equal to one as long as $\boldsymbol{h} \neq 0$. The pullback operation allows us, therefore, to simplify the topological characterization of the Bloch bundle for the two-band model, since all the information is now contained in the map $\boldsymbol{h}$ from the d-dimensional torus to $\mathbb{R}^3$, which is restricted to S^2 since the normalized eigenstates of the two-level Hamiltonian do not depend on the length $|\boldsymbol{h}|$ as long as it is non-zero. The Chern number of the Bloch bundle is then given by the *degree* of the map, this is, the number of times that the torus wraps around the sphere under the map, since this counts the number of times that the singularity is encircled. The degree is a topological invariant for a continuous map, which coincides with its homotopy class if, like in this case, the range manifold corresponds to S^n—a result known as the Hopf theorem [MW97]. One can therefore modify $\boldsymbol{h}$ continuously and, as long as $\boldsymbol{h} \neq 0$, this is, if the gap does not close, the bands will preserve their global topological properties. As we will see in the following examples, the calculation of the Chern number is very much simplified by writing it as a function of the map $\boldsymbol{h}$.

Example 1: 2D Chern insulator

Consider the case $d = 2$, where the B.Z. corresponds to a 2-dimensional torus and the Bloch Hamiltonian is described by the map $\boldsymbol{h}\colon \mathbb{T}^2 \to \mathbb{R}^3$. As $\boldsymbol{q}$ traverses the B.Z., $\boldsymbol{h}$ describes a closed surface $\Sigma \subset \mathcal{R}^3$, which can be projected on S^2. Maps from $\mathbb{T}^2$ to S^2 are classified by the corresponding set of homotopy classes. In particular, one can first compactify the torus onto the sphere. In that case, the topological classification of $\boldsymbol{h}$ reduces to finding the second homotopy group of the sphere, which is $\pi_2(S^2) = \mathbb{Z}$. Each class is labeled by the first Chern number, defined in Eq. (1.17) which can be easily shown to be expressed solely in terms of $\boldsymbol{h}$ as

$$c_0 = \frac{1}{4\pi} \int_{\text{B.Z.}} \mathrm{d}q_x \wedge \mathrm{d}q_y \, \frac{\boldsymbol{h}}{\|\boldsymbol{h}\|^3} \cdot \left(\frac{\partial \boldsymbol{h}}{\partial q_x} \times \frac{\partial \boldsymbol{h}}{\partial q_y} \right) \in \mathbb{Z}. \tag{1.40}$$

This equation can be interpreted as the normalized flux through Σ from a magnetic monopole located at the origin. In particular, the Chern number vanishes if Σ does not completely cover S^2, or if it does not contain the origin. Otherwise one obtains a non-zero integer that corresponds to the number of times that Σ encircles S^2.

As an example of a non-trivial topological insulators in two dimensions, consider the Haldane model on an hexagonal lattice,

$$\hat{H} = t \sum_{\langle i,j \rangle} \hat{c}_i^\dagger \hat{c}_j + t' \sum_{\langle\langle i,j \rangle\rangle} e^{i\phi_{i,j}} \hat{c}_i^\dagger \hat{c}_j + \sum_i M_i \hat{c}_i^\dagger \hat{c}_i, \tag{1.41}$$

over $\mathcal{M}'$ with the same fiber $\mathcal{F}$, called the *pullback bundle* of $\mathcal{P}$ by f. The pullback bundle is defined by $f^*\mathcal{P} \equiv \{(p, e) \in \mathcal{M}' \times \mathcal{P} \,|\, f(p) = \pi(e)\}$ with a protection map $\pi'\colon f^*\mathcal{P} \to \mathcal{M}$ given by $\pi'((p, e)) = p$.

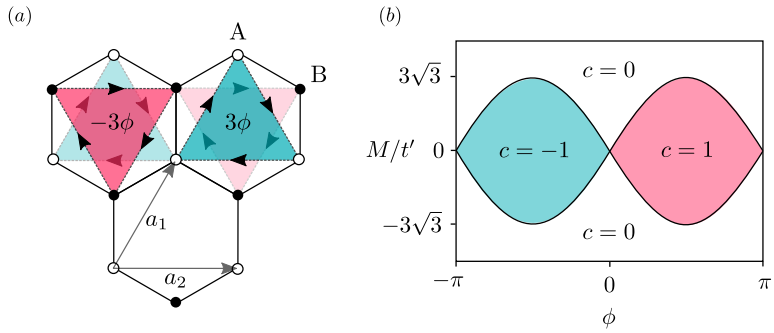

Fig. 1.8 Haldane model: **(a)** The model is defined on an hexagonal lattice composed of two triangular sublattices A and B, giving rise to a two-site unit cell. The Bravais lattice corresponds to a triangular lattice with primitive vectors $\boldsymbol{a}_1$ and $\boldsymbol{a}_1$. The nearest-neighbor tunneling elements connecting sites from the same sublattice A/B carry a complex phase $\pm\phi$, creating a $\pm 3\phi$ flux piercing each triangular plaquette. Time-reversal symmetry is thus broken, opening a gap at half filling, while the net magnetic flux is kept to zero. Inversion symmetry is also broken by adding a chemical potential imbalance M between the sublattices. **(b)** The phase diagram of the Haldane model in terms of the flux ϕ and the imbalance M presents three insulating phases characterized by different Chern numbers.

where t and t' are the nearest and next-nearest tunneling elements, respectively, connecting sites between different and the same sublattice. For the latter, a complex phase ϕ is added such that a magnetic flux is created on each triangular plaquette, with different signs in different sublattices (Fig. 1.8**(a)**). This choice guarantees that time-reversal symmetry is broken, while the total magnetic flux vanishes. Moreover, an on-site energy imbalance is added between the sublattices, $M_{\mathrm{A/B}} = \pm M$, breaking also inversion symmetry in the model. After a Fourier transform, the Hamiltonian (1.41) gives rise to a two-band single-particle Bloch Hamiltonian characterized by the maps,

$$\begin{aligned} h_0(\boldsymbol{q}) =& 2t' \cos\phi \sum_{\boldsymbol{\delta}\in\Delta_{\mathrm{A}}} \cos\left(\boldsymbol{q}\cdot\boldsymbol{\delta}\right) \\ h_x(\boldsymbol{q}) =& t\left[1 + \cos\left(\boldsymbol{q}\cdot\boldsymbol{a}_1\right) + \cos\left(\boldsymbol{q}\cdot\boldsymbol{a}_2\right)\right] \\ h_y(\boldsymbol{q}) =& t\left[\sin\left(\boldsymbol{q}\cdot\boldsymbol{a}_1\right) + \sin\left(\boldsymbol{q}\cdot\boldsymbol{a}_2\right)\right] \\ h_z(\boldsymbol{q}) =& M - 2t' \sin\phi \sum_{\boldsymbol{\delta}\in\Delta_{\mathrm{A}}} \sin\left(\boldsymbol{q}\cdot\boldsymbol{\delta}\right), \end{aligned} \tag{1.42}$$

where $\boldsymbol{a}_1$ and $\boldsymbol{a}_2$ are the primitive vectors of the Bravais lattice (Fig. 1.8**(a)**), and δ denotes vectors that connect the nearest-neighbor sites forming triangular plaquettes Δ_{A} is the sublattice A. The spectrum of the model presents two bands

separated by a a gap, that only closes at the critical lines, which are given by

$$|M_c| = 3\sqrt{3}\, t'_c \sin\phi_c. \tag{1.43}$$

These lines separate three distinct insulating phases characterized by their different Chern numbers (Fig. 1.8**(b)**). Using Eq.(1.40), one finds the general expression for the Chern number in terms of the Hamiltonian parameters,

$$c_0 = \frac{1}{2}\left[\text{sign}\left(\frac{M}{t'} + 3\sqrt{3}\sin\phi\right) - \text{sign}\left(\frac{M}{t'} - 3\sqrt{3}\sin\phi\right)\right]. \tag{1.44}$$

The phases with non-zero Chern number are topologically non-trivial. In particular, they present an QAHE, this is, a non-zero quantized Hall conductivity in the absence of a magnetic field. They are examples of 2D *Chern insulators*. Similar insulators exists in higher dimensions, in particular there are Chern insulators for all even dimensions, characterized by higher Chern numbers [CTSR16].

Example 2: 1D Chiral-symmetric insulator

Chern numbers are not defined for odd dimensions. However, we can still use other topological invariants to classify topologically-distinct phases of matter in these cases. One example is the Zak phase γ defined in Eq. 1.29, that characterizes Bloch bundles on a 1D B.Z. in the presence of chiral symmetry. For higher dimensions, one can define *Chern-Simon invariants*, CS, which reduces to the Zak phase in 1D, $\mathsf{CS} = \gamma/2\pi$. In general, these quantities can take any value. In the presence of chiral symmetry, however, they are quantized to integer or half-integer values, and can be used to define a gauge-invariant *Wilson loop*, $W = e^{i2\pi\mathsf{CS}}$. In this thesis we consider only quantum systems in dimensions one and two. Therefore, the Zak phase and the first Chern number will suffice to describe the topological properties of the models we study. Definitions of the corresponding topological invariants in higher dimensions can be found in [CTSR16].

As we showed in the previous example, here the computation of the Zak phase can also be simplified in the case of a two-band Bloch Hamiltonian. Invariance under chiral symmetry implies the following condition for the single-particle Hamiltonian,

$$\hat{\Gamma}\hat{H}(k)\hat{\Gamma}^{-1} = -\hat{H}(k), \tag{1.45}$$

where $\hat{\Gamma}$ is a unitary representation of the symmetry. For a two level-system we have $\hat{\Gamma} = \hat{\sigma}^z$, and the condition (1.45) implies $h_z(k) = 0$. In $d = 1$, the map that characterizes the Bloch bundle reduces then to $\boldsymbol{h}\colon S^1 \to S^1$, and the Zak phase can be written in terms of it as

$$\gamma = \frac{1}{2}\int_{\text{B.Z.}} \mathrm{d}q \left(\frac{\boldsymbol{h}}{\|\boldsymbol{h}\|} \times \partial_q \frac{\boldsymbol{h}}{\|\boldsymbol{h}\|}\right)\cdot \hat{\boldsymbol{e}}_z, \tag{1.46}$$

which is just π times the winding number of $\boldsymbol{h}$ [AOP16], and the different Bloch bundles are given by the first homotopy group $\pi_1(S^1) = \mathbb{Z}$.

As an example of a chiral-symmetric insulator, consider the commonly referred to as the Su-Schrieffer-Heeger (SSH) model in 1D,

$$\hat{H}_{\mathrm{SSH}}(t_1, t_2) = t_1 \sum_i \hat{c}^\dagger_{2i} \left(\hat{c}_{2i+1} + \mathrm{H.c.} \right) + t_2 \sum_i \left(\hat{c}^\dagger_{2i+1} \hat{c}_{2i+2} + \mathrm{H.c.} \right). \tag{1.47}$$

This model describes a chain of non-interacting spinless electrons with different tunneling elements for even and odd bonds (Fig. 1.9**(a)**). As we describe in detail in chapter 3, the Hamiltonian (1.47) is an effective description of the full model introduced by Su, Shcrieffer and Heeger to study the physics of polyacetylene [SSH79], that includes interactions between fermions and phonons.

The SSH Hamiltonian can be described using a two-site unit cell. For $t_1 \neq t_2$, a gap opens in the middle of the spectrum, and the system is an insulator at half filling (Fig. 1.9**(b)**). The single-particle Bloch Hamiltonian is described by the maps

$$\begin{aligned} h_x(q) =& t_1 + t_2 \cos q, \\ h_y(q) =& t_2 \sin q, \\ h_z(q) =& 0. \end{aligned} \tag{1.48}$$

We can now compute the Zak phase associated to the lower band using (1.46), obtaining two topologically-distinct phases (Fig. 1.9**(c)**): for $t_1 < t_2$ the ground state is a topological insulator with $\gamma = \pi$, while it is topologically trivial for $t_1 > t_2$, with $\gamma = 0$. The Zak phase does not change its value until the gap closes at $t_1 = t_2$, even if we add perturbations to the Hamiltonian—as long as they respect chiral symmetry. If this symmetry is broken, however, the Zak phase will no longer be a quantized topological invariant, and we could modify its value continuously without closing the gap. The topological phase of the SSH model is an example of a *symmetry-protected topological phase* (SPT), showing non-trivial topological behavior only when a protecting symmetry is present. This contrasts with the case of the Chern insulator described above, where no symmetry is required.

As a consequence of the non-trivial topological structure of the Bloch bundle that describes one of the insulating phases of the SSH model, the system shows non-trivial transport properties. This can be seen through a pumping protocol, where we modulate the Hamiltonian's parameters periodically in time

$$\hat{H}_{\mathrm{RM}}(\varphi) = -\sum_i \left[t + (-1)^i \delta(\varphi) \right] \left(\hat{c}^\dagger_i \hat{c}_{i+1} + \mathrm{H.c.} \right) + \Delta(\varphi) \sum_i (-1)^i \hat{c}^\dagger_i \hat{c}_i \tag{1.49}$$

with

$$\delta(\varphi) = \delta \cos \varphi, \quad \Delta(\varphi) = \Delta \sin \varphi \tag{1.50}$$

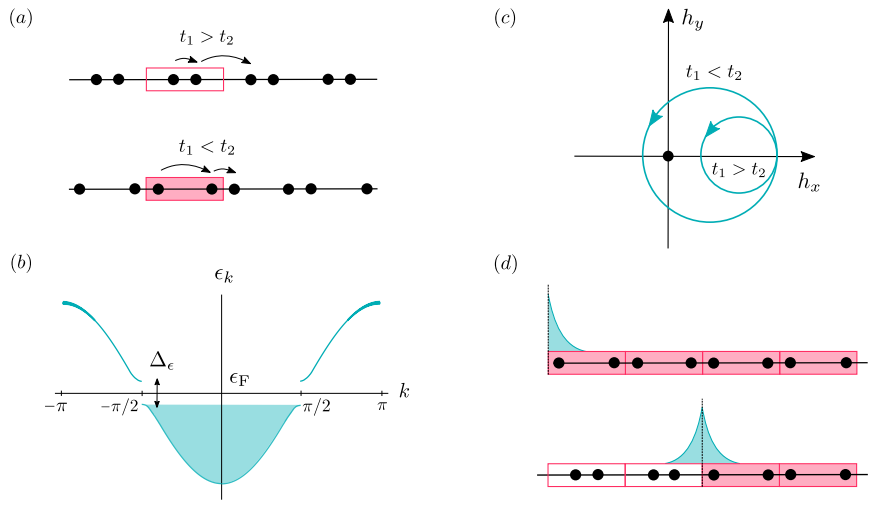

Fig. 1.9 Su-Schrieffer-Heeger model: (a) The underlying 1D chain can be described using a two-site unit cell, where the origin of the difference between tunneling elements can be interpreted from the different distances between lattice sites. **(b)** The band structure presents a gap $\Delta_\epsilon = |t_1 - t_2|$ at the Fermi energy $\epsilon_F = 0$. At half filling, the ground state is thus gapped for any $t_1 \neq t_2$ and gapless if $t_1 = t_2$. **(b)** These two insulating phases have different topological properties. For $t_1 < t_2$, in particular, the loop described by $\boldsymbol{h}(q)$ as q traverses the B.Z. encircles the gap-closing point where $\boldsymbol{h} = 0$, giving rise to a non-zero Zak phase. This is not the case, Fhowever, for $t_1 > t_2$, and the corresponding ground state is topologically trivial in that parameter region. **(d)** Topological insulators presents protected states localized at points where the topological invariant of the bulk changes, such as the edge of a finite system or a defect in the bulk.

where the angle $\varphi\colon [0, T] \to [0, 2\pi]$ is a time-dependent periodic modulation. The Hamiltonian given by Eq. (1.49) is known as the Rice-Mele model [RM82], where an on-site energy imbalance between the two sublattices is added to the SSH model. This term breaks chiral symmetry, allowing us to avoid the degeneracy point at $t_1 = t_2$. If the modulation (1.50) is adiabatic, the ground state encircles the degeneracy point and, using Eq. (1.33), we find a non-zero quantized charge transported after each cycle. Notice that the transported charge would be zero if the loop in the (q, φ) parameter space did not enclose any singularity.

As we showed above, this quantization can be understood as the Chern number of 2D system if φ is taken as the momentum of an extra second dimension. We can construct explicitly the 2D Hamiltonian associated to the Thouless pumping

in the Rice-Mele model, defined as

$$\hat{H}_{\mathrm{HHH}} = \int_0^{2\pi} \mathrm{d}\varphi\, \hat{H}_{\mathrm{RM}}(\varphi), \tag{1.51}$$

which can be written in real-space by taking the inverse Fourier transform of φ, $c^\dagger_{i_1,\varphi} = \sum_{i_2} e^{i\varphi i_2} c^\dagger_{i_1,i_2}$, obtaining

$$\begin{aligned}\hat{H}_{\mathrm{HHH}} = &-\sum_{i_1,i_2}\left(t\hat{c}^\dagger_{i_1,i_2}\hat{c}_{i_1+1,i_2} + \frac{\Delta}{2}e^{-i\pi(i_1-1/2)}\hat{c}^\dagger_{i_1,i_2}\hat{c}_{i_1,i_2+1} + \mathrm{H.c.}\right)\\ &-\sum_{i_1,i_2}\left(\frac{\delta}{2}e^{-i\pi i_1}\hat{c}^\dagger_{i_1,i_2}\hat{c}_{i_1+1,i_2+1} + \frac{\delta}{2}e^{i\pi i_1}\hat{c}^\dagger_{i_1,i_2+1}\hat{c}_{i_1+1,i_2} + \mathrm{H.c.}\right).\end{aligned} \tag{1.52}$$

This 2D Hamiltonian corresponds to the Harper-Hofstadter-Hatsugai model [Har55, Hof76, HK90]—describing non-interacting fermions on a 2D lattice under the influence of a magnetic flux, including nearest and next-nearest neighbor tunnelings —for a flux equal to π. At half filling, the ground state is a Chern insulator with Chern numbers $c_0 = 0, \pm 1$. These are the possible quantized values of the transported charge after one pumping cycle, being non-zero only if cycle in parameter space described by the ground state along this process encircles the degeneracy point at $\delta = \Delta = 0$.

Bulk-edge and bulk-defect correspondence

One important feature of topological insulators is the presence of protected states in the spectrum, exponentially localized at surfaces where the bulk topology changes. We can see an example of this in the SSH model. In the non-trivial topological phase, one finds localized *edge states* at the boundary of a finite chain (Fig. 1.9**(d)**). The boundary separates the topological insulator from the vacuum. It is thus an interface where the corresponding topological invariant, the Zak phase in this case, changes value. This can only occur if the gap closes at the boundary, which is the case if the edge states are gapless, i.e. zero-energy in-gap modes. In this example, chiral symmetry ensures that these states are pinned at zero energy, making them robust against local symmetry-preserving perturbations [RH02]. This is true for general edge states in SPT phases. As long as the protecting symmetry is preserved, the states will remain within the gap, preserving the localization, and will not disappear until the gap closes and they eventually merge with the bulk bands.

Protected states are not restricted to the boundaries of finite systems, as they can also appear in the bulk. In Fig. 1.9**(d)** we can see how a localized states arises at a topological defect of an otherwise perfectly dimerized chain. The defect separates regions with different bulk topology, where $t_1 - t_2$ changes sign. In the SSH model, localized states at edges and defects have an associated fermionic charge that is

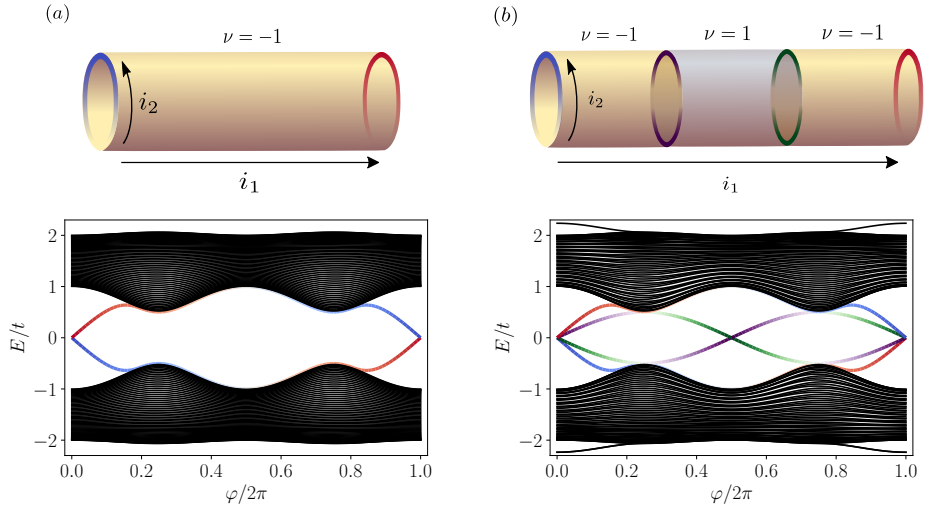

Fig. 1.10 Thouless pumping: **(a)** Band structure of a finite SSH chain showing spectral flow. At the chiral-symmetric points, the protected edge state are degenerate in the middle of the gap. During the pumping process, they delocalize into the bulk as chiral symmetry is broken. At the beginning of the pump, only the left edge state is populated by a fermion with fractional charge in a half-filled state, which ends up localized at the right boundary. This changes the center of mass by $\Delta n = 1/2 - (-1/2)$, contributing to the quantized particle transport during the cycle. In the 2D picture, the same spectrum is associated to a finite cylinder with protected 1D edge states that circulate during the cycle, where the pumping protocol can be understood as a flux insertion through the cylinder. **(b)** The situation is similar if we include defects separating regions with different bulk topology. In this case, the associated edge states cross twice inside the gap, since the Chern number difference in the associated cylinder is now double, giving rise to a particle transport of $\Delta n = 2$ through the defects after each cycle.

fractional. In particular, this charge is $\pm 1/2$ if the state is occupied or empty, respectively. We will consider this property in more detail in chapter 5.

The situation is similar in non-trivial Chern insulators. In 2D, for instance, 1D conducting edge states appear at the boundary of the system if the bulk is characterized by a non-zero Chern number [Hat93b]. These states are responsible for the non-zero Hall conductivity in quantum states that would be insulators otherwise, as recognized first by Laughlin [Lau81]. In general, there exists various *index theorems* that relate the non-trivial topological bulk properties of topological insulators and superconductors with the existence of low-dimensional protected states located at edges and topological defects [CTSR16].

Further insight into the properties of topologically-protected edge states can be

obtained by applying the Thouless pumping to a finite chain. The quantization of the transported charge given by Eq. (1.33) requires an infinite system. However, a non-zero charge can also be transported in a finite system, approaching a quantized value as the system size increases. In that case, the origin of this particle transport can be traced to the existence of topologically-protected edge states [HF16], using a similar argument to Laughlin's explanation of the IQHE [Lau81].

Consider again the pumping protocol given by Eq. (1.49) for the SSH chain. Figure 1.10**(a)** shows the full energy spectrum of the single-particle Hamiltonian in terms of the pumping parameter φ. At $\varphi = 0$ the half-filled ground state is in the topological phase, and we find two degenerate edge states in the middle of the gap. Following the bulk-edge correspondence argument [Hat93b], the number of topologically protected edge states at each boundary is equal to the transported charge $|\Delta n|$, and the sign of Δn determines the direction of the charge transport. These states connect the two bands as φ is modified, which is commonly referred to as *spectral flow*, and are responsible for transporting the charge during the pumping process. We find a Chern number of $c_0 = -1$ for this pumping sequence.

Figure 1.10**(a)** can also be interpreted as the spectrum of the Harper-Hofstadter-Hatsugai model (1.52) in a cylindrical geometry with open boundary conditions in the real dimension i_1 and periodic ones in the synthetic dimensions i_2—with corresponding quasi-momentum φ. The localized edge states become, in this picture, the 1D conducting edge states at the boundaries of the synthetic cylinder. The phase of this synthetic 2D system corresponds to a Chern insulator and, as opposed to the 1D case, the bulk-boundary correspondence guarantees the presence of topologically-protected edge states even in the absence of chiral symmetry. Therefore, this 2D extension through the Thouless pumping establishes a generalized bulk-boundary correspondence, where the localized states in 1D can be seen as remnants of protected edge states in 2D. Abusing the notation, we can associate Chern numbers to 1D phases, keeping in mind that this requires the specification of not only the initial state for the pumping protocol, but also of its direction. In this case, if we reverse the direction of the pumping we would get $c_0 = 1$. Following Laughling argument for the IQHE, the variation in the momentum $\varphi(t)$ through the modulation (1.50) can be interpreted in the 2D cylinder as the insertion of an axial flux that pierces the cylinder. The circulation of the 1D edge states due to the change in the flux generates then a quantized Hall current, whose direction depends on the sign of the Chern number, this is, on the details of the modulation.

A similar argument can be made for the states localized at defects separating regions with different bulk topology. We first notice that these point defects in the 1D chain can be understood as extended 1D interfaces between regions with different Chern numbers in the adiabatic pumping (Fig. 1.10**(b)**). We consider a configuration with two of them at $\varphi = 0$, where four degenerate localized states appear in the spectrum. Far from the defects, the bulk of the three regions can be characterized by different Chern numbers: $\nu_{\bar{\mathrm{A}}} = -1$, $\nu_{\mathrm{A}} = 1$ (Fig. 1.10**(b)**). Again,

the bulk-defect correspondence predicts that the periodic particle pumping across one point of the chain will depend on the Chern numbers of the corresponding regions. In particular, the number of bound states that circulates around each ring defect is equal to the difference of Chern numbers between the regions it connects. This can be observed in Figure 1.10**(b)**, where we represent the spectral flow of a finite chain with two defect. Apart from the two localized states associated to the edges of the chain, two extra localized states cross the gap connecting both bands. These are associated with the defects, and cross at the chiral-symmetric points ($\varphi = 0$ and $\varphi = \pi$), where they are degenerate. The extended 2D cylinder consists then of different regions with different Chern numbers, and the localized states associated to the defects in 1D can be interpreted as topologically-protected conducting states that reside at the 1D circular boundaries between these regions. Note that these states circulate twice as fast compared to the states on the boundaries, since the Chern number difference is doubled.

The bulk-defect correspondence in the Thouless pumping is true as long as the 1D bulk has a non-zero topological invariant. In chapter 5, we will use this connection to uncover the topological origin of localized states in systems where, even if chiral symmetry is broken and these states are not protected, the bulk topological invariant is still quantized due to another protecting symmetry.

General classification

Before we consider the role of interactions, we summarize the main results concerning the classification of topological phases of non-interacting symmetric Hamiltonians. The first example of a topological phase introduced above, the Chern insulator, belongs to the A symmetry class. This class is formed by the Hamiltonians that do not require any symmetry to show non-trivial topological phenomena. However, in the second example, chiral symmetry is essential to protect the topological features of the SSH model. This model is in the so-called AIII symmetry class, corresponding to the Hamiltonians invariant under chiral transformations. If chiral symmetry is broken, the Zak phase will not be a well-defined topological invariant—unless some other spatial symmetry, such as inversion symmetry, is present in the system, as we shall see. In particular, its value will not be quantized, but could change continuously from π to 0 without closing the gap. The edge states will no be protected at zero energy either, and they could be removed by perturbing the system, again without closing the gap. Non-interacting gapped Hamiltonian, whose ground states could be either insulators or superconductors, are in general classified in terms of non-spatial symmetries into ten symmetry classes. These symmetries are the already mentioned chiral symmetry, as well as particle hole and time reversal, and the corresponding ten-fold classification was originally described by Altland and Zirnbauer (AZ) [AZ97].

The complete topological classification of all possible gapped phases of such

				δ							
Class	T	C	S	0	1	2	3	4	5	6	7
A	0	0	0	$\mathbb{Z}$	0	$\mathbb{Z}$	0	$\mathbb{Z}$	0	$\mathbb{Z}$	0
AIII	0	0	1	0	$\mathbb{Z}$	0	$\mathbb{Z}$	0	$\mathbb{Z}$	0	$\mathbb{Z}$
AI	+	0	0	$\mathbb{Z}$	0	0	0	$2\mathbb{Z}$	0	$\mathbb{Z}_2$	$\mathbb{Z}_2$
BDI	+	+	1	$\mathbb{Z}_2$	$\mathbb{Z}$	0	0	0	$2\mathbb{Z}$	0	$\mathbb{Z}_2$
D	0	+	0	$\mathbb{Z}_2$	$\mathbb{Z}_2$	$\mathbb{Z}$	0	0	0	$2\mathbb{Z}$	0
DIII	−	+	1	0	$\mathbb{Z}_2$	$\mathbb{Z}_2$	$\mathbb{Z}$	0	0	0	$2\mathbb{Z}$
AII	−	0	0	$2\mathbb{Z}$	0	$\mathbb{Z}_2$	$\mathbb{Z}_2$	$\mathbb{Z}$	0	0	0
CII	−	−	1	0	$2\mathbb{Z}$	0	$\mathbb{Z}_2$	$\mathbb{Z}_2$	$\mathbb{Z}$	0	0
C	0	−	0	0	0	$2\mathbb{Z}$	0	$\mathbb{Z}_2$	$\mathbb{Z}_2$	$\mathbb{Z}$	0
CI	+	−	1	0	0	0	$2\mathbb{Z}$	0	$\mathbb{Z}_2$	$\mathbb{Z}_2$	$\mathbb{Z}$

Fig. 1.11 Periodic table of topological insulators and superconductors: Different rows correspond to the ten different symmetry classes, characterized by the time-reversal (T), particle-hole (C) and chiral symmetries (S). In the table, 0 corresponds to the non-symmetric case, while 1 means that S symmetry is satisfied. The corresponding operators for T and C can square to ± 1, which is denoted by $+$ and $-$ in the table. Different columns represent systems with different *topological dimension* δ, which depends on the spatial dimension d as well as the dimension of the possible defects. If there are none, we have $\delta = d$. Finally, different entries indicate the possible topological phases, where $\mathbb{Z}$ and $2\mathbb{Z}$ indicate that they are characterized by an integer or even-integer topological invariant, while $\mathbb{Z}_2$ and 0 corresponds to either just two distinct topological phases or only the trivial one, respectively. Reprinted from Ref. [CTSR16].

symmetric Hamiltonian was achieved by Kitaev [Kit09] and by Ryu, Schnyder, Furusaki and Ludwig [RSFL10], and can be summarized in the so-called periodic table of topological insulators and superconductors (Fig. 1.11). This classification depends on the space dimension d, as well as on the presence of topological defects. We note that, in this context, the notion of topological defect is not related to any broken symmetry, such as those we considered in the first section of this chapter. They correspond to lower-dimensional objects that separate regions in the system with different bulk topology, hosting localized gapless states that are topologically protected under the same symmetry as the bulk. In certain situations, as in the SSH case, these defects also correspond, simultaneously, to topological defects that emerge after a SSB. We will explore this possibility in detail in chapter 5.

Apart from internal symmetries, topological phases can be protected also by spatial symmetries, giving rise to *crystalline topological insulators* [Fu11]. In chapters 3 and 4 we will analyze in detail one example where, even if chiral symmetry is broken by interactions, non-trivial topology is still protected by inversion symmetry. One important difference between topological phases protected by spatial and non-spatial symmetries is that the former do not present a bulk-boundary correspondence as the latter do. This means that, even if the bulk is topologically non-trivial, the system might not present protected edge states at the boundaries.

The presence of spatial symmetries enlarges the periodic table of non-interacting topological phases. We will not review the full classification here, and refer the interested reader to the review [CTSR16] and references therein.

1.3.3 Symmetry-protected topological phases

So far we have only considered non-interacting topological phases, which, as we have seen, can be classified based on the topological properties of the corresponding Bloch bundle. This approach can not be applied, however, once interactions are included in the system. The periodic table of topological insulators and superconductors, in particular, is modified in the presence of interactions [CTSR16]. Some of these topological phases can be connected to trivial phases adiabatically by modifying the interaction parameters [FK10]. Other phases, however, can survive to small interactions, giving rise to correlated topological insulators [Rac18], separated from trivial ones by symmetry-breaking transitions at sufficiently strong interactions. In some cases, such as fractional Chern insulators [LS09] or the topological Mott insulator [PB10], the topological properties are enabled by interactions, with no non-interacting counterpart adiabatically connected to them.

Similar to the non-interacting case, many topological phases of interacting systems require certain symmetries to protect their non-trivial topological properties. The term SPT [GW09], therefore, includes these as well as all the non-interacting topological insulators and superconductors—except from the ones in the A class, which do not required any symmetry. A general classification of SPT phases in one dimension has been achieved for fermionic [FK11] as well as for bosonic matter [CGW11, SPGC11], based on the use of tensor network techniques [VMC08] and group cohomology. A full classification of SPT phases for arbitrary dimensions, however, is still in progress.

Projective representation

To gain more insight into the classification of interacting SPT phases, it is important to notice that, although symmetry groups act on the bulk of the system forming a *linear representation*, they act on the edge states through a *projective representation*, as it was first noted for the case of Majorana edge states [FK11, TPB11]. A (unitary) linear representation is a group homomorphism from the symmetry group $\mathcal{G}$ to the unitary group $U(\mathcal{H})$—formed by unitary operators acting on the Hilbert space $\mathcal{H}$. Instead, a projective representation is a group homomorphism to the projective unitary group $PU(\mathcal{H}) = U(\mathcal{H})/\mathbb{C}^*$, which corresponds to the quotient group of $U(\mathcal{H})$ by the subgroup of scalar transformations $\mathbb{C}^*$, this is, the operators of the form $e^{i\alpha}\mathbb{I}$, where $\mathbb{I}$ is the identity. This means, in particular, that the group multiplication is preserved only up to a phase,

$$\hat{V}(g)\hat{V}(h) = e^{i\alpha(g,h)}\hat{V}(gh) \tag{1.53}$$

for any g, $h \in \mathcal{G}$, and V unitary operators in $U(\mathcal{H})$. If $e^{i\alpha(g,h)} = 1$ for every element of the group, the projective representation is lifted to a linear one. This occurs for trivial phases of matter. The impossibility to do so, also known as an obstruction, signals non-trivial topological properties. Different topological phases are then classified by the different projective representations, which can be characterized using group cohomology [Nak03].

Edge states are present only for finite systems, and only for certain protecting symmetries. For instance, the Haldane phase that appears in integer spin chains [Hal83] and other bosonic systems [DTBA06] is an example of a SPT phase with a non-trivial bulk but without edge states. However, the analysis introduced above based on projective representations can be applied to any SPT phase in 1D by first representing the ground state as a Matrix Product State (MPS), as we will see in chapter 2.

Many-body Berry phase

An alternative method to detect interacting SPT phases is to generalize some of the topological invariants we introduced for non-interacting systems. In the previous section, we introduced the Zak phase (1.29) as a topological invariant to characterize the global properties of a Bloch bundle. This phase is just the Berry phase calculated by integrating the Berry curvature along the B.Z., where the quasi-momentum q is regarded as an external parameter. In a system with periodic boundary conditions, modifying the quasi-momentum is equivalent to introducing a flux φ that pierces the system through one periodic dimension, this is, $q \to q + \varphi$. In an interacting system, the quasi-momentum can not be used as an external parameter anymore. However, we can still emulate an external flux by using twisted boundary conditions (TBC),

$$|\Psi_n(x_1, \cdots, x_i + L, \cdots, x_N)\rangle = e^{i\kappa L} |\Psi_n(x_1, \cdots, x_i, \cdots, x_N)\rangle , \tag{1.54}$$

where $|\Psi_n\rangle$ is the many-body ground state for certain interacting Hamiltonian $\hat{H}$, and we require the same boundary condition for every dimension x_i. The parameter κ corresponds here to the degree of twisting or, equivalently to the flux that pierces the system in every dimension. We can now transform the Hamiltonian by applying the unitary transformation

$$\hat{H}'(\kappa) = e^{i\kappa \sum_i x_i} \hat{H} e^{-i\kappa \sum_i x_i} \tag{1.55}$$

The corresponding ground state,

$$|\Psi'_n(\kappa, x_1, \cdots, x_N)\rangle = e^{i\kappa \sum_i x_i} |\Psi_n(\kappa, x_1, \cdots, x_N)\rangle , \tag{1.56}$$

satisfies now periodic boundary conditions, and depends on the parameter κ. We can calculate the Berry phase associated to a closed path in parameter space by

integrating the corresponding Berry curvature,

$$\gamma_n = \int_0^{2\pi} \mathrm{d}\kappa \, \langle \Psi'_n(\kappa) | \, i\partial_\kappa \, | \Psi'_n(\kappa) \rangle \,, \tag{1.57}$$

This many-body Berry phase generalizes the Zak phase used in non-interacting systems, and can be used to detect non-trivial topological phases in the presence of interactions. For gapped systems in 1D, for instance, this phase is quantized, and can take the values 0 or π, provided that either chiral or inversion symmetry are satisfied [XCN10]. In 2D, a many-body Chern number is associated to the ground state by integrating the corresponding Berry curvature, which depends now on two twisting parameters. In chapters 4, 5 and 7 we use the many-body Berry phase to characterize the topological properties of various strongly-correlated topological phases.

1.3.4 Topological order

The quantum states associated to SPT phases are examples of *short-range entangled* (SRE) states, which means that they can be transformed into product states using finite-depth quantum circuits [ZCZW19]. On the other hand, states that do not fulfill this property are referred to as *long-range entangled* (LRE) states. This is the case for topologically-ordered states, as witnessed by the presence of a topological term in the entanglement entropy [LW06, KP06]. In general, ground states of gapped local Hamiltonian satisfy the so-called *area law* for the entanglement entropy [VLRK03, CC04, Sre93, ECP10],

$$S_A = \alpha \partial \mathcal{A} + \dots \tag{1.58}$$

where S_A is the entanglement entropy for a bipartition of the full system into two subsystems A and B, calculated from the corresponding reduced density matrix $\rho_\mathrm{A} = \mathrm{Tr}_\mathrm{B} \left(|\psi\rangle \langle\psi| \right)$, this is $S_\mathrm{A} = \mathrm{Tr} \left(\rho_\mathrm{A} \log \rho_\mathrm{A} \right)$. Here $\partial\mathcal{A}$ is the area of A, α is a proportionality constant and the ellipsis denotes subleading terms that can be neglected in the thermodynamic limit when compared to the area-law contribution. In contrast, states with topological order include an extra term, $S_A = \alpha\partial\mathcal{A} - \gamma + \dots$, where γ does not depend on the geometry of A, and serves as a hallmark of LRE.

The term topology order (TO) was first coined in the context of chiral spin states [Wen90], introduced in an attempt to explain high-temperature superconductivity [WWZ89], motivated by the description of their low-energy properties in terms of topological quantum field theories [Wit89]. There are many of these states having exactly the same symmetries [Wen89]. Their classification thus falls out of the scope of Landau's paradigm. Contrary to SPT phases, this new type of order is robust in the sense that, even if it is not protected by any symmetry, it survives to small perturbations that do not close the gap. Although chiral spin

states were soon discarded as the underlying description of high-temperature superconductors, it was realized that many of its features were shared by fractional quantum Hall states [KL87], which were discovered experimentally just a few years earlier [TSG82].

Contrary to its integer counterpart, the fractional quantum hall effect (FQHE), where plateaus in the Hall conductivity are found at fractional electron densities, is a genuine quantum many-body effect that requires strong electron-electron interactions [Lau83], and can not be described in a single-particle picture. In this case, the Hall conductivity is quantized to fractional values,

$$\sigma_{\mathrm{H}} = \frac{e^2}{h}\frac{p}{q} \tag{1.59}$$

where p and q are co-prime integers. As in the case of the IQHE, where the p/q is also an integer (1.36), different Hall conductivities correspond to different phases of matter with the same symmetries. Fractional quantum Hall states are thus topologically-ordered phases of matter, one of their hallmarks being the presence of anyonic quasi-particles showing fractional statistics [Lau83].

In general, phases of matter with TO can be characterized by the dependence of the ground state degeneracy on the topology of the underlying manifold where the Hamiltonian is defined [ZCZW19]. This means that the number of degenerate ground states is different, for instance, if the system is placed on a sphere or on a torus. But more importantly, this degeneracy is robust: in contrast to topologically-trivial phases of matter, where the origin of the degeneracy is related to the symmetry properties of the states, in this case it survives to any local symmetry-breaking perturbation. To distinguish phases with different types of TO, however, the presence of degeneracy is not enough. This can be done, nevertheless, by means of a *non-abelian Berry phase* [XCN10]. In Sec. 1.2.2, we introduced the Berry phase assuming no degeneracy in the spectrum. This abelian Berry phase can be generalized to its non-abelian version, by promoting the phase to a n-dimensional matrix, where n is the number of degenerate ground states. From an experimental point of view, TO can be detected by the presence of quasi-particles with fractional quantum numbers and fractional statistics, as in the case of the FQHE [Lau83]. Similar to SPT phases, phases with TO can also present gapless edge modes, which in this case are topologically-protected again any local perturbation, even if they break the system's symmetries.

Toric code

In order to explain some of these properties in more detail, we make use of the Toric code (TC) as a simple example where most of these can be proven analytically. The toric code was originally proposed by Kitaev as an error correcting code for quantum computation [Kit03], where topological qubits can be encoded precisely

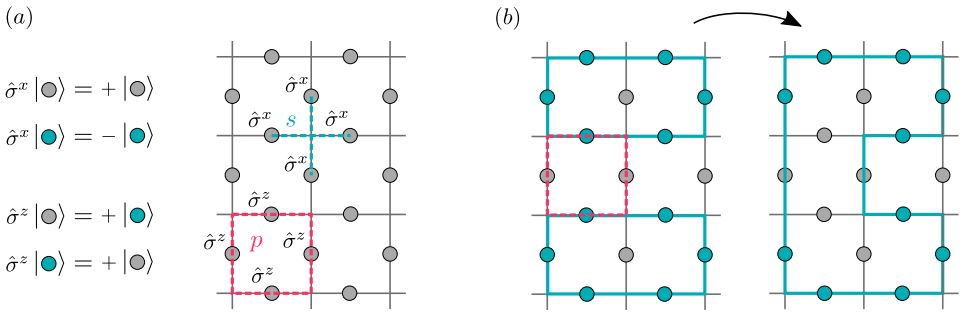

Fig. 1.12 Toric code: (a) The TC Hamiltonian (1.60) contains star and plaquette operators acting on the links of a two-dimensional spin-1/2 lattice. **(b)** The ground state of the model is a superposition of closed strings as the ones shown in the figure, minimizing the energy corresponding to the star operators, while the plaquette terms connect different strings.

into its different degenerate ground states, such that global information can be protected against local errors by exploiting an underlying stabilizer formalism of the following Hamiltonian,

$$\hat{H}_{\mathrm{TC}} = -J\sum_{s}\prod_{(\mathbf{i},\mathbf{j})\in s}\hat{\sigma}^x_{(\mathbf{i},\mathbf{j})} - J\sum_{p}\prod_{(\mathbf{i},\mathbf{j})\in p}\hat{\sigma}^z_{(\mathbf{i},\mathbf{j})}, \tag{1.60}$$

with $J>0$. $\hat{\sigma}^x_{(\mathbf{i},\mathbf{j})}$ and $\hat{\sigma}^z_{(\mathbf{i},\mathbf{j})}$ are Pauli operators acting on spin-1/2 degrees of freedom located on the links $(\mathbf{i},\mathbf{j})$ of a two-dimensional square lattice, joining neighboring sites $\mathbf{i}=(i_1,i_2)$ and $\mathbf{j}=(j_1,j_2)$ The first part of the Hamiltonian (1.60) contains the so-called *star* operators, $\hat{A}_s=\prod_{(\mathbf{i},\mathbf{j})\in s}\hat{\sigma}^x_{(\mathbf{i},\mathbf{j})}$, acting on the four links connected to each site s, while the second contains the *plaquette* operators, $\hat{B}_p=\prod_{(\mathbf{i},\mathbf{j})\in p}\hat{\sigma}^z_{(\mathbf{i},\mathbf{j})}$, that are applied to the four links of each plaquette p (Fig. 1.12(a)).

Since all the operators commute among themselves, $[\hat{A}_s,\hat{A}'_s]=[\hat{B}_p,\hat{B}'_p]=[\hat{A}_s,\hat{B}_p]=0$, the ground state of the TC Hamiltonian is also an eigenstate of each of them. Both $\hat{A}_s$ and $\hat{B}_p$ have eigenvalues ±1, and according to the definition of the Hamiltonian ((1.60)), the ground state will be the common $+1$ eigenstates of all plaquette and star operators. One says that the ground state is stabilized by the $\hat{A}_s$ and $\hat{B}_p$ operators, which actually span a stabilizer subspace where one can encode a logical qubit for certain topologies of the underlying manifold, i.e. a topological qubit. The eigenstates of $\hat{A}_s$, in particular, have an eigenvalue $+1$ if an even number of spins connected to the site s are in the $|-\rangle$ eigenstate of $\hat{\sigma}^x$, and -1 if this number is odd. Therefore, any state composed of *closed strings* minimizes the energy corresponding to the first part of (1.60), where a string is formed by a path in the lattice composed of nearest-neighbor links with spins in the local $|-\rangle$ state,

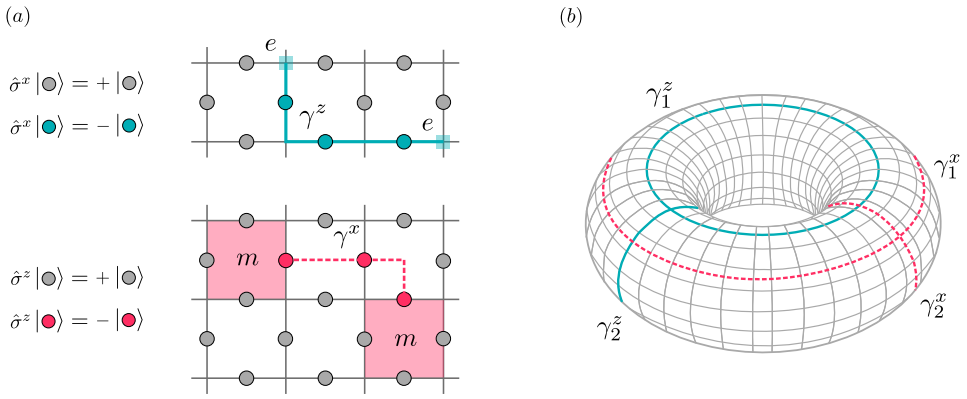

Fig. 1.13 Non-local string operators: (a) The string operators (1.61) create pairs of deconfined electric (e) or magnetic (m) quasi-particles on top of the ground state of the Toric code. **(b)** When the system is placed on a torus, one can apply four types of non-contractible closed strings that do not change the energy.

while the rest is in the $|+\rangle$ state (Fig. 1.12(b)). Since B_p transforms every closed string into another one by flipping the spins around a plaquette p, the ground state of the full Hamiltonian corresponds to a highly-entangled equal-amplitude superposition of all such strings, $|\psi\rangle_{\rm TC} = \sum_{\Gamma_C} |\Gamma_C\rangle$. The ground state has an energy $E_{\rm TC} = -2JN_{\rm p}$, where $N_{\rm p}$ is the number of plaquettes in the lattice.

To show that $|\psi\rangle_{\rm TC}$ has topological order, we demonstrate that it becomes degenerate when we place it on a torus, which can be exploited to encode topological qubits and performed active methods to detect and correct local errors. Let us first introduce two types of string operators,

$$\hat{W}_{\gamma^x} = \prod_{(\mathbf{i},\mathbf{j})\in\gamma^x} \hat{\sigma}^x_{(\mathbf{i},\mathbf{j})}, \quad \hat{W}_{\gamma^z} = \prod_{(\mathbf{i},\mathbf{j})\in\gamma^z} \hat{\sigma}^z_{(\mathbf{i},\mathbf{j})}, \tag{1.61}$$

where $\gamma^{x/z}$ denote strings in the lattice as depicted in Fig. 1.13**(a)**. These operators create two different types of excitations on top of the ground state. $\hat{W}^z_\gamma$ creates an open string with one *electric* quasi-particle e at each end of the string, while $\hat{W}^x_\gamma$ creates two *magnetic* quasi-particles at the corresponding end plaquettes with a π flux. In both cases the excitation energy with respect to the ground state is $2J$. Note that the energy of either of these two quasi-particles does not depend on the length of the string, and we say that the quasi-particles are *deconfined*. We will come back to this notion and study it in more detail in chapters 6 and 7.

Consider now the two types of closed paths in the torus that can not be contracted to a point, $\gamma_1^{x/z}$ and $\gamma_2^{x/z}$ (Fig. 1.13**(a)**). The corresponding string operators

fulfill the following commutation relations,

$$\begin{aligned} \left\{\hat{W}_{\gamma_1^x}, \hat{W}_{\gamma_2^z}\right\} = 0, \quad \left\{\hat{W}_{\gamma_1^z}, \hat{W}_{\gamma_2^x}\right\} = 0, \\ \left[\hat{W}_{\gamma_1^x}, \hat{W}_{\gamma_1^z}\right] = 0, \quad \left[\hat{W}_{\gamma_2^x}, \hat{W}_{\gamma_2^z}\right] = 0. \end{aligned} \tag{1.62}$$

and, moreover, the four of them commute with the Hamiltonian. Let us consider the common eigenstates of $\hat{W}_{\gamma_1^x}$ and $\hat{W}_{\gamma_2^x}$ that have eigenvalues ± 1. The anticommutation relations (1.62) allow us to classify these eigenstates by the number of strings (modulo two) created by $\hat{W}_{\gamma_1^z}$ and $\hat{W}_{\gamma_2^z}$. In particular, if $|{+}{+}\rangle$ is an eigenstate of $\hat{W}_{\gamma_1^x}$ and $\hat{W}_{\gamma_2^x}$ with an even number of strings of each type, with $\hat{W}_{\gamma_1^x}|{+}{+}\rangle = |{+}{+}\rangle$ and $\hat{W}_{\gamma_2^x}|{+}{+}\rangle = |{+}{+}\rangle$, we get $\hat{W}_{\gamma_1^x}\hat{W}_{\gamma_2^z}|{+}{+}\rangle = -\hat{W}_{\gamma_2^z}|{+}{+}\rangle$. We can thus identify $\hat{W}_{\gamma_2^z}|{+}{+}\rangle = |{-}{+}\rangle$. Since both operators commute with the Hamiltonian, we also have $\hat{H}_{\mathrm{TC}}|{+}{+}\rangle = E_{++}|{+}{+}\rangle$ and $\hat{H}_{\mathrm{TC}}|{-}{+}\rangle = \hat{H}_{\mathrm{TC}}\hat{W}_{\gamma_2^z}|{+}{+}\rangle = E_{++}|{-}{+}\rangle$. Therefore, both type of states, while being orthogonal, have the same energy. A similar argument can be made for the states $|{+}{-}\rangle$ and $|{-}{-}\rangle$. We conclude that the whole spectrum of the Toric code Hamiltonian becomes four-fold degenerate when the system is placed on a torus. This degeneracy is protected since a non-local operation is required to connect the different degenerate eigenstates, where the number of local terms increases linearly with the system size, which is considered a fingerprint of topological order. Accordingly, one can encode two logical qubits using the non-contractible string operators as their logical operators, and perform active error correction by measuring all local the star and plaquette operators to detect possible errors, and correct them without compromising the encoded quantum information.

Ising gauge theory

We finish this section with another example of a system that displays topological order. One important feature of topologically-ordered phases of matter that we have not yet mentioned is the possibility to describe their low-energy properties using gauge theories [ZCZW19]. The use of gauge theories, characterized by local symmetries, is ubiquitous in theoretical physics, ranging from the description of fundamental particles such as quarks [Sch14] to the physics behind high-temperature superconductors [BA88]. In chapter 7, we study a model where fermionic matter is coupled to dynamical gauge fields, invariant under a local $\mathbb{Z}_2$ symmetry. Here we introduce a simpler $\mathbb{Z}_2$ gauge theory on the lattice, the so-called *Ising gauge theory* (IGT) [Weg71], and explain the relation between gauge invariance and topological order. In chapter 7, we show how the presence of fermionic matter gives rise, moreover, to novel intertwined topological effects. The IGT in the presence of Ising-type

matter is described by the following spin Hamiltonian [FS79],

$$\begin{aligned}\hat{H}_{\mathrm{IGT}} = &- g\sum_{(\mathbf{i},\mathbf{j})}\hat{\sigma}^{x}_{(\mathbf{i},\mathbf{j})} - \frac{1}{g}\sum_{p}\prod_{(\mathbf{i},\mathbf{j})\in p}\hat{\sigma}^{z}_{(\mathbf{i},\mathbf{j})} \\ &- \frac{1}{\lambda}\sum_{\mathbf{i}}\hat{\tau}^{x}_{\mathbf{i}} - \lambda\sum_{(\mathbf{i},\mathbf{j})}\hat{\tau}^{z}_{\mathbf{i}}\hat{\sigma}^{z}_{(\mathbf{i},\mathbf{j})}\hat{\tau}^{z}_{\mathbf{j}},\end{aligned} \tag{1.63}$$

where $\hat{\tau}^{x/z}_{\mathbf{i}}$ and $\hat{\sigma}^{x/z}_{(\mathbf{i},\mathbf{j})}$ are Pauli matrices acting on spin-1/2 systems located on the sites $\mathbf{i} = (i_1, i_2)$ and links $(\mathbf{i},\mathbf{j})$, respectively, of a two-dimensional square lattice. In this model, degrees of freedom on the sites and links correspond to matter and gauge fields, respectively. The first two terms of the Hamiltonian form the *pure-gauge* part of the theory, and include the so-called *electric field* term, as a well as a plaquette or *magnetic field* term, similarly to the TC Hamiltonian (1.60). The second part includes a mass term for the matter fields, as well as the matter-gauge interaction.

The IGT has a $\mathbb{Z}_2$ gauge symmetry, this is, the Hamiltonian (1.66) is invariant under local transformations that can be performed independently on each site, $\hat{\tau}^{z}_{\mathbf{i}} \to e^{i\alpha_{\mathbf{i}}}\hat{\tau}^{z}_{\mathbf{i}}$ and $\hat{\sigma}^{z}_{(\mathbf{i},\mathbf{j})} \to e^{-i\alpha_{\mathbf{i}}}\hat{\sigma}^{z}_{(\mathbf{i},\mathbf{j})}e^{i\alpha_{\mathbf{j}}}$, with $\alpha_{\mathbf{i}} \in \{0,\pi\}$. These transformations are generated by the following operators,

$$\hat{G}_{\mathbf{i}} = \hat{\tau}^{x}_{\mathbf{i}}\prod_{(\mathbf{i},\mathbf{j})\in s}\hat{\sigma}^{x}_{(\mathbf{i},\mathbf{j})}. \tag{1.64}$$

Notice that these local generators coincide with the star operators of the TC Hamiltonian (1.60), with an additional matter operator $\hat{\tau}^{x}_{\mathbf{i}}$ acting on the sites. Since the generators commute with the Hamiltonian, $[\hat{H}_{\mathrm{IGT}}, \hat{G}_{\mathbf{i}}] = 0$, all of them share a common eigenbasis,

$$\hat{G}_{\mathbf{i}}\left|\psi\right\rangle = (-1)^{q_{\mathbf{i}}}\left|\psi\right\rangle. \tag{1.65}$$

Each symmetry sector is thus characterized by an extensive number of conserved quantities, known as $\mathbb{Z}_2$ *static charges* $q_{\mathbf{i}} \in \{0,1\}$.

Let us consider the *even sector*, where $q_{\mathbf{i}} = 0\ \forall\,\mathbf{i}$. In this situation, the IGT presents two different phases (Fig. 1.14), one where matter quasi-particles are deconfined, similar to the case of the excitations described above for the TC, and another one where these are *confined*. In the confined phase, the potential energy between pairs of quasi-particles increases with the distance between them, instead of being independent of the distance, as in a deconfined phase. We can connect the latter to the ground state of the TC, by using the redundancy implicit in the gauge symmetry to express the matter degrees of freedom in terms of gauge fields. For states in the even sector, we can make the substitution $\hat{\tau}^{x}_{\mathbf{i}} = \prod_{(\mathbf{i},\mathbf{j})\in s}\hat{\sigma}^{x}_{(\mathbf{i},\mathbf{j})}$. This can be formalized in terms of a unitary operations $\hat{U}$ that decouple both degrees

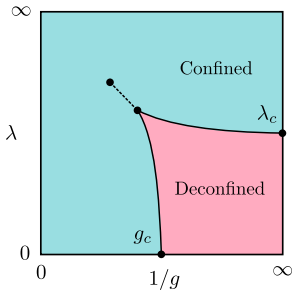

Fig. 1.14 Phase diagram of the Ising gauge theory: this model present two quantum phases at zero temperature, a topologically-ordered deconfined phase and a topologically-trivial confined phase. In the figure, the dashed and solid lines represent first-order and continuous phase transitions, respectively.

of freedom in the gauge-invariant Hamiltonian [Fra13], which are just CNOT operations for this particular case [HVAS+15]. The IGT Hamiltonian (1.60) is thus equivalent to a TC Hamiltonian with transverse and parallel fields [TKPS10],

$$\begin{aligned}\hat{U}\,\hat{H}_{\mathrm{IGT}}\hat{U}^{\dagger} = &- g\sum_{(\mathbf{i},\mathbf{j})}\hat{\sigma}^{x}_{(\mathbf{i},\mathbf{j})} - \frac{1}{g}\sum_{p}\prod_{(\mathbf{i},\mathbf{j})\in p}\hat{\sigma}^{z}_{(\mathbf{i},\mathbf{j})} \\ &- \frac{1}{\lambda}\sum_{\mathbf{i}}\prod_{(\mathbf{i},\mathbf{j})\in s}\hat{\sigma}^{x}_{(\mathbf{i},\mathbf{j})} - \lambda\sum_{(\mathbf{i},\mathbf{j})}\hat{\sigma}^{z}_{(\mathbf{i},\mathbf{j})},\end{aligned} \tag{1.66}$$

which coincides with Eq. (1.60) for $g, \lambda \to 0$. The deconfined phase of the IGT is thus topologically ordered, while the confined phase is trivial, and the transition between them is not associated to a SSB process. In the TC model, the confined phase appears for large enough fields [VDS09]. In chapter 7, we show how confinement can be frustrated by coupling the $\mathbb{Z}_2$ gauge fields to fermionic matter.

1.4 Summary

In this chapter, we have reviewed the main mathematical tools required to analyze topological phenomena in quantum many-body systems. In particular, we have focused on the description and classification of topological defects in ordered media and topological phases of matter, using tools from differential geometry and algebraic topology. In parts II and III of this thesis, we will encounter different situations where topological features are behind some very interesting phenomena that appear in condensed-matter and high-energy physics, such as confinement or charge fractionalization. Moreover, we will also see examples where more than one

topological feature appear simultaneously, giving rise to novel intertwined topological effects for strong enough interactions. As we mentioned above, the study of topological effects is far from trivial in the presence of interactions. In the next and last chapter of this first introductory part, we review two different approaches to investigate strongly-interacting quantum many body systems.

Chapter 2

From classical to quantum simulations

From a computational point of view, the study of quantum many-body systems is a very complicated task. As the number of particles in the system increases, the computational resources that are required to fully characterize the relevant quantum states grow exponentially. This is specially problematic in the case of *strongly-correlated* phenomena, which, except from a few paradigmatic situations, cannot be approximated using other solvable problems, by means, for example, of perturbation theory or other analytical techniques. This is the case for many of the interaction-induced topological phenomena described in chapter 1, such as topologically-ordered phases of matter. In those cases, numerical simulations are required to investigate the properties of the system. The most fruitful example of this strategy is based on the use of the quantum Monte Carlo algorithm to study the equilibrium properties of many lattice models in condensed matter and high-energy physics. However, this approach fail in many situations, for example when a finite density of fermionic particles is considered, as well as for systems out of equilibrium.

In the last decades, two different but complementary approaches have gain recognition due to their ability to overcome some of these problems. The first one, that we introduce in Sec. 2.1 of this chapter, involves the representation of quantum states in terms of *tensor networks*, allowing for efficient analytical and numerical studies beyond the possibilities of other classical approaches. These techniques have been developed to target only the relevant information such that, by disregarding non-important features, an efficient simulation can be achieved. The second one aims to develop *quantum simulators*, where a quantum system is studied using a different one, which is also quantum and can be controlled experimentally. In

Sec. 2.2 we introduce the notion of a quantum simulator, focusing on the case of ultracold atoms in optical lattices. Along the next parts of this thesis, we will make extensive use of these two approaches.

2.1 Tensor networks

In this section, we briefly review the notion of tensor networks (TN), and the numerical methods based on them that were used in this thesis. TN methods are based on the description of a quantum state as a network of interconnected tensors, where the focus lies on the entanglement properties of the state. This description lies at the core of the density matrix renormalization group algorithm (DMRG) [Whi92, Whi93, OR95, VPC04, Sch11], introduced in 1992 by Steven White, which has been the most successful technique in the last decades to study one dimensional quantum lattice systems. Since then, many other methods based on TN have emerged, extending this framework to the study of quantum physics in many other situations: PEPS for higher dimensions [VMC08], MERA for critical systems [Vid07], tDMRG and TEBD for time evolution [DKSV04, Vid04], etc. These methods overcome some of the difficulties that are present in other numerical techniques, such as restrictions in the system size (exact diagonalization), the inability to include quantum correlations (mean-field theory) or the sign problem in the case of fermionic matter and frustrated systems (quantum Monte Carlo) [Oru14].

2.1.1 Matrix product states

Before explaining the main ideas behind DMRG, we first describe some basic properties of TN states. A tensor is a multidimensional array of complex numbers. The dimension of the array, this is, the number of indices, is called *rank* of the tensor. They generalize the concept of scalar, vector and matrix, which are tensors of rank zero, one and two, respectively. Two tensors can be contracted by summing over the values of repeated indices, forming a new tensor. Consider, for example, the rank-3 tensor,

$$C_{\alpha,\delta,\epsilon} = \sum_{\beta,\gamma} A_{\alpha,\beta,\gamma,\delta} B_{\beta,\epsilon,\gamma}\,, \tag{2.1}$$

which is formed after contracting two of the indices of tensors A and B (Fig. 2.1**(a)**). A TN is just a set of tensors connected to each other by contracting some of their indices according to some pattern [Oru14].

Consider now a quantum many-body system in 1D composed of L particles. A d-dimensional Hilbert space $\mathcal{H}$ is attached to each of them, and the states in $\mathcal{H}$ are given in terms of an orthonormal basis $\{|i_r\rangle\}_{i_r=1,\ldots,d}$, with $r = 1, \ldots, L$. The

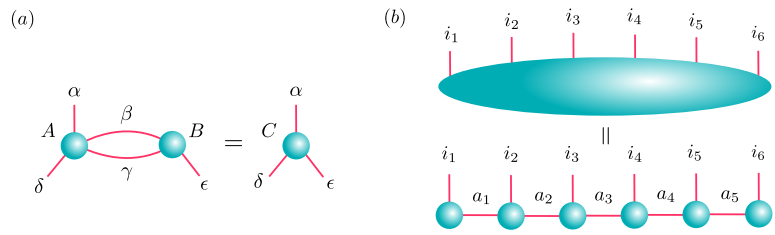

Fig. 2.1 Tensor networks: (a) Two tensors A and B can be contracted into a single one C by summing over its common indices. **(b)** The tensor describing the coefficients of a many-body quantum state can be decomposed into a network of smaller tensors contracted along virtual indices. In the figure, we represent the case of an MPS, describing the state of a 1D system with six physical indices and five virtual ones.

wavefunction describing a many-body state can be written with respect to the basis of the tensor product space as

$$|\psi\rangle = \sum_{i_1,i_2,\dots i_L=1}^{d} C_{i_1,i_2,\dots i_L} \, |i_1, i_2 \dots i_L\rangle \,, \tag{2.2}$$

where $C_{i_1,i_2,\dots i_L}$ is a set of d^L complex numbers, or a rank-L tensor. A TN representation of a state consists on the decomposition of the big tensor C on a set of smaller tensors, with some of their indices contracted [Sch11]. Consider, for example, the decomposition

$$C_{i_1,\dots,i_L} = \sum_{a_1,\dots a_{L-1}} A^{i_1}_{a_1} A^{i_2}_{a_1,a_2} \dots A^{i_{L-1}}_{a_{L-2},a_{L-1}} A^{i_L}_{a_{L-1}}, \tag{2.3}$$

in terms of rank-3 tensors A (rank-2 on the boundaries) (Fig. 2.1**(b)**). This is the standard form of a *matrix product state* (MPS) [FNW92], a TN representation for one dimensional systems, which can be generalized to higher dimensions [**?**]. The open indices i_l are called *physical indices*, and the contracted ones, a_l, *virtual indices*. Usually, the dimension of the latter is truncated to a value D, called the *bond dimension* of the MPS. By doing this, the state of the system is approximated by specifying $\mathcal{O}(LdD^2)$ complex parameters, scaling polynomially with the system size, rather than the exponential scaling with d^L parameters of the most generic state. When the TN is contracted, it gives rise to d^L coefficients, which are no longer independent [Oru14].

The reason why TN are good approximations to interesting quantum states is related to their entanglement properties. Both the bond dimension and the structure of the network determines the amount and structure of entanglement in the state. Although the number of possible many-body states is exponentially large

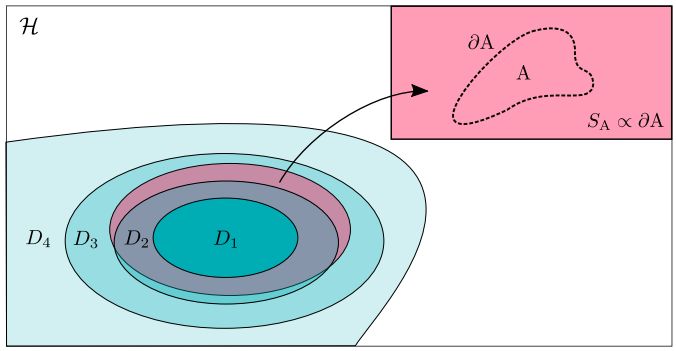

Fig. 2.2 Area law : The number of physically relevant quantum states is very small compared to the exponentially large Hilbert space $\mathcal{H}$ of a quantum many-body system. Ground states of local gapped Hamiltonians, for instance, have much less entanglement than general quantum states. In particular, the entanglement entropy corresponding to a certain subsystem A scales only with its area ∂A, a property known as the area law. Tensor network states can be built to reproduce this property. As the bond dimension increases ($D_1 < D_2 < D_3 < D_4 \ldots$), this variational family captures larger portions of $\mathcal{H}$. Although to describe every possible state in $\mathcal{H}$ D should increase exponentially in the system size, area-law states can be approximated efficiently with a finite value of D.

in size of the system, in many situations only a small subset of them has physical relevance. In particular, ground states of local gapped Hamiltonians are known to obey an *area law* [VLRK03, CC04, Sre93, ECP10]. This implies that the entanglement entropy between a subsystem and the rest of the system grows only with the area ∂A of the former, this is, $S_A \propto \partial A$ to the leading order (Fig. 2.2). For the majority of quantum states, on the other hand, the entanglement entropy increases with the volume. Moreover, the number of states that can be reached by evolving a quantum state after a time $\mathcal{O}(log(L))$ is exponentially small [PQSV11]. Therefore, starting from a state that belongs to the subset that obeys the area law, most likely one will end up with a state that also belongs to it. Tensor Network states also obey this type of area law by construction, making them efficient approximations of many classes of physically relevant quantum states [Has06, Has07] (Fig. 2.2). For MPS, in particular, the entanglement entropy corresponding to a block of size l is $S(l) \sim \mathcal{O}(D)$, this is, it is independent of l. Moreover, it grows with D, which means that the bond dimension controls the amount of entanglement in the MPS. It can be shown, in particular, that, since the entanglement entropy does not grow with the system size for ground states of local gapped Hamiltonians in 1D, these states can be approximated to arbitrary precision in an efficient way using a MPS with fixed bond dimension [VMC08].

2.1.2 Classification of topological phases

From a theoretical point of view, tensor networks can be used to classify different phases of matter, including topological phases, as we mentioned in chapter 1. To see this, it is important to consider how the matrices $A^{i_l}_{a_{l-1},a_l}$ behave under symmetry transformations. In particular, the physical indices transform under linear representations of the symmetry group, while the virtual ones do so under projective representations. For simplicity, consider a symmetry transformation acting on a single physical index, $|i_l\rangle \to \hat{U}(g)^{i_l'}_{i_l} |i_l'\rangle$. This transformation should leave the state invariant up to a phase $e^{i\theta_g}$, which induces the following transformation on the virtual indices,

$$\hat{U}(g)^{i_l'}_{i_l} A^{i_l} = \hat{V}^{-1}(g) A^{i_l'} \hat{V}(g) e^{i\theta_g}. \tag{2.4}$$

The operators $\hat{V}(g)$ acting on the virtual space thus form a projective representation of the group, carrying the same information about the topological properties of the system as the edge states. One can thus characterize the possible topological phases associated to a certain protecting symmetry by studying the different projective representations of the corresponding symmetry group.

These non-trivial topological properties can be detected by looking at the entanglement spectrum (EE) of the system, which contains information of what can be regarded as artificial edge states in the bulk. This notion was introduced first to detect topological order in fractional quantum hall states [LH08], and was later applied to the Haldane phase of spin-1 chains [PTBO10]. The EE is obtained by first diving the system into two halves, A and B, and calculating the corresponding Schmidt decomposition,

$$|\psi\rangle = \sum_i \lambda_i |\psi_i\rangle_{\mathrm{A}} \otimes |\psi_i\rangle_{\mathrm{B}}. \tag{2.5}$$

The entanglement spectrum ξ_i can be extracted from the Schmidt coefficients through the relation $\lambda_i = e^{-\xi_i/2}$. The elements of the spectrum can be interpreted as the energies of a so-called *entanglement Hamiltonian* $\hat{H}_{\mathrm{E}}$, defined in terms of one of the reduced density matrices, for instance,

$$\rho_{\mathrm{A}} = \mathrm{Tr}_{\mathrm{B}} \left(|\psi\rangle \langle\psi| \right) \equiv e^{-\hat{H}_{\mathrm{E}}} \tag{2.6}$$

where Tr_{B} denotes the trace with respect to subsystem B. Using this relation, one can interpret ρ as the density matrix of a thermodynamic system described by $\hat{H}_{\mathrm{E}}$ at temperature $T = 1$, such that its thermodynamic entropy coincides with the entanglement entropy,

$$S_{\mathrm{A}} = \mathrm{Tr} \left(\rho_{\mathrm{A}} \log \rho_{\mathrm{A}} \right) = \sum_i \xi_i e^{-\xi_i} \tag{2.7}$$

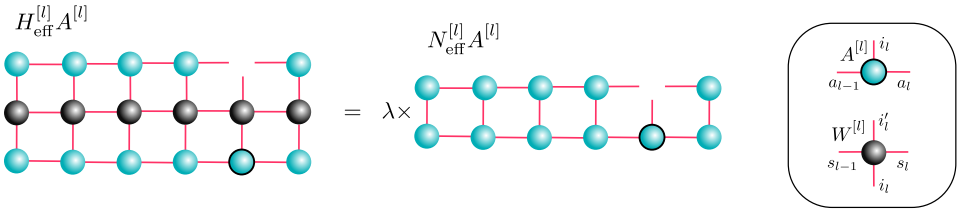

Fig. 2.3 DMRG : Instead of trying to optimize all MPS tensors simultaneously, DMRG runs iteratively by locally optimizing each tensor $A^{[l]}$, sweeping through the chain back and forth until it converges to the global optimum. Each local optimization reduces to a generalized eigenvalue problem for an effective Hamiltonian H_{eff}, computed by contracting the Hamiltonian in a MPO form with all the MPS matrices except the one being optimized. In the figure, we represent the eigenvalue equation in a diagrammatic form , where $W^{[l]}$ are the tensors that form the Hamiltonian MPO.

It can be proven that the EE is doubly degenerate for non-trivial SPT phases [PTBO10], and that this degeneracy cannot be lifted unless the gap closes or the protecting symmetry is broken. This degeneracy mimics the double degenerate part of the energy spectrum corresponding to the edge states of a finite system with real boundaries, and it is protected even if edge states are absent. Note that, since TN states are constructed to reproduce certain entanglement structure, the computation of entanglement related quantities, such as the topological entanglement entropy and the entanglement spectrum, is more straightforward than for general states.

2.1.3 Density-matrix renormalization group

As we mentioned, TN states are very useful tools to perform numerical simulations of quantum many-body systems. In particular, they serve as a variational family that can be optimized to find relevant quantum states, as in the case of DMRG. More specifically, the goal of this algorithm is to minimize the ground state energy of a 1D Hamiltonian as a functional of the tensors $A^{i_l}_{a_{l-1},a_l}$ forming an MPS, constrained by the normalization condition of the state,

$$\min_{\{A\}} \left(\langle\psi[A]|\, \hat{H}\, |\psi[A]\rangle - \lambda \langle\psi[A]|\psi[A]\rangle \right), \tag{2.8}$$

where we have introduced the Lagrange multiplier λ. In order to calculate the energy, the Hamiltonian $\hat{H}$ has to be written first as a tensor network and then contracted with the MPS. Such a tensor network is known in 1D as a *matrix product operator* (MPO),

$$\hat{H} = \sum_{\{i_l\},\{i'_l\}} \sum_{\{s_l\}} W^{i_1,i'_1}_{s_1} W^{i_2,i'_2}_{s_1,s_2} \ldots W^{i_L,i'_l}_{s_{L-1}} \, |i_1, i_2 \ldots i_L\rangle \, \langle i'_1, i'_2 \ldots i'_L| \,. \tag{2.9}$$

The objects $W^{i_l,i'_l}_{s_{l-1},s_l}$ are rank-4 tensors with two physical and two virtual indices. The dimension of the former depends on the number of different terms in $\hat{H}$ and, if these terms are local, $\hat{H}$ can be written as an exact MPO of finite dimension [VMC08].

The DMRG algorithm performs an efficient optimization of the MPS by locally optimizing each tensor $A^{[l]}$ while keeping the other ones fixed,

$$\min_{A^{[l]}} \left(A^{[l]\dagger} H^{[l]}_{\text{eff}} A^{[l]} - \lambda A^{[l],\dagger} N^{[l]}_{\text{eff}} A^{[l]} \right) \tag{2.10}$$

where H_{eff} is an effective Hamiltonian obtained by contracting $\hat{H}$ with all the MPS tensors except from $A^{[l]}$ (Fig. 2.3). The tensor $N^{[l]}_{\text{eff}}$ guarantees that the resulting MPS is always normalized, and can be transformed into the identity with a proper gauge choice [VMC08]. Finding the minimum for this quadratic optimization is equivalent to solving a generalized eigenvalue equation,

$$H^{[l]}_{\text{eff}} A^{[l]} = \lambda N^{[l]}_{\text{eff}} A^{[l]} \tag{2.11}$$

which is a standard optimization problem that can be solved efficiently. The algorithm runs by sweeping the MPS back and forth, optimizing each tensor one at a time. This procedure is efficient and, moreover, its convergence to a global minimum is guaranteed [Sch11].

We finish this section by noting how one can also access the thermodynamic limit directly using infinite MPS states, where translational invariance is assumed by considering a repeating unit cell formed by a certain number of A tensors [Sch11]. Similarly to the finite case, one can use an infinite version of the DMRG algorithm (iDMRG) to calculate the ground state directly in the thermodynamic limit. In parts II and III we will make extensive use of both the finite and infinite version of the MPS-based DMRG algorithm, where the majority of the calculations were performed using the TenPy library in Python [HP18].

2.2 Cold-atom quantum simulators

Despite the success of TN techniques to study the properties of many strongly-correlated quantum systems in 1D, there are still limitations when it comes to higher dimensions [VMC08]. Here we describe an alternative approach to investigate those situations based on the use of quantum simulators. Quantum simulators were first introduced by Feynman in 1982 [Fey82]. They consist of quantum systems with a high degree of controllability that can be used to study the properties of other quantum systems that are in general less accessible. Although quantum simulators are not universal quantum computers—in particular, they cannot perform any type of computational operation—they can be designed to efficiently solve

specific problems using current quantum technology [CZ12, BN09]. Here we focus on *analog* quantum simulators, whose degrees of freedom can be mapped to those of the simulated system. The former can be manipulated experimentally in such a way that its dynamics accurately approximates from a mathematical point of view those of the latter. Even if the corresponding physical scales differ, this allows to perform an efficient simulation by first initializing the quantum simulator in the desired initial state and then measuring the final state after certain time, going beyond the possibilities of numerical simulations performed in classical computers.

Many atomic, optical and solid-state systems serve as good candidates to build quantum simulators, due to the large degree of experimental control over its properties. These include ultracold neutral atoms [JBC+98, JZ05, BDZ08, LSA+07, LSA17], trapped ions [CZ95, LBMW03, BR12, LHN+11, PC04], photonic systems [AGW12], Rydberg atoms [WML+10], quantum dots [LD98, Man02, BKKY08] or superconducting circuits [YN03, vOM96]. These ideas have led to the quantum simulation of many condensed matter and high energy physics models. Some examples include spin systems [FSG+08], the Bose [GME+02] and Fermi Hubbard models [MCJ+17], the Tonks-Girardeau gas [PWM+04], supersolid phases [LLH+17], artificial gauge potentials [AAN+11, AAL+13, MSK+13], lattice gauge theories [M+16] and black hole physics [LIB+10].

In this thesis, we considered quantum simulators based on ultracold atoms in optical lattices. These are gases of neutral atoms that can be cooled down to very low temperatures using different methods such as evaporative cooling in magneto-optical traps [CT98, Phi98]. In these regimes, quantum effects become relevant in the macroscopic description of the atomic gas, leading, for instance, to the Bose-Einstein condensation of dilute gases of bosonic atoms [AEM+95, DMA+95]. One can also use counter-propagating laser beams to create periodic potentials for the atoms, known as *optical lattices*. These and other techniques allow to obtain quantum systems described by a huge variety of many-body Hamiltonians, mimicking several condensed matter and high-energy physics models, in a platform where its properties can be investigated in a controllable fashion. This approach was first applied to the Bose-Hubbard model [JBC+98], where a quantum phase transition between a superfluid and a Mott insulating phase was measured experimentally [GME+02].

In this section, we review the main ingredients that are required to describe ultracold atoms in optical lattices. First, we show how the latter can be implemented using off-resonant lasers, and how atoms in periodic potentials present similar band structures as electrons in crystals. Then, we introduce atomic interactions, and how they can be simplified in the ultracold regime. Finally, we derive the many-body lattice Hamiltonians that describe cold atoms, focusing on bosonic species with one or more internal states.

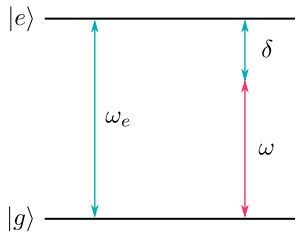

Fig. 2.4 Level structure of a two-level atom with ground state $|g\rangle$ and excited state $|e\rangle$, separated by an energy difference ω_e. We also represent the frequency ω of a laser beam, red-detuned with respect to ω_e by a frequency δ.

2.2.1 Optical lattices

Neutral atoms can be trapped with the help of off-resonant laser fields. These fields generate attractive potentials that can be engineered to create periodic arrays of atoms, resembling the structure of ions in solid crystals [JBC+98]. To see this, let us consider a single atom under the influence of the electric field associated to a laser. The latter will be considered classical and, moreover, we neglect the back action of the atom onto the field. The atomic part of the Hamiltonian is given by

$$\hat{H}_{\mathrm{a}} = \frac{\hat{\mathbf{p}}^2}{2m} + \sum_j \omega_j \left|e_j\right\rangle \left\langle e_j\right|, \tag{2.12}$$

where m is the mass of an atom with momentum $\hat{\mathbf{p}}$, and $|e_j\rangle$ denote the internal levels of the atom with corresponding energies ω_j, where we have shifted the zero of energies such that it corresponds with the internal ground state $|g\rangle$. The interaction between one Alkali atom and the electric field is described in the dipole approximation by the Hamiltonian

$$\hat{H}_{\mathrm{d}} = -\hat{\boldsymbol{\mu}} \cdot \mathbf{E}\left(\hat{\boldsymbol{r}}, t\right) + \mathrm{H.c.}, \tag{2.13}$$

where $\mathbf{E}\left(\hat{\boldsymbol{r}}, t\right) = E\left(\hat{\boldsymbol{r}}\right) e^{-i\omega t} \boldsymbol{\epsilon}$ is the field generated by a laser with frequency ω, polarization $\boldsymbol{\epsilon}$ and spatial profile $E(\hat{\boldsymbol{r}})$, and $\hat{\boldsymbol{\mu}} = e\,\hat{\boldsymbol{r}}$ is the corresponding dipole operator for the electron in the highest partially-occupied orbital, with charge e and position $\hat{\boldsymbol{r}}$.

We restrict the discussion to the case of a two-level atom, where we denote the ground state and excited state by $|g\rangle$ and $|e\rangle$, respectively. In the interaction picture, the total Hamiltonian takes the form

$$\begin{aligned} \hat{H}_{\mathrm{I}} &= e^{i\hat{H}_{\mathrm{a}}t} \left(\hat{H}_{\mathrm{a}} + \hat{H}_{\mathrm{d}}\right) e^{-i\hat{H}_{\mathrm{a}}t} \\ &= \frac{\hat{\boldsymbol{p}}^2}{2m} + \delta \left|e\right\rangle \left\langle e\right| + \left(\frac{\Omega\left(\hat{\boldsymbol{r}}\right)}{2} \left|e\right\rangle \left\langle g\right| + \mathrm{H.c.}\right), \end{aligned} \tag{2.14}$$

where $\delta = \omega_e - \omega$ and $\Omega(\hat{\boldsymbol{r}}) = -2E(\hat{\boldsymbol{r}}) \langle e| \hat{\boldsymbol{\mu}} \cdot \boldsymbol{\epsilon} |g\rangle$ are the detuning and the Rabi frequency, respectively, and we have neglected highly oscillating terms. This approximation, known as the rotating-wave approximation (RWA), is valid as long as $\Omega(\hat{\boldsymbol{r}}) \ll \omega_e + \omega$.

If the detuning is large, $\delta \gg \Omega$, we can obtain an effective Hamiltonian acting on the ground state of the atom, by considering second-order processes induced by the last term of the Hamiltonian (2.14), which lead to a so-called ac-Stark shift that can be rewritten as

$$\hat{H}_{\text{eff}} = \frac{\hat{\boldsymbol{p}}^2}{2m} + V(\hat{\boldsymbol{r}}), \tag{2.15}$$

where the potential is given by $V(\hat{\boldsymbol{r}}) = -|\Omega(\hat{\boldsymbol{r}})|^2/4\delta$, which is proportional to the intensity of the laser field, $|E(\hat{\boldsymbol{r}})|^2$. For a red-detuned laser ($\delta > 0$), the atom feels attracted towards the high intensity regions, whereas for a blue-detuned laser ($\delta < 0$) it does so to the low intensity regions.

A periodic trapping potential can be generated by using two counter-propagating laser beams with the same polarization in each spatial dimension, giving rise to standing waves of the form $E(\hat{r}_i) = E_0^i \cos(k_i \hat{r}_i)$, for $i \in \{x, y, x\}$, where $k = 2\pi/\lambda$ and λ is the wavelength of the laser. The total potential is then given by

$$V(\hat{\boldsymbol{r}}) = \sum_i V_0^i \cos^2(k\hat{r}_i), \tag{2.16}$$

forming an optical lattice with separation $d = \lambda/2$ between different minima. The lattice depth V_0 is usually expressed in terms of the so-called *recoil energy* $E_r = \hbar^2 k^2/2m$. Eq. 2.16 is an example of a cubic lattice. By modifying the intensity, phase and frequency of the laser beams many other geometries can be implemented [BDZ08].

Band structure

In the single-particle picture, the wavefunction of one atom in an optical lattice can be expressed in terms of Bloch wavefunctions, $\psi_{n\boldsymbol{q}}(\mathbf{r}) = e^{i\boldsymbol{q}\cdot\mathbf{r}} u_{n\boldsymbol{q}}(\mathbf{r})$, similarly to the case of electrons in a crystal. In one dimension, the periodic function $u_{nq}(x)$ is given by the solution of the following eigenvalue equation,

$$\left[\frac{(p+\hbar q)^2}{2m} + V(x)\right] u_{nq}(x) = E_{nq} u_{nq}(x) \tag{2.17}$$

obtained by substituting the Bloch wavefunction in the Schrödinger equation under the effective Hamiltonian (2.15). Eq. (2.17) can be solved by taking the Fourier transform of both the wavefunction and the potential. In Fig. 2.5 we represent the band structure corresponding to a 1D optical lattice given by a sinusoidal potential for different lattice depths. If the lattice depth is zero, the bands present a parabolic

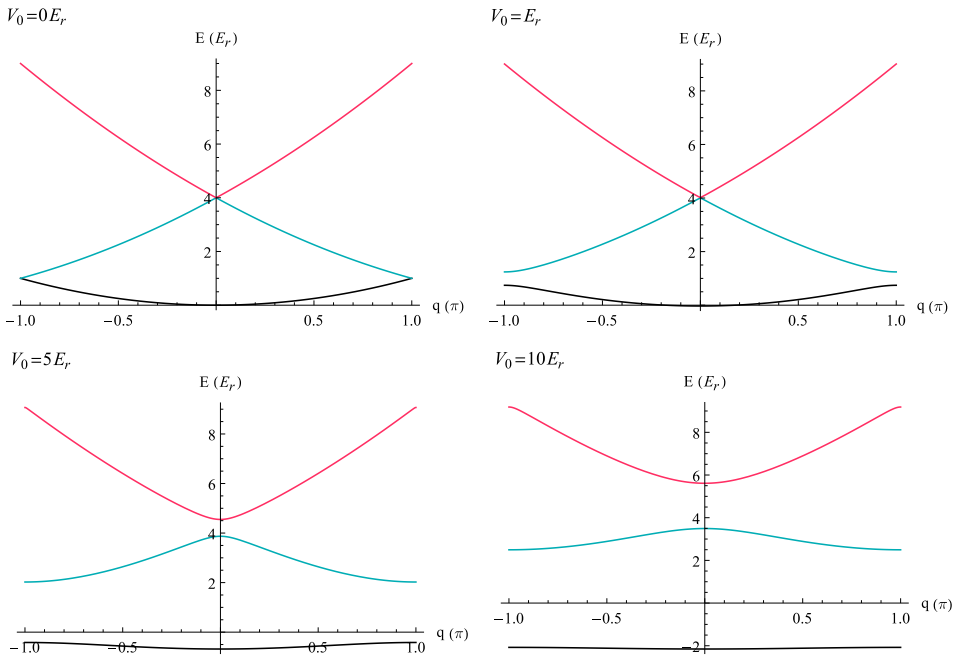

Fig. 2.5 In rhe figure, we represent the band structure corresponding to an atom in an optical lattice for different potentials depths V_0. The energy E is given in terms of the recoil energy E_r and the quasi-momentum q is represented in the first Brillouin zone.

dispersion relation. Any finite value of V_0 opens a gap between each pair of bands, which become more flat for larger values of V_0

In certain cases it is more useful to write the single-particle wavefunctions in a different basis. The so-called *Wannier basis* consists on wavefunctions that are localized on the potential minima, and are defined via the Fourier transformation of the Bloch wavefunctions,

$$w_n(x - x_i) = \frac{1}{\sqrt{L}} \sum_q e^{-iqx_i} \psi_{qn}(x) \tag{2.18}$$

where L is the number of lattice sites. At very large lattice depths, the Wannier functions approach the eigenfunctions of a harmonic oscillator located at site x_i with frequency $\omega_{\mathrm{HO}} = \sqrt{4V_0 E_r}$ [JZ05]. We will use this basis below to write the atomic Hamiltonian in the presence of interactions for large lattice depths.

2.2.2 Atomic interactions

So far we have considered only a single atom in an optical lattice. To describe many-body phenomena, however, it is important to take into account the effect of the atomic interactions. As we will see, in certain circumstances we can forget about most of the microscopic details and describe the interactions using a single parameter [BDZ08].

Scattering length

Let us first introduce some basic concepts from scattering theory to describe the collision between quantum particles [Lan37]. Consider two particles interacting during a short time through a spherically symmetric potential $V(\boldsymbol{r})$, where $\boldsymbol{r}$ is the inter-particle distance. Long before and after the interaction time the particles are considered to be free, and can be described asymptotically by the wavefunction

$$\psi(r) \approx e^{ikz} + f(\theta)\frac{e^{ikr}}{r}. \tag{2.19}$$

The first term in this expression corresponds to an incoming plane wave in the z direction, and the second represents an outgoing spherical wave, where $f(\theta)$ is the so-called *scattering amplitude* and θ is the angle between both waves.

We introduce now the differential *cross section*, defined as the ratio between the probability per unit of time of a particle passing through the differential surface $dS = r^2 d\Omega$, where Ω is the solid angle, and the current density of the incoming wave, which can be expressed as

$$\mathrm{d}\sigma = |f(\theta)|^2 \mathrm{d}\Omega \tag{2.20}$$

The scattering amplitude can be expanded as a superposition of Legendre polynomials $P_l(x)$ corresponding to different angular momenta l (partial wave approximation),

$$f(\theta) = \frac{1}{2ik}\sum_{l=0}^{\infty}(2l+1)(e^{i2\delta_l(k)} - 1)P_l(\cos\theta). \tag{2.21}$$

where $\delta_l(k)$ are known as *phase shifts* [PS08]. Using this expansion, and integrating the differential cross section in terms of the solid angle, we arrive to the following expression for the total cross section,

$$\sigma = \int \mathrm{d}\Omega\, |f(\theta)|^2 = \frac{4\pi}{k^2}\sum_{l=0}^{\infty}\sin^2\delta_l. \tag{2.22}$$

For low energies, this is, if the wavelength of the particles colliding is large compared to the range R of the potential ($kR \ll 1$), the phase shifts in the expansion (2.21)

can be approximated by powers of the momentum, $\delta_l \sim k^{2l+1}$. The dominating term corresponds to the zeroth order with $l = 0$, known as *s-wave scattering*. In the low-energy limit, one can disregard the rest of the terms and write the cross section in terms of a single parameter called the *scattering length*, $\sigma = 4\pi a^2$, with

$$a = -\lim_{k\to 0} \frac{\delta_0(k)}{k} \tag{2.23}$$

The scattering length can be positive or negative, and its value depends on the specific type of atom-atom interaction. Moreover, it can be tuned with the help of magnetic fields by making use of Feshbach resonances [BDZ08].

Ultracold limit

At low energies, all the details about the atom-atom interactions are contained in the scattering length. In particular, we can substitute the exact atomic potential by a contact interaction given by,

$$V(\mathbf{x}) = \frac{2\pi a}{m}\delta(\mathbf{x}) \equiv g\delta(\mathbf{x}) \tag{2.24}$$

where $\delta(\mathbf{x})$ is a Dirac delta, this is, two atoms interact only when they are at the same position. This interaction is attractive for positive scattering lengths, and repulsive for negative ones.

For neutral atoms, the regime where the s-wave approximation is correct is known as the *ultracold limit*. To estimate this regime, consider the cut-off Van der Waals potential,

$$V(\mathbf{r}) = \begin{cases} -C/r^6 & \text{if } r > r_c \\ \infty & \text{if } r \leq r_c \end{cases} \tag{2.25}$$

This potential describes a Van der Waals interaction between two atoms at large distances and a hardcore repulsion when the atoms are closer than a distance r_c of the order of the atomic radius. For non-zero values of the angular momentum $l \neq 0$ this potential has a centrifugal barrier with a height $E \simeq \hbar^2 l^3/ma_c^2$, where $a_c = (2mC/\hbar^2)^{1/4}$ is a characteristic length. For energies smaller than this barrier, only the s-wave scattering is relevant. Converting it to temperatures, we can estimate that, for typical atoms, this occurs at around 1mk. In this ultracold regime, all the scattering channels with $l \neq 0$ are effectively frozen, and we can substitute the Van der Waals potential by a contact potential (2.24). Sub-milikelvin temperatures can be reached in atomic experiments using several cooling techniques [Phi98].

2.2.3 Many-body Hamiltonians

Now that we have discussed all the necessary ingredients, we can introduce the complete many-body Hamiltonian describing ultracold atoms in optical lattices.

We start with the case of a single bosonic species, described by the Bose-Hubbard Hamiltonian [JBC+98], that we will then generalize to take into account spinor gases with more than one internal state.

The Bose-Hubbard model

The Hamiltonian of a system of interacting bosonic atoms on an optical lattice can be expressed in second quantization as

$$\begin{aligned}\hat{H}(t) = &\int \mathrm{d}\mathbf{r}\, \hat{\Psi}^\dagger(\mathbf{r}) \left[-\frac{\hbar^2}{2m}\nabla^2 + V_{\mathrm{ext}}(\mathbf{r})\right] \hat{\Psi}(\mathbf{r}) \\ &+ \frac{1}{2}\int \mathrm{d}\mathbf{r}\, \mathrm{d}\mathbf{r}'\, \hat{\Psi}^\dagger(\mathbf{r})\hat{\Psi}^\dagger(\mathbf{r}')V(\mathbf{r}-\mathbf{r}')\hat{\Psi}(\mathbf{r})\hat{\Psi}(\mathbf{r}').\end{aligned} \tag{2.26}$$

The first part include the single-particle terms, where V_{ext} corresponds to the external potential, including the periodic lattice (2.16) as well as a possible (harmonic) trapping potential $V_{\mathrm{T}}(\boldsymbol{r})$. The second part includes the two-body atomic interactions given by a contact potential $V(\mathbf{r}-\mathbf{r}')$ as the one described above (2.24). Finally, $\hat{\Psi}^\dagger(\mathbf{r})$, $\hat{\Psi}(\mathbf{r})$ are creation and annihilation field operators, respectively, fulfilling the bosonic commutation relations,

$$[\hat{\Psi}(\mathbf{r},t), \hat{\Psi}^\dagger(\mathbf{r}',t)] = \delta^{(3)}(\mathbf{r}-\mathbf{r}'). \tag{2.27}$$

These operators can be expanded in terms of Wannier functions (2.18), since the latter form a complete orthonormal basis. For deep enough lattices, and for low enough temperatures, one can make use of the *tight-binding approximation* and consider only terms that correspond to the lowest energy band,

$$\hat{\Psi}(\mathbf{r}) \approx \sum_i w_0(\mathbf{r}-\mathbf{r}_i)\hat{b}_i, \tag{2.28}$$

where $\hat{b}_i$ ($\hat{b}_i^\dagger$) are bosonic operators annihilating (creating) a particle on lattice site i on the lowest band, with $[\hat{b}_i, \hat{b}_j^\dagger] = \delta_{ij}$. Inserting the expressions (2.28) into the Hamiltonian (2.26) we obtain the Bose-Hubbard model

$$H = -\sum_{\langle i,j\rangle} t_{ij}(\hat{b}_i^\dagger \hat{b}_j + h.c.) + \frac{U}{2}\sum_i \hat{n}_i(\hat{n}_i - 1) - \sum_i \mu_i \hat{n}_i \tag{2.29}$$

where the first sum runs over pairs of nearest-neighbor sites and $\hat{n}_i = \hat{b}_i^\dagger \hat{b}_i$ is the local bosonic density. The parameters in the Hamiltonian can be expressed in terms of overlaps between Wannier functions, where

$$t_{i,j} = -\int \mathrm{d}\mathbf{r}\, w^*(\mathbf{r}-\mathbf{r}_i)\left[-\frac{\hbar^2}{2m}\nabla^2 + V_{\mathrm{ext}}\right] w(\mathbf{r}-\mathbf{r}_j) \tag{2.30}$$

is a tunneling element between nearest-neighbor sites and

$$U_i = g \int \mathrm{d}\mathbf{r}\, |w(\mathbf{r} - \mathbf{r}_i)|^4 \tag{2.31}$$

is the on-site density-density interaction. In Eq. 2.29 we have assumed that the Wannier function are strongly localized around lattice sites, and we neglect tunneling elements beyond nearest-neighbors sites and interactions that are not on the same site [JZ05]. The last term in (2.29) corresponds to a local on-site energy given by the external trap

$$\mu_i = -\int \mathrm{d}\mathbf{r}\, V_{\mathrm{T}}(\mathbf{r}) w(\mathbf{r} - \mathbf{r}_i) \approx V_{\mathrm{T}}(\mathbf{r}_i). \tag{2.32}$$

If the external potential is sufficiently homogeneous we can regard these parameters as site independent, $t_{ij} \equiv t$ and $\mu_i \equiv \mu$. This approximation is valid if the trapping potential $V_{\mathrm{T}}(\mathbf{r})$ varies slowly.

The parameters of the Bose-Hubbard Hamiltonian depend only on the scattering length a, the mass of the atoms m and the properties of the optical potential, which is characterized by the lattice depth V_0 and the wavelength λ. In the limit of very deep lattices these parameters are approximated by the following expressions [BDZ08],

$$t \approx \frac{4}{\sqrt{\pi}} E_r \left(\frac{V_0}{E_r}\right)^{3/4} \exp\left(-2\left(\frac{V_0}{E_r}\right)^{1/2}\right) \tag{2.33}$$

and

$$U \approx \sqrt{8\pi} a \frac{k}{\pi} E_r \left(\frac{V_0}{E_r}\right)^{3/4}. \tag{2.34}$$

The ratio between the tunneling and the Hubbard interactions characterizes the phase diagram of the model, and can be easily controlled by modifying the lattice depth

$$U/t \sim a\frac{k}{\pi} \exp\left(2\left(\frac{V_0}{E_r}\right)^{1/2}\right) \tag{2.35}$$

At zero temperature, the Bose-Hubbard model presents two different phases separated by a quantum critical point at a certain value U_c/t [FWGF89]. For $U/t < U_c/t$, the system is in a gapless superfluid phase characterized by off-diagonal long-range correlations (except for $d = 1$, where the correlations decay algebraically). For $U/t > U_c/t$, it enters into a Mott insulating phase with a finite gap and exponentially-decaying correlations. The transition between the two of them was shown experimentally by Greiner *et al.* [GME+02] using a system of bosonic atoms by modifying the depth of the optical lattice. This seminal experiment showed the possibility to quantum simulate strongly correlated many-body systems using ultracold atoms.

Spinor gases

At the beginning of this section, we showed how the internal structure of neutral atoms can be used to engineer periodic optical potentials using off-resonant lasers. These potentials act effectively on the internal ground state of the atoms, and so far we have disregarded the presence of other energy levels. The Bose-Hubbard model (2.29), in particular, describes the many-body dynamics of ultracold atoms in an optical lattice using scalar field operators, and does not take into account processes that change the internal state of the atoms. This model can be generalized, however, to take into account the atomic spin and to describe the so-called *spinor gases* [SKK01, LSA17, JBC+98].

In general, cold-atom experiments use alkali atoms. In their outer energy level, the latter posses one unpaired electron in the s orbital, with a corresponding electronic spin $S = 1/2$ and zero orbital angular momentum, $L = 0$. The total electronic angular momentum is thus $J = 1/2$. Taking into account the nuclear spin I, the total angular momentum of the atom F can take two values, $|I + 1/2|$ and $|I - 1/2|$. In the absence of a magnetic field, each of them consists on a degenerate manifold of *hyperfine levels*, labeled by the magnetic quantum number $m_F = -F, ..., F$. The corresponding Hamiltonian has a $SU(2F + 1)$ symmetry, which is explicitly broken if a magnetic field is present, lifting also the degeneracy.

Spinor gases are described by the following many-body Hamiltonian, which generalizes Eq. (2.26) to include more than one bosonic state [SKK01],

$$\begin{aligned}\hat{H} = &\sum_{\alpha,\beta} \int \mathrm{d}\mathbf{r}\, \hat{\Psi}^\dagger_\alpha(\mathbf{r}) \left(\delta^{\alpha\beta} \left(-\frac{\hbar^2}{2m}\nabla^2 + V^\alpha_{\mathrm{ext}}(\mathbf{r}) + E^\alpha(B_0) \right) + \Omega^{\alpha\beta}(\mathbf{r}) \right) \hat{\Psi}_\beta(\mathbf{r}) \\ &+ \sum_{\alpha\beta\delta\gamma} \frac{1}{2} \int \mathrm{d}\mathbf{r}\, \mathrm{d}\mathbf{r}'\, \hat{\Psi}^\dagger_\alpha(\mathbf{r}) \hat{\Psi}^\dagger_\beta(\mathbf{r}') V_{\alpha\beta\delta\gamma}(\mathbf{r} - \mathbf{r}') \hat{\Psi}_\delta(\mathbf{r}) \hat{\Psi}_\gamma(\mathbf{r}')\end{aligned} \tag{2.36}$$

where the Greek indices denote the different hyperfine and, possibly, Zeeman sublevels $\{-F, \dots F\}$. Although here we are considering only one type of atom, the Hamiltonian (2.36) can also describe atomic mixtures. The non-interacting part of the Hamiltonian includes, apart from the usual single-particle terms corresponding to each hyperfine level—where $E^\alpha(B_0)$ corresponds to the Zeeman shift due to an external magnetic field B_0—a term that couples different levels through two-photon Raman or microwave transitions [JBC+98], proportional to a Rabi frequency $\Omega^{\alpha\beta}$. The second part of the Hamiltonian describes to the interaction terms, including both intra-species as well as inter-species two-body collisions.

As we have seen, in the ultracold regime each potential $V_{\alpha\beta\delta\gamma}(\mathbf{r} - \mathbf{r}')$ depends only on a single parameter, the scattering length (2.24), that can be different for different internal states. In the presence of symmetries, however, the number of independent parameters can be greatly reduced. In particular, the total spin

$\mathbf{f} = \mathbf{F_1} + \mathbf{F_2}$, where $\mathbf{F_1}$ and $\mathbf{F_2}$ are the corresponding spins of two atoms, is conserved in atomic collisions. If all the atoms have a spin F, the total spin f of the two-body system can take values from 0 to $2F$, with only even (odd) values allowed for bosonic (fermionic) atoms. The number of different scattering channels, and the corresponding scattering lengths, is therefore reduced from $(2F+1)^4$ to $F+1$. The interaction potential can be written as a sum over these channels,

$$V(\mathbf{r}-\mathbf{r}') = \frac{4\pi}{m}\delta(\mathbf{r}-\mathbf{r}')\sum_f a_f \mathcal{P}_f \tag{2.37}$$

where $\mathcal{P}_f$ is the projector operator to the states with total spin f, and $V_{\alpha\beta\gamma\delta}(\mathbf{r}-\mathbf{r}') = \langle\alpha\beta|\, V(\mathbf{r}-\mathbf{r}')\,|\delta\gamma\rangle$. This sum can also be written using spin operators [Ho98],

$$V(\mathbf{r}-\mathbf{r}') = \left(\sum_{n=0}^{F} \alpha_n (\vec{F}_1\cdot\vec{F}_2)^n\right)\delta(\mathbf{r}-\mathbf{r}') \tag{2.38}$$

Consider as an example the case $F=1$, which corresponds, for instance, to one of the hyperfine manifolds of the bosonic species ^{23}Na, that will appear again in chapter 3. In this case, the total spin during a collision can be either 0 or 2, and the interaction potential can be written as

$$V(\mathbf{r}-\mathbf{r}') = \left(g_0 + g_1 \vec{F}_1\cdot\vec{F}_2\right)\delta(\mathbf{r}-\mathbf{r}') \tag{2.39}$$

with

$$g_0 = \frac{4\pi}{m}\frac{2a_{f=2}+a_{f=0}}{3}, \tag{2.40}$$

$$g_1 = \frac{4\pi}{m}\frac{a_{f=2}-a_{f=0}}{3}. \tag{2.41}$$

The total Hamiltonian reduces to

$$\begin{aligned}\hat{H} = &\sum_{\alpha,\beta}\int \mathrm{d}\mathbf{r}\,\hat{\Psi}^\dagger_\alpha(\mathbf{r})\left(\delta^{\alpha\beta}\left(-\frac{\hbar^2}{2m}\nabla^2 + V^\alpha_{\mathrm{ext}}(\mathbf{r}) + E^\alpha(B_0)\right) + \Omega^{\alpha\beta}(\mathbf{r})\right)\hat{\Psi}_\beta(\mathbf{r}) \\ &+ \sum_{\alpha\beta\delta\gamma}\frac{1}{2}\int \mathrm{d}\mathbf{r}\,\mathrm{d}\mathbf{r}'\left[g_0\hat{\Psi}^\dagger_\alpha(\mathbf{r})\hat{\Psi}^\dagger_\beta(\mathbf{r}')\hat{\Psi}_\alpha(\mathbf{r})\hat{\Psi}_\beta(\mathbf{r}')\right. \\ &\left. + g_1\sum_\eta\left(\hat{\Psi}^\dagger_\alpha(\mathbf{r})(F_\eta)_{\alpha,\beta}\hat{\Psi}^\dagger_\beta(\mathbf{r}')\right)\cdot\left(\hat{\Psi}_\delta(\mathbf{r})(F_\eta)_{\delta,\gamma}\hat{\Psi}_\gamma(\mathbf{r}')\right)\right],\end{aligned} \tag{2.42}$$

where the second term will be responsible for the so-called spin-changing collisions. By expanding the spinor field in terms of Wannier functions (2.28) we obtain the

following lattice Hamiltonian in the tight-binding approximation,

$$\hat{H} = \sum_{\alpha,\beta} \sum_{i,j} t_{i,j}^{\alpha,\beta} \hat{b}_{i,\alpha}^{\dagger} \hat{b}_{j,\beta} + \sum_{i,j,k,l} \sum_{\alpha,\beta,\delta,\gamma} U_{i,j,k,l}^{\alpha,\beta,\delta,\gamma} \hat{b}_{i,\alpha}^{\dagger} \hat{b}_{j,\beta}^{\dagger} \hat{b}_{k,\delta} \hat{b}_{l,\gamma} \tag{2.43}$$

where the Hubbard interactions $U_{i,j,k,l}^{\alpha,\beta,\delta,\gamma}$ present the same internal structure as the corresponding scattering lengths. As we mentioned before, the Hamiltonian (2.43) can be easily generalized to include more than one type of atom, as well as both bosonic and fermionic species. Along this thesis, we will do so by considering Bose-Bose (chapter 3) as well as Bose-Fermi (chapter 6) atomic mixtures.

2.3 Summary

In this second introductory chapter, we have reviewed two different approaches to investigate strongly-correlated physics that will be used in the rest of the thesis. First, we considered how to perform efficient numerical simulations, in particular in low-dimensional systems, by representing the corresponding quantum states with tensor networks. These approximate physically-relevant states efficiently by targeting relevant entanglement structures. However, they also show limitations, in particular in higher dimensions where the contraction of the corresponding tensor networks required to calculate expectation values cannot always be performed efficiently. The second approach considered in this chapter tries to overcome these problems by using quantum simulators to investigate quantum systems that are not accessible either experimentally or by classical simulations. We focused on the case of ultracold atoms, that can be used to engineered several many-body Hamiltonians relevant both to condensed matter and high-energy physics.

Part II

Solid-state physics in optical crystals

Chapter 3

Bosonic Peierls insulators

3.1 Introduction: electrons and phonons

The study of interactions between particles and lattice degrees of freedom is of central importance in solid-state physics. The interplay between electrons and phonons has been extensively studied, leading to the description of paradigmatic effects such as superconductivity, polaron formation or charge density waves [AS06, Emi12]. The analogous problem for bosonic matter, on the other hand, has been less investigated. The basic feature of phononic systems is that the lattice degrees of freedom can fluctuate and order at various wavelengths. In one dimension, a system of itinerant particles on a deformable lattice can undergo a Peierls transition [Pei55], characterized by the spontaneous breaking of the lattice translational symmetry. This gives rise to long-range order, with a periodic modulation that depends on the particle density. For fermionic particles, the statistical correlations induced by Pauli's exclusion principle are sufficient to drive such effect, where a gap opens around the Fermi surface. Although the latter is absent in the bosonic case, we will see how similar effects appear in the presence of sufficiently strong interactions.

The study of boson-lattice problems becomes very relevant in the context of quantum simulators, where model Hamiltonians can be engineered with an unprecedented degree of control [BN09, CZ12], as we introduced in chapter 2. Ultracold atoms in optical lattices, in particular, allow to experimentally address systems of strongly-correlated bosons and to study their properties in detail [JZ05, BDZ08, LSA17]. One of the earliest examples was the observation in 2002 of a quantum phase transition between a Mott insulator and a superfluid [GME+02], using an atomic system described by the Bose-Hubbard model [FWGF89]. Since then, many different bosonic models have been implemented, showing how quantum simulators can be used not only to study the properties of materials that are found in Nature,

but also to investigate new quantum many-body phenomena using synthetic matter [SDS05, DGH+15, GJOS14, DGJbuO11, BHS06, DTBA06].

The strongly-correlated regime is usually accessed through optical lattices created with laser beams, mimicking the crystalline structure of solids and enhancing atomic interactions. However, as discussed in the previous chapter, these lattices are static and do not present quantum fluctuations. The particles do not influence the lattice structure and, therefore, phonons are usually not taken into account. Systems of trapped ions can also simulate many-body Hamiltonians [BR12, SPS12, JVW09]. In these systems, phonons appear naturally [LBMW03], and can be used to mediate interactions between the ions [PC04]. However, trapped ions are confined at lattice sites, making the simulation of itinerant particles more challenging. Recently, advances in designing systems composed of both neutral atoms and ions [NGI+14, BCN+13, GND+12, JNG14, HD14, GCOcvacVac09, ZPSK10, SHD10] suggest the possibility of simulating itinerant particles and dynamical lattices simultaneously. This strategy was explored for a chain of fermionic atoms, where a Peierls transition was predicted [BCN+13]. Alternative approaches include the use of molecules in self-assembled dipolar lattices [PGM+08], optical cavities [MMR07, LDML08, BGBE10, PS14, LHD+16, MRP17] or trapped nanoparticles [GTC+12].

In this and the following chapters composing the second part of the thesis, we propose and analyze a one-dimensional model of interacting bosons coupled to a simplified dynamical lattice, the $\mathbb{Z}_2$ Bose-Hubbard model, and discuss possible implementation schemes using mixtures of ultracold bosons. This allows to consider analogous phenomena to those encountered in electron-phonon systems in cold-atomic setups. In particular, we discover a bosonic analog of the Peierls transition, leading to various Peierls insulators for commensurate bosonic densities. Moreover, the investigation of the topological properties of these phases leads to different intertwined topological effects, which arise from the interplay between symmetry breaking and symmetry-protected topology.

Before entering into more details, we devote the rest of this section to introduce some relevant concepts from solid-state physics. We do so by focusing on a particular electron-phonon model, the Su-Schrieffer-Heeger model (SSH), where most of these concepts appear. In Sec. 3.2, we show how to simulate lattice degrees of freedom in cold-atomic systems using bosonic mixtures. Finally, in Sec. 3.2, we investigate the presence of bosonic Peierls insulators in the $\mathbb{Z}_2$ Bose-Hubbard model.

3.1.1 The Su-Schrieffer-Heeger model

The SSH model is a paradigmatic model in solid-state physics [SSH79]. This model was first introduced to study the properties of polyacetylene (Fig. 3.1**(a)**), a quasi-one-dimensional conducting polymer with solitonic excitations [HKSS88]. The orig-

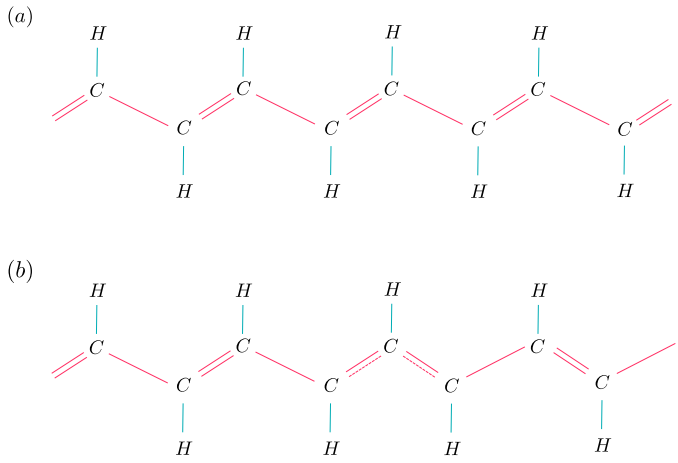

Fig. 3.1 Polyacetylene: (a) *Trans*-$(CH)_x$ molecule showing a dimerized structure of single and double covalent bonds between carbon atoms. **(b)** Soliton in the bond structure.

inal SSH Hamiltonian describes a one-dimensional atomic chain where electrons are coupled to phononic degrees of freedom,

$$\begin{aligned}\hat{H} = &- \sum_{i,\sigma} \left[t + \alpha(\hat{q}_i - \hat{q}_{i+1})\right] \left(\hat{c}^\dagger_{i,\sigma}\hat{c}_{i+1,\sigma} + \text{H.c.}\right) \\ &+ \sum_i \frac{\hat{p}_i^2}{2M} + \frac{K}{2}\sum_i (\hat{q}_i - \hat{q}_{i+1})^2.\end{aligned} \tag{3.1}$$

Here atoms are located at sites i, and $\hat{c}^\dagger_{i,\sigma}$ and $\hat{c}_{i,\sigma}$ are the corresponding fermionic creation and annihilation operators, respectively, acting on those sites for a spin state $\sigma \in \{\uparrow, \downarrow\}$, with $\{\hat{c}^\dagger_{i,\sigma}, \hat{c}_{j,\sigma'}\} = \delta_{i,j}\delta_{\sigma,\sigma'}$. The movement of the atoms around their equilibrium positions is described by quantum harmonic oscillators with position and momentum operators $\hat{q}_i$ and $\hat{p}_i$, respectively, with $[\hat{q}_i, \hat{p}_j] = i\delta_{i,j}$. The first part of the Hamiltonian describes the electron tunneling, which depends on the atom positions. The second part corresponds to a set of coupled harmonic oscillators with frequency $\omega_0 = \sqrt{K/M}$, where K is an elastic constant and M is the mass of the atoms.

In the original formulation of the SSH model, electrons interact with acoustic phonons. Alternatively, one can consider a model of optical phonons [SSC03], by replacing the atomic positions with bond operators, $\hat{q}_i - \hat{q}_{i+1} \to \hat{q}_{i,i+1}$. The latter are also described by a set of, now uncoupled, harmonic oscillators. Such replacement simplifies the treatment of the model without modifying its main prop-

erties [WAH15]. The optical SSH model can be written in second quantization as

$$\begin{aligned}\hat{H} = &-\sum_{i,\sigma}\left[t + g(\hat{a}_{i,i+1} + \hat{a}^\dagger_{i,i+1})\right]\left(\hat{c}^\dagger_{i,\sigma}\hat{c}_{i+1,\sigma} + \text{H.c.}\right) \\ &+ \omega_0 \sum_i \hat{a}^\dagger_{i,i+1}\hat{a}_{i,i+1}\end{aligned} \tag{3.2}$$

where $\hat{a}^\dagger_{i,i+1}$ and $\hat{a}_{i,i+1}$ are bosonic creation and annihilation operators, respectively, with $[\hat{a}^\dagger_{i,i+1}, \hat{a}_{j,j+1}] = \delta_{i,j}$, and the coupling constant is given by $g = \alpha/\sqrt{2M\omega_0}$.

3.1.2 Peierls transitions

In the following, we focus on the spinless version of the SSH model. Let us consider first the case of half filling, with an electron density of $\rho = N/L = 1/2$, where N is the number of electrons and L is the number of sites. According to Peierls' theorem [Pei55], within the mean-field approximation, the ground state of a 1D chain spontaneously breaks translation invariance through a lattice distortion, where $\langle \hat{a}_{i,i+1} + \hat{a}^\dagger_{i,i+1}\rangle$ acquires a non-homogeneous value. This is easy to see in the large mass limit, $M \to \infty$ ($\omega_0 = 0$), where the phonons become classical and the mean-field approximation is exact. In this case, the problem reduces to finding the set of classical variables $\langle \hat{a}_{i,i+1} + \hat{a}^\dagger_{i,i+1}\rangle$ that minimizes the energy of the effective non-interacting Hamiltonian,

$$\hat{H} = -\sum_i \left[t + g\langle \hat{a}_{i,i+1} + \hat{a}^\dagger_{i,i+1}\rangle\right]\left(\hat{c}^\dagger_i \hat{c}_{i+1} + \text{H.c.}\right). \tag{3.3}$$

At half filling, the electronic energy is minimized for one of the two possible dimerized configurations, $\langle \hat{a}_{i,i+1} + \hat{a}^\dagger_{i,i+1}\rangle = \pm(-1)^i\delta$, that are degenerate in the thermodynamic limit. In the classical limit, the amplitude δ corresponds to the maximum atomic displacement. The ground state is then in a *bond order wave* (BOW) phase, where a non-zero value of the order parameter $\mathcal{O} = \langle \sum_i (-1)^i(\hat{c}^\dagger_i \hat{c}_{i+1} + \text{H.c.})\rangle$ characterizes the presence of long-range order in the bonds. This spontaneous breaking of translational symmetry is known as *Peierls transition*. It is not restricted to the ground state, but occurs also for finite temperatures lower than a critical one, $T < T_c$ (Fig. 3.2). The BOW phase is an example of a *Peierls insulator*, where the insulating properties arise from the interaction between electrons and lattice degrees of freedom. Another example of a Peierls insulator is the charge density wave that appear in the Holstein model [Hol59], where phonons are located on the same sites as electrons and are coupled to the electron density.

In the classical limit, every rational filling gives rise to a Peierls insulator. In general, it is always energetically favorable to open a gap around the Fermi energy. This occurs whenever translational invariance is spontaneously broken, giving rise

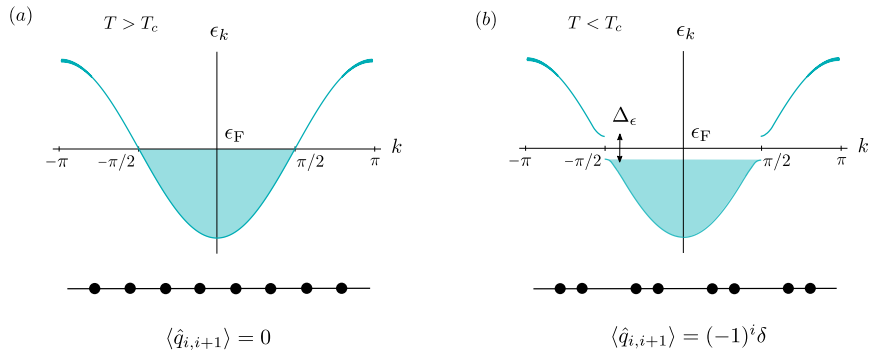

Fig. 3.2 Peierls transtion: (a) At high temperature, the atoms are located at their equilibrium position at zero displacement, $\langle \hat{q}_{i,i+1} \rangle = 0$, and the electronic spectrum consists on a single band. At half filling, the system is thus in a conducting metallic phase. **(b)** If the temperature is low enough, the atoms equilibrate in a dimerized configuration, $\langle \hat{q}_{i,i+1} \rangle = (-1)^i \delta$, breaking spontaneously the translational symmetry of the Hamiltonian. Such configuration is energetically favorable at half filling as it opens a gap $\Delta_\epsilon = 2\delta$ around the Fermy i energy ϵ_F, lowering the electronic energy of the occupied states. The system is then in a Peierls insulating phase, where one of the two electronic bands are completely occupied.

to long-range order. The latter can be observed in the structure factor of the corresponding order parameter—in this case the expectation value of the electron hopping—which shows a peak at momentum $k_0 = \pi/\lambda_0$, where λ_0 is the length of the unit cell. In particular, such an ordered state presents two gaps in the single-particle spectrum, and the Peierls transition implies thus the following relation,

$$1 - \frac{k_0}{\pi} = \left| 1 - 2\frac{k_\mathrm{F}}{\pi} \right|, \tag{3.4}$$

where $k_\mathrm{F} = \pi\rho$ is the Fermi momentum.

For non-zero values of ω_0, one has to take into account the effect of quantum fluctuations. If ω_0 is small, however, the mean-field ansatz still provides a good approximation to the ground state, where the value of δ is now reduced, and so is the size of the gap. A qualitative phase diagram of the model is given in Fig. 3.3. In the case of quantum phonons, a gapless Luttinger liquid (LL) phase appear if the value of the coupling is below a critical value g_c. The value of the critical coupling remains finite for any value of ω_0, and a quantum Peierls transition always leads to a BOW phase at $T = 0$ for sufficiently strong electron-phonon interactions [FH83]. For other fillings, the Peierls gap is smaller, and the quantum Peierls transition occurs at higher values of g_c.

As a final comment, notice that the effective Hamiltonian (3.3) corresponds to

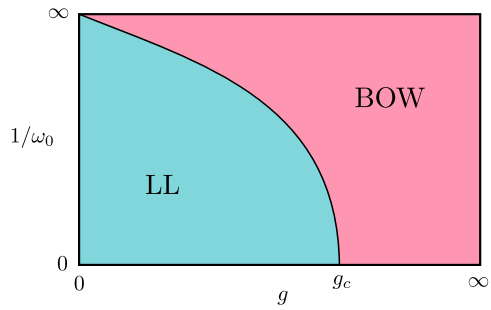

Fig. 3.3 Qualitative phase diagram of the spinless SSH model at $T = 0$: In the classical limit ($\omega_0 = 0$) the ground state is in a BOW phase for any coupling $g \neq 0$. Quantum fluctuations move the critical point $g_c(\omega)$ to a finite value. For $g < g_c$, the ground state is a gapless LL phase.

the one considered in chapter 1 as an example of a model with a chiral topological insulator (1.47). As explained there, one of the two degenerate ground state configurations of the BOW phase corresponds to a topological insulator, while the other one is trivial. Such topological BOW (TBOW) phase is an example of an *intertwined topological phase*, where long-range order coexists with non-trivial topological properties. The interplay between symmetry breaking and symmetry protection that appear in this kind of matter-lattice models is crucial to observe various intertwined topological effects, as we show in the next chapters.

3.1.3 Solitons

As we have seen, Peierls insulators are associated with the SSB of translational invariance. It is then natural to ask about the possibility of finding topological defects in the spectrum of the theory. Indeed, the presence of solitons in the ground state of polyacetylene was the original motivation to introduce the SSH model [SSH79]. In chapter 1 we associated the presence of defects to the topological structure of the ground state manifold in the ordered phase. We can directly apply the theory of topological defects to the present case by first interpreting discrete translational invariance in the disordered phase as the product of a $\mathbb{Z}_n$ symmetry within a n-site unit cell and translations of the whole unit cell, this is, of integer multiples of n sites. After a Peierls transition leading to an ordered state characterized by a momentum $k_0 = \pi/n$, the $\mathbb{Z}_n$ symmetry is completely broken, while the unit-cell translational invariance remains intact. As indicated in Sec. 1.1, a broken discrete symmetry in 1D can only give rise to 0-dimensional defects. The possible defects are given by the number of connected components of the 0-dimensional ground-state manifold, which corresponds to $\mathbb{Z}_n$ in this case.

One interesting feature of topological defects in Peierls insulators is that they appear not only as excited states for a certain electron filling, but also in the ground state when the system is doped with extra electrons or holes. In the SSH model, in particular, one soliton-antisoliton pair appears as we dope the half-filled BOW state with one fermion. Each defect interpolates between the two degenerate ground-state configurations at half filling (Fig. 3.1**(b)**), where the mean-field atom displacement is given by

$$\langle \hat{q}_i \rangle = (-1)^i \tanh\left(\frac{i - i_0}{\xi}\right) \tag{3.5}$$

where i_0 is the location of the defect and ξ its localization length [HKSS88]. These defects are not bound to each other and can move freely along the chain due to the remaining translational symmetry.

The reason why solitons appear in the ground state of the system is that they create electronic states in the middle of the gap. In the SSH model, if only a few extra fermions are introduced in the system above a certain rational filling, it is thus more favorable to create defects that will accommodate these particles rather than to rearrange the whole system into a new ordered configuration. When the doping increases to reach a new rational filling, however, a new Peierls insulator will form characterized by a new wavelength. The fermionic states associated with the solitons present fractional charges. The phenomenon of charge fractionalization was first studied in the context of quantum field theory by Jackiw and Rebbi [JR76], and was later investigated in solid-state physics [SS81]. In chapter 5, we show how similar effects can also take place in cold-atomic system and, in particular, how bosonic matter can also fractionalize.

3.2 Synthetic dynamical lattice

In this section, we introduce a modified version of the SSH model, better suited to implement lattice degrees of freedom in cold-atomic systems. We also extend the standard matter-lattice models to include bosonic matter, and propose an experimental implementation using bosonic mixtures.

3.2.1 Rotor SSH

The Hilbert space associated to each phonon subsystem is infinite dimensional. To simulate it with cold atoms it is necessary first to truncate it in a controlled way, and to approximate it by a finite-dimensional space. We use here the Holstein-Primakoff transformation to formalize the truncation process [HP40]. These transformation represents angular momentum operators in terms of bosonic creation

and annihilation operators,

$$\begin{aligned}\hat{S}^{+} &= \sqrt{2S}\sqrt{1-\frac{\hat{a}^{\dagger}\hat{a}}{2S}}\,\hat{a},\\ \hat{S}^{-} &= \sqrt{2S}\,\hat{a}\sqrt{1-\frac{\hat{a}^{\dagger}\hat{a}}{2S}},\\ \hat{S}^{z} &= S-\hat{a}^{\dagger}\hat{a}\end{aligned} \tag{3.6}$$

where S is the total angular momentum and $\hat{S}^{+}=\hat{S}^{x}+i\hat{S}^{y}$ and $\hat{S}^{-}=\hat{S}^{x}-i\hat{S}^{y}$ are ladder operators. The angular momentum operators $\hat{S}^{i}$, with $i\in\{x,y,z\}$, satisfy the commutation relations $[\hat{S}^{i},\hat{S}^{j}]=i\sum_{k}\epsilon_{ijk}\hat{S}^{k}$, where ϵ_{ijk} is the Levi-Civita symbol. Finally, $\hat{a}^{\dagger}$ and $\hat{a}$ are bosonic creation and annihilation operators satisfying the canonical commutation relations $[\hat{a},\hat{a}^{\dagger}]=1$. These transformations (3.6) can be inverted, expressing the bosonic operators in terms of the angular momentum ones, effectively truncating the infinite Hilbert space to a space of dimension $2S+1$, with $0<\langle\hat{a}^{\dagger}\hat{a}\rangle<2S$. The error in the approximation decreases, therefore, as S increases. In particular, in the limit $S\gg 1$, we can approximate the square root in (3.6) by its power expansion,

$$\sqrt{1-\frac{\hat{a}^{\dagger}\hat{a}}{2S}}=1-\frac{1}{2}\frac{\hat{a}^{\dagger}\hat{a}}{2S}+\mathcal{O}(S^{-2}) \tag{3.7}$$

By restricting ourselves to the zeroth-order term we obtain the following expression,

$$\hat{a}^{\dagger}+\hat{a}\approx\sqrt{\frac{2}{S}}\,\hat{S}^{x} \tag{3.8}$$

We can define now an S-dependent *rotor SSH* Hamiltonian by applying the Holstein-Primakoff transformation (3.6) to the spinless SSH Hamiltonian introduced in the last section, and using the approximation (3.8),

$$\hat{H}_{S}=-t\sum_{i}\left[t+g_{S}\hat{S}^{x}_{i,i+1}\right]\left(\hat{c}^{\dagger}_{i}\hat{c}_{i+1}+\text{H.c.}\right)-\omega_{0}\sum_{i}\hat{S}^{z}_{i,i+1}, \tag{3.9}$$

with $g_{S}=g\sqrt{\frac{2}{S}}$. Let us consider now the importance of the approximation (3.8) for different physical regimes:

- High-frequency limit ($\omega_{0}\gg t,g_{S}$): in this regime the number of phonons is small at low energies, $\hat{a}^{\dagger}\hat{a}\ll 2S$, and the approximation (3.8) holds even for small values of S.
- Low-frequency limit ($\omega_{0}\ll t,g_{S}$): in this case, there are large fluctuations in the photon number, while $a+\hat{a}^{\dagger}$ becomes well defined, so the truncation is not justified. However, as we will see, the relevant physics survives even in this limit.

After a spin rotation, we can expressed the rotor SSH model as

$$\hat{H}_S = -t \sum_i \left[t + g_S \hat{S}^z_{i,i+1} \right] \left(\hat{c}^\dagger_i \hat{c}_{i+1} + \text{H.c.} \right) + \omega_0 \sum_i \hat{S}^x_{i,i+1}, \tag{3.10}$$

3.2.2 Quantum simulation with bosonic mixtures

We propose how to simulate a dynamical lattice using a mixture of ultracold bosons trapped in an optical lattice. The simulated Hamiltonian extends the rotor SSH model (3.10) introduced above, allowing us to simultaneously investigate the interaction between both fermionic and bosonic matter coupled to lattice degrees of freedom. We focus here on a particular choice for the atomic species. However, the proposed implementation is valid for other bosonic species.

Experimental Setup

We employ two different atomic species, ^{7}Li and ^{23}Na, both having a total hyperfine angular momentum $F = 1$ with three internal levels given by the magnetic quantum number $m_F \in \{-1, 0, 1\}$ (Fig. 3.4). In the following, we restrict ourselves to the levels $m_F = 1$ for lithium and $m_F \in \{0, 1\}$ for sodium. Both species are trapped using an optical dipole trap (ODT) [GWO00]. The latter uses three laser beams, one for each spatial dimension, and generates the following harmonic trapping potential for the atoms,

$$V^s_{\mathrm{T}}(x, y, z) = \frac{1}{2} m_s (\omega^s_x x^2 + \omega^s_y y^2 + \omega^s_z z^2), \tag{3.11}$$

where m_s is the mass of the atomic species $s \in \{\mathrm{N}, \mathrm{L}\}$ and ω^s are the trapping frequencies, which are independent of m_F.

On top of the ODT we add a Ti-Sapphire laser in the y (axial) direction that can be tuned to a wavelength where the beams are blue detuned for ^{7}Li and red detuned for ^{23}Na [KHJ+17]. Two counter-propagating lasers create a periodic lattice potential for each species (shifted by half period) [MO06],

$$\begin{aligned} V^{\mathrm{L}}_{\mathrm{L}}(y) &= V^{\mathrm{L}}_0 \cos^2(ky) \\ V^{\mathrm{N}}_{\mathrm{L}}(y) &= V^{\mathrm{N}}_0 \sin^2(ky), \end{aligned} \tag{3.12}$$

where $k = \frac{2\pi}{\lambda}$ and λ is the wavelength of the laser. The lattice spacing is $a = \frac{\lambda}{2}$. We assume that the potential strength $V^{\mathrm{N/L}}_0$ is independent of the magnetic quantum number and can be controlled with the laser intensity and the detuning $|\delta|^{\mathrm{N/L}}$. The minima of $V^{\mathrm{L}}_{\mathrm{L}}(y)$ (resp. $V^{\mathrm{N}}_{\mathrm{L}}(y)$) represent the sites (resp. bonds) of the model, hosting the matter (resp. lattice) degrees of freedom.

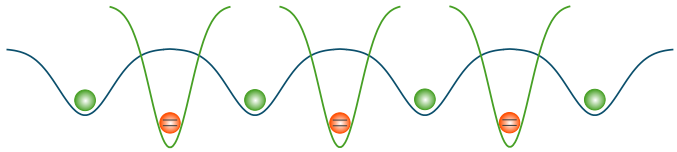

Fig. 3.4 Bose-Bose mixture: In the figure, we represent the proposed experimental setup to implement the rotor SSH model (3.10). Two bosonic species, sodium (green) and lithium (orange), simulate the matter and lattice degrees of freedom, respectively. A single optical lattice generates a periodic potential for each species, shifted by half a period. The optical potential for the sodium atoms is shallow, and they are described by a Bose-Hubbard model. The potential is much deeper for lithium, preventing any tunneling between different minima, and allowing the description of its two internal states in terms of spin operators.

Finally, the atoms also feel a gravitational force in the z direction, $V^s_{\mathrm{G}}(z) = -m_s g z$. With this, the total potential for each atomic species is

$$V^s(\mathbf{x}) = V^s_{\mathrm{T}}(x, y, z) + V^s_{\mathrm{L}}(y) + V^s_{\mathrm{G}}(z). \tag{3.13}$$

Atomic Hamiltonian

For each atomic species, we can write the non-interacting part of the atomic Hamiltonian in second quantization as

$$\hat{H}^{s,\alpha}_0 = \int_{\mathbf{x}} \hat{\psi}^\dagger_{s,\alpha}(\mathbf{x}) \left[-\frac{\hbar^2 \nabla^2}{2m_s} + V^s(\mathbf{x}) + E^s_\alpha(B_0) \right] \hat{\psi}_{s,\alpha}(\mathbf{x}), \tag{3.14}$$

where α corresponds to the allowed internal states ($\alpha = 1$ for lithium and $\alpha \in \{0, 1\}$ for sodium). $E^s_\alpha(B_0)$ includes the linear and the quadratic Zeeman shifts due to an external magnetic field B_0. In the following, we denote $V^s_\alpha(\mathbf{x}) \equiv V^s(\mathbf{x}) + E^s_\alpha(B_0)$. The bosonic field operators $\hat{\psi}_{s,\alpha}(\mathbf{x})$ fulfill the canonical commutation relations,

$$\left[\psi_{s,\alpha}(\mathbf{x}), \psi^\dagger_{s',\beta}(\mathbf{y}) \right] = \delta_{ss'} \delta_{\alpha\beta} \delta(\mathbf{x} - \mathbf{y}). \tag{3.15}$$

Moreover, we can drive transitions between the two internal states of sodium using a radio-frequency field,

$$\hat{H}^{\mathrm{N},01}_0 = \Omega \int_{\mathbf{x}} \left(\hat{\psi}^\dagger_{\mathrm{N},0}(\mathbf{x}) \hat{\psi}_{\mathrm{N},1}(\mathbf{x}) + \mathrm{H.c.} \right), \tag{3.16}$$

where Ω is the corresponding Rabi frequency. The total non-interacting Hamiltonian is $\hat{H}_0 = \hat{H}^{\mathrm{L},1}_0 + \hat{H}^{\mathrm{N},0}_0 + \hat{H}^{\mathrm{N},1}_0 + \hat{H}^{\mathrm{N},01}_0$.

The interacting part of the Hamiltonian takes into account both intraspecies and interspecies collisions, where we assume contact interactions and conservation of the total hyperfine angular momentum during the collisions [LSA+07]. The intraspecies interactions are given by

$$\hat{H}_{\mathrm{I}}^{\mathrm{L}} = \frac{g_{11}^{\mathrm{L}}}{2} \int_{\mathbf{x}} \hat{\psi}_{\mathrm{L},1}^{\dagger}(\mathbf{x}) \hat{\psi}_{\mathrm{L},1}^{\dagger}(\mathbf{x}) \hat{\psi}_{\mathrm{L},1}(\mathbf{x}) \hat{\psi}_{\mathrm{L},1}(\mathbf{x}) \tag{3.17}$$

and

$$\hat{H}_{\mathrm{I}}^{\mathrm{N}} = \frac{g_{11}^{\mathrm{N}}}{2} \int_{\mathbf{x}} \hat{\psi}_{\mathrm{N},1}^{\dagger}(\mathbf{x}) \hat{\psi}_{\mathrm{N},1}^{\dagger}(\mathbf{x}) \hat{\psi}_{\mathrm{N},1}(\mathbf{x}) \hat{\psi}_{\mathrm{N},1}(\mathbf{x}) \tag{3.18}$$

$$+ \frac{g_{00}^{\mathrm{N}}}{2} \int_{\mathbf{x}} \hat{\psi}_{\mathrm{N},0}^{\dagger}(\mathbf{x}) \hat{\psi}_{\mathrm{N},0}^{\dagger}(\mathbf{x}) \hat{\psi}_{\mathrm{N},0}(\mathbf{x}) \hat{\psi}_{\mathrm{N},0}(\mathbf{x}) \tag{3.19}$$

$$+ g_{10}^{\mathrm{N}} \int_{\mathbf{x}} \hat{\psi}_{\mathrm{N},1}^{\dagger}(\mathbf{x}) \hat{\psi}_{\mathrm{N},0}^{\dagger}(\mathbf{x}) \hat{\psi}_{\mathrm{N},1}(\mathbf{x}) \hat{\psi}_{\mathrm{N},0}(\mathbf{x}), \tag{3.20}$$

with

$$g_{\alpha\beta}^{s} = \frac{4\pi\hbar^2}{m_s} a_{\alpha\beta}^{s}. \tag{3.21}$$

$a_{\alpha\beta}^{s}$ are the scattering coefficients given by $a_{11}^{N} = a_{10}^{N} = 55\,a_{\mathrm{B}}$, $a_{00}^{N} = 53\,a_{\mathrm{B}}$, $a_{11}^{L} = a_{10}^{L} = 6.8\,a_{\mathrm{B}}$, $a_{00}^{L} = 12.5\,a_{\mathrm{B}}$, and a_{B} is the Bohr radius. The interspecies part of the interaction is described by

$$H_{\mathrm{I}}^{\mathrm{NL}} = g_{11}^{\mathrm{NL}} \int_{\mathbf{x}} \hat{\psi}_{\mathrm{N},1}^{\dagger}(\mathbf{x}) \hat{\psi}_{\mathrm{N},1}(\mathbf{x}) \hat{\psi}_{\mathrm{L},1}^{\dagger}(\mathbf{x}) \hat{\psi}_{\mathrm{L},1}(\mathbf{x}) \tag{3.22}$$

$$+ g_{10}^{\mathrm{NL}} \int_{\mathbf{x}} \hat{\psi}_{\mathrm{N},0}^{\dagger}(\mathbf{x}) \hat{\psi}_{\mathrm{N},0}(\mathbf{x}) \hat{\psi}_{\mathrm{L},1}^{\dagger}(\mathbf{x}) \hat{\psi}_{\mathrm{L},1}(\mathbf{x}), \tag{3.23}$$

with

$$g_{\alpha\beta}^{\mathrm{NL}} = \frac{4\pi\hbar^2}{\mu} a_{\alpha\beta}^{NL} \tag{3.24}$$

and $a_{00}^{\mathrm{NL}} = a_{10}^{\mathrm{NL}} = 19.65\,a_{\mathrm{B}}$, $a_{11}^{\mathrm{NL}} = 20\,a_{\mathrm{B}}$. The interaction Hamiltonian is given by $\hat{H}_{\mathrm{I}} = \hat{H}_{\mathrm{I}}^{\mathrm{N}} + \hat{H}_{\mathrm{I}}^{\mathrm{L}} + \hat{H}_{\mathrm{I}}^{\mathrm{NL}}$, and the total atomic Hamiltonian by $\hat{H} = \hat{H}_0 + \hat{H}_{\mathrm{I}}$.

Tight-Binding Approximation

If the lattice is deep enough, we can expand the field operators in the tight-binding approximation in terms of localized Wannier wavefunctions (2.18), as we introduced

in chapter 2,

$$\begin{aligned}\hat{\psi}^{\mathrm{L}}_{\alpha}(\mathbf{x}) &\approx \sum_i w^s_{i,\alpha}(\mathbf{x})\,\hat{b}^s_{i,\alpha},\\ \hat{\psi}^{\mathrm{N}}_{\alpha}(\mathbf{x}) &\approx \sum_i w^s_{i,i+1,\alpha}(\mathbf{x})\,\hat{b}^s_{i,i+1,\alpha},\end{aligned} \tag{3.25}$$

where i $(i, i+1)$ is the lattice site (bond) denoting each potential minimum in the axial direction, and $\hat{b}^{s,\dagger}_{i,\alpha}$ and $\hat{b}^s_{i,\alpha}$ are bosonic creation and annihilation operators, respectively, fulfilling the canonical commutation relations $[\hat{b}^s_{i,\alpha}, \hat{b}^{s',\dagger}_{j,\beta}] = \delta_{s,s'}\delta_{i,j}\delta_{\alpha,\beta}$. In the following, we denote $\hat{b}_{i,\alpha} \equiv \hat{b}^{\mathrm{L}}_{i,\alpha}$ and $\hat{a}_{i,i+1,\alpha} \equiv \hat{b}^{\mathrm{N}}_{i,i+1,\alpha}$ to simplify the notation. Introducing the tight-binding approximation (3.25) into the atomic Hamiltonian we obtain the tight-binding model $\hat{H} = \hat{H}^{\mathrm{N}} + \hat{H}^{\mathrm{L}} + \hat{H}^{\mathrm{NL}}$. In the case of sodium we have assume that the potential is so deep that the tunneling between different sites can be safely neglected,

$$\begin{aligned}\hat{H}^{\mathrm{N}} = &\frac{U^{\mathrm{N}}_{00}}{2}\sum_i \hat{a}^\dagger_{i,i+1,0}\hat{a}^\dagger_{i,i+1,0}\hat{a}_{i,i+1,0}\hat{a}_{i,0} + \frac{U^{\mathrm{N}}_{11}}{2}\sum_i \hat{a}^\dagger_{i,i+1,1}\hat{a}^\dagger_{i,i+1,1}\hat{a}_{i,i+1,1}\hat{a}_{i,i+1,1}\\ &+ U^{\mathrm{N}}_{10}\sum_i \hat{a}^\dagger_{i,i+1,1}\hat{a}^\dagger_{i,0}\hat{a}_{i,i+1,0}\hat{a}_{i,i+1,1} + \Omega\sum_i\left(\hat{a}^\dagger_{i,i+1,0}\hat{a}_{i,i+1,1} + \mathrm{H.c.}\right)\\ &- \sum_i \mu^{\mathrm{N}}_{i,0}\hat{a}^\dagger_{i,i+1,0}\hat{a}_{i,i+1,0} - \sum_i \mu^{\mathrm{N}}_{i,i+1,1}\hat{a}^\dagger_{i,i+1,1}\hat{a}_{i,i+1,1}.\end{aligned} \tag{3.26}$$

The lithium atoms, on the other hand, are described by the standard Bose-Hubbard model,

$$\hat{H}^{\mathrm{L}} = -\tilde{t}\sum_i\left(\hat{b}^\dagger_i\hat{b}_{i+1} + \mathrm{H.c.}\right) + \frac{U^{\mathrm{L}}_{11}}{2}\sum_i \hat{b}^\dagger_i\hat{b}^\dagger_i\hat{b}_i\hat{b}_i - \sum_i \mu^{\mathrm{L}}_i\hat{b}^\dagger_i\hat{b}_i. \tag{3.27}$$

Finally, we restrict the sodium-lithium interactions to nearest-neighbor density-density as well as density-dependent tunneling terms,

$$\begin{aligned}\hat{H}^{\mathrm{NL}} = &\sum_i\left(\hat{b}^\dagger_i\hat{b}_i + \hat{b}^\dagger_{i+1}\hat{b}_{i+1}\right)\left(U^{\mathrm{NL}}_{10}\hat{a}^\dagger_{i,i+1,0}\hat{a}_{i,i+1,0} + U^{\mathrm{NL}}_{11}\hat{a}^\dagger_{i,i+1,1}\hat{a}_{i,i+1,1}\right)\\ &+ \sum_i\left(\hat{b}^\dagger_i\hat{b}_{i+1} + \hat{b}^\dagger_{i+1}\hat{b}_i\right)\left(\tilde{U}^{\mathrm{NL}}_{10}\hat{a}^\dagger_{i,0}\hat{a}_{i,0} + \tilde{U}^{\mathrm{NL}}_{11}\hat{a}^\dagger_{i,i+1,1}\hat{a}_{i,i+1,1}\right).\end{aligned} \tag{3.28}$$

Finally, the tight-binding coefficients depend on the different scattering lengths as well as on the properties of the Wannier functions.

Angular Momentum Representation

We can express the previous Hamiltonian in terms of angular momentum operators acting on the bonds by representing them in terms of Schwinger bosons,

$$\begin{aligned}\hat{L}^z_{i,i+1} =& \frac{1}{2}\left(\hat{a}^\dagger_{i,i+1,0}\hat{a}_{i,i+1,0} - \hat{a}^\dagger_{i,i+1,1}\hat{a}_{i,i+1,1}\right),\\ \hat{L}^x_{i,i+1} =& \frac{1}{2}\left(\hat{a}^\dagger_{i,i+1,1}\hat{a}_{i,i+1,0} + \text{H.c.}\right).\end{aligned} \tag{3.29}$$

The angular momentum $l = \frac{1}{2}\left(\hat{a}^\dagger_{i,i+1,0}\hat{a}_{i,i+1,0} + \hat{a}^\dagger_{i,i+1,1}\hat{a}_{i,i+1,1}\right)$ is a conserved quantity since the total number of atoms on each bond is conserved to great accuracy. The total atomic Hamiltonian can be written as

$$\begin{aligned}\hat{H} =& -\sum_i \left[t + g\hat{L}^z_{i,i+1}\right]\left(\hat{b}^\dagger_i\hat{b}_{i+1} + \text{H.c.}\right) + \frac{U}{2}\sum_i \hat{n}_i(\hat{n}_i - 1) - \sum_i \mu_i\hat{n}_i\\ &+ \Omega\sum_i \hat{L}^x_{i,i+1} + V\sum_i \hat{L}^{z\,2}_{i,i+1} + \sum_i \Delta_i\hat{L}^z_{i,i+1} - \tilde{g}\sum_i(\hat{n}_i + \hat{n}_{i+1})\hat{L}^z_{i,i+1},\end{aligned} \tag{3.30}$$

where

$$\begin{aligned}V &= \frac{U^{\text{N}}_{11}}{2} + \frac{U^{\text{N}}_{00}}{2} - U^{\text{N}}_{10},\\ \Delta_i &= (2l-1)\left(\frac{U^{\text{N}}_{00}}{2} - \frac{U^{\text{N}}_{11}}{2}\right) - (\mu^{\text{N}}_{0,i} - \mu^{\text{N}}_{1,i}),\\ g &= \tilde{U}^{\text{NL}}_{11} - \tilde{U}^{\text{NL}}_{10},\\ \tilde{g} &= U^{\text{NL}}_{11} - U^{\text{NL}}_{10},\\ t &= \tilde{t} - l(\tilde{U}^{\text{NL}}_{11} + \tilde{U}^{\text{NL}}_{10}),\\ \mu_i &= \mu^{\text{L}}_i - 2l(\tilde{U}^{\text{NL}}_{11} + \tilde{U}^{\text{NL}}_{10}),\end{aligned} \tag{3.31}$$

and we denote $U \equiv U^{\text{L}}_{11}$. In the hard-core limit ($U/t \to \infty$), the atomic Hamiltonian (3.30) coincides with the rotor SSH model (3.10) up to some extra terms. In the following, we do not take into account the last interaction term and make $\tilde{g} = 0$. A more detail investigation is required to obtain the values of the tight-binding coefficients in terms of the experimental parameters, as well as to the effect that the extra terms could have on the phase diagram presented below. We also assume an homogeneous system and denote $\mu \equiv \mu_i$ and $\Delta \equiv \Delta_i$.

3.3 Interacting bosons on a dynamical lattice

In this section, we show that the rotor SSH model gives rise to similar phenomena as the original SSH model. We focus in particular on the $S = 1/2$ case—and we

refer to it as the $\mathbb{Z}_2$ Bose-Hubbard model ($\mathbb{Z}_2$BH)—where the truncation of the phononic Hilbert space is maximal. This choice simplifies both the classical and quantum simulation of the model. However, we will see how, even if quantum fluctuations are enhanced in this case as compared to the large S case, the relevant phases are equivalent to those that appear in the phonon model. Moreover, we investigate how the departure from the hardcore boson limit affects the Peierls insulators.

3.3.1 The $\mathbb{Z}_2$ Bose-Hubbard model

The $\mathbb{Z}_2$BH Hamiltonian describes the minimal model of interacting bosons coupled to lattice degrees of freedom. It takes the following form,

$$\begin{aligned}\hat{H}_{\mathsf{Z_2BH}} = &-t\sum_i \left[t+\alpha\hat{\sigma}^z_{i,i+1}\right]\left(\hat{b}^\dagger_i\hat{b}_{i+1}+\text{H.c.}\right)+\frac{U}{2}\hat{n}_i(\hat{n}_i-1)\\ &-\mu\sum_i\hat{n}_i+\frac{\Delta}{2}\sum_i\hat{\sigma}^z_i+\beta\sum_i\hat{\sigma}^x_i,\end{aligned} \tag{3.32}$$

where $\hat{\sigma}^z_i$ and $\hat{\sigma}^x_i$ are Pauli operators associated with Ising fields living on the bond between sites i and $i+1$. The parameters of the Hamiltonian coincide with those of the atomic system (3.30) by identifying $\alpha = g/2$ and $\beta = \Omega/2$. Apart from the standard terms present in the Bose-Hubbard Hamiltonian [FWGF89], the $\mathbb{Z}_2$BH Hamiltonian includes a lattice-dependent boson tunneling (Fig. 3.5). The total hopping through a bond is maximized (resp. minimized) for a spin in the "up" ("down") state. Finally, the last two terms control the spin dynamics. We note that the Hamiltonian (3.32) bears similarities with other models with spin dependent hopping elements, such as quantum link models [Wie13].

Consider first the static lattice case, with $\beta/t = 0$. In the hardcore boson limit, $U/t \to \infty$, a Jordan-Wigner transformation maps the system to a model of spinless fermions [JW28], $b_i \to \mathrm{e}^{\mathrm{i}\pi\sum_{j<i}c^\dagger_j c_j}c_i$, $b^\dagger_i b_i \to c^\dagger_i c_i$. The transformed Hamiltonian is quadratic in the fermionic operators,

$$\hat{H} = -\sum_i\left[t+\alpha\hat{\sigma}^z_{i,i+1}\right]\left(\hat{c}^\dagger_i\hat{c}_{i+1}+\text{h.c.}\right)-\mu\sum_i\hat{n}_i+\frac{\Delta}{2}\sum_i\hat{\sigma}^z_{i,i+1}, \tag{3.33}$$

where $\hat{c}^\dagger_i$ and $\hat{c}_i$ are creation and annihilation fermionic operators, respectively, and $\hat{n}_i = \hat{c}^\dagger_i\hat{c}_i$ is the number of fermions at site i. This Hamiltonian (3.33) describes a system of non-interacting fermions coupled to classical degrees of freedom. For a given configuration of the classical variables, the Hamiltonian can be diagonalized analytically using a single-particle picture.

For large enough values of Δ/t the fermionic and spin subsystems decouple. The spin configuration that minimizes the total energy is the one with all spins down.

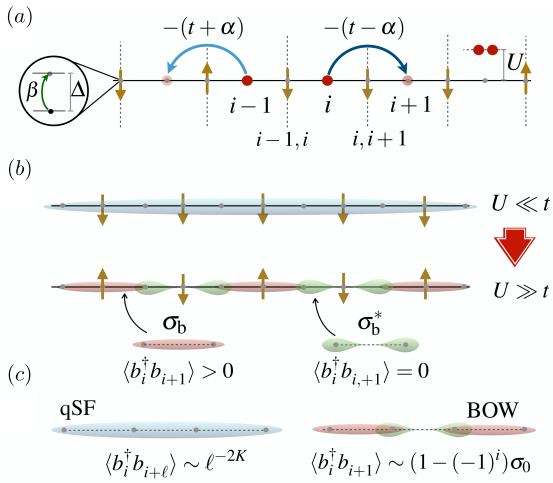

Fig. 3.5 Scheme of the bosonic Peierls transition: (a) Representation of the lattice model of bosons coupled to an Ising field according to Eq. (3.32). Bosons (red dots) reside on the lattice sites, where they interact with strength U, and can tunnel through the links with a $\mathbb{Z}_2$-valued tunneling strength $-t \pm \alpha$, which depends on the configuration of the Ising field on the links (yellow arrows). These fields can be represented by a two-level system (inset) with energy difference Δ, and spin-flipping strength β. **(b,c)** Interaction-induced Peierls transition between a bosonic quasi-superfluid (qSF) in a homogeneous Ising background, and a bond-ordered wave (BOW) in a Néel-ordered type background, such that translational invariance is spontaneously broken. The BOW phase can be understood as an alternation of bonding σ_b and anti-bonding σ_b^* units with a different distribution of the bosons within the bonds. The homogeneous qSF phase is characterized by an algebraic decay of correlations.

Conversely, for $\Delta/t = 0$ the spin configuration in the ground state of the system is the one that minimizes the energy of the fermion subsystem. For $\rho \notin \{0, 1\}$, this happens when all spins are in the up state, making the fermion hopping uniform and maximal. For other values of Δ/t, the energies of these two configurations become comparable and other spin configurations are possible in the ground state.

We focus on the half-filling case ($\rho = 1/2$). In the uniform “down" and “up" spin configurations, the ground state energy per site is $\varepsilon = -\Delta/2 - 2(t-\alpha)/\pi$ and $\varepsilon = \Delta/2 - 2(t+\alpha)/\pi$, respectively. There is another important spin configuration, the Neel ordered or staggered spin structure. In this configuration, the values of the fermion hopping are also staggered ($t \pm \alpha$), the unit cell doubles and a gap opens around the Fermi energy. There are two branches of single-particle energies

in the reduced Brillouin zone ($-\pi/2 < k < \pi/2$),

$$\epsilon_{\pm}(k) = \pm 2t\sqrt{\tilde{\delta}^2 \sin^2 k + \cos^2 k}\,, \tag{3.34}$$

where $\tilde{\delta} = \alpha/t$. This leads to a ground state energy per site of $\varepsilon = -2t\mathsf{E}(1-\delta^2)/\pi$ where $\mathsf{E}(x) = \int_0^{\pi/2} \mathrm{d}k(1 - x\sin^2 k)^{1/2}$ is the complete elliptic integral of the second kind. By comparing the aforementioned energies, we conclude that the staggered spin pattern energy is lower between two critical values of the parameter Δ,

$$\Delta_c^{\pm} = \frac{4t}{\pi}[\tilde{\delta} \pm (\mathsf{E}(1-\tilde{\delta}^2) - 1)]. \tag{3.35}$$

On the other hand, the uniform “down" and uniform “up" configurations have a lower energy for $\Delta > \Delta_c^+$ and $\Delta < \Delta_c^-$,respectively. We have checked numerically that, indeed, these configurations correspond to the ground state of the system in the respective regimes, being the only possible ones at half filling.

From the fermions' viewpoint, this leads to the development of a staggered order on the bonds, this is, to a BOW phase, and the system becomes insulating. Since the latter is associated to a lattice deformation, which breaks translational invariance, and the resulting order depends on the fermionic density, with $k_0 = 2k_\mathrm{F}$, we consider such phase a Peierls insulator. Our minimal model is thus capable of describing analogous phenomena to those appearing in more complicated fermion-lattice systems [HKSS88], such as the SSH model introduced in the last section.

3.3.2 Bosonic Peierls transitions

For finite values of U, we enter into the strongly-correlated boson regime, where the mapping to non-interacting fermions is no longer possible. To calculate the ground state of the system, we use a DMRG algorithm with bond dimension $D = 40$ [Sch11]. We consider a system size of $L = 60$ sites (and $L - 1$ bonds), and work with open boundary conditions. We truncate the maximum number of bosons per site to $n_0 = 2$. This approximation is justified for low densities and strong interactions. In the following, we fix the values of the parameters to $\alpha = 0.5t$ and $\beta = 0.02t$.

At the bosonic density $\rho = 1/2$, the Neel order survives for finite values of U, and disappears for small interactions. Strong correlations are needed, therefore, to obtain a bosonic Peierls insulator (Fig. 3.5). The Bose-Hubbard model on a fixed bond-dimerized lattice was previously studied, revealing an insulating phase at $\rho = 1/2$ [BPV04], and the presence of topological edge states [GHF13]. Here, the same superlattice structure is obtained dynamically, in the spirit of the original SSH model for fermions and phonons [HKSS88]. In chapter 4, we investigate in detail the topological properties of the corresponding BOW phase at half filling, as well as the interaction-induced nature of the bosonic Peierls transition.

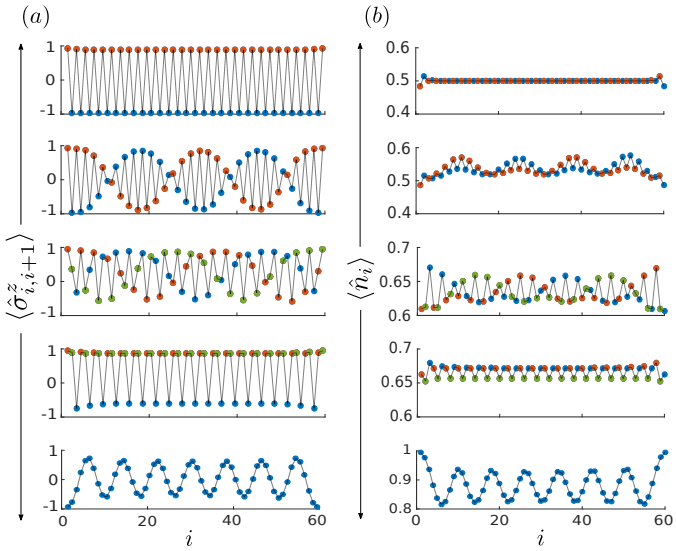

Fig. 3.6 Bond order waves: Spatial structure of bond (a) and site (b) expectation values for $\Delta = 0.85$ and different bosonic densities, showing some of the representative orders that can develop. From above to below: $\rho = 1/2$, $\rho = 1/2 + 2/60$, $\rho = 2/3 - 2/60$, $\rho = 2/3$ and $\rho = 0.88$. Different colors represent different sublattice elements, making explicit the long-wavelength modulations on top of the underlying order.

For $U = 10t$, we study the phase diagram of the model in terms of Δ and ρ. For $\Delta \gg \alpha$ or $\Delta \ll \alpha$, the spin configuration in the ground state is uniform. The bosonic part of the Hamiltonian (3.32) is qualitatively similar to the Bose-Hubbard model [FWGF89], with a Mott insulator (MI) and a quasi-superfluid phase (aSF). In an intermediate regime ($\Delta \approx 0.6 - 1.0$), the translational symmetry is broken in the ground state for a substantial range of densities. Figure 3.6 shows the spatial structure on the bonds (a) and sites (b) for $\Delta = 0.85t$. For $\rho = 1/2$ and $2/3$, the unit cell is enlarged to two and three sites, respectively. Similarly to $\rho = 2/3$, a trimer configuration appears for $\rho = 1/3$ at a different Δ. For densities close to the mentioned ones, long wavelength modulations appear on top of the corresponding patterns. These are solitonic configurations where the underlying order—staggered in the half-filled case—is reversed periodically forming kinks; the extra bosons or holes lead to increased density modulations, located around the kinks (2nd or 3rd row in panel (b)). Finally, close to $\rho = 1$, long wavelength structures appear.

The bosonic hopping $\langle \hat{b}_i^\dagger \hat{b}_{i+1} + \text{h.c.} \rangle$ presents the same spatial pattern as $\langle \hat{\sigma}_i^z \rangle$ in all the cases. We therefore focus on the latter quantity for simplicity. The ground states shown in Fig. 3.6 possess long-range order in the bonds, and the

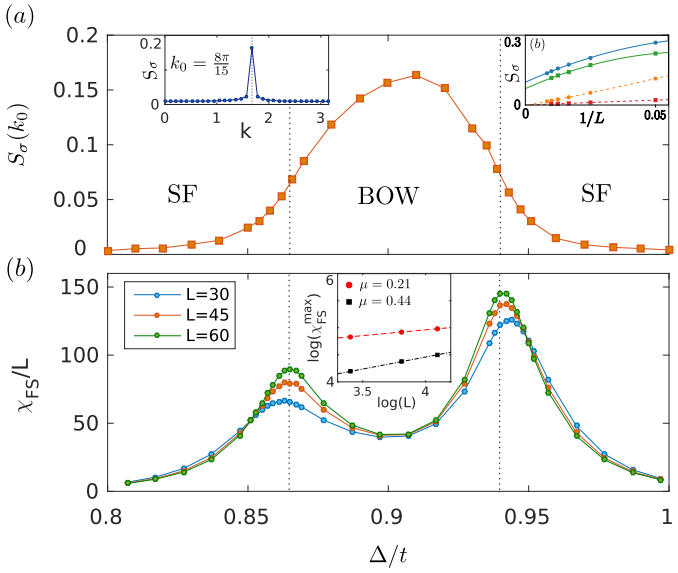

Fig. 3.7 BOW - SF quantum phase transition: (a) Structure factor at k_0 in terms of Δ/t, serving as an order parameter that distinguishes between the BOW and the SF phases. Inset: (a) Structure factor $S_\sigma(k)$ in the BOW phase, for $\rho = 0.733$ and $\Delta = 0.90$. A clear peak is observed at $k_0 = 8\pi/15$. (b) Finite-size scaling of $S_\sigma(k)$ for $\rho = 0.55$ (circles) and $\rho = 0.85$ (squares), for $k = k_0(\rho)$ (continuous line) and $k = \pi$ (dashed line). **(b)** The exact location of the critical points (dotted lines) between the SF and S phases is found using the fidelity susceptibility χ_{FS}. In the figure, χ_{FS} is represented in terms of Δ for different system sizes. The critical points are located by extrapolating the positions of the peaks, where χ_{FS} grows algebraically with the system size, $\chi_{FS}/L \sim L^{\mu}$. In the inset, the scaling of the value of χ_{FS} at the peak is represented for the left (black) and right (red) ones. The critical coefficients μ are obtained by fitting it to a line.

corresponding quantum phases are BOW phases. We consider the spin structure factor

$$S_\sigma(k) = \frac{1}{L^2} \sum_{i,j} e^{(x_i - x_j)ki} \langle \left(\hat{\sigma}^z_{i,i+1} - \bar{\sigma^z}\right) \left(\hat{\sigma}^z_{j,j+1} - \bar{\sigma^z}\right) \rangle \,, \tag{3.36}$$

with $\bar{\sigma}^z = \sum_i \langle \hat{\sigma}_i \rangle / L$, where the summations run over all bonds. This quantity develops a peak for some k_0 in the presence of long-range order, and its height can be used as an order parameter. Figure 3.7**(a)** shows $S_\sigma^{\max}$ in terms of Δ for $\rho = 0.733$, which qualitatively distinguishes a uniform SF phase from a BOW phase. The inset (a) presents S_σ for $\Delta = 0.90$, where a peak develops for $k_0 = 8\pi/15$, which fulfills the Peierls relation. The inset (b) shows the scaling of $S_\sigma(k)$ with the system size, for $k = k_0$ and $k = \pi$ and for two BOW phases: $\rho = 0.55$ and $\rho = 0.85$.

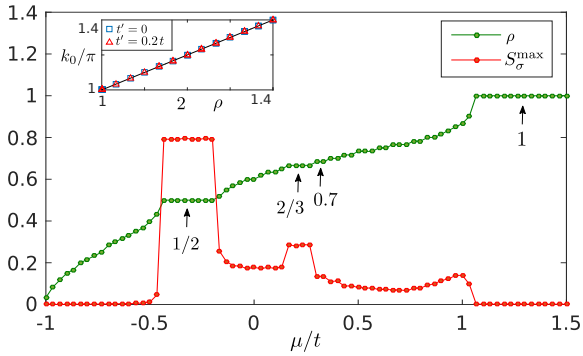

Fig. 3.8 Staircase of bosonic Peierls insulators: Density ρ and maximum structure factor S^{max} in terms of the chemical potential μ/t for $\Delta = 0.87t$ and $L = 60$. The structure factor has non-zero values for the BOW phases. Plateaus in the density are related to incompressible phases. Insets: k_0 vs ρ for $t' = 0$ and $t' = 0.2$. The straight line indicates that the Peierls relation is satisfied for very BOW phase.

The fit, containing terms up to $O(1/L^3)$, shows that the long-range order exists in the thermodynamic limit.

Although the BOW and superfluid phases can still be qualitatively distinguished using the structure factor as an order parameter, the exact location of the corresponding critical points can be challenging for small system sizes. For this reason, we use the fidelity susceptibility χ_{FS} [GU10] to find the critical points in the thermodynamic limit. This quantity can be calculated using the following expression,

$$\chi_{\mathrm{FS}}(\Delta) = \lim_{\delta\to 0} \frac{-2\log|\langle\Psi_0(\Delta)|\Psi_0(\Delta+\delta)\rangle|}{\delta^2}\,. \tag{3.37}$$

The fideliy susceptibility χ_{FS} shows a clear peak near a quantum phase transition, even for small systems. Figure 3.7**(b)** shows χ_{FS} in terms of Δ for different system sizes and a fixed density of $\rho = 0.733$. The critical points are found at $\Delta_1 = 0.865$ and $\Delta_2 = 0.940$, by extrapolating the position of the peaks in the thermodynamic limit. In those points, the value of χ_{FS} grows algebraically as $\chi_{FS}/L \sim L^{\mu}$ (inset). The critical exponents are different in the two transitions.

Bosonic Peierls transitions, and the corresponding BOW phases, appear for a large range of densities forming a staircase structure. Figure 3.8 depicts the density ρ in terms of μ/t for $\Delta = 0.87t$. Here, a superfluid phase occurs for $0 < \rho < 1/2$, and BOW phases appear for $1/2 \leqslant \rho < 1$. Finally, $\rho = 1$ corresponds to a MI. The plateaus in the $\mu - \rho$ line signal the incompressible nature of the BOW phases. One of the principal features of the theory of Peierls transition is the relation between the order wavevector and the Fermi wavevector [Pei55]. In one-dimensional systems with a two-point Fermi surface, the theory predicts

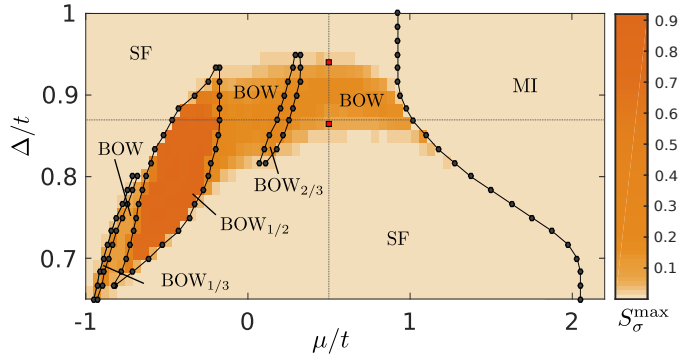

Fig. 3.9 Phase diagram of the $\mathbb{Z}_2$BH model (3.32) for a system size of $L = 60$ in terms of Δ/t and μ/t. The solid black lines delimit the incompressible phases (cBOW and MI). The maximum value of the structure factor is represented by the color plot, qualitatively distinguishing between the iBOW and SF phases. The dotted lines correspond to the cuts for $\mu = 0.5$ (Fig. 3.7) and $\Delta = 0.87$ (Fig. 3.8). For the former, the red squares mark two critical points in the thermodynamic limit.

$k_0 = 2k_F = 2\rho\pi$, independently of the fermion dispersion and the form of the fermion-lattice interaction. Remarkably, we found the same relation for bosonic Peierls transitions (inset), where the Fermi surface is absent. This relation holds in the presence of next neighbor hopping $-t' \sum_i \left(\hat{b}_i^\dagger \hat{b}_{i+2} + \text{h.c.}\right)$, where even hard-core bosons cannot be mapped onto fermions.

For a wide range of values of Δ/t, we calculate the plateau size and the maximum structure factor in terms of μ/t. These two properties are sufficient to identify all the phases of the model. The results are summarized in the phase diagram (Fig. 3.9). Inside the MI, the spins are uniform and $\langle \hat{\sigma}_i^z \rangle$ changes continuously from $+1$ to -1 as Δ increases. As a consequence, the boundary between this phase and the SF is modified. The phase diagram also shows the extensions of the BOW phases, the most stable one being at $\rho = 1/2$.

3.4 Summary

In this chapter, we have investigated how a dynamical lattice can be implemented in cold-atomic systems. In particular, we have presented a proposal to simulate lattice degrees of freedom using bosonic mixtures, by first truncating the infinite phonon Hilbert space with finite-dimensional rotors. We then focused on the simplest version of a dynamical lattice, where matter particles are coupled to spins, and showed that the main properties of electron-phonon systems survive in this limit.

Moreover, we have shown how these properties can be extended to strongly-

correlated bosons, and we demonstrated the possibility of obtaining bosonic analogs of the Peierls insulator. We characterized the phases of the system in the quasi-adiabatic limit (slow lattice dynamics), using the spin structure factor. We found, besides the uniform SF and MI phases, different BOW phases for a large range of bosonic densities. In these phases, the Peierls relation is satisfied even in the absence of a Peierls surface, provided that bosonic interactions are sufficiently strong. Although the boson-spin interaction α might be difficult to tune in an experiment, the phases we study in this chapter are present for a broad range of values of this parameter, provided that Δ is suitably chosen. The different phases could be detected by measuring the spin structure factor [HDY+15, PMC+16, MCJ+17] and the compressibility in the atomic system [SHW+08, SPOT09].

Chapter 4

Intertwined topological phases

4.1 Introduction: from symmetry breaking to symmetry protection

The notion of symmetry is paramount to unveil the fundamental laws of Nature, while spontaneous symmetry breaking (SSB) is essential to understand Nature's different guises [Gro96]. As we introduced in chapter 1, at long length-scales, various phases of matter can be understood by the pattern of SSB and corresponding local order parameters [Lan37]. Although different SSB patterns tend to compete with one another, a genuine cooperation can also arise in strongly-correlated systems with intertwined orders [FKT15]. More recently, topology has been recognised as an exotic driving force shaping the texture of Nature, and leading to phases characterised by topological invariants rather than by local order parameters [Wen17]. It is no longer the breaking of certain symmetries but, actually, their conservation [CTSR16], which gives rise to novel states of matter, the so-called symmetry-protected topological (SPT) phases [Sen15]. In the non-interacting limit, topological insulators and superconductors provide well-understood examples of this paradigm [QZ11], while current research aims at understanding strong-correlation effects, such as the competition of SPT and SSB phases due to interactions [Rac18].

Alternatively, a cooperation between SPT and SSB may allow for intertwined topological phases that simultaneously display a local order parameter and a topological invariant. For integer and fractional Chern insulators, such intertwined orders have been already identified in the literature [RQHZ08, SYFK09, KD14]. Nonetheless, in these cases, the topological phases exist in the absence of any protecting symmetry. In more generic situations, the existence of intertwined topological phases will depend on how the symmetry responsible for the SPT phase can be embedded into the broader symmetry-breaking phenomenon. Arguably,

the first instance of this situation is the Peierls instability [Pei55] in polyacetylene, introduced in chapter 3. There, we saw how such instability leads to a dimerized lattice distortion and a bond-order-wave (BOW), where electrons are distributed in an alternating sequence of bonding and anti-bonding orbitals. A closer inspection shows that neither chiral nor inversion symmetry are broken after SSB, which leads to a topological quantization of the electronic polarization [HPB11], and is ultimately responsible for the protection of the SPT phase.

In chapter 3, we studied the $\mathbb{Z}_2$ Bose-Hubbard model model in the context of bosonic Peierls transitions, as the $\mathbb{Z}_2$ field can be considered as a simplified version of a dynamical lattice with the vibrational phonons substituted by discrete Ising variables. The focus there was the elucidation of this bosonic Peierls mechanism for different bosonic densities, as well as the study of topological solitons (i.e. kinks) interpolating between different bond-density modulations at commensurate fillings. The latter are a direct consequence of the degeneracies associated to the symmetry-breaking process. In this chapter, we focus on a different topological aspect: we give compelling evidence that, at various fillings, the bond-ordered wave (BOW) caused by the bosonic Peierls mechanism corresponds to an interaction-induced SPT phase. This topological phase occurs simultaneously with the Landau symmetry-breaking order described by the bond-density modulation. We will show that, in addition to the BOW phases, the pattern of broken symmetry also allows for topological bond-ordered waves (TBOW) phases that display all the characteristics of an interaction-induced SPT phase: (1) the appearance of non-vanishing bulk topological invariants for the many-body interacting model, and (2) the presence of non-trivial many-body edge states. We will emphasize how interactions and symmetry breaking are fundamental necessary ingredients for these topological effects to take place.

The goal of this chapter is to present a thorough description of the ground state of the $\mathbb{Z}_2$ Bose-Hubbard model at various fillings, showing that it can host interaction-induced intertwined topological insulators. In Sec. 4.2, we will show that a one-dimensional bosonic SPT phase arises at half filling for finite boson-boson interactions, and cannot be adiabatically connected to the non-interacting system. This SPT phase occurs via the spontaneous breaking of lattice translational invariance, which also produces a long-range order in the bond density of bosons. Therefore, the bosonic ground state combines a topological-insulating behavior with Landau-type order, leading to a particular instance of intertwined topological insulators: a topological bond-order wave (TBOW). These results constitute the first instance of a bosonic interaction-induced intertwined topological insulator.

In Sec. 4.3, we study a hitherto unknown possibility: the occurrence of an intertwined topological phase when the SSB pattern does not generally imply the existence of a protecting inversion symmetry. Instead, this protecting symmetry emerges from a larger set of configurations allowed by the SSB. We demonstrate this topological mechanism in the $\mathbb{Z}_2$-Bose-Hubbard model at various fractional fillings, such that its interplay with topology and strong correlations endows the system

with very interesting, yet mostly unexplored, static and dynamical behavior, including interaction-induced topological phase transitions constrained by symmetry breaking, as well as a self-adjusted fractional pumping.

4.2 TBOW at half filling

In this section, we provide a thorough description of our findings supporting the existence of bosonic TBOW in the $\mathbb{Z}_2$ Bose-Hubbard model (3.32) at half filling. In Sec. 4.2.1, we show our model exhibits a spontaneous breaking of the translational symmetry, similarly to the SSH model, giving rise to long-range Landau-type order. We study this phenomenon in detail, focusing first on the hardcore boson limit. Using a Born-Oppenheimer approximation for quasi-adiabatic $\mathbb{Z}_2$ fields, we predict the opening of a single-particle gap at half filling, associated to a dimerization in the structure of the $\mathbb{Z}_2$ fields. We show that one of the symmetry-broken sectors of this ordered phase leads to a topological hardcore-boson insulator: a TBOW, which is characterized by a quantized topological invariant, the Zak phase. We check that this TBOW phase survives in the softcore regime as the interaction strengths are reduced, and show how the size of the gap decreases, suggesting that a quantum phase transition may occur at finite interactions that would prove that the TBOW phase is a bosonic instance of an interaction-induced intertwined topological insulator. In Sec. 4.2.2, we test these predictions numerically using the density matrix renormalization group algorithm. We give several signatures to characterize the TBOW as a SPT phase, and discuss the existence of fractional many-body edge states. We also analyze the phase transition between the topological insulator and a non-topological superfluid phase for small interactions, presenting a phase diagram of the mode, and showing the importance of strong correlations to stabilize the topological phase.

4.2.1 Born-Oppenheimer mean-field approach

Hardcore bosons coupled to $\mathbb{Z}_2$ fields

Let us analyze first the case of hardcore bosons, where clear analogies with the standard Peierls transition in fermion-phonon systems can be drawn, and discuss the interplay between symmetry breaking and symmetry protection.

Born-Oppenheimer ground-state ansatz.– Let us elaborate on the analogy we introduced in chapter 3 between the ground state behavior of the $\mathbb{Z}_2$BHM (3.32) to the standard Peierls transition and SSH-type phenomena . The hardcore-boson limit $U \to \infty$ is a good starting point to draw these analogies, since the strongly-interacting bosons of Eq. (3.32) can be transformed into free spinless fermions

coupled to the $\mathbb{Z}_2$ fields. By applying the Jordan-Wigner transformation in the hardcore-boson limit, we find

$$H^{U\to\infty}_{\mathsf{Z}_2\mathsf{BH}} = \sum_i \Big(-(t+\alpha\sigma^z_{i,i+1})c^\dagger_i c_{i+1} + \frac{\beta}{2}\sigma^x_{i,i+1} + \frac{\Delta}{4}\sigma^z_{i,i+1} + \text{H.c.} \Big). \tag{4.1}$$

As we commented in the last chapter, a background Néel-type anti-ferromagnetic ordering of the $\mathbb{Z}_2$ fields $\big|\cdots,\uparrow_{i-1,i},\downarrow_{i,i+1},\uparrow_{i+1,i+2},\cdots\big\rangle$ introduces a dimerized pattern of the fermionic tunneling strengths (see Fig. 3.5**(a)**). This would constitute a $\mathbb{Z}_2$ analogue of the dimerized lattice distortion that underlies the fermionic Peierls instability at half filling [Pei55]. However, the dynamics of the $\mathbb{Z}_2$ fields differs from the acoustic vibrational branch of the original (SSH) Hamiltonian [SSH79], which can lead to crucial differences.

In order to understand these differences, we shall focus on the quasi-adiabatic regime $\beta \ll t$, where the $\mathbb{Z}_2$ fields are much slower than the lattice bosons. Following a Born-Oppenheimer-type reasoning, we consider that the hardcore bosons adapt instantaneously to the background static spins. In this way, they provide an effective potential energy for the $\mathbb{Z}_2$ fields which is used, in turn, to determine the ground state spin configuration. In our context, this can be formalized by means of the following variational ansatz

$$|\Psi_{\rm gs}(\{d_{\boldsymbol{n}},\boldsymbol{\theta}\})\rangle = |\psi_{\rm f}(\{d_{\boldsymbol{n}}\})\rangle \bigotimes \mathrm{e}^{-\mathrm{i}\sum_i \frac{\theta_{i,i+1}}{2}\sigma^y_{i,i+1}} |-\rangle_{\rm s} \tag{4.2}$$

where $|\psi_{\rm f}(\{d_{\boldsymbol{n}}\}\rangle = \sum_{\boldsymbol{n}} d_{\boldsymbol{n}} |\boldsymbol{n}\rangle_{\rm f}$ is a generic fermionic wavefunction. This wavefunction is defined by the set of variational amplitudes $\{d_{\boldsymbol{n}}\}$ in the Fock basis $|\boldsymbol{n}\rangle_{\rm f} = |n_1,\cdots,n_N\rangle_{\rm f}$ with $n_i \in \{0,1\}$ fermions at site $i \in \{1,\cdots,L\}$. On the other hand, this ansatz (4.2) describes the slow $\mathbb{Z}_2$ fields in terms of spin coherent states with variational angles $\boldsymbol{\theta} = (\theta_{1,2}...\theta_{i,i+1}...)$, and reference state $|-\rangle_{\rm s} = \otimes_i(|\uparrow_{i,i+1}\rangle - |\downarrow_{i,i+1}\rangle)/\sqrt{2}$.

Our Born-Oppenheimer-type variational ansatz (4.2) can be applied at arbitrary boson filling, where complex $\mathbb{Z}_2$ fields patterns (*i.e.* solitonic, incommensurate) may arise due to Peierls instability [GCGDL18]. Here we focus on the half-filled case in which, according to the previous discussion, a Peierls instability can lead to the doubling of the unit cell. Therefore, for periodic boundary conditions, it suffices to consider only two variational angles, namely $\boldsymbol{\theta} = (\theta_A, \theta_B)$ for the links joining odd-even (even-odd) lattice sites. As detailed in Appendix A.1, the variational problem reduces to the minimization of the following ground-state energy

$$\begin{aligned} \epsilon_{\rm gs}(\boldsymbol{\theta}) = &-\frac{2}{\pi}t(\boldsymbol{\theta})\mathsf{E}\big(1-\delta^2(\boldsymbol{\theta})\big) \\ &+\frac{\Delta}{4}(\sin\theta_A+\sin\theta_B) - \frac{\beta}{2}(\cos\theta_A+\cos\theta_B), \end{aligned} \tag{4.3}$$

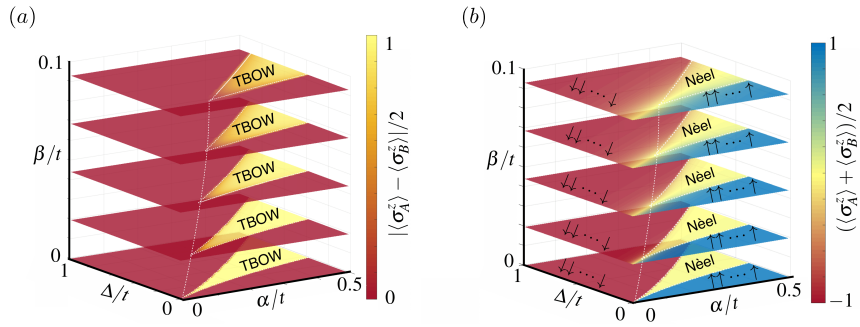

Fig. 4.1 Born-Oppenheimer phase diagram of the $\mathbb{Z}_2$ Bose-Hubbard model: **(a)** Representation of the magnetization difference $|\langle\sigma_A^z\rangle - \langle\sigma_B^z\rangle|$ between the even-odd sub-lattices for the variational ground state obtained by minimizing Eq. (4.3) for different parameters $(\Delta/t, \alpha/t, \beta/t)$. The yellow region corresponds to the two possible Néel configurations of the $\mathbb{Z}_2$ fields leading to a bond-density order parameter, and a symmetry-broken TBOW. **(b)** Representation of the magnetization sum $|\langle\sigma_A^z\rangle + \langle\sigma_B^z\rangle|$ between the even-odd sub-lattices for the variational ground state obtained by minimizing Eq. (4.3) for different parameters $(\Delta/t, \alpha/t, \beta/t)$. The red and blue regions correspond to the fully polarized configurations of the $\mathbb{Z}_2$ fields, which do not induce any modulation of the bosonic tunnelings, and thus lead to trivial insulators.

where we have introduced $t(\boldsymbol{\theta}) = t + \frac{\alpha}{2}\big(\sin\theta_A + \sin\theta_B\big)$, $\delta(\boldsymbol{\theta}) = \alpha(\sin\theta_A - \sin\theta_B)/(2t+\alpha(\sin\theta_A+\sin\theta_B))$, and $\mathsf{E}(x) = \int_0^{\pi/2} \mathrm{d}k(1-x\sin^2 k)^{1/2}$ is the complete elliptic integral of the second kind. Note that this minimization shall yield the particular angles $\boldsymbol{\theta}^\star = (\theta_A^\star, \theta_B^\star)$, which determine the $\mathbb{Z}_2$-field background experienced by the hardcore bosons.

At this variational level, we can draw a clear analogy between the $\mathbb{Z}_2$BHM (3.32) and the standard Peierls instability of the SSH model [SSH79]. In the SSH model, the energy reduction of the fermions due to a gap opening in the 1D metal compensates for the elastic energy increase of the lattice distortion (i.e. static limit of the acoustic branch) [Pei55]. In our case, the quadratic elastic energy of the standard Peierls problem is substituted by a trigonometric function describing the energy of the $\mathbb{Z}_2$-field background (see the second line of Eq. (4.3)). A direct consequence of this difference is that, whereas the 1D metal of the SSH model is always unstable towards a BOW phase at $T = 0$ in the large mass limit, $M \to \infty$ (which corresponds to the $\beta = 0$ case here), the $\mathbb{Z}_2$ Peierls instability of our hardcore bosons does indeed depend on the ratio Δ/α, such that one can observe a Peierls transition even at zero temperatures.

Born-Oppenheimer excitation ansatz.– In order to carry further this analogy, we discuss the gap opening in the $\mathbb{Z}_2$BHM (3.32), which requires generalizing the Born-

Oppenheimer ansatz (4.2) to account for the low-energy single-particle excitations. In a first step, we consider that the spin fluctuations about the $\mathbb{Z}_2$-field background are small, and introduce a spin-wave-type [BBM+02] formulation based on a Holstein-Primakoff transformation [HP40], namely

$$\begin{aligned}\sigma^z_{i,i+1} &\approx \cos\theta^\star_{i,i+1}\left(a_i + a_i^\dagger\right) - \sin\theta^\star_{i,i+1}\left(2a_i^\dagger a_i - 1\right),\\ \sigma^x_{i,i+1} &\approx \sin\theta^\star_{i,i+1}\left(a_i + a_i^\dagger\right) + \cos\theta^\star_{i,i+1}\left(2a_i^\dagger a_i - 1\right),\end{aligned} \tag{4.4}$$

where $a_i^\dagger, a_i$ are bosonic creation-annihiliation operators for the excitations of the $\mathbb{Z}_2$ fields localized at link $(i, i+1)$.

In a second step, we introduce a family of single-particle excitations over the previous variational ground-state $|\Psi_{\rm gs}(\{d_{\boldsymbol{n}}, \boldsymbol{\theta}^\star\})\rangle$ obtained from Eq. (4.2) by setting to the optimum variational angles $\boldsymbol{\theta}^\star = (\theta^\star_A, \theta^\star_B)$, namely

$$|\Psi_{\rm exc}(\boldsymbol{\eta})\rangle = \left(\sum_{k\in{\rm BZ}} \eta_{{\rm f},k}\gamma^\dagger_{k,+} + \sum_{i=1}^{N}\eta_{{\rm s},i}a_i^\dagger\right)|\Psi_{\rm gs}(\{d_{\boldsymbol{n}}, \boldsymbol{\theta}^\star\})\rangle\,, \tag{4.5}$$

where $\boldsymbol{\eta} = (\eta_{{\rm f},k}, \eta_{{\rm s},i})$ are the variational amplitudes, and $\gamma^\dagger_{k,+}$ are Bogoliubov-type fermion creation operators in the single-particle conduction band of the hardcore boson sector (see Appendix A.1 for details). In this case, the variational functional for the excitation energies depend on

$$\begin{aligned}\epsilon^{\rm f}_k(\boldsymbol{\theta}^\star) &= 2t(\boldsymbol{\theta}^\star)\sqrt{\cos^2 q + \delta^2(\boldsymbol{\theta}^\star)\sin^2 q},\\ \epsilon^{\rm s}_{2i-1}(\boldsymbol{\theta}^\star) &= 2\beta\cos\theta^\star_A - \sin\theta^\star_A\left(\frac{\Delta}{2} - 2\alpha \mathsf{B}_A(\boldsymbol{\theta}^\star)\right),\\ \epsilon^{\rm s}_{2i}(\boldsymbol{\theta}^\star) &= 2\beta\cos\theta^\star_B - \sin\theta^\star_B\left(\frac{\Delta}{2} - 2\alpha \mathsf{B}_B(\boldsymbol{\theta}^\star)\right),\end{aligned} \tag{4.6}$$

which themselves depend on the properties of the variational ground state, such as the the fermionic bond densities between odd-even sites $\mathsf{B}_A(\boldsymbol{\theta}^\star) = \mathsf{B}_{2i-1,2i}$, and between even-odd sites $\mathsf{B}_B(\boldsymbol{\theta}^\star) = \mathsf{B}_{2i,2i+1}$, where $\mathsf{B}_{i,j} = \langle c_i^\dagger c_j\rangle_{\rm gs} + {\rm c.c.}$.

The variational minimization then yields two types of low-energy excitations: *(i)* delocalized fermion-like excitations with $\epsilon_{\rm exc}(\boldsymbol{\theta}^\star) = \epsilon^{\rm f}_k(\boldsymbol{\theta}^\star)\ \forall k \in [-\frac{\pi}{2}, \frac{\pi}{2})$, or *(ii)* localized spin-wave-type excitations with $\epsilon_{\rm exc}(\boldsymbol{\theta}^\star) = \epsilon^{\rm s}_i(\boldsymbol{\theta}^\star)\ \forall i \in \{1, \cdots N\}$. Therefore, in our context, the gap opening is caused by a Néel-type alternation of the spins $\theta^\star_A - \theta^\star_B \neq 0$, which leads to $\delta(\boldsymbol{\theta}^\star) \neq 0$ and, according to Eq. (4.6), to the aforementioned gap opening

$$\Delta\epsilon = \min_k \epsilon_{\rm exc}(\boldsymbol{\theta}^\star) = 2t(\boldsymbol{\theta}^\star)|\delta(\boldsymbol{\theta}^\star)| > 0. \tag{4.7}$$

Adiabatic regime: Peierls transition and SPT phases.– After introducing this variational machinery, we can explore the rich physics of the $\mathbb{Z}_2$BHM (3.32) by focusing first on the adiabatic regime $\beta = 0$, where various results can be obtained analytically. In this limit, where the spins are static, it is possible to solve analytically the variational minimization of Eq. (4.3) for the ground-state ansatz (4.2), finding two critical lines

$$\Delta_c^{\pm} = \frac{4t}{\pi}\left(\tilde{\delta} \pm \mathsf{E}\left(1-\tilde{\delta}^2\right) \mp 1\right), \tag{4.8}$$

where we have defined $\tilde{\delta} = \alpha/t$. These critical lines, represented in the lowest planar sections of Fig. 4.1, are in perfect agreement with our previous results (3.35). For $\Delta > \Delta_c^+$ ($\Delta < \Delta_c^-$), the $\mathbb{Z}_2$-field background $\theta_A^\star = \theta_B^\star = -\frac{\pi}{2}$ ($\theta_A^\star = \theta_B^\star = \frac{\pi}{2}$) yields a polarized state $|\downarrow\downarrow\cdots\downarrow\rangle$ ($|\uparrow\uparrow\cdots\uparrow\rangle$), such that the translational invariance remains intact. Instead, for $\Delta \in (\Delta_c^-, \Delta_c^+)$, the variational minimization leads to the spontaneous breaking of the translational symmetry, yielding two possible perfectly-ordered Néel states, either $|\downarrow\uparrow\downarrow\uparrow\cdots\downarrow\uparrow\downarrow\rangle$ for $\theta_A^\star = -\theta_B^\star = -\frac{\pi}{2}$, or $|\uparrow\downarrow\uparrow\downarrow\cdots\uparrow\downarrow\uparrow\rangle$ for $\theta_A^\star = -\theta_B^\star = +\frac{\pi}{2}$. Let us now use the variational ansatz for the excitations (4.5) to show that this phase transition is marked by a gap opening, as occurs for the standard Peierls instability in 1D metals.

According to our previous discussion (4.7), as a consequence of $|\delta(\pm\pi/2, \mp\pi/2)| = \tilde{\delta} > 0$, a gap of magnitude $\Delta\epsilon = 2t\tilde{\delta}$ will be opened. This signals a Peierls transition accompanied by a BOW density modulation

$$\begin{aligned}
\mathsf{B}_A\left(-\frac{\pi}{2}, +\frac{\pi}{2}\right) &= \frac{2}{\pi(1-\tilde{\delta})}\left(\mathsf{E}(1-\tilde{\delta}^2) - \tilde{\delta}\mathsf{K}(1-\tilde{\delta}^2)\right), \\
\mathsf{B}_B\left(-\frac{\pi}{2}, +\frac{\pi}{2}\right) &= \frac{2}{\pi(1+\tilde{\delta})}\left(\mathsf{E}(1-\tilde{\delta}^2) + \tilde{\delta}\mathsf{K}(1-\tilde{\delta}^2)\right),
\end{aligned} \tag{4.9}$$

where we assume the symmetry-broken state $|\downarrow\uparrow\cdots\uparrow\downarrow\rangle$ (for $|\uparrow\downarrow\cdots\downarrow\uparrow\rangle$, the expressions for the A and B sublattices must be interchanged), and make use of the complete elliptic integral of the first kind $\mathsf{K}(x) = \int_0^{\pi/2} \mathrm{d}k (1 - x\sin^2 k)^{-1/2}$. Note that $\mathsf{B}_A = \mathsf{B}_B = 2/\pi$ for $\tilde{\delta} \to 0$, whereas in the limit $\tilde{\delta} \to 1$, we recover the alternation $\mathsf{B}_A = 0, \mathsf{B}_B = 1$ between perfect antibonding-bonding links (see Fig. 3.5**(b)**). For spin-boson couplings $\alpha < t$, there will be a period-two modulation with a smaller antibonding-bonding character. Let us emphasize again that, contrary to the SSH ground state that is always unstable towards the Peierls insulator for arbitrary fermion-phonon couplings, the $\mathbb{Z}_2$BHM (3.32) does support a Peierls transition as the spin-boson coupling is modified in the adiabatic regime.

Let us now discuss the interplay of symmetry-breaking order and symmetry-protected topological features in this BOW phase. The direct-product structure of our Born-Oppenheimer ansatz (4.2) allows us to extract an effective Hamiltonian

for the hardcore boson sector when $\Delta \in (\Delta_c^-, \Delta_c^+)$,

$$\begin{aligned}&\left\langle \Psi_{\rm gs}(\{d_{\boldsymbol{n}}\}, \{\pm\frac{\pi}{2}, \mp\frac{\pi}{2}\}) \right| H_{\mathsf{Z}_2\mathsf{BH}}^{U\to\infty} \left| \Psi_{\rm gs}(\{d_{\boldsymbol{n}}\}, \{\pm\frac{\pi}{2}, \mp\frac{\pi}{2}\}) \right\rangle \\ &= \langle \psi_{\rm f}(\{d_{\boldsymbol{n}}\})| \, H_{\rm SSH}(t \pm \alpha, t \mp \alpha) \, |\psi_{\rm f}(\{d_{\boldsymbol{n}}\})\rangle \,,\end{aligned} \tag{4.10}$$

which corresponds to two possible instances of the static SSH model (1.47). The corresponding dimerization parameter depends on the two possible symmetry-breaking patterns for the case of hard-wall boundary conditions:

(a) If the $\mathbb{Z}_2$ fields break the translational symmetry by adopting the Néel configuration $|\uparrow\downarrow\uparrow\downarrow\cdots\uparrow\downarrow\uparrow\rangle$, the hardcore bosons are subjected to $H_{\rm SSH}(t+\alpha, t-\alpha)$ with the pattern of dimerized tunnelings $\{t(1+\tilde{\delta}), t(1-\tilde{\delta})\cdots, t(1-\tilde{\delta}), t(1+\tilde{\delta})\}$, where we recall that $\tilde{\delta} > 0$. According to our discussion in chapter 1, in this regime the ground state corresponds to a trivial insulator with a vanishing Zak phase (1.46) $\gamma = 0$.

(b) If the $\mathbb{Z}_2$ fields, instead, break the translational symmetry via $|\downarrow\uparrow\downarrow\uparrow\cdots\downarrow\uparrow\downarrow\rangle$, the hardcore bosons are subjected to $H_{\rm SSH}(t-\alpha, t+\alpha)$, and thus see the pattern of dimerized tunnelings $\{t(1-\tilde{\delta}), t(1+\tilde{\delta})\cdots, t(1+\tilde{\delta}), t(1-\tilde{\delta})\}$. According to our discussion in chapter 1, in this case the half-filled ground state is a BDI topological band insulator with a non-vanishing Zak phase $\gamma = \pi$ for $\tilde{\delta} < 2$. Note that the symmetry-breaking long-range order of the BOW phase (4.9) occurs simultaneously with the symmetry-protected topological invariant $\gamma = \pi$. Moreover, both of these orders develop in the same degree of freedom: the hardcore bosons. Accordingly, our model yields a clear instance of an intertwined topological insulator [KD14]: a *topological bond-ordered wave* (TBOW). Let us also emphasize that this interplay between spontaneous symmetry breaking and symmetry-protected topological phases is characteristic of our model of lattice bosons coupled to Ising fields (3.32), and cannot be accounted for with the dimerised Bose-Hubbard model studied in [GHF13].

Another feature of this non-trivial topological state is the presence of localized edge states for finite system sizes. In the hardcore limit, chiral symmetry guarantees that these edge states are protected against perturbations that respect the symmetry, as long as the gap does not close [RH02]. The bulk-boundary correspondence relates a quantize topological invariant in the bulk of the system with protected edge states at the boundaries [AOP16].

Finally, we note that, since the two Néel configurations are degenerate in the thermodynamic limit, both can be obtained experimentally in the ground state of the system. After a symmetry-breaking transition, one of the two will result due to quantum fluctuations. By introducing a small staggered field, $\epsilon \sum_i (-1)^i \sigma^z_{i,i+1}$, the degeneracy is broken and one specific configurations can be selected: (a) trivial for $\epsilon > 0$ and (b) topological for $\epsilon < 0$.

Quasi-adiabatic regime: fluctuation-induced topological phase transitions.– We have seen that the Born-Oppenheimer ansatz (4.2) allows us to draw a clear analogy with the Peierls transition in the $\beta = 0$ limit, and a transparent understanding of intertwined topological insulators in the $\mathbb{Z}_2$BHM (3.32). We can extend this analysis to the quasi-adiabatic regime $\beta \ll t$, expanding thus the analytical understanding of the bosonic Peierls mechanism presented in chapter 3 to a situation where the $\mathbb{Z}_2$ field dynamics introduce quantum fluctuations that can modify the Peierls mechanism.

As shown in Fig. 4.1, the quantum dynamics of these fields competes against the formation of the bond-ordered density modulations, modifying the static phase boundaries (4.8) that delimit the TBOW phase. In fact, it is possible to get analytical expressions of how these critical lines get deformed by considering the variational energies (4.3) of the previous polarized/Néel-type phases for small deviations of the angles $\boldsymbol{\theta}$ around the corresponding values $\boldsymbol{\theta}^\star$. A comparison of these energies leads to the following critical lines

$$\Delta_{\mathrm{c}}^{\pm} = \frac{4t}{\pi}\left(\tilde{\delta} \pm \left(\mathsf{E}\big(1-\tilde{\delta}^2\big) - 1\right)\right) \mp \frac{\pi\beta^2}{4t\tilde{\delta}\mathsf{E}\big(1-\tilde{\delta}^2\big)}, \tag{4.11}$$

which are represented by the dashed white lines of Fig. 4.1, and yield a very good approximation of the yellow region enclosing the symmetry-broken TBOW phase. As advanced previously, these critical lines predict that the area of the TBOW phase decreases as β increases, and lead to fluctuation-induced topological phase transitions connecting the TBOW phase to other trivial band insulators as the $\mathbb{Z}_2$ field dynamics becomes more relevant.

Softcore bosons coupled to $\mathbb{Z}_2$ fields

In the previous subsection, we have presented a Born-Oppenheimer variational treatment of the $\mathbb{Z}_2$BHM (3.32) in the limit of hardcore bosons and quasi-adiabatic $\mathbb{Z}_2$ fields. Our variational ansatz for the ground state (4.2) and low-energy excitations (4.5) has allowed us to draw a clear analogy with the Peierls instability of 1D metals via the fermionization of the hardcore bosons: at $U \to \infty$, a Fermi surface emerges and an energy gap can be opened. This analogy has allowed us to show that symmetry-breaking quantum phase transitions can take place at various $(\alpha_{\mathrm{c}}, \Delta_{\mathrm{c}})$, delimiting a finite region of a TBOW for hardcore bosons (see Fig. 4.1). The question we would like to address in this subsection is if such a TBOW phase can only be defined at the singular "$U = \infty$" point or if, on the contrary, it persists within the physically-relevant regime of finite Hubbard interactions.

The regime of strong, yet finite, interactions can give rise to interesting strongly-correlated behavior that cannot be accounted for by considering solely the "$U = \infty$" point. For instance, for the Fermi-Hubbard model close to half-filling, whereas the ground state is a fully-polarized ferromagnet [Nag66, SKA90, LYB+12] for

infinite interactions, the regime of finite repulsion $0 < t/U \ll 1$ gives rise to anti-ferromagnetic super-exchange interactions [And59, MGY88] that are believed to play a key role in high-temperature superconductivity [And87]. Similar super-exchange interactions also appear in the strongly-interacting limit of two-component Bose-Hubbard models [DDL03]. Such spin-spin interactions are absent in the single-component Bose-Hubbard model, where one obtains density-density interactions between bosons at nearest-neighboring sites, as well as density-dependent correlated tunnelings [Caz03].

We note that in our $\mathbb{Z}_2$BHM (3.32), despite consisting of single-component bosons, the strongly-interacting limit can be richer as the virtual tunnelings are dressed by the corresponding $\mathbb{Z}_2$ link fields. Therefore, in addition to the aforementioned effects, an effective spin-spin interaction between the spins at neighboring links can also appear as corrections to the $U \to \infty$ limit are studied. To leading order in a $0 < \max\{t/U, \alpha/U\} \ll 1$ expansion, we find that the $\mathbb{Z}_2$BHM (3.32) can be expressed as $H_{\mathsf{Z}_2\mathsf{BH}} \approx H_{\mathsf{Z}_2\mathsf{BH}}^{U\to\infty} + \Delta H$, where the leading corrections are

$$\Delta H = -\frac{4t^2}{U}\sum_i \left(1 + 2\tilde{\delta}\sigma^z_{i,i+1} + \tilde{\delta}^2\right) n_i n_{i+1}$$
$$+ \frac{2t^2}{U}\sum_i \left(1 + \tilde{\delta}\left(\sigma^z_{i,i+1} + \sigma^z_{i+1,i+2}\right) + \tilde{\delta}^2\sigma^z_{i,i+1}\sigma^z_{i+1,i+2}\right)\left(c_i^\dagger n_{i+1} c_{i+2} + \text{H.c.}\right), \tag{4.12}$$

The first term describes the second-order process where the boson virtually tunnels back and forth to a neighboring occupied site, giving rise to a virtual double occupancy and to density-density couplings, which cannot be accounted in the hardcore-boson limit $U \to \infty$. Note that this virtual tunneling is mediated by the link $\mathbb{Z}_2$ field, which can thus modify the strength of the density-density coupling depending on the background configuration of the spins. The second term describes the second-order process where a boson virtually tunnels between two sites apart via an intermediate occupied site, giving rise to a density-dependent correlated tunneling. Note again, that this virtual tunneling is dressed by the link $\mathbb{Z}_2$ fields, and its strength can depend on their configuration, including spin-spin correlations. From a different perspective, these mediated virtual tunnelings give rise to an effective coupling between neighboring link spins, as announced above.

As discussed in the hardcore-boson limit below Eq. (4.9), the Born-Oppenheimer approximation allows us to extract an effective Hamiltonian for the bosonic sector, which depends on the $\mathbb{Z}_2$ field configuration in the ground state. Due to the finite U corrections (A.15), the effective Hamiltonian for softcore bosons contains interaction terms and cannot be reduced to a single-particle model. Moreover, these terms break the chiral symmetry of the system, which protects the TBOW phase in the limit $U \to \infty$. Nevertheless, the effective Hamiltonian with corrections (A.15) is still invariant under a bond-centered inversion symmetry [GHF13].

Therefore, in analogy to the Bose-Hubbard model with dimerized fixed tunnelings [GHF13], the ground state of the effective Hamiltonian shall correspond to a SPT phase protected by inversion symmetry as long as the $\mathbb{Z}_2$ field displays a Néel-type anti-ferromagnetic ordering and the gap remains open. Following a topological argument, as long as the gap remains open and the symmetry is present, the many-body generalization [XCN10] of the topological invariant (1.29) will be quantized to the same value as in the hardcore limit, even in softcore regimes away from the singular "$U = \infty$" point. In the next subsection, we will confirm this prediction by computing numerically the topological invariant in the strongly-correlated bosonic regime.

In order to show that the energy gap remains open in the softcore regime, we can explicitly calculate how the variational excitation energies (A.12) get modified due to the perturbations in Eq. (A.15). Our variational ansatz for the excitations allows us to go beyond standard mean-field theory, and obtain corrections to the excitation branches of Eq. (4.6), giving rise to dispersive spin-wave-type excitations, or coupled spin-boson quasi-particles. For the many-body gap, as discussed in Appendix A.1, the TBOW energy gap (4.7) is shifted to

$$\Delta\epsilon \approx 2t(\boldsymbol{\theta}^\star)|\delta(\boldsymbol{\theta}^\star)| - \frac{4t^2}{U}\left(1+\frac{1}{\pi}\mathsf{E}(1-\tilde{\delta}^2)\right)\left(1+\tilde{\delta}\left(\sin\theta_A^\star+\sin\theta_B^\star\right)\right), \qquad (4.13)$$

to leading order in $\tilde{\delta} \ll 1$. At the level of our Born-Oppenheimer ansatz, we see that the energy gap remains finite, such that the TBOW phase extends to the soft-core regime. Moreover, one can also see that the TBOW gap decreases as the interactions are lowered. This trend can be also be understood from the following alternative perspective. As discussed above, the virtual tunnelings give rise to an effective coupling between neighboring link spins. Since fermions are much faster than the spins, and the t/U corrections (A.15) are assumed to be small, the value of this coupling can be approximated using the fermionic unperturbed ground state in Eq. (4.2) $\langle\psi_{\mathrm{f}}(\{d_{\boldsymbol{n}}\})|\left(c_i^\dagger n_{i+1}c_{i+2}+\mathrm{H.c.}\right)|\psi_{\mathrm{f}}(\{d_{\boldsymbol{n}}\})\rangle$. We can evaluate this expectation value by applying Wick's theorem, as the variational ansatz is built with free spinless fermions. This calculation shows that effective spin-spin interaction is ferromagnetic, which would compete against the Néel-type order of the $\mathbb{Z}_2$ fields, making the TBOW phase less stable (i.e. lowering the corresponding energy gap).

Although it cannot be captured by our variational approach, this tendency opens the possibility that the energy gap closes for sufficiently small interactions, such that a quantum phase transition to a non-topological phase takes place. Accordingly, the TBOW phase may not be adiabatically connected to a bosonic non-interacting SPT phase, and one could claim that it is an instance of an interaction-induced intertwined topological insulator. In order to explore this possibility further, and to benchmark the qualitative correctness of our predictions based on the Born-Oppenheimer variational approach, we now move onto a quasi-exact numer-

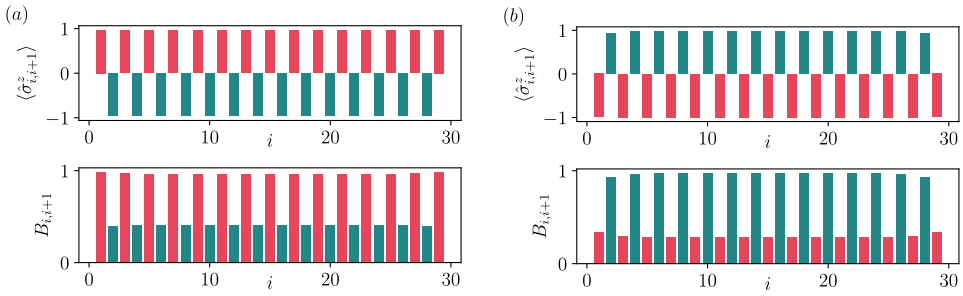

Fig. 4.2 Symmetry-breaking order parameters: Spin pattern $\langle \hat{\sigma}^z_{i,i+1} \rangle$ and particle density $\mathsf{B}_{i,i+1}$ on the bonds of the lattice for a half-filled system. Different colors depict even and odd bonds. **(a)** Symmetry-broken sector with the $\mathbb{Z}_2$ fields in the approximate Néel configuration $|\uparrow\downarrow\uparrow\downarrow\cdots\uparrow\downarrow\uparrow\rangle$, which leads to a period-two strong-weak modulation of the bond density. **(b)** Symmetry-broken sector with the $\mathbb{Z}_2$ fields in the approximate Néel configuration $|\downarrow\uparrow\downarrow\uparrow\cdots\downarrow\uparrow\downarrow\rangle$, which leads to a period-two weak-strong modulation of the bond density.

ical method based on the density-matrix renormalization group (DMRG).

4.2.2 Density-matrix renormalization group approach

We use now the DMRG algorithm [HP18] to study the properties of the TBOW phase. In the following, we use open boundary conditions and fix the bond dimensions to $D = 100$. We also truncate the maximum number of bosons per site to $n_0 = 2$. We benchmark the previous variational results by exploring the strongly-correlated regime of finite Hubbard interactions U, and dynamical $\mathbb{Z}_2$ fields $\beta > 0$. We start by giving compelling evidence to show that the BOW phase is indeed a SPT phase protected by a bond-centered inversion symmetry. To this end, we use both the entanglement spectrum and a local topological invariant to characterize the topological nature of the phase. We also show the presence of many-body localized edge states with a fractional particle number. Finally, we study the transition from the TBOW phase to a non-topological quasi-superfluid (qSF) phase as the Hubbard interactions are lowered, and present a phase diagram of the model. Our numerical results clearly show the need of both strong interactions and symmetry breaking in order to stabilize the TBOW phase, which cannot be connected to a non-interacting topological insulator.

Symmetry-breaking order parameters

According to our variational ansatz in the hardcore limit, and the discussion below Eq. (4.9), there should be a finite region of parameter space hosting a TBOW

phase (see Fig. 4.1). Figure 4.2 shows the numerical DMRG results for the order parameters characterizing the BOW phase of the $\mathbb{Z}_2$BHM (3.32), focusing on strongly-correlated bosons coupled to quasi-adiabatic $\mathbb{Z}_2$ fields (i.e. $U = 20t$, and $\beta = 0.01t$). For these results, and for the rest of the section, we use a chain of $L = 30$ sites and fix the rest of the Hamiltonian parameters to $\alpha = 0.5t$, $\Delta = 0.8t$, unless we explicitly say otherwise. As described above, the BOW phase is partially characterized by the spontaneous breaking of translational invariance, which is captured by the alternation of the $\mathbb{Z}_2$ magnetization $\langle\sigma^z_{i,i+1}\rangle$, and the modulation of the bond density $B_{i,i+1}$. Moreover, this phase is gapped and incompressible, as it was shown in chapter 3. Long-range order develops in the system after the symmetry breaking, whereby the unit cell of the system is doubled. The two possible symmetry-broken ground-states of Figs. 4.2 **(a)** and **(b)** are completely degenerate in the thermodynamic limit, and they can be connected by a one-site lattice translation. For finite lattice sizes, they differ at the edge of the system. Let us remark, however, that these bonding/antibonding order parameters do not suffice to capture all the physics of the BOW phase, as they do not account for the topological features that make the two symmetry-broken sectors fundamentally different from each other.

Topological characterization of the TBOW

Entanglement spectrum.– We first explore numerically the entanglement properties of the ground-state. In particular, we compute the entanglement spectrum [LH08]. We define a bipartition of the system, and write the ground-state as $|\psi_{\rm gs}\rangle = \sum_n \tilde{\lambda}_n |\psi_n\rangle_{\mathfrak{L}} \otimes |\psi_n\rangle_{\mathfrak{R}}$, where $\mathfrak{L}$ and $\mathfrak{R}$ are the two subsystems, and $\{\tilde{\lambda}_n\}$ are the corresponding Schmidt coefficients. The entanglement spectrum is defined as the set of all the Schmidt coefficients in logarithmic scale $\epsilon_n = -2\log(\tilde{\lambda}_n)$. It has been established that the entanglement spectrum is degenerate for symmetry-protected topological phases [PTBO10]. In particular, this degeneracy is robust against perturbations that respect the symmetry as long as the many-body gap of the system is open.

In Fig. 4.3 (left panel), we present the entanglement spectrum for the BOW phase in the hardcore-boson limit. We consider a bipartition at the middle of the chain, and explore the two possible degenerate ground-state configurations that appear as a consequence of the spontaneous breaking of translational symmetry. As discussed below Eq. (4.9), we expect that the weak-strong bond-density modulation (Fig. 4.2**(b)**) due to the symmetry-broken background of $\mathbb{Z}_2$ fields gives rise to a SPT phase. As follows from Fig. 4.3 (left panel), the entanglement spectrum is two-fold degenerate for one of the ground-states, while it clearly lacks an exact two-fold degeneracy for the other configuration. These numerical results provide a clear signature of the topological nature of the BOW phase, and confirm the scenario of the interplay between symmetry breaking and SPT phase of the $\mathbb{Z}_2$BHM (3.32)

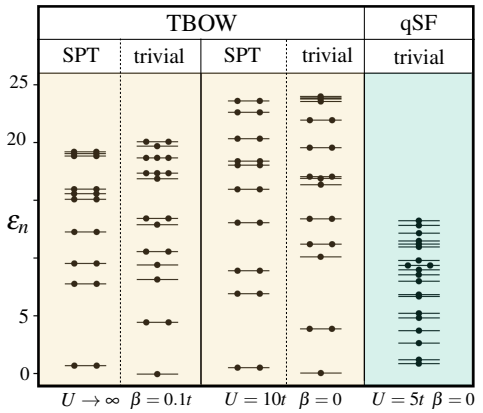

Fig. 4.3 Entanglement spectrum degeneracies: Lower 20 eigenvalues of the entanglement spectrum for different states in the TBOW and the quasi-SF phases. For the former, we show the spectrum in the two different symmetry-breaking sectors. We can see how the spectrum is double degenerate in one case, which corresponds to the non-trivial topological sector (see our discussion below Eq. (4.9)). We observe how the degeneracies survive in two strongly-correlated regimes: for hardcore bosons ($U = \infty$) coupled to dynamical $\mathbb{Z}_2$ fields ($\beta = 0.1t$), and for soft-core bosons ($U = 10t$) coupled to static $\mathbb{Z}_2$ fields ($\beta = 0$). This degeneracy is lost for small enough interactions in the non-topological quasi-SF phase.

predicted by the Born-Oppenheimer variational approach.

In the central panel of Fig. 4.3, we show the entanglement spectrum for strongly-correlated bosons on a static lattice ($U = 10t$, $\beta = 0$), thus exploring the departure from the hardcore constraint. As discussed below Eq. (4.13), for strong yet finite interactions, we expect that the energy gap is finite, and that the TBOW phase persists as one lowers the interactions. This expectation is supported by our numerical results, which again display a clear two-fold degeneracy of the entanglement spectrum in one of the symmetry-broken ground states. Let us finally note that, for sufficiently weak interactions ($U = 5t$, $\beta = 0$), the degeneracy of the spectrum is completely lost for the single ground-state of the system (see the right panel of Fig. 4.3). This non-topological phase for the weakly-interacting bosons corresponds to the quasi-superfluid (SF), that will be discussed in more detail below. The latter facts again support our claim that this strongly-correlated TBOW phase has an interaction-induced nature, as the topological features are completely absent in the weakly-interacting regime.

Let us finally emphasize that our entanglement spectrum analysis away from the hardcore limit has been restricted to static $\mathbb{Z}_2$ fields, which is necessary as the calculation of the entanglement spectrum requires a bipartition of the system

that respects the protecting symmetry of the topological phase. In the case of hardcore bosons, the system is protected by chiral symmetry and the half-chain bipartition respects that symmetry. On the other hand, for finite interactions, the phase is instead protected by inversion symmetry (see our discussion below Eq. (A.15)). For our DMRG implementation, the presence of the $\mathbb{Z}_2$ fields does not allow us to cut the system into two halves in such a way that the two parts respect the bond-centered inversion symmetry. This is only possible for static spins ($\beta = 0$), since they form a product state and do not contribute to the entanglement properties of the system. This particularity of our model prevents us from using the entanglement spectrum to characterize the topological properties in the regime of strongly-correlated bosons coupled to dynamical fields (U finite, $\beta > 0$), although the topological nature of the TBOW phase must also be preserved as the transverse field β is slightly increased (see Fig. 4.1). For this reason, we introduce now a robust topological invariant that yields an alternative route to characterize the topological properties of the BOW phase in any parameter regime.

Berry phase.– We now characterize the topology with the help of the local Berry phase introduced by Hatsugai [Hat06]. It is a topological invariant that serves as a local "order parameter" to distinguish symmetry-protected topological phases in the presence of interactions. Considering a periodic Hamiltonian $H(\lambda)$, which depends on an external parameter $\lambda \in [\lambda_0, \lambda_f]$ through an adiabatic cyclic evolution $H(\lambda_0) = H(\lambda_f)$. As shown in [**?**], if there exists an antiunitary operator $\Theta = KU_\Theta$, where U_Θ is unitary and K is the complex conjugation, which commutes with $H(\lambda)$, the Berry phase [Ber84] acquired by the ground state $|\psi_\lambda\rangle$ during the parallel transport on a loop C with $\lambda_f = \lambda_0$,

$$\gamma_C = \mathrm{i} \oint_C \mathrm{d}\lambda \, \langle \psi_\lambda | \partial_\lambda \psi_\lambda \rangle \mathrm{mod} 2\pi, \tag{4.14}$$

is quantized to finite values 0 and π. Let us note that, for non-interacting systems, considering the quasi-momentum as the cyclic parameter $\lambda = k$ as one traverses the Brillouin zone, Eq. (4.14) reduces to the previously-introduced Zak's phase (1.29). However, this free-fermion topological invariant cannot be directly applied to interacting systems. Alternatively, we shall use Eq. (4.14) with a different adiabatic parameter that introduces the notion of locality, and allows us to generalize the topological invariant to a many-body scenario.

This quantity is topological in the sense that it cannot change without closing the gap, as long as the corresponding symmetry is preserved. One can add, in particular, a local perturbation to the initial Hamiltonian (3.32), like a local twist in one of the hopping strengths $t \to t\lambda = te^{i\theta}$, which does not close the gap of the BOW phase. Note that this is similar to the use of twisted boundary conditions to calculate the Zak phase in the presence of interactions (1.57). However, as noticed

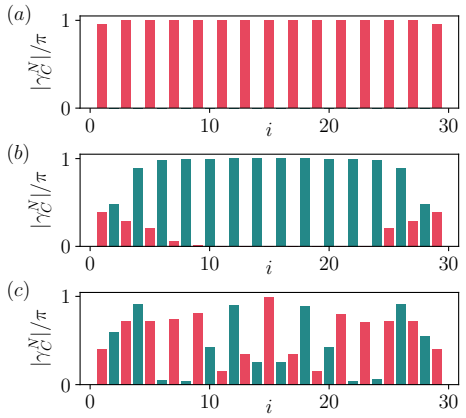

Fig. 4.4 Local Berry phase quantization: local Berry phase (4.15) calculated for each bond $\gamma_C^N(i, i+1)$, such that even and odd bonds are depicted in different colors. We use a value of $N = 5$ for three different ground states: **(a)** and **(b)** correspond to the trivial and topological symmetry-broken sectors of the BOW phase, respectively, for $U = 20t$ and $\beta = 0.02t$. In the bulk, the phases are quantized to values 0 and π, alternating between even and odd bonds, and for each bond between the two sectors. **(c)** Configuration for a state in the quasi-superfluid phase, with $U = 5t$ and $\beta = 0.02$, where the translational symmetry is not broken. In this case, the phases are not quantized since the phase is not a SPT phase.

by Hatsugai [Hat06], this perturbation should not be necessarily put on the edges of the system, but can be placed on any bond as long as it preserves the symmetry. This choice is appropriate in our case, since we can add local perturbations that respect inversion symmetry, and constitute therefore a local measure in the bulk of the system. Moreover, it only depends on quantities that decay exponentially and, thus, this measurement is valid not only for periodic, but also for open hard-wall boundary conditions, as long as the perturbation is not applied too close to the edge of the system.

In practice, the integral of Eq. (4.14) can be challenging to compute as the integrand is gauge dependent (the integral on the loop, however, is gauge invariant), requiring a numerical gauge fixing at each discretized point of the loop. Alternatively, we compute here the integral using a Wilson loop formulation, which is gauge invariant and avoids the gauge fixing problem [Hat06, FHS05], namely

$$\gamma_C^N = \mathrm{Arg} \prod_{n=0}^{N-1} \langle \widetilde{\psi}_n | \widetilde{\psi}_{n+1} \rangle \tag{4.15}$$

where $|\widetilde{\psi}_n\rangle = |\psi_{\lambda_n}\rangle \langle \psi_{\lambda_n}\rangle \phi$ is the projection of a reference state $|\phi\rangle$ onto the

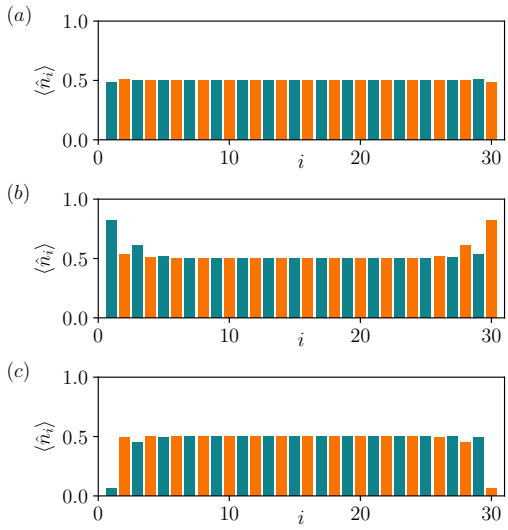

Fig. 4.5 Many-body edge states: Real-space configuration of the bosonic occupation number $\langle \hat{n}_i \rangle$, using different colors for even and odd sites. **(a)** The trivial topological sector of the BOW phase is characterized by the absence of edge states in the bosonic sector. The non-trivial sector is represented in **(b)** and **(c)** for one extra particle and one extra hole, respectively. We can see how the extra particle (resp. hole) generates two edge states, each one carrying a fractional particle number of $+1/2$ (resp. $-1/2$).

adiabatic ground state, with λ_0, λ_1, ..., $\lambda_N = \lambda_0$ being the N points in which the loop C is discretized. The discretized local Berry phase (4.15) depends in general on N and on the way the loop is discretized, but not on the reference state as far as it has a finite overlap with the ground-state. However, we note that γ_C^N converges rapidly to the local Berry phase (4.14) in the large N limit.

We define the local phase $\gamma_C^N(i, i+1)$, corresponding to the bond $(i, i+1)$, by adding a local perturbation to the bare tunneling coefficient, $te^{i2\pi n/N}$, with $n \in \{0, ...N\}$. Note that this perturbation preserves the bond-centered inversion symmetry, and thus does not present the limitations of the entanglement spectrum mentioned in the previous section. Therefore, we can use it to explore the topological features of the TBOW phase away from the hardcore boson limit and considering dynamical $\mathbb{Z}_2$ fields in the quasi-adiabatic regime. Figure 4.4 shows the local Berry phases at every bond for the TBOW and the qSF phases. Figs. 4.4**(a)** and **(b)** correspond to the two degenerate ground states of the TBOW for $U = 20t$ and $\beta = 0.02t$, where we observe a Berry phase quantized to values of 0 and π in the bulk of the system. The quantized values alternate for even and odd bonds, and the pattern is reversed for the two ground states, allowing us to assign two

different SPT sectors using the following reasoning.

For finite system sizes, we define the two-site unit cells in such a way that the even bonds—$(i, i+1)$ with i even—are intercell, whereas the odd bonds are intracell (i.e. they couple bosons within the same unit cell). If we then focus only on the intercell bonds (green in the figure), we can see how the corresponding local Berry phases are all quantized to 0 (Fig. 4.4**(a)**) for the $\mathbb{Z}_2$-field configuration of Fig. 4.2**(a)** adiabatically connected to $|\uparrow\downarrow\uparrow\downarrow\cdots\uparrow\downarrow\uparrow\rangle$, which is in agreement with our variational ansatz that predicted a trivial band insulator for such symmetry-breaking pattern. On the other hand, the local Berry phases for intercell bonds for the configuration (Fig. 4.2**(b)**) adiabatically connected to $|\downarrow\uparrow\downarrow\uparrow\cdots\downarrow\uparrow\downarrow\rangle$ are all quantized to π (Fig. 4.4**(b)**), which again is in accordance with our variational ansatz predicting a inversion-symmetric SPT phase. Using this convention, the latter can be regarded as the non-trivial topological configuration, and the value of the local Berry phase connects to that of the Zak phase obtained in the previous section for hardcore bosons in the Born-Oppenheimer approximation. These results confirm our previous expectation that the TBOW phase extends to the softcore regime and for dynamical $\mathbb{Z}_2$ fields, and is characterized by a many-body generalization of Eq. (1.29) with the same quantized value. For $U = 5t$, the ground state is in a non-topological qSF phase, and the Berry phase does not show a quantized pattern. We will show now that this ground state support many-body edge states with fractional particle number.

Many-body edge states and fractionalization

For a system with boundaries, an alternative signature of the topological nature of the TBOW phase is the presence of localized edge states, which lie in the middle of the gap for 1D SPT phases with chiral symmetry [RH02]. These edge states are topologically robust against perturbations that respect the symmetry and do not close the gap. Let us note that this bulk-boundary correspondence does not always hold for generic SPT phases, since the presence of edge states might not be guaranteed even if the bulk presents non-trivial topological properties, as is the case of phases protected by inversion symmetry [TZV10, HPB11]. In some of these cases, however, localized edge states can be observed in the spectrum as remnants of the protected edge states of a extended two-dimensional system [Hat93b]. As shown below, this is precisely the situation for the $\mathbb{Z}_2$BHM (3.32).

Figure 4.5 shows the real-space density configuration of bosons for the two degenerate ground state configurations of the symmetry-broken BOW phase for finite Hubbard interactions ($U = 20t$, $\beta = 0.02t$). In the topologically-trivial configuration, which is characterized by the long-range order displayed in Fig. 4.2**(a)**, which leads to a period-two strong-weak alternation of the bonds, we do not observe any localized edge states (Fig. 4.5**(a)**). On the contrary, for the long-range order characterizing the other symmetry-broken sector in Fig. 4.2**(b)**, which leads to a

period-two weak-strong alternation of the bonds, we see localized peaks or drops in the occupation number when we either add **(b)** or subtract **(c)**, respectively, one particle above or below half filling.

These many-body edge states possess a fractional particle number of $\pm 1/2$, which constitutes a bosonic analogue of the predicted charge fractionalization in fermionic quantum field theories [JR76]. In particular, the occupation number $\langle \hat{n}_i \rangle$, which is equal to $1/2$ in the bulk, differs at the edges for the two states. Fractionalization implies that an extra particle or hole is "divided" into two separate quasi-particles, each carrying half of the particle number. These quasi-particles are localized in different parts of the system and are independent of each other, although they can only be created/annihilated in pairs. The latter can be formed by two fractional $+1/2$ particles, two fractional $+1/2$ holes, or one of each.

As already mentioned, the bulk-boundary correspondence only guarantees the presence of protected edge states in SPT phases protected by chiral symmetry. This is the case for hardcore bosons, where we find protected localized states at the boundaries of the system. However, our DMRG results show that these states are still present for finite Hubbard interactions, even if the protected symmetry is changed from chiral symmetry to a bond-centered inversion symmetry. Although we can not guarantee the protection of these states, their origin can be understood if we extend the chain to a two-dimensional system, where the bulk-boundary correspondence is restored, and the topological bulk guarantees the existence of one-dimensional conducting states at the boundaries [Hat93a].

With the help of these three observables, we have characterized the topological nature of the BOW phase. In particular, using both the entanglement spectrum and the local Berry phase (4.15), we proved that one of the two degenerate symmetry-broken states of the BOW phase has a non-trivial bulk topology. Moreover, this topological property persists for finite Hubbard interactions and dynamical $\mathbb{Z}_2$ fields. These numerical evidences confirm the qualitative predictions of the Born-Oppenheimer approximation, and can also be used to explore regimes that lie beyond the applicability of the variational ansatz. Finally, we discussed the presence of many-body edge states in the TBOW phase. All these signatures allow us to regard the TBOW phase as an interaction-induced intertwined topological insulator protected by a bond-centered inversion symmetry.

Interaction-induced nature of the TBOW

In this section, we discuss the importance of strong correlations for the existence of the TBOW phase. Using the Born-Oppenheimer approximation, we were able to calculate the single-particle gap in the hardcore boson limit (4.7), and show that it gets reduced if we introduce corrections (A.15) for large but finite Hubbard interactions (4.13). This result suggested the existence of a phase transition for small enough values of U, such that the TBOW phase cannot be adiabatically

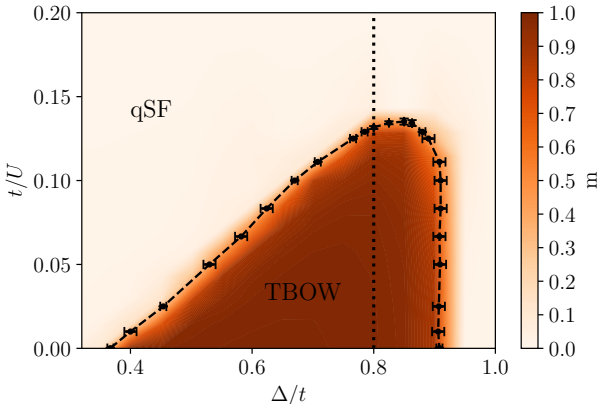

Fig. 4.6 Phase diagram: Phase diagram of the Hamiltonian (3.32) in terms of the parameters Δ/t and t/U for the half-filled case using DMRG. The rest of the parameters are fixed to $\alpha = 0.5t$, $\beta = 0.02t$. The staggered magnetization m for a system size $L = 60$ is represented by the color plot: it has a non-zero value in the TBOW phase and goes to zero in the qSF, allowing the distinction between these two phases. The black dots (with the corresponding error bars) represent the critical points in the thermodynamic limit obtained by a finite-size scaling of m (see Fig. 4.7), and the dashed line connecting them is drawn to guide the eye. The dotted vertical line corresponds to the transition for $\Delta = 0.80$ represented in Fig. 4.7. For small enough values of the interaction strength, the ground state of the system is in a qSF phase for any value of Δ. This supports our claim that the TBOW phase is an interaction-induced intertwined topological insulator.

connected to a non-interacting SPT phase. Moreover, in the previous subsection we showed how the signatures of non-trivial topological properties —such as the degeneracies of the entanglement spectrum (Fig. 4.3) and the quantization of the local Berry phase (Fig. 4.4)—disappear for small interactions, where one expects the ground state to be in a non-topological qSF phase. In this section, we explore this conjecture and show that, indeed, the TBOW phase can be considered as an interaction-induced SPT phase as one starts from a qSF, and crosses a quantum critical point by increasing the Hubbard interactions.

To support this claim, we present in Fig. 4.6 the phase diagram of the model at half filling in terms of Δ/t and t/U using DMRG. The color plot represent the staggered magnetization,

$$m = \frac{1}{L}\sum_i (-1)^i \langle \hat{\sigma}^z_{i,i+1} \rangle, \tag{4.16}$$

for a system size of $L = 60$. This order parameter allows one to distinguish between

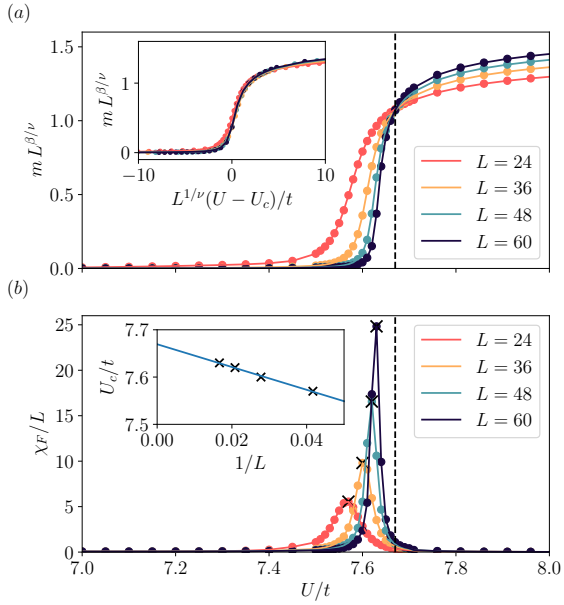

Fig. 4.7 Finite-size scaling for the quantum phase transition between the TBOW and the qSF phase: (a) Rescaling of the staggered magnetization m as a function of the interaction strength U/t for $\Delta/t = 0.80$ and for different system sizes. The former serves as an order parameter to distinguish between the TBOW phase, where it has a non-zero value, and the qSF phase, where it vanishes. The critical point, $U_c = 7.67t$, is located at the crossing point between the different lines, by assuming the critical exponents of the Ising universality class, $\beta = 1/8$ and $\nu = 1$. Inset: These coefficients lead to the collapse of the data to a single line. (b) The location of the critical point is confirmed using the fidelity susceptibility χ_F. This quantity develops a peak near the critical point, and its hight diverges with the system size. In the inset, the critical point is found by extrapolating the location of the peaks for different sizes.

the TBOW and the qSF phase. The phase diagram also shows the critical line obtained in the thermodynamic limit, separating the TBOW and the qSF phase for small enough values of U.

We now discuss the the analysis required to calculate one the critical points. In particular, Figure 4.7**(a)** shows the change of m in terms of U for a fixed value of Δ and for different system sizes. By introducing a proper rescaling factor, we observe how all the lines cross at the quantum critical point U_c. In the inset, we show the collapse of the data to a universal line, $m^{\beta/\nu} \sim f\left(L^{1/\nu}(U - U_c)\right)$, where we observe good agreement using the critical exponents of the Ising universality class, $\beta = 1/8$ and $\nu = 1$. This contrasts with other transitions in the one-dimensional

BHM between an insulator and a SF phase, for which the universality class is of the Kosterlitz-Thouless type [CCG+11]. Figure 4.7**(b)** depicts the scaling of the fidelity susceptibility,

$$\chi_F = \lim_{\delta U \to 0} \frac{-2 \log |\langle \psi(U+\delta U) | \psi(U) \rangle|}{\delta U^2}, \tag{4.17}$$

which provides an alternative confirmation of the existence of a quantum phase transition. This quantity is super-extensive at the critical point [GU10], allowing to extract its location by extrapolating the position of the peak to the thermodynamic limit, $L \to \infty$ (inset). Since the TBOW phase cannot be adiabatically connected to the non-interacting boson limit ($U = 0$), it can be regarded as an interaction-induced symmetry-broken topological phase, where the interplay between strong correlations and spontaneous symmetry breaking is crucial to stabilize the SPT phase.

4.3 TBOW at fractional fillings

In this section, we study the intertwined topological phases that appear at various bosonic densities other than half filling. In particular, at one-third and two-third filling, and for sufficiently-strong interactions, we find a period-3 BOW with a three-fold degenerate ground state that displays a non-zero Berry phase. We show that inversion symmetry emerges from the larger SSB landscape of a bosonic Peierls' mechanism, protecting the intertwined topological BOW, and making it fundamentally different from other non-topological BOWs (Fig. 4.8). We unveil a rich phase diagram with first- and second-order quantum phase transitions caused by the interplay of this emergent symmetry, topology and strong correlations. We also identify a dynamical manifestation of the underlying topology that is genuinely rooted in strong correlations and the interplay of the emergent and symmetry-broken symmetries: a self-adjusted fractional pump. As discussed by Thouless et *al.* [Tho83, NT84], the quantization of adiabatic charge transport in weakly-interacting insulators uncovers a profound connection to higher-dimensional topological phases, as recently exploited in cold-atom experiments [NTT+16, LSZ+16]. Strong interactions can lead to fractional pumped charges [MCO15, TCR+17], showing a clear reminiscence to the fractional quantum Hall effect (FQHE) [TT83, BK08, GSF12, BA13]. We show that, following a dynamical modulation of the interactions in the $\mathbb{Z}_2$-Bose-Hubbard model, the system self-adjusts within the landscape of SSB sectors, allowing for a cyclic path that displays a fractional pumped charge 1/3, such that the correlated intertwined topological phase has no free-particle counterpart.

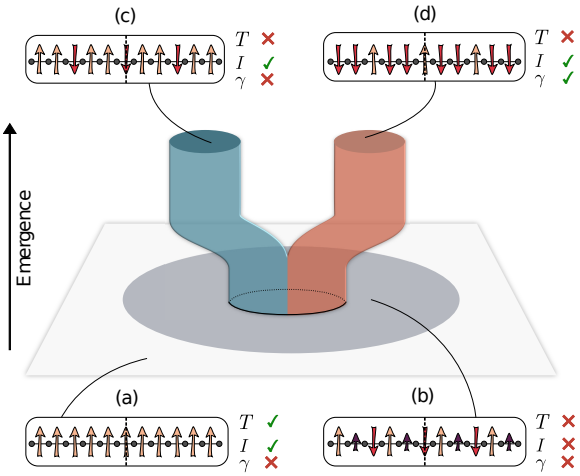

Fig. 4.8 Emergent symmetry protection: We represent qualitatively a ground state manifold where different quantum phases are characterized by their symmetry and topological properties, and use spin patterns on the bonds of a 1D lattice to exemplify the different configurations. (a) Ground state satisfying both translation (T) and inversion (I) symmetry, but lacking any non-zero topological invariant (γ). The spontaneous breaking of translation symmetry results in a phase with a three-site unit cell, represented in (b) with different arrows accounting for the three possible magnetizations, which may not respect the inversion symmetry, lacking a non-zero topological invariant. Remarkably, such inversion symmetry can emerge from all the possible configurations constrained by the SSB pattern, leading to the low-energy sectors depicted in (c, d). Note that these two phases are not only distinguished by the SSB pattern but also, and more importantly, by topology. Accordingly, whereas (c) is topologically trivial, (d) presents both a local order parameter and a non-zero topological invariant, and thus corresponds to an intertwined topological phase where the protecting symmetry emerges.

4.3.1 Emergent symmetry protection

We fix the bosonic density to $\rho = 2/3$ (similar results appear for $\rho = 1/3$). As we showed in chapter 3, for $\Delta \ll t$ and $\Delta \gg t$ the spins are uniformly polarized in the z direction, $\langle \sigma^z_{i,i+1} \rangle = \sigma_0$, with $\sigma_0 > 0$ and $\sigma_0 < 0$, respectively. For intermediate values, a Peierls-type SSB leads to a trimerization of the $\mathbb{Z}_2$ fields, namely a periodic repetition of a 3-site unit cell with bonds characterized by arbitrary expectation values $\langle \sigma^z_{1,2} \rangle, \langle \sigma^z_{2,3} \rangle, \langle \sigma^z_{3,4} \rangle$. The resulting phase is an insulator, with a gap that increases with the value of the coupling α. Note that this trimerization still leaves freedom for various bond configurations that do not necessarily imply a protecting symmetry for the bosons (Fig. 4.8(b)). One of the main results described in this section is to show how, for certain parameter regimes, such a protecting symmetry

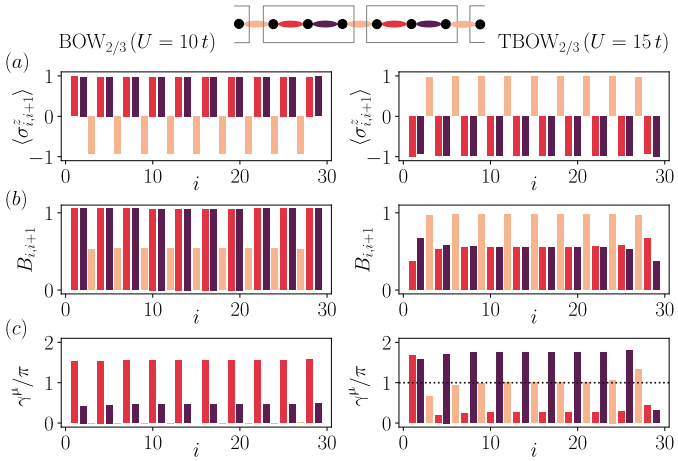

Fig. 4.9 Simultaneous orders in intertwined topological phases: Real-space configuration of (a) the $\mathbb{Z}_2$ field $\langle \sigma^z_{i,i+1} \rangle$ and (b) the bosonic bond-densities $B_{i,i+1} = \langle b^\dagger_i b_{i+1} \rangle + \text{c.c.}$, using different colours for each element of the unit cell at $\beta = 0.01\,t$. Different permutations within the unit cell lead to a 3-fold quasi-degenerate ground state, each obtained from one another by translating the modulation patterns of the ferrimagnetic and BOW orders. The quasi-degeneracy comes from the finite-size effects, but degeneracy is recovered in the thermodynamic limit. (c) The local Berry phases γ^μ display a quantized value of 0 ($U = 10\,t$) or π ($U = 15\,t$) on the bonds preserving the inversion symmetry of the unit cell, allowing us to distinguish between the trivial and topological BOW phases. We note that the topological BOW phase (right panels) does not have a fermionic analogue [GC15] in the ground state of the SSH model [SS81, Su83], which instead realizes the trivial BOW (left panels) for energetic reasons.

becomes effective at low energies, whereas higher-energy excitations of the $\mathbb{Z}_2$ fields do not necessarily lead to it. Therefore, the inversion symmetry can be understood as an emergent symmetry that is crucial to protect the intertwined TBOW$_{2/3}$ (Fig. 4.8(d)). In the following, we set $\alpha = 0.5t$ and $\Delta = 0.85t$.

We first study a system of $L = 30$ with sites and open boundary conditions using DMRG [HP18][1], for $\beta = 0.01\,t$ and different Hubbard interactions U. For weak interactions ($U \lessapprox 9t$), the $\mathbb{Z}_2$ field is polarized along the same axis (Fig. 4.8(a)), and the bosons display a quasi-superfluid behavior with algebraically decaying off-diagonal correlations. Increasing the interactions leads to a bosonic Peierls transition, whereby translational symmetry is spontaneously bro-

[1] For the finite-size calculations we used a matrix product state (MPS) based algorithm with bond dimension D = 100. To directly access the thermodynamic limit we used an infinite MPS (iMPS) with a repeating unit cell composed of three sites and D = 150. The Hilbert space of the bosons is truncated to a maximum number of bosons per site of $n_0 = 2$.

ken, leading to a three-fold degenerate ground-state with ferrimagnetic-type ordering $\langle\sigma^z_{1,2}\rangle = \langle\sigma^z_{2,3}\rangle > \langle\sigma^z_{3,4}\rangle$, together with a bosonic period-3 BOW that displays inversion symmetry with respect to the central inter-cell bond (see Fig. 4.9(a,b), left panel). The BOW phase describes here exhibits similar properties to the charge density waves in extended Hubbard models [GSF12, BA13], albeit without the need of longer-range interactions. We note that a fermionic counterpart of this phase has been predicted in charge-transfer salts [SS81, Su83]. To characterize its topology, we use again the local Berry phase $\gamma^\mu = \mathrm{i}\int_0^{2\pi} \mathrm{d}\theta\langle\psi^\mu(\theta)|\partial_\theta\psi^\mu(\theta)\rangle$, where $|\psi^\mu_\theta\rangle$ is the μ-th ground state of the Hamiltonian (5.11) with a single bond twisted according to $t \to t\mathrm{e}^{\mathrm{i}\theta}$ [Hat06]. The left panel of Fig. 4.9(c) depicts the local Berry phase for one of the ground states, which clearly vanishes on the inter-cell bonds relevant for the inversion symmetry of Fig. 4.8. We note that the three possible ground states become degenerate in the thermodynamic limit, which can be characterized by the total Berry phase $\gamma = \sum_\mu \gamma^\mu$. In this limit, the value of γ^μ for the three degenerate states on a fixed bond coincides, up to permutations, with the value of this quantity on the three bonds of the unit cell for each one of the states. Therefore, the sum gives the same value in both cases. For the present $\mathrm{BOW}_{2/3}$, we find $\gamma = 0$, indicating that this phase is topologically trivial.

By further increasing the interactions, a phase with a different SSB pattern $\langle\sigma^z_{1,2}\rangle = \langle\sigma^z_{2,3}\rangle < \langle\sigma^z_{3,4}\rangle$ arises (right panels Fig. 4.9(a,b)). Although the ferrimagnetic and BOW patterns look rather similar to the previous case, the local Berry phase at the inter-cell bonds is now quantized to $\gamma_\mu = \pi$ (right panel Fig. 4.9(c)). Note again that this phase presents three degenerate ground states in the thermodynamic limit, and we find a total Berry phase $\gamma = \pi$, indicating a non-trivial $\mathrm{TBOW}_{2/3}$ phase. This exemplifies the scenario of Fig. 4.8: from all the trimerized configurations possible a priori, the system chooses one with additional bond-centered inversion symmetry, allowing for a topological crystalline insulator [CTSR16]. In combination with the local order parameters (right panel Fig. 4.9(a,b)), this shows that the $\mathrm{TBOW}_{2/3}$ is an interaction-induced intertwined topological phase in which, contrary to the half-filled case described in the last section, the protecting symmetry is emergent and not fixed a priori by the SSB pattern. The occurrence of this mechanism is a hallmark of our $\mathbb{Z}_2$-Bose-Hubbard model and does not have an analogue in the standard SSH model [SS81, Su83].

4.3.2 Interaction-induced topological phase transitions

Topological phase transitions delimiting free-fermion SPT phases, and those found due to their competition with SSB phases, are typically continuous second-order phase transitions. In the presence of strong correlations, however, first-order topological phase transitions may arise [ABC+15, RGS16, JcvacAB17, BSB19]. We now discuss how critical lines of different orders delimit the intertwined $\mathrm{TBOW}_{2/3}$ in a strongly-interacting region of parameter space, showing that the $\mathrm{TBOW}_{2/3}$

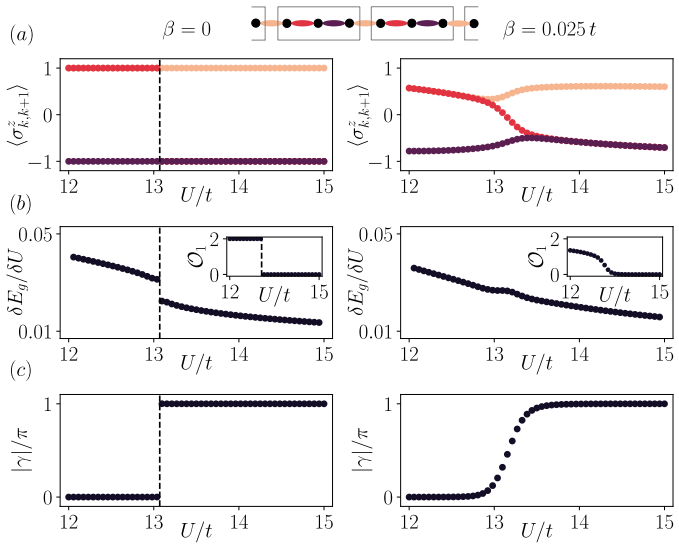

Fig. 4.10 Interaction-induced topological phase transitions: (a) Unit-cell fields $\langle\sigma^z_{k,k+1}\rangle$ as we increase U, where $k \in \{1,2,3\}$ are the three different bonds. The left and right panels correspond to $\beta = 0$ and $\beta = 0.025t$, respectively. In the first case, there is an abrupt transition between the trivial and topological BOW. In the second case, the transition is continuous, and we find a finite region where inversion symmetry is broken. (b) First derivative of the ground-state energy per unit cell E_g through the transition. For $\beta = 0$ there is a discontinuous jump, signaling a first-order topological phase transition. The inset shows also a jump in the observable $\mathcal{O}_1$. For $\beta = 0.025t$, both quantities behave smoothly. (c) Total berry phase, where the same behaviour is observed. The results shown are obtained directly in the thermodynamic limit using iDMRG.

cannot be adiabatically connected to a free-boson SPT phase.

In the completely adiabatic regime $\beta = 0$, we observe that the transition between trivial $\mathrm{BOW}_{2/3}$ and intertwined $\mathrm{TBOW}_{2/3}$ is of first order using an infinite DMRG algorithm (iDMRG) [HP18]. Figure 4.10(a) shows the Ising fields $\langle\sigma^z_{k,k+1}\rangle$ within the unit cell as the Hubbard interaction is increased, while keeping β fixed. For $\beta = 0$ (left column) we observe an abrupt transition characterized by a discontinuity in the first derivative of the ground state energy $\delta E_\mathrm{g}/\delta U = (E_\mathrm{g}(U + \Delta U) - E_\mathrm{g}(U))/\Delta U$ [RGS16], signaling a first-order phase transition (Fig. 4.10(b)). Introducing the bond observables,

$$\mathcal{O}_k = \langle E_\mathrm{g}|\, \sigma^z_{k,k+1} - \sigma^z_{k+1,k+2}\, |E_\mathrm{g}\rangle \tag{4.18}$$

with k even or odd, we can characterize the corresponding bond-inversion symmetry within the unit cell. The inset of Fig. 4.10(b) shows how $\mathcal{O}_1$ displays a discontinuous

jump. The total Berry phase, computed here with the help of the entanglement spectrum [ZMP14], also changes abruptly, as depicted in Fig. 4.10(c). To the best of our knowledge, this is the first topological characterization of a first-order phase transition in an intertwined topological phase.

The situation changes as one departs from the adiabatic regime. Figure 4.10 (right panel) shows a continuous second-order transition both in $\delta E_{\mathrm{g}}/\delta U$ and in $\mathcal{O}_1$ for $\beta = 0.025t$. Remarkably, there is a finite region between the trivial and topological BOW phases where the $\mathbb{Z}_2$ fields have different expectation values, breaking the emergent inversion symmetry within the larger Peierls' trimerization. These results are in accordance with the behaviour of the total Berry phase in Fig. 4.10(c), which shows a non-quantized value in this intermediate asymmetrical region. In fact, the appearance of this region originates from a very interesting interplay between the emergent inversion symmetry and the Peierls SSB phenomenon: a direct continuous transition between the trivial and topological BOWs would require a gap closing point in the bosonic sector, where every bond had the same expectation value and the BOW would disappear. However, this comes with an energy penalty, since the Peierls' mechanism favors the formation of a 3-site unit cell [GCGDL18]. Therefore, the system energetically prefers to keep the trimerized unit cell at the expense of breaking the bond-inversion symmetry within the unit cell, and continuously setting the emergent inversion symmetry responsible for the quantized Berry phase $\gamma = \pi$ of Fig. 4.10(c). This non-trivial interplay between symmetry protection and symmetry breaking, driven solely by correlations, is another hallmark of our $\mathbb{Z}_2$-Bose-Hubbard model, absent at other fillings or in the fermionic SSH model [SS81, Su83]. The intermediate phase could extend up to $\beta = 0$, although first-order transitions are also possible for low enough values of β. An extended numerical analysis would be required to distinguish between these two situations.

It is interesting to note that, although the ground state of the system preserves a trimerized unit cell to satisfy the underlying Peierls mechanism and minimize its energy, the gap of the system does indeed close in this intermediate region, which guarantees that the $\mathrm{TBOW}_{2/3}$ is a well-defined phase that cannot be adiabatically connected to the trivial $\mathrm{BOW}_{2/3}$. In order to show the occurrence of such a gap closure, we use entanglement spectroscopy in the thermodynamic limit.

Fig. 4.11 shows the scaling of the entanglement entropy $S(\rho_\ell) = -\mathrm{Tr}\{\rho_\ell \log(\rho_\ell)\}$, where ρ_ℓ is the reduced density matrix for a bipartition of the ground state into two blocks. This entanglement entropy is expressed in terms of the infinite matrix-product state (iMPS) correlation function ξ [TdOIL08] for different values of the bond dimension D and for different Hubbard interactions U, where we set $\beta = 0.03t$. If the ground state is gapped, this entropy saturates [TdOIL08]. On the contrary, in a gapless critical point/region, the following scaling relation holds

$$S = \frac{c}{6} \log \xi, \tag{4.19}$$

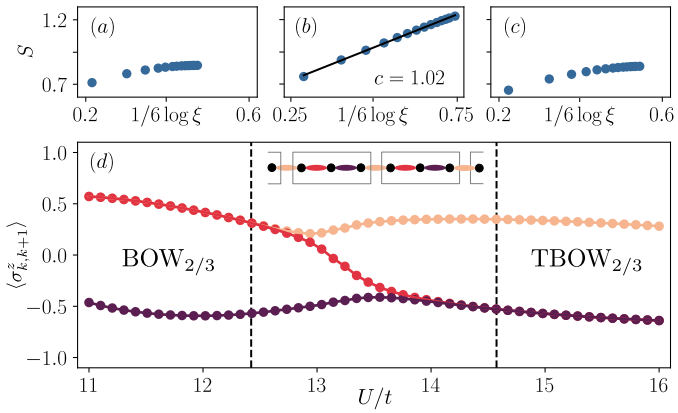

Fig. 4.11 Entropy scaling: In (a), (b) and (c) we show the entanglement entropy S for an iMPS as a function of the correlation length ξ for a state in the $\mathrm{BOW}_{2/3}$, intermediate region and $\mathrm{TBOW}_{2/3}$, respectively. In the BOW phases, the entropy saturates, signaling a gapped ground state. In the intermediate region, the scaling is logarithmic. Different points are calculated using different bond dimensions D, and we set $\beta = 0.03t$. (d) Evolution of the $\mathbb{Z}_2$ field on the bonds of the unit cell $\langle\sigma^z_{k,k+1}\rangle$, with $k \in \{1,2,3\}$ in terms of U. The calculations were performed using an iMPS with fixed bond dimension of $D = 150$. The three different phases are separated qualitatively by two dotted lines.

for sufficiently large ξ. To capture this saturation or the logarithmic scaling, instead of performing a finite-size scaling, one may conduct a finite-D scaling, which shows how both $\mathrm{BOW}_{2/3}$ (Fig. 4.11(a)) and $\mathrm{TBOW}_{2/3}$ are gapped (Fig. 4.11(c)). In the intermediate symmetry-broken region, we find instead a logarithmic scaling of the entanglement entropy consistent with a conformal charge $c = 1$ (Fig. 4.11(b)). Accordingly, we can conclude that both phases cannot be adiabatically connected, neither at weak nor at stronger transverse fields.

Finally, we present the phase diagram as a function of β and U in Fig. 6.8(a) by depicting the product of $\mathcal{O}_1\mathcal{O}_2$: it can only attain a non-zero value if the bond inversion symmetry within the unit cell is broken (i.e. if the transition occurs continuously via an intermediate non-symmetric region). Figure. 6.8(b) shows the phase diagram in terms of the total Berry phase, quantized to 0 and π in the regions with inversion symmetry and with non quantized values in the region where the symmetry is broken.

4.3.3 Self-adjusted fractional pumping

As we introduced in chapter 1, topology can also become manifest through dynamical effects, such as the quantized transport of charge in electronic systems evolv-

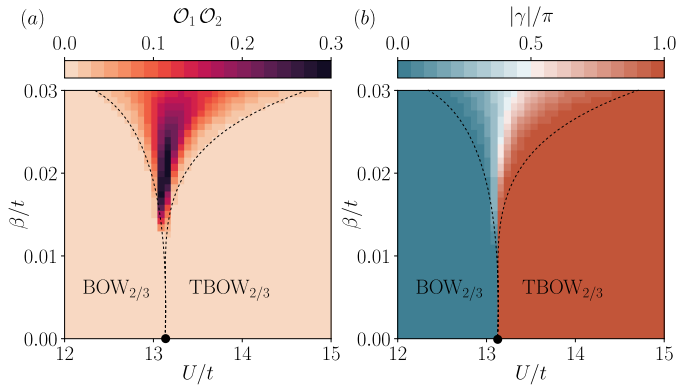

Fig. 4.12 Phase diagram: (a) In the background, we represent the product of observables $\mathcal{O}_1\mathcal{O}_2$, which has a non-zero value only in the intermediate phase where bond-inversion symmetry is broken. The black dot marks the first-order critical point separating the BOW$_{2/3}$ and TBOW$_{2/3}$ phases at $\beta = 0$. The dotted lines qualitatively denotes the critical lines for $\beta > 0$. For large values of this parameter, we find an intermediate phase where the bond-inversion symmetry is broken. This phase is separated from the BOW$_{2/3}$ and TBOW$_{2/3}$ phases by continuous transitions. This situation might extend up to $\beta = 0$, although first order transitions are also possible for small but not-zero values of β. (b) We also present the total berry phase. The latter has a non-quantized value in the region where the protecting inversion symmetry is broken. The phase diagram is calculated in the thermodynamic limit using iDMRG.

ing under cyclic adiabatic modulations, the so-called Thouless pumping [Tho83]. This topological pumping lies at the heart of our current understanding of free-fermion SPT phases [QZ11], and can also be generalized to weakly-interacting systems [NT84]. Moreover, 1D and quasi-1D systems at sufficiently-strong interactions can exhibit a fractional pumping [**?**, GMZP15, ZWZ15, ZZS16, LF17, TCR+17] that cannot be accounted for using non-interacting topological pumping.

Here we show that adiabatic dynamics traversing through intertwined topological phases allows for a self-adjusted fractional pumping, due to the interplay of the SSB mechanism and other gap-opening perturbations. By introducing guiding fields that only act on a subset of the $\mathbb{Z}_2$ fields, and raising/lowering the Hubbard interactions, the free $\mathbb{Z}_2$ fields self-adjust dynamically during the adiabatic cycle. As a consequence, the bosonic sector traverses a sequence of ground states that are energetically favorable due to the Peierls' mechanism. In this way, the system self-adjusts along this adiabatic sequence, allowing for an exotic fractional pumping induced by interactions [GH14, GMZP15, ZWZ15, ZZS16, LF17, TCR+17]. The details of this self-adjusted topological pumping are explained in Figure 4.13.

For finite systems, the pumped charge can be inferred from the center of mass

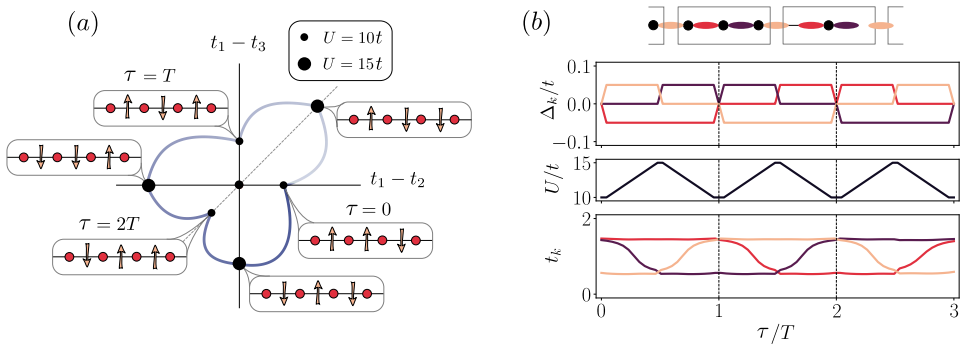

Fig. 4.13 Self-adjusted pumping protocol: (a) The trivial and topological BOW phases are three-fold degenerate each. The six different states are represented here as different points on an effective parameter space characterized by the expectation values of the bond fields $t_k = 1 + \alpha/t\langle\sigma^z_{k,k+1}\rangle$, with $k \in \{1, 2, 3\}$. To define an adiabatic cycle through these different BOWs, the protecting inversion symmetry must be broken at intermediate states in order to enclose the degeneracy point at $t_1 = t_2 = t_3$. (b) The Peierls mechanism forces the system to break this symmetry spontaneously when interactions are increased, connecting states in the trivial and topological BOW phases (Fig. 4.10(b)). In order to select which state from the degenerate manifold the system will transition to, we introduce an external inhomogeneous $\mathbb{Z}_2$ field Δ_k that is only applied to a subset bonds within the unit cell. The fields partially break the degeneracy of the BOWs, and restrict the possible adiabatic evolution. A sequential combination of local fields and interaction-driven self-adjustments allows the system to cycle around the degeneracy point in the effective parameter space. Note that the protocol must be repeated three times for the ground state to reach the initial configuration.

(COM) $P_L(\tau) = \frac{1}{L}\sum_j (j - j_0)\,\langle\Psi(\tau)|\,\hat{n}_j\,|\Psi(\tau)\rangle$, where j_0 is the center of a chain of size L, and $|\psi(\tau)\rangle$ is the adiabatically-evolved state at time τ. Figure 4.14 shows the DMRG results describing how the COM changes along the cycle connecting the $\text{BOW}_{2/3}$ and $\text{TBOW}_{2/3}$ possible ground states for a finite chain of size $L = 90$. After $\tau = T$, we observe a COM displacement of $\Delta n^T_{L=90} = P_{L=90}(T) - P_{L=90}(0) = 0.316$, reflecting the fractional charge. To obtain precisely the charge, we perform a finite-size scaling analysis and find $\Delta n^T_\infty = \lim_{L\to\infty} \Delta n^T_L = 1/3$ (inset). At $\tau = 2T$, the COM displacement reaches a value consistent with 2/3 in the thermodynamic limit. We note that these fractional values are characteristic of a strongly-correlated SPT phase with ground state degeneracy, and cannot be found for any non-interacting topological phase. In our present case, the adiabatic path in parameter space can be understood as a dynamical analogue of the spatial interpolation between the different ground states, which leads to topological solitons and fractionally-quantized charges bound to them [SS81]. During each period T, we interpolate between two such ground states, and a fractional charge is pumped

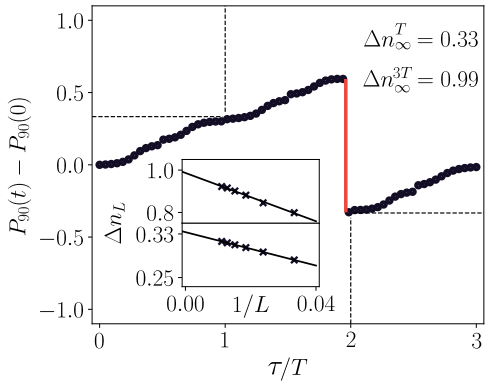

Fig. 4.14 Fractional pumping: Center of mass $P_L(t)$ through the cycle for a finite chain of size $L = 90$ and for $\beta = 0.025t$. The discontinuous jump (red), related to the presence of edge states, allows us to obtain the total charge transported in the bulk during one cycle, $\Delta n_{L=90} = 0.92$. Inset: finite-size scaling yields a transported fractional charge at $\tau = T$, and an integer charge at the end of the adiabatic path ($\tau = 3T$).

without creating any spatial solitonic profile.

Let us now turn our attention to the discontinuous jump of the pumped charge towards $-1/3$, as this is related to the presence of many-body edge states for a finite system [HF16], and can be used to define a bulk-boundary correspondence for our intertwined $\text{TBOW}_{2/3}$. The transported charge across the bulk, Δn_L^{3T}, can be related to the discontinuous jumps during the cycle [HF16], namely $\Delta n_L^{3T} = -\sum_i \Delta P_L(\tau_i)$, where $\Delta P_L(\tau_i) = P_L(\tau_i^+) - P_L(\tau_i^-)$ quantify the discontinuities occurring at instants τ_i, and $\tau_i^\pm = \tau_i \pm \epsilon$ with $\epsilon \to 0$. In the thermodynamic limit, it converges to the quantized value of the pumped charge $\Delta n_\infty^{3T} = \lim_{L\to\infty} \Delta n_L^{3T} = 1$ related to the integer Chern number in an extended 2D system [HF16]. Since these discontinuities depend on the presence of edge states in a finite system, the center-of-mass approach establishes a sort of bulk-boundary correspondence that can be explicitly proven via the adiabatic pumping. Moreover, the COM can be measured in cold-atomic experiments [WTD13], and it has been used to reveal the topological properties of fermionic and bosonic SPT phases [NTT+16, LSZ+16].

By estimating the discontinuity, we can extract the transported charge across the bulk during the whole adiabatic evolution that bring the BOW back to itself after $\tau = 3T$, obtaining a nearly quantized value $\Delta n_{L=90} = 0.92$. As it is shown in the inset, a truly quantized charge is recovered in the thermodynamic limit, signaling the topological nature of the system. These results allow us to establish a bulk-boundary correspondence in the pumping process [HF16], even though this was not guaranteed a priori due to the lack of the global symmetries regarding the ten-fold classification of topological insulators. In particular, one may understand

the edge states of the $\mathrm{TBOW}_{2/3}$ as remains of topologically-protected conducting edge states of an extended 2D system, as we will see now. We note that, even if the topological degeneracy point does not appear in the phase diagram of the model, the quantized transported charge reveals its presence in an effective parameter space, as a non-zero quantized charge can only be obtained when the parameter modulation encircles such a degeneracy point [BLA11].

Effective single-particle pumping

Before finishing this section, we clarify different aspects of the pumping scheme introduced above using an effective non-interacting model. We show that, whereas some qualitative features of the topological pumping in the $\mathbb{Z}_2$ Bose-Hubbard model can be understood through a non-interacting analogue, the very fractional nature lacks a non-interacting simile, and must be consider as a direct manifestation of the strongly-correlated nature of the $\mathrm{TBOW}_{2/3}$. To see this consider the following non-interacting Hamiltonian,

$$\hat{H}_{\mathrm{eff}} = -\sum_i t_i \left(\hat{c}_i^\dagger \hat{c}_{i+1} + \mathrm{H.c.} \right) \tag{4.20}$$

where $\hat{c}_i$ and $\hat{c}_i^\dagger$ are fermionic operators. $\hat{H}_{\mathrm{eff}}$ is related to the hard-core boson limit of the $\mathbb{Z}_2$BHM, with $U \to \infty$, and a totally adiabatic or classical $\mathbb{Z}_2$ fields ($\beta = 0$) that are treated in a mean-field-like manner. Accordingly, one may consider that the expectation values $\langle \hat{\sigma}^z_{i,i+1} \rangle$ behave as external parameters that can be used to control the effective tunneling coefficients, $t_i = 1 + \alpha/t \langle \hat{\sigma}^z_{i,i+1} \rangle$.

However, we note that in this simplified effective model, the tunnelings $\{t_i\}$ are free model parameters that can be changed adiabatically at will. In particular, the effective tunneling strengths are changed following the same path as for the interacting case (Fig. 4.13**(b)**). Note that the expectation values $\langle \hat{\sigma}^z_{i,i+1} \rangle$ extracted from the ground states throughout the self-adjusted many-body pumping are different in general for different unit cells. Being non-interacting, the Hamiltonian (4.20) can be exactly diagonalized, and the band structure can be obtained at any instant of the adiabatic cycle. This calculation leads to the spectral flow shown in Figure 4.15(a). Throughout the cycle, the instantaneous energy levels can be arranged into three different bands separated by two gaps that remain finite through the whole adiabatic path. Note also that these spectral bands are connected by two in-gap modes, which correspond to the localized single-particle edge states crossing at some intermediate instant of the cycle. Let us highlight that, in contrast to the adiabatic path of the full interacting model that is composed of three adiabatic cycles, the non-interacting case consists of a single cycle where the effective tunnelings are periodically modulated.

Fig. 4.15(b) shows the change in time of the center or mass (COM) $P_L(\tau)$ for densities $\rho = 1/3$ and $\rho = 2/3$, i.e. when the lowest or the two lowest bands

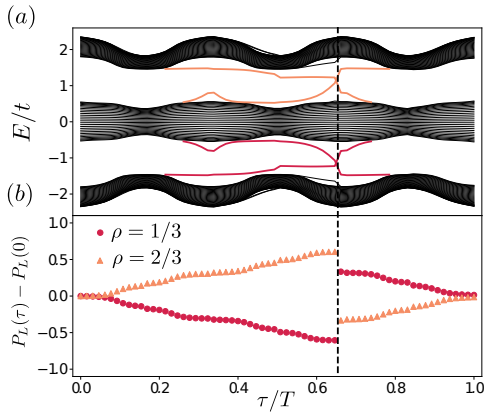

Fig. 4.15 Effective pumping: (a) spectral flow during the adiabatic cycle. At each time τ we draw the energy levels by diagonalizing the non-interacting effective Hamiltonian (4.20). We observe three distinct bands that remain open during the cycle. There are two energy levels corresponding to the localized edge states inside each band gap. These states connect the different bands and cannot be adiabatically removed without closing the gap. (b) Change in the center of mass during the cycle for densities $\rho = 1/3$ and $\rho = 2/3$. A discontinuous jump occurs when the edge states in (a) cross in energy.

are filled, respectively. We consider a finite chain of size $L = 90$, and show that in both cases a discontinuous jump occurs when the corresponding edge states cross in energy, where the COM changes by 1 or -1. For $\rho = 1/3$, before this instant of time only the left edge state is occupied, while it gets empty and the right edge state gets occupied right after it. This shows the fractionalization of the edge states: if each possesses a particle number of $1/2$, this process changes the COM by $-(-1/2) + (1/2) = 1$. For $\rho = 2/3$, the opposite process takes place. From this discussion it is clear the role that the fractionalization of the edge states plays during the pumping. This pumping appears in both interacting and non-interacting systems and has topological origin. However, as described below, the factional pumping can only appear in interacting systems and is related to the degeneracy of the ground state. In those situations the fractionalization of the pumping is a different effect that goes beyond the fractionalization of the charge of the edge states.

As explained above, we can calculate the transported charge in the bulk from the change in the COM at the discontinuous jumps. We obtain $\Delta n^{1/3}_{L=90} = -0.94$ and $\Delta n^{1/3}_{L=90} = 0.94$. The fact that these are not totally quantized is due to finite-size effects, and they would converge to strictly quantized values in the thermodynamic limit. We thus see that this effective model allows for a net transport of a single quantum of charge across the bulk, either from the left edge to the right one, or vice

versa. Note however that the period T of this single-particle cycle corresponds to the three consecutive cycles $3T$ of the many-body pumping described in Fig. 4.13. Therefore, the integer nature of the pumped single-particle charge after one cycle is consistent with the integer value of the pumped many-body charge after three cycles.

As noted in chapter 1, the transported charge in an infinite chain over one period, Δn, gives access to topological phases in higher dimensions. In this case, the pumped charge can be related to the Chern number of an extended two-dimensional system, where time is taken as a synthetic dimension (1.33). We can calculate the associated Chern number for the effective model (4.20) in the thermodynamic limit using the efficient numerical method [FHS05], obtaining $c_1 = 1$ and $c_2 = -2$ for the first and second bands, respectively. Using Eq. (1.33), we obtain the respective charges, $\Delta n^{1/3} = -1$ and $\Delta n^{2/3} = 1$.

This quantized pumping allows to shed light on the origin of the edge states of the trimerized configuration. In contrast to the dimerized half-filling model, the topological origin of the single-particle edge states in this case is not guaranteed a priori due to the lack of chiral/sub-lattice symmetry [RH02]. However, they can be understood as remains of edge states in the extended two-dimensional system, which are indeed topologically protected even in the absence of chiral symmetry [**?**]. This is clear from the spectral flow represented in Fig. 4.15(a), which can be seen as the band structure of a two-dimensional system in a cylindrical geometry [KLR+12]. There, the edge states connect the bands separated by a gap, and this means that they cannot disappear under perturbations that do not close the gap. Although this spectral flow can not be computed in the interacting case, we expect the argument to hold based on the quantization of the pumped charge, and the extension of Eq. (1.33) for many-body systems [NT84]. Therefore, the observation of the integer pumped charge in the $\mathbb{Z}_2$-Bose-Hubbard model can be used as a bulk-boundary correspondence that clarifies the topological origin of the many-body edge states.

A crucial difference between the many-body self-adjusted pumping presented above and the effective pumping described here is that, for the latter, the robust fractionalization of the pumped charge is absent. The main reason behind this is that the ground state of the effective Hamiltonian (4.20) is not degenerate in the topological phase. Therefore, the adiabatic path can not be decomposed in three independent periodic cycles as in the protocol presented in the main text. As a consequence the transported charge after a time $T/3$ is not necessarily quantized to 1/3, only the total charge transported at T is quantized to 1. This can be seen clearly in Figure 4.16. There, we present two adiabatic pumping cycles, connected by a local deformation. Even if in the first case the transported charge might seem to be fractional quantized for fractions of the period, we observe how this fractionalization is lost in the second deformed cycle. Since the latter is just an adiabatic deformation of the first one, we conclude that the fractional charge is not topologically protected. This is different in the many-body pumping presented in

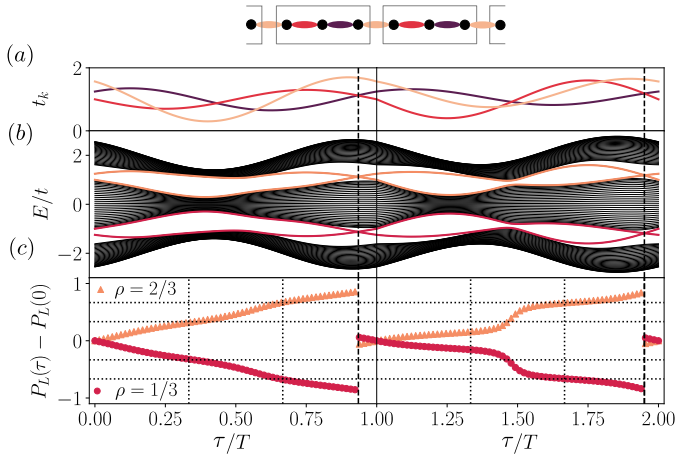

Fig. 4.16 Loss of fractionalization: (a) Change in the unit-cell tunneling t_k during two pumping cycles which are equal up to an adiabatic deformation. (b) Spectral flow for each cycle. (c) Change in the center of mass during the two cycles. Even if for the first case the transported charge at fractions of the cycle might seem quantized, the second case shows that this is not necessary the case.

the main text: since the total adiabatic path is decomposed in three closed cycles, any adiabatic deformation would preserve the nature of the pumping, which is robust and quantized to fractional values .

4.4 Summary

In this chapter, we have characterized the TBOW phases that appears in the $\mathbb{Z}_2$BHM at various bosonic densities. At half filling, and by focusing first on the hardcore boson limit, we showed how, for a quasi-adiabatic field, the system undergoes a spontaneous breaking of the translational symmetry. This can be regarded as a Peierls transition, where the staggerization of the field opens a gap in the single-particle fermionic spectrum. Using the Zak phase, we characterized this gapped phase as an SPT phase protected by chiral symmetry, where the topological effects coexist with the presence of long-range order. For finite Hubbard interactions, chiral symmetry is broken, but the phase is still protected by a bond-centered inversion symmetry. Moreover, the spontaneous symmetry breaking remains, even though the standard Peierls mechanism cannot be directly applied in the bosonic case. The TBOW phase extends, therefore, for strong but finite Hubbard interactions. We confirmed numerically our predictions using DMRG. By characterizing the quantum phase transition between the TBOW and a qSF phase for low in-

teractions, we have established the importance of strong correlations to stabilize the former. Our results allow us to regard this phase as an interaction-induced intertwined topological insulator.

After that we showed how symmetry protection can emerge through an interplay between symmetry breaking and strong correlations, giving rise to intertwined topological phase for certain fractional fillings. The unique properties of these phases are manifest in the special static and dynamical features we discussed, such as interaction-induced topological phase transitions and a self-adjusted fractional pumping. The latter, in particular, could be used to reveal the topological properties of the system and its fractional nature in cold-atom experiments.

Chapter 5

Fractionalized ultracold matter

5.1 Introduction: symmetry-protected topological defects

Topological defects were introduced in chapter 1 as non-perturbative solutions of the Schrödinger equation that are topologically distinct from the vacuum, which is usually characterized by a set of broken symmetries. This interplay between symmetry and topology can give rise, in particular, to soliton configurations in 1D after a SSB phase transition. Solitons can be seen as relics of the original disordered phase that distort the symmetry-broken ground state around a certain core/center where the order parameter vanishes. Moreover, the winding of the order parameter around such defect cores yields a topological invariant, underlying the topological characterization of such defects. These winding numbers can only change via non-local deformations, guaranteeing the robustness of the soliton to physical, primarily local, perturbations [Mer79]. Let us remark that topological solitons are finite-energy non-perturbative solutions of classical field equations. Despite the fact that they can be quantized formally [Jac77], the interesting interplay of symmetry and topology is, in this case, a classical feature.

Genuine quantum effects can become manifest when these solitons interact with quantum matter. As we mentioned in chapter 3, topological solitons can bind quasi-particles with a fractional numbers and exotic quantum statistics. This phenomenon was first predicted in relativistic quantum field theories [JR76, JR81] and, independently, in linear polymers [SSH79] and p-wave superconductors [RG00]. As such, these *bound fractionalized quasi-particles* cannot be adiabatically connected to the original particle content of the theory, as typically occurs in more standard situations such as Fermi liquids [Lan56] or, more generally, perturbatively-renormalized quantum field theories [WK74]. Let us note that, in contrast to the topological soli-

ton, these quasi-particles are not necessarily protected by any quantized topological invariant.

With the advent of topological insulators [KM05, BHZ06, KWB+07, HQW+08], however, a quantum-mechanical protection mechanism has been unveiled [TK10], giving rise to the concept of *symmetry-protected topological defects* (SPT-d). Under certain symmetry constraints, the characterization of the bulk gapped matter comprised in between two of these solitons requires yet another topological invariant. In this case, the relevant topological invariant is no longer the winding number of a classical field, such as the order parameter, but is instead determined by the Berry connection of the matter sector via the quantum-mechanical wavefunction. We note that these invariants are quantized and cannot change under external symmetry-preserving perturbations, unless these perturbations suffice to close the bulk energy gap, inducing a quantum phase transition where the protecting symmetry is spontaneously broken. Moreover, the so-called bulk-defect correspondence connects this bulk topological invariant to the fractional quasi-particles bound to the defect, and justifies the protection of these quasi-particles with respect to symmetry-preserving perturbations.

The current theory of SPT-d typically assumes a background solitonic profile that is static and externally fixed, focusing on the properties of the matter sector and the robustness of the bound quasi-particles [TH17]. This simplifies the description, as one deals with non-interacting matter in an inhomogeneous classical background, allowing one to identify the mechanism responsible for their protection, and even to classify all possible SPT-d according to the underlying global/crystalline symmetries [CTSR16], as we introduced in chapter 1. Let us emphasize that, in this limit, there is no intrinsic soliton dynamics, nor any SSB order parameter that would justify the topological protection of the soliton. Therefore, by assuming/engineering such externally-adjusted solitonic profiles, one is missing half of the topological robustness of the SPT-d. Moreover, from a fundamental point of view, this approach misses a key property: SPT-d can only arise in intertwined topological phases, which simultaneously display SSB and topological symmetry protection. Although one typically finds claims in the literature about the absence of any local order parameter characterizing the SPT-d, the reality is that the matter sector can also display long-range order as a consequence of the SSB, as we showed in chapter 4. It is the possibility of simultaneously encompassing both SSB long-range order and topological symmetry protection, which makes these intertwined SPT-d so exotic and interesting. This ambivalent role of symmetry is a consequence of interactions and, by exploring the full non-perturbative nature of SPT-d, as well as the back action of the matter on the semi-classical topological soliton, we expect that exotic many-body effects will be unveiled, and new avenues of research will be open.

In this chapter, we explore the existence of SPT-d in the $\mathbb{Z}_2$BH model (3.32). As discussed in chapter 4, this model gives rise to intertwined topological phases.

These phases are driven by the interplay of SSB and topological symmetry protection, both of which occur simultaneously in the ground state at commensurate fillings. As mentioned above, SSB also allows for the existence of topological defects/solitons and SPT-d. Given the pioneering results on solitons in the fermionic SSH model [HKSS88], and the number of similarities discussed between this and the $\mathbb{Z}_2$BH model, it is a fair question to assess if topological solitons and fractionalization of bosons could be observed in systems described by the latter. This question is even more compelling given the possibility of implementing this model using ultracold bosonic atoms in optical lattices. As substantiated in the following sections, this implementation would allow for a real breakthrough in the field: the first direct experimental observation of fractionalization of matter by a non-static soliton.

The soliton model of SSH has been argued to play a key role in the physics of a linear conjugate polymer, namely polyacetylene [HKSS88]. Despite indirect evidence, there has always been a certain degree of controversy about the role of solitons in the properties of polyacetylene [Lau99]: long-range dimerized order, let alone a solitonic configuration, has never been observed directly. Moreover, the spin-full character of electrons in polyacetylene, which is half-filled, masks the fractionalization. Despite leading to reversed spin-charge relations, which yield an indirect evidence [HKSS88], this spin doubling of polyacetylene forbids a direct experimental confirmation of the bound fractionalized nature of quasi-particles. Accordingly, the existence of topological solitons and bosonic fractionalization shown below, together with the possible implementation of the $\mathbb{Z}_2$BHM in experiments of ultra-cold atoms, opens a new promising route in the study of SPT-d.

Here we study the $\mathbb{Z}_2$ Bose-Hubbard model for incommensurate densities, and characterized the different symmetry-protected topological defects that appear. The chapter is organized as follows. In Sec. 5.2, we show how topological solitons appear spontaneously in the ground state of the $\mathbb{Z}_2$BHM when it is doped above/below certain commensurate fillings, and we characterize them in terms of topological charges associated to the underlying SSB sectors. Moreover, we demonstrate how these defects bind fractionalized bosonic quasi-particles. These composite objects can propagate through the chain, repelling each other at short distances. For a finite density of defects, this interaction gives rise to a fractional soliton lattice. In Sec. 5.3, we explore how the topological properties of the matter sector can bring extra protection to these bound quasi-particles. In particular, we characterize the different SSB sectors as intertwined topological phases using symmetry-protected topological invariants. This allows one to track the origin of fractionalization in the system through a bulk-defect correspondence. Remarkably, the later can be generalized to situations where the regions separated by the defects are in the same topological sector. This requires extending the system to two dimensions using a pumping mechanism, where the 2D topological invariant can be recovered by measuring the quantized inter-soliton transport.

5.2 Topological solitons and boson fractionalization

5.2.1 $\mathbb{Z}_n$ solitons: doping and pinning

As advanced in the chapter 1, topological solitons are stable finite-energy excitations that may arise when different values of the order parameter are allowed by SSB [Raj82]. These excitations can be dynamically generated by crossing a symmetry-breaking critical point in a finite time. In this way, the ordered phase gets distorted by such solitons, the density of which scales with the crossing rate according to the Kibble-Zurek scaling [Kib76, Zur85]. Let us remark that, once the phase transition has been crossed, an extensive number of excitations are present in the system. These solitons evolve in time, scattering off each other, or escaping through the edges of the system, which gives rise to a complex out-of-equilibrium problem. In this subsection, we argue that the $\mathbb{Z}_2$BH model can host solitons in the ground state, and that they can be pinned externally, leading to a simpler equilibrium situation.

The crucial condition to find solitons directly in the ground state is to allow for their coupling with matter, which turns the situation into a very interesting quantum many-body problem. This is predicted to occur in the SSH model of polyacetylene by doping above/below half-filling [SS80, BK81, CB81] and, recently, also in a system of fermionic atoms inside an optical waveguide [FP19]. As shown below, solitons also appear in the $\mathbb{Z}_2$BH model, with characteristic differences. For instance, a single boson above half-filling can fractionalize, giving rise to two quasi-particles bound to a soliton-antisoliton pair in the ground state (see the qualitative scheme in Fig. 5.1**(c)**). For one-third and two-third fillings, a single boson can give rise to a richer profile of topological solitons and bound fractional quasi-particles (Fig. 5.1**(e)**). One of the key differences with respect to the soliton model of polyacetylene is that, during the doping process in the polymer, all sorts of additional disorder and randomness are inevitably introduced [Kiv01]. This disorder is likely the underlying source of difficulties in providing an unambiguous proof of the dimerized long-range order and the associated solitonic profiles in polyacetylene [Lau99]. In this context, an advantage of the $\mathbb{Z}_2$BH model, and its potential cold-atom realization, is that the atomic filling does not introduce impurities. In this way, one gets access to the ground state of the doped system in a pristine environment, where the existence of solitons/fractionalization is not masked by uncontrolled disorder.

Let us now present a more systematic study of topological solitons in the $\mathbb{Z}_2$BH model, and provide quantitative evidence of the correctness of Figs. 5.1**(c)** and **(e)**. In the introduction, we presented solitons as localized finite-energy solutions moving at constant speed and, yet, Figs. 5.1**(c)** and **(e)** represent static solitonic configurations. In a continuum model of polyacetylene [TLLM80], the solitons are indeed free to move. However, in a realistic situation, charged impurities appear

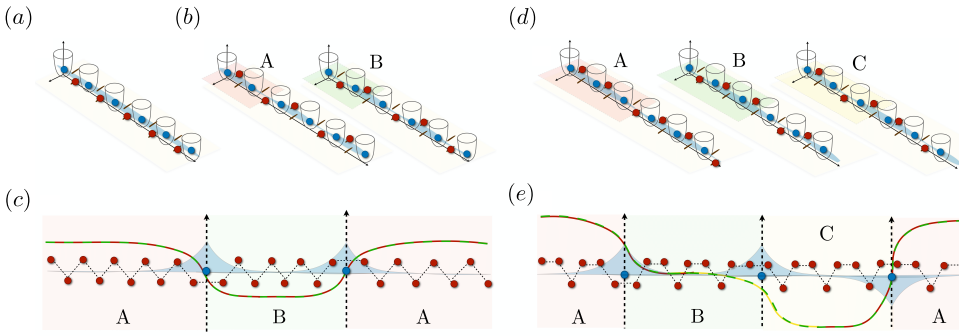

Fig. 5.1 Topological solitons in the $\mathbb{Z}_2$ Bose-Hubbard model: Bosonic particles (blue spheres) can tunnel between neighboring sites of a chain, and their tunneling depends on the state of the $\mathbb{Z}_2$ fields (red spheres) at the bonds. **(a)** For weak Hubbard interactions, the ground state of a half-filled system ($\rho = 1/2$) is described by a bosonic quasi-superfluid delocalized over the chain, and a polarized background where all $\mathbb{Z}_2$ point in the same direction. **(b)** At stronger interactions, the $\mathbb{Z}_2$ fields order antiferromagnetically according to two degenerate patterns (A and B), spontaneously breaking translational invariance. Simultaneously, the bosons display a long-range order with an alternating bond density. Note that, in addition to the bond order wave, one of the SSB sectors (B) hosts a symmetry-protected topological phase. **(c)** As a consequence of the SSB, the $\mathbb{Z}_2$ fields may adopt an inhomogeneous configuration with topological solitons, such as the ABA background hereby displayed. These configurations appear when extra particles are added above or below half filling, which are then bound to the solitons (blue). Each degenerate configuration is characterized by a different non-zero value of an order parameter. Solitons interpolate between these values in real space, as depicted here by a solid line. **(d)-(e)** Analogue situation for the trimer bond-ordered waves phases (valid for $\rho = 1/3$ and $\rho = 2/3$). In this case, the $\mathbb{Z}_2$ fields order ferri-magnetically according to three possible patterns (A, B and C), and a richer variety of topological solitons with bound quasi-particles can form.

upon doping, and play an additional important role: they pin the charged quasiparticles bound to the solitons at random positions [HKSS88]. Here we introduce a simple and deterministic pinning mechanism which, as shown below, allows us to precisely control the position of the solitons and fractional bosons in the $\mathbb{Z}_2$BHM.

Such a deterministic pinning is achieved by introducing a local perturbation of the $\mathbb{Z}_2$ fields, $H \to H + H_{\rm p}$, where

$$H_{\rm p} = \sum_i \beta_i \, \sigma^x_{i,i+1}, \quad \beta_i \, = \sum_{j_{\rm p} \in {\rm P}} \beta\epsilon \, (\delta_{i-1,j_{\rm p}} + \delta_{i,j_{\rm p}}). \tag{5.1}$$

Here, ϵ stands for the relative strength of the pinning potential, and we sum over all pinning centers labeled by $j_{\rm p} \in {\rm P}$. Essentially, this perturbation modifies the

transverse field at two consecutive bonds that surround each of the pinning centers, $\beta \to \beta_0 = \beta(1+\epsilon)$, selecting the corresponding solitonic profile that will depend on the particular filling.

Solitons with $\mathbb{Z}_2$-valued topological charges

Let us start by discussing the simplest situation, and address the appearance of topological solitons in the ground state of the $\mathbb{Z}_2$BHM doped above/below half-filling. As described above, there is a bosonic Peierls transition where the Ising spins develop an antiferromagnetic Néel-type order (Fig. 5.1**(b)**). In this case, the order parameter can be defined as

$$\varphi = \frac{1}{N_{\text{u.c.}}} \sum_{j=1}^{N_{\text{u.c.}}} \varphi_j, \;\; \varphi_j = \frac{1}{2} \sum_{i \in \text{u.c.}} \sin\left(\frac{\pi}{2}(2i-1)\right) \left\langle \sigma^z_{i,i+1} \right\rangle , \tag{5.2}$$

where $N_{\text{u.c.}}$ is the number of unit cells (u.c.) labelled by j, and φ_j is averaged over the elements of such unit cell $i \in$ u.c. φ is the total average staggered magnetization, and has two possible values $\varphi = \pm\varphi_0 \to \pm 1$ depending on the SSB sector. Solitons will interpolate between these two vacua (Fig. 5.1**(c)**).

The existence of such solitons can be understood starting from the $\beta = 0$ limit, where no quantum fluctuations exist, and they get reduced to static domain walls. Precisely at half-filling, the Peierls mechanisms results in antiferromagnetic Néel-like order the Ising spins. We recall that, in the hard-core regime $U \to \infty$, the Peierls transition is solely controlled by Δ. In this case, one can find analytical solutions showing that Néel order coexists with a bosonic bond-ordered wave if $\Delta \in [\Delta_c^-, \Delta_c^+]$ (3.35). Conversely, for $\Delta \notin [\Delta_c^-, \Delta_c^+]$, the spins polarize along the same direction and the bosons form a quasi-superfluid state.

In this section, we explore a new situation that goes beyond the scope of the results presented in chapter 4: we set $\Delta \in [\Delta_c^-, \Delta_c^+]$, but explore lattices with an odd number of sites, such that perfect half-filling is never possible. In this case, one can analytically show that the ground state is not a single Néel antiferromagnet in the Ising sector and a dimerized bond-ordered wave for the bosons, but that it is composed of neighboring domains displaying the possible SSB orders. In particular, we find that the ground state can accommodate for a single domain wall.

As β is increased, we show below that these domain walls widen into a soliton profile that coincides with the kink solutions of the (1+1) relativistic φ^4 theory [DHN74], namely

$$\varphi_j = \tanh\left(\frac{j - j_{\text{P}}}{\xi}\right), \tag{5.3}$$

where j_{P} is the soliton center and ξ is the width in lattice units. By analogy with the relativistic scalar quantum field theory, one can define a topological charge [Raj82]

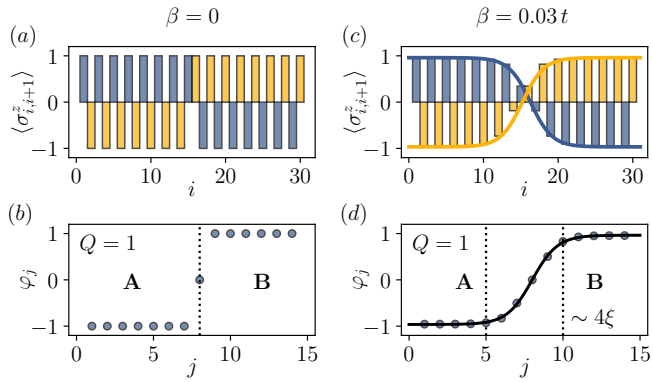

Fig. 5.2 $\mathbb{Z}_2$ **topological defects: (a)** Spin magnetization $\langle \sigma^z_{i,i+1} \rangle$ with a single topological defect modifying the dimerized pattern of the $\mathrm{BOW}_{1/2}$ phase, where different colors are used for the two sub-lattices. The defect corresponds to a domain wall ($\beta = 0$) connecting the two SSB sectors. **(b)** The defect interpolates between two values of the order parameter φ_j, which converges to -1 and $+1$ for $j = r - j_p$ and $j = r + j_p$, respectively, with $r \gg \xi$, and has a topological charge $Q = 1$. **(c)-(d)** Analogous topological defect for $\beta = 0.03t$, where we observe how quantum fluctuations broaden the defect, leading to a soliton of finite width ξ. The order parameter, which was discontinuous for a domain wall, is smoothened for $\beta > 0$, and can be accurately fitted to Eq. (5.3). The parameters of the model are fixed to $U = 10\,t$ and $\Delta = 0.80\,t$, and we use a chain with $L = 31$ sites and $N = 16$ particles.

as follows

$$Q = \tfrac{1}{2} \left(\varphi_{j_\mathrm{p}+r} - \varphi_{j_\mathrm{p}-r} \right), \tag{5.4}$$

where the order parameter is evaluated at points that are well separated from the soliton center, namely $r/\xi \to \infty$. In this case, the topological charge of the soliton is $Q = +1$, whereas anti-solitonic solutions carrying $Q = -1$ can be obtained with the alternative interpolating profile $\varphi_j \to -\varphi_j$. These $\mathbb{Z}_2$ topological charges, which cannot be modified by local perturbations, guarantee the robustness of the soliton.

To make contact with our previous analytical results, we note that the $\beta = 0$ limit of classical $\mathbb{Z}_2$ fields should yield an order parameter $\varphi_j \sim \theta(j - j_\mathrm{p}) - \theta(j_\mathrm{p} - j)$, where we have introduced the Heaviside step function. In this case, the topological soliton would have a vanishing width, and be localized within a single lattice site. To verify this prediction, we study the $\mathbb{Z}_2$BHM on a chain of $L = 31$ sites, filled with $N = 16$ bosons. The ground-state has been obtained numerically using a density matrix renormalization group (DMRG) algorithm based on matrix product

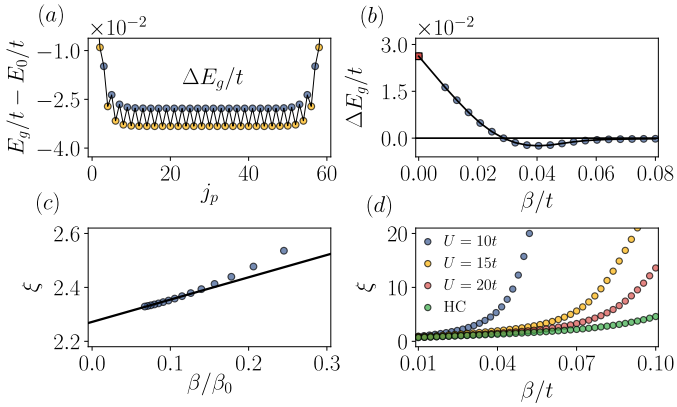

Fig. 5.3 Effect of quantum fluctuations on topological defects: **(a)** Ground state energy $E_{\mathrm{g}}(j_{\mathrm{p}})$ with one topological defect as we vary the pinning location j_{p} on a chain of $L = 61$ sites, measured with respect to some reference E_0, for $\beta = 0.02\,t$. Odd and even sites are represented in different colors, showing the Peierls-Nabarro potential between them. Note that, far from the boundaries, the state is degenerate due to translational invariance. **(b)** Peierls-Nabarro barrier ΔE_{g} as a function of β/t, which goes to zero as the quantum fluctuations increase, for $L = 91$. For $\beta = 0$ we obtain a non-zero value for $\Delta E_g/t$ (red square). In this limit, the defects are immobile. For $\beta \neq 0$ they can tunnel through the barriers. **(c)** The pinning perturbation (Eq. (5.1)) localizes the defect at a certain position. Here we show how the soliton width ξ varies as we increase the pinning strength β_0/β, converging to a finite value for an infinite pinning. This finite-size scaling was performed by fitting the points to a line (black). In every panel, ξ should be understood as the converged value. **(d)** Soliton width ξ as a function of β for different values of the Hubbard interaction U, and we now work with a chain of $L = 121$ sites. All the calculations where performed for one defect on top of the $\mathrm{BOW}_{1/2}$ phase, with $U = 10\,t$ and $\Delta = 0.80\,t$.

states (MPS) [HP18].[1]. Figure 5.2**(a)** shows the magnetization of the $\mathbb{Z}_2$ fields in the ground state. As can be clearly observed, an SS domain wall is formed by interpolating between the two possible anti-ferromagnetic Néel patterns. In this case, the defect is generated in the ground state since the odd number of sites does not allow for perfect half-filling, but rather $\rho = N/L > 1/2$. The existence of the domain wall becomes more transparent in Fig. 5.2**(b)**, where the corresponding order parameter (5.2) displays the aforementioned step-like behavior.

Let us note that, in this classical limit, the solitons can be centered around any lattice site j_{p} within the bulk of the system (i.e. the ground state has an extensive degeneracy). Moreover, in contrast to continuum field theories where solitons are

[1]For the rest of the chapter, we use open boundary conditions and bond dimension $D = 100$. The maximum number of bosons per site is truncated to $n_0 = 2$

free to move, lattice solitons are static as they find finite energy barriers that inhibit their transport. These energy penalties, known as Peierls-Nabarro barriers, arise due to the lack of translational invariance on the lattice, and are typically arranged forming a periodic Peierls-Nabarro potential [Pei40, Nab47].

As the quantum fluctuations of the $\mathbb{Z}_2$ fields are switched on, $\beta > 0$, the topological solitons start tunneling through these barriers, and delocalize along the lattice. In order to study static soliton properties in this quantum-mechanical regime, it is important to switch on the pinning terms of Eq. (5.1), which will effectively localize the soliton to the desired pinning center j_{p}. However, as a result of quantum fluctuations, the soliton is no longer strictly localized to a single site, but will spread over a width $\xi > 0$.

By externally modifying the position of the pinning center j_{p}, we can confirm the existence of such Peierls-Nabarro barriers by numerically computing the ground-state energy as a function of the position of the soliton $E_{\mathrm{g}}(j_{\mathrm{p}})$ (Fig. 5.3**(a)**). Due to the Peierls' dimerization, we find a periodic arrangement of energy barriers ΔE_{g} separating neighboring unit cells. As shown in Fig. 5.3**(b)**, the height of these barriers converges to a non-zero value when $\beta \to 0$, leading to the aforementioned Peierls-Nabarro barrier. This numerical result justifies our previous statement about the static nature of the solitons in the classical regime: the finite barriers inhibit the movement of the topological solitons. The small magnitude of the Peierls-Nabarro barrier also justifies our previous claim: as soon as quantum fluctuations are switched on, the solitons tunnel and delocalize, justifying the requirement of pinning (5.1).

In Fig. 5.2**(c)**, we represent such a pinned solitonic profile in presence of quantum fluctuations. The pinning center is positioned at the middle $j_{\mathrm{p}} = (L-1)/2$ of a chain of $L = 31$ sites. As can be observed in Fig. 5.2**(d)**, the order parameter interpolates between the two SSB ground states according to the smooth profile of Eq. (5.3), and an accurate fit can be used to extract the soliton width ξ. In Figure 5.3**(c)**, we show how the soliton width gets modified as one increases the strength of the pinning potential, eventually converging to a fixed value as the pinning strength is sufficiently strong $\beta/\beta_0 = 1/(1+\epsilon) \to 0$. Let us remark, however, that the modification of the soliton width for moderate pinnings lies at the 10% level, which is consistent with the contraction effect of other pinning mechanisms, such as the dopant impurities in the SSH model of polyacetylene [Kiv86]. In Figure 5.3**(d)**, we represent the widths ξ of the topological soliton as a function of the transverse field strength β, for different values of the Hubbard repulsion. We note that in all numerical simulations, we use a pinning strength such that convergence of the soliton width has been reached. As expected, the width increases (i.e. more delocalized defects) as the quantum fluctuations are raised. On the other hand, we observe that the soliton width, at fixed β, decreases as the Hubbard repulsion U is increased. This is a clear demonstration of the back-action of the matter sector on the topological soliton that was briefly mentioned in the introduction: as the

bosons become more repulsive, eventually reaching the hard-core constraint that forbids double occupancies, they can be accommodated more comfortably within the $\mathbb{Z}_2$ soliton, which then becomes more localized.

Solitons with $\mathbb{Z}_4$-valued topological charges

Let us note that, around half-filling, it is only possible to obtain two types of topological defects, solitons with charge $Q = +1$ and anti-solitons with $Q = -1$. By doping, the ground state configuration can only correspond to a succession of neighboring soliton and anti-solitons, such that the overall charge is either $Q_{\text{tot}} = 0$, or $Q_{\text{tot}} = \pm 1$ (i.e. even and odd topological sectors). For such configurations, one can imagine externally moving the defect centers by adjusting the pinning potentials, such that a soliton and anti-soliton scatter, annihilating each other. By repeating this process, one would reach a final situation where either one or none topological solitons remains. As discussed below, solitons and possible scattering are much richer around other fractional fillings.

We shall now focus on two-third filling, where the Peierls' mechanism can yield a three-fold degenerate ferrimagnetic ordering in the Ising sector (Fig. 5.1 **(d)**). The situation is analogous for filling one-third. The order parameter that can differentiate between these SSB ground states is

$$\tilde{\varphi} = \frac{1}{N_{\text{u.c.}}} \sum_{j=1}^{N_{\text{u.c.}}} \tilde{\varphi}_i, \quad \tilde{\varphi}_j = \frac{2}{\sqrt{3}} \sum_{i \in \text{u.c.}} \sin\left(\frac{2\pi}{3}(i-1)\right) \left\langle \sigma^z_{i,i+1} \right\rangle, \tag{5.5}$$

which attains the following values for the the three ground states $\tilde{\varphi} \in \{-2, 0, 2\}$. As there are more SSB vacua, there will be more types of solitons that interpolate between them. For instance, an anti-soliton interpolating between the A and B ground states (Fig. 5.1 **(e)**) can be described as

$$\tilde{\varphi}^{\text{AB}}_j = \left(1 - \tanh\left(\frac{j - j_{\text{AB}}}{\xi}\right)\right), \tag{5.6}$$

which has topological charge $Q_{\text{AB}} = -1$ according to Eq. (5.4). The anti-soliton interpolating between the B and C is

$$\tilde{\varphi}^{\text{BC}}_j = \left(1 + \tanh\left(\frac{j - j_{\text{BC}}}{\xi}\right)\right), \tag{5.7}$$

which also has topological charge $Q_{\text{BC}} = -1$. Finally, the soliton interpolating between C and A can be written as

$$\tilde{\varphi}^{\text{CA}}_j = 2\tanh\left(\frac{j - j_{\text{CA}}}{\xi}\right), \tag{5.8}$$

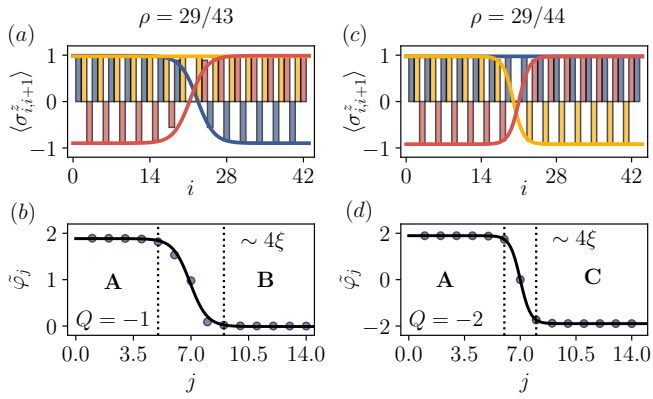

Fig. 5.4 $\mathbb{Z}_4$ **topological defects:** **(a)** Spin magnetization $\langle\sigma^z_{i,i+1}\rangle$ with a topological defect distorting the trimerized pattern, and corresponding to an anti-soliton on the $\mathrm{BOW}_{2/3}$ phase connecting two of the three SSB sectors, A and B, for a chain of $L = 43$ sites and $N = 29$ particles. **(b)** We represent the order parameter $\tilde{\varphi}_j$, where j is the unit cell index. The black line is obtained by fitting $\tilde{\varphi}_j$ using eq. (5.6) and eq. (5.8). Far from the defect, the order parameter distinguishes the different SSB sectors, and leads to an associated topological charge of $Q = -1$. The parameters of the model are fixed to $\beta = 0.01\,t$, $\Delta = 0.85\,t$ and $U = 10\,t$. **(c)-(d)** Same as **(a)-(b)**, but for an anti-soliton connecting the sectors A and C, for $L = 44$ and $N = 29$. This defect has an associated topological charge of $Q = -2$.

which has a larger topological charge $Q_{\mathrm{CA}} = +2$. We note that solitons with the inverse orderings BA, CB and AC, are also possible, and would lead to reversed topological charges, such that solitons are restricted to a $\mathbb{Z}_4$-valued topological charge.

In Figs. 5.4**(a)** and **(c)** we provide numerical confirmation of this phenomenon, displaying two examples of defects connecting different SSB sectors of the $\mathrm{BOW}_{2/3}$ phase. In both cases, the order parameter (5.5) adjusts very accurately to the expected shapes in Eqs. (5.6) and (5.8) (Figs. 5.4**(b)** and **(d)**). As it can be appreciated in the figure, different types of defects are generated depending on the bosonic density. In the next section we will analyze this mechanism in detail. However, before turning into this discussion, let us emphasize that the wider variety of solitons hereby discussed leads to further possibilities regarding their scattering. In the ABCA sequence of Fig. 5.1**(e)**, we see that this fractional filling allows for a richer multi-solitonic profile with respect to the half-filling. In particular, one is no longer restricted to neighboring soliton-atisoliton pairs, but it becomes possible to find two neighboring defects with the same topological charges $Q_{AB} = Q_{BC} = -1$. In this case, by externally adjusting the pinning potentials, these two defects can

collide and lead to a larger conserved charge $Q_{AB}+Q_{BC}=-2$, which corresponds to a new type of anti- soliton AC with charge $Q_{\rm AC}=-2$ instead of the trivial vacuum, as occurred for half-filling.

5.2.2 Boson fractionalization

So far, we have only focused on the Ising-spin sector, and proved the existence of various topological solitons in the ground state of the $\mathbb{Z}_2$BH model. Although the existence of these solitons is triggered by the coupling of the $\mathbb{Z}_2$ fields to the bosonic quantum matter, we recall that these solitons can be fully understood classically, as they are characterized by the topological charge of a classical field, i.e. the order parameter of Eq. (5.4). In this section, we will explore the bosonic sector, and show that there are bound quasi-particles localized within the soliton, which clearly display the bosonic version of the quantum-mechanical phenomenon of fractionalization. Charge fractionalization was first predicted for relativistic quantum field theories of fermions coupled to a solitonic background [JR76, NS86], and find a remarkable analogue in the physics of conjugated polymers [CB81]. As outlined previously, the direct experimental observation of this effect would be a real breakthrough in the field, overcoming past limitations in lightly-doped and disordered polyacetylene [Lau99].

Arguably, the clearest manifestation of fractionalization arises by doping a Peierls-type system with a single particle above/below a given commensurate filling, such as half filling. As it turns out, in order to accommodate for this additional particle, the ground state of the $\mathbb{Z}_2$BHM develops a soliton/anti-soliton pair of the $\mathbb{Z}_2$ fields, each of which hosts a bound quasi-particle/quasi-hole with a fractionalized number of bosons, i.e. the boson splits into two halves. Figure 5.5 (left column) contains all the numerical evidence that supports this mechanism in a chain of $L=90$ sites filled with $N=46$ bosons. Note that this yields precisely an extra particle above half filling $\rho=N/L=1/2+1/L=\rho^\star+1/L$.

As shown in Fig. 5.5**(a)**, the Ising sector of the $\mathbb{Z}_2$BHM ground state clearly displays the predicted soliton/anti-soliton profile ABA, and its finite width is a result of the finite quantum fluctuations of the Ising spins. In Fig. 5.5**(b)**, we represent the bosonic particle number for the different sites of the chain. As can be observed, away from the soliton/anti-soliton, the average particle number is consistent with the half-filling condition. Remarkably, as one approaches the topological defects, a build-up in density becomes apparent, which signals the presence of a quasi-particle bound to the topological soliton/anti-soliton. Moreover, the density profile of this fractional quasi-particle can be accurately fitted to

$$\langle :n_j: \rangle = \langle n_j \rangle - \rho^\star = \frac{1}{4\xi}\mathrm{sech}^2\left(\frac{j-j_{\rm p}}{\xi}\right), \tag{5.9}$$

where $j=2i$ or $j=2i+1$ is the sub-lattice index, and $\rho^\star$ is the closest commen-

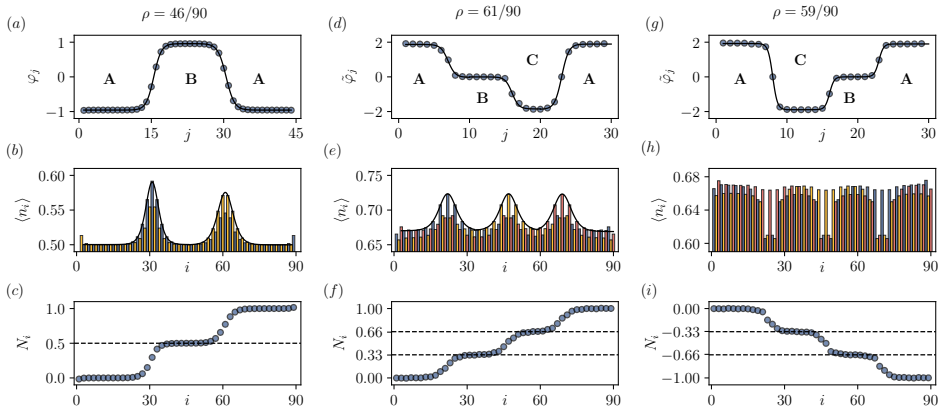

Fig. 5.5 Fractionalization of bound quasi-particles: **(a)** We represent the order parameter φ_j (5.2) at each unit cell j for the ground state configuration when we add one extra particle on top of half-filling. In this case a soliton-antisoliton pair is created, dividing the chain into ABA consecutive sectors. In **(b)**, we show the bosonic occupation $\langle n_i \rangle$ in real space. We observe how, inside the bulk of each sector, the occupation corresponds to 0.5. Around the defects, however, we find peaks where the occupation increases, with a different profile for each sublattice. The black line corresponds to a fit to Eq. (5.9). **(c)** The integrated particle number $N_i = \sum_{j<i} \langle : n_j : \rangle$ shows how each peak is associated with half a boson. Each bound bosonic quasi-particle is, thus, fractionalized. The situation is similar around two-third filling when adding or substracting a single particle above **(d)**, or below **(g)** the corresponding filling. We represent the order parameter $\tilde{\varphi}_j$ (5.5), showing how three defects appear, creating the SSB patterns ABCA, or ACBA, respectively. The bosonic occupation shows **(e)** peaks and **(h)** drops with respect to 2/3 around the defects (which agains follows accurately Eq. (5.9)). In this case, the each extra boson is fractionalized into three bound quasi-particles with associated particle number **(f)** 1/3 and **(i)** $-1/3$. The calculations were performed using a chain of $L = 90$ sites and taking $U = 10\,t$. In the first column we took $N = 46$ particles, $\Delta = 0.80\,t$ and $\beta = 0.02\,t$. In the center and right columns we used $\Delta = 0.85\,t$ and $\beta = 0.01\,t$, with $N = 61$ and $N = 59$ particles, respectively. The solitons were pinned as discussed in the previous section.

surate filling (i.e. $\rho^\star = 1/2$ in this case). Remarkably, this expression coincides exactly with the profile of the zero-modes for the relativistic quantum field theory of fermions [CB81], providing a clear instance of universality: regardless of having bosonic/fermionic matter coupled to a $\mathbb{Z}_2$/scalar field, the profiles of the solitons and the fractionalized quasi-particles are completely equivalent.

Finally, in order to display clearly the fractionalization phenomenon, let us

compute the integrated number of bosons above the half-filled vacuum

$$N_i = \sum_{j \leq i} \langle : n_j : \rangle, \tag{5.10}$$

As shown in Fig. 5.5**(c)**, this integrated boson number displays two clear plateaux connected by jumps of 1/2 in the density. Accordingly, the localized quasi-particles of Fig. 5.5**(b)** indeed carry a fractional number of bosons, namely 1/2 boson each, that is spread within the soliton according to Eq. (5.9).

A similar situation occurs when we dope with extra particles or holes around two-third filling, as it can be appreciated in the center and right columns of Fig. 5.5. In both cases, three defects appear in the ground state (Fig. 5.5**(d)** and **(g)**), separating different SSB sectors with a density of 2/3 far from the defects. The latter are associated with peaks or drops in the density that are localized within the different solitons/anti-solitons (Figs. 5.5**(e)** and **(h)**). Moreover, the integrated density of bosons (5.10) displayed in Figs. 5.5**(f)** and **(i)** is fully consistent with the fractional $\pm 1/3$ bosonic quasi-particles.

In Figure 5.6, we summarize the different types of topological solitons and the fractional particle number of the associated quasi-particles. Around two-third filling, in particular, the defects can host fractional bosons with particle number $\pm 1/3$ and $\pm 2/3$. In addition to the situation discussed in the previous paragraph, we note that one extra particle could also be fractionalized into two $+2/3$ and one $-1/3$ quasi-particles. However, this configuration would not be homogeneous, and is not spontaneously realized in the ground state, where we have only found configurations associated to $\pm 1/3$ fractionalized quasi-particles. We note, however, that these configurations can still occur as excitations, and are relevant to understand the possible soliton scattering discussed in the previous section, which must be consistent with the fractionalization phenomena. Recall that the AB and BC defects can collide and lead to a larger conserved charge $Q_{\mathrm{AB}} + Q_{\mathrm{BC}} = -2$, which corresponds to a new type of anti-soliton AC with charge $Q_{\mathrm{AC}} = -2$. This picture is also consistent with the bound number of bosons, as the AC defect of Fig. 5.6 is associated to a fractional value of $2/3 = 1/3 + 1/3$.

5.2.3 Polaron excitations and fractional soliton lattices

Let us now comment on the possibility that the extra bosons/holes about the commensurate fillings, instead of fractionalizing into quasi-particles bound to the solitons/anti-solitons, lead to a simpler excitation: a topologically-trivial polaron. In fact, in the fermionic SSH model, a single fermion above the half-filled ground state does not lead to the fractionalized pair of quasi-particles. Instead, a lower-energy quasi-particle is formed, corresponding to the electron being surrounded by a cloud of phonons, the so-called electronic polaron [SS80, CB81]. We note that,

ρ^*	Defect	Occupied	Empty
1/3	**A – B – C – A**	+2/3	−1/3
	A – C – B – A	+1/3	−2/3
1/2	**A – B – A**	+1/2	−1/2
2/3	**A – B – C – A**	+1/3	−2/3
	A – C – B – A	+2/3	−1/3

Fig. 5.6 Topological defects and fractionalized states: The table summarizes the particle numbers associated to the localized states bound to the topological solitons, when the state is occupied (particle) or empty (hole). We write defect A-B-C-A, for example, referring to the defects corresponding to each pair of consecutive sectors: AB, BC and CA, which have the same particle numbers. We highlight the configurations that are generated spontaneously by doping the commensurate densities $\rho^\star$ with one particle or hole. In shaded areas, we highlight the instances realized in the ground state.

in the context of the SSH model, this polaron solution can be understood as a confined soliton-antisoliton pair. The separation between both defects d is smaller than their corresponding widths ξ, such that the fermion is not fractionalized into a pair of $1/2$ charges bound to each defect, but instead distributed across the entire polaron with the same total charge [CB81, HKSS88]. If one studies the energy of the soliton-antisoliton pair as a function of the distance $E_g(d)$, a global energy minimum is found for the separation of the polaron mentioned above [Kiv86].

In the $\mathbb{Z}_2$BH model we can calculate numerically the ground state energy as a function of the soliton-antisoliton distance $E_g(d)$, which is controlled though the pinning centers of the perturbation (5.1). In Fig.5.7**(a)**, we show how this energy does not present any global minimum corresponding to a polaronic solution, which in this case would stand for the bosonic particle surrounded by spin-wave fluctuations.

According to this result, we can rule out the existence of any confining mechanism, and ensure that the ground state corresponds to the distant soliton-antisoliton pair with fractionalized bound quasi-particles. This results are also useful to discuss the following type of ground state, the so-called soliton lattice, which corresponds to the soliton BOW phases presented in chapter 3 for a finite density of bosons above half filling (Fig. 3.7). Since the energy decreases exponentially with the soliton distance (see the fit in Fig.5.7**(a)**), solitons tend to repel each other seeking for ground state configurations with the maximal inter-soliton distance. If we keep on adding additional particles above/below half-filling, but do not fix their relative positions by the external pinning (5.1), the solitons-antisolitons pairs will self-assemble in a crystalline configuration that maximises the inter-soliton distance: a soliton lattice.

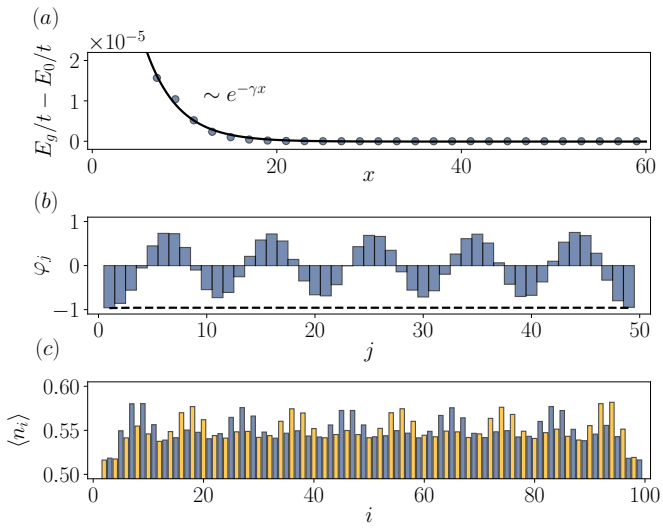

Fig. 5.7 Polarons and the soliton lattice: **(a)** Ground state energy $E_{\rm g}(x)$ for a chain of $L = 120$ sites filled with $N = 62$ bosons, as a function of the distance x between the pinned soliton-antisoliton pair. The absence of a miniminum for a given distnace x_0 shows that topologically-trivial polarons are absent in the ground state of the $\mathbb{Z}_2$BHM. **(b)** The order parameter φ_j (5.2) for a chain of $L = 100$ sites filled with $N = 55$ bosons self-assembled in a periodic configuration of soliton-antisolitons, maximizing the inter-soliton distance, and leading to the a soliton lattice.. The dotted line represents the corresponding staggered polarization of the half-filled ground state without any topological defect. **(c)** The local boson density displays the localized nature of the bound quasi-particles, which again display a fractionalized density upon a closer inspection.

Such type of solutions were originally predicted for the SSH model of polyacetylene [Hor81, Hor87], and are also known as kink-antikink crystals in relativistic field theories of self-interacting fermions at finite densities [TU03, BmcD08].

In Fig. 5.7 **(b)**, we represent the Ising sector of the $\mathbb{Z}_2$BHM ground state for a chain with $L = 100$ sites and $N = 55$ bosons. As can be readily appreciated, in the absence of pinning (5.1), the $\mathbb{Z}_2$ fields self-assemble in a periodic configuration of soliton-antisoliton pairs that delocalize over the chain while maximising the inter-soliton distance. In this way, the background spins form a soliton lattice, and lead to a periodic configuration of fractionalized bosonic quasi-particles: a fractional soliton lattice (Fig. 5.7**(c)**). As can be observed in Fig. 5.7 **(b)**, the value of order parameter in between a consecutive soliton-antisoliton pair does not reach the value of the defect-free configuration at precisely half-filling. As occurs for the SSH model [Hor81, Hor87], this can be considered as evidence that the energy gap

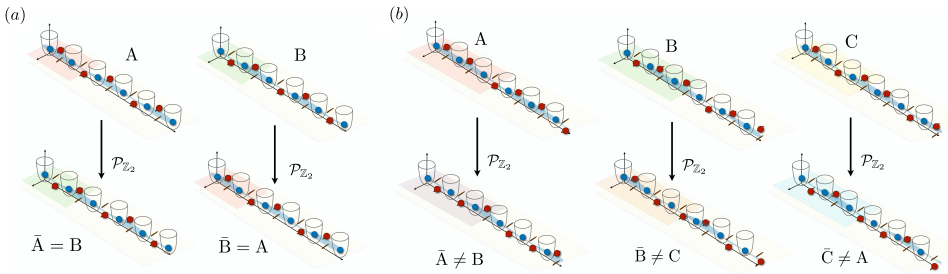

Fig. 5.8 Topological Bond Order Wave phases: **(a)** The Bond Order Wave phase at half filling ($\mathrm{BOW}_{1/2}$) is doubly degenerate. The two SSB sectors, A and B, are related by a one-site translation, and can be distinguished by their topological properties: while A is topologically trivial, B is a symmetry-protected topological phase. Note that, by applying a $\mathcal{P}_{\mathbb{Z}_2}$ inversion $\sigma^z \to -\sigma^z$, we can transform states in the A sector to states in the B sector and vice versa. **(b)** This property is not satisfied, however, at one-third and two-third fillings. For each of these densities, we find again a BOW phase with a three-fold degeneracy. A, B and C denote the three SSB sectors, connected again by one-site translations. Note that now the $\mathcal{P}_{\mathbb{Z}_2}$ transformation takes states from these sectors to a different phase. We denote the later as $\mathrm{TBOW}_{1/3}$ (respectively $\mathrm{TBOW}_{2/3}$), which is again three-fold degenerate $\bar{\mathrm{A}}$, $\bar{\mathrm{B}}$ and $\bar{\mathrm{C}}$, and appears at stronger Hubbard interactions. The latter is a symmetry-protected topological phase, as opposed to the $\mathrm{BOW}_{1/3}$ (respectively $\mathrm{BOW}_{2/3}$), which possesses a zero topological invariant. The fact that, as opposed to the half-filled case, $\mathcal{P}_{\mathbb{Z}_2}$ do not coincide with the one-site translation has an important consequence: while in the former case topological defects separate regions with different topological properties in the bulk, this is not true for the latter, and localized states associated to the defects are not expected a priori based on topological arguments. We will see, however, that a topological origin for such states can be recovered by extending the system to two dimensions through a pumping mechanism.

of the soliton lattice is smaller than that of the defect-free configuration or the pinned-soliton ground state, signaling that the topological defects in the soliton lattice are not independent excitations above the perfectly-dimerized ground state. Instead, the topological defects in the soliton lattice are coupled and form an energy band, leading to ground states that are fundamentally different from a collection of uncoupled topological solitons. We would like to emphasize that, although this type of solutions has been analytically predicted before [Hor81, Hor87, TU03, BmcD08], our DMRG results for the $\mathbb{Z}_2$BH model provide, to the best of our knowledge, the first numerically-exact confirmation of their existence without the approximations underlying previous analytical works (e.g. large-N methods) .

5.3 Bulk-defect correspondence

So far, we have solely focused on the topological properties of the $\mathbb{Z}_2$-field sector, and discussed the fractionalized nature of the bound bosonic quasi-particles. In this section, we delve into the full topological characterization of the defects, and show how the fractionalized matter can bring an extra topological protection to the ground state, making connections to the notion of symmetry-protected topological defects (SPT-d). We remark, once more, that previous studies typically consider the properties of SPT-d in the presence of externally-adjusted static solitons [TK10, TH17]. Here, on the other hand, we focus on the full many-body problem where the solitons have their own dynamics, and the back action of the matter sector on the solitons becomes relevant. Moreover, we will unveil the particular topological origin of the associated fractional bosons through a generalized bulk-defect correspondence.

5.3.1 Symmetry protection of bound quasi-particles

Paralleling our discussion of the previous sections, let us start with the simplest situation: the half-filled configuration, where the Peierls' mechanism gives rise to a two-fold degenerate ground state with a dimerization of the $\mathbb{Z}_2$ field (see Fig. 5.8). In the hardcore limit $U/t \to \infty$, the bosons can be mapped onto fermions by means of a Jordan-Wigner transformation [JW28], which shows that the resulting ground state has both inversion symmetry and a sub-lattice, so-called chiral, symmetry. According to the general classification of symmetry-protected topological phases [CTSR16], the bulk $\mathrm{TBOW}_{1/2}$ is a clear instance of a BDI topological insulator. The two degenerate ground states A and B can be characterized as trivial or topological, respectively, with the help of a topological invariant, namely the local Berry phase γ, as we did in chapter 4. In particular, the local Berry phase takes the value $\gamma = 0$ in the trivial A phase, and $\gamma = \pi$ in the topological B phase. Furthermore, the chiral symmetry ensures the so-called bulk-edge correspondence: a ground state that displays a Berry phase $\gamma = \pi$ will have one edge state at each boundary of the chain.

Let us now revisit the case of one extra particle above half filling. Figure 5.9**(a)** shows the real-space occupation of bosonic in the ground state of a finite system of $L = 90$ sites. The system displays the pattern A-B-A with two solitons separating the degenerate SSB configurations. To understand the topological origin of these states, we show in Fig. 5.9**(b)** our numerical calculation of the local Berry phase in real space [Hat06], computed on the intercell bond (i.e. the bond joining two neighboring unit cells). As can be observed in this figure, the local Berry phase in the configuration A is equal to $\gamma = 0$, while the one in the B configuration yields $\gamma = \pi$. In such a situation, the theory of topological defects [TK10, TH17] predicts that localized and topologically-protected boundary states will appear at the in-

terface of the two topologically-distinct regions. Furthermore, as a consequence of chiral symmetry, these states have support in just one of the two sub-lattices. This makes them robust against perturbations that respect the chiral symmetry, but are not sufficiently strong to close the gap of the system. Therefore, apart from the inherent robustness of the classical topological solitons, the total defects formed by a soliton and a fractionalized bosonic quasi-particle are also protected against chiral-preserving perturbations, leading to the aforementioned SPT-d [TK10, TH17].

From a pragmatic point of view, these SPT-d constitute an alternative to observe topological edge states in a cold atom experiment. We note that the presence of topological edge states at the boundaries of a cold-atom system can be sometimes hampered by the presence of an additional trapping potential [SGDS10]. Previous attempts to overcome these difficulties rely on externally adjusting inhomogeneous configurations [GSN+10], imposing background solitonic profiles on a superlattice structure [GHF13], or by shaking the optical lattice [PDZ15]. Here, on the contrary, the topological solitons are dynamically generated by doping the system, and self-adjust to certain positions of the chain depending on the doping. In particular, there are certain configuration where the SPT-d can be found at the middle of the system (see Fig. 5.2), where the deleterious effect of the trapping potential would be absent.

Having clarified the topological protection of these SPT-d in the simpler half-filled and hardcore limits, let us now turn into more complex situations, and assess the nature of the topological protection of these defects *(i)* away from the hardcore constraint, or *(ii)* around other fractional fillings.

For finite values of the Hubbard repulsion U, the chiral symmetry is explicitly broken even in the half-filled case. Nevertheless, the system still possesses inversion symmetry, which can lead to a quantized non-zero Berry phase and an intertwined topological phase, as we showed in the previous chapter. We emphasize that the bulk-boundary correspondence is no longer guaranteed for these phases: the edge states break the inversion symmetry, and are therefore not protected by the topology of the bulk. Let us now discuss the situation for fillings above/below half-filling. Figure 5.9**(c)** shows the real-space bosonic occupation for $U = 10t$. The soliton-antisoliton pair is still present for such finite interactions but, as a direct consequence of the loss of chiral symmetry, the support of the fractionalized modes is no longer restricted to a single sub-lattice. Nonetheless, Figure 5.9**(d)** shows that the local Berry phase is still quantized to $\gamma = 0$ and $\gamma = \pi$ in the bulk of the trivial and topological configurations, respectively. This quantization is preserved even in the absence of chiral symmetry, as there still exists the discrete inversion symmetry. We observe how, in the region where the solitons interpolate between the two inversion-symmetric ground states, and inversion symmetry is thus not maintained, the Berry phase attains intermediate values connecting the two quantized values that appear far away from the soliton cores. In summary, the bulk can be characterized by a topological invariant, but there is no direct bulk-defect cor-

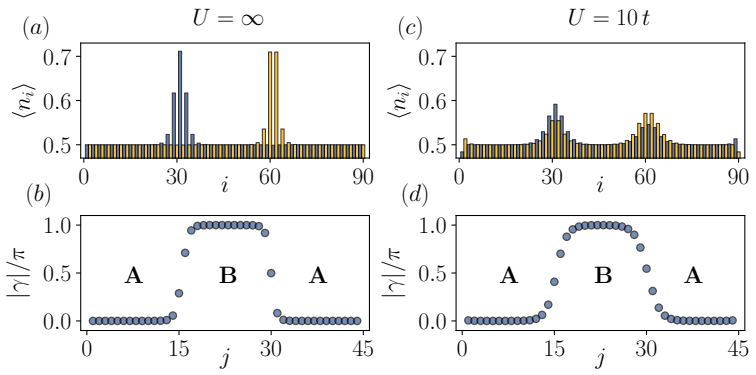

Fig. 5.9 Topological invariant and fractionalization: **(a)** Occupation number $\langle n_i \rangle$ for a chain with $L = 90$ sites in the hardcore limit, $U/t \to \infty$, when we dope a state in the BOW phase with one extra particle above half filling. At the location of the defects, two peaks in the occupation can be observed, each one localized only in one sublattice (represented in different colors) as a consequence of chiral symmetry. **(b)** Local Berry phase γ calculated on the bonds that separate different unit cells j. This quantity is quantized to 0 and π in the different SSB sectors, and interpolates between these two values in the region where the defects are located. **(c)** For a finite value of U we can still observe peaks in the occupation. These are no longer localized in specific sublattices, since chiral symmetry is broken. However, the topological Berry phase is still quantized far from the defects **(d)** since inversion symmetry is still preserved. In the hardcore limit we used the parameters $\Delta = 0.70t$ and $\beta = 0.03t$, and for the softcore case $\Delta = 0.80t$ and $\beta = 0.02t$.

respondence responsible for the protection of the defects. In the following section, we shall revisit this scenario in search for a generalized bulk-defect correspondence.

Let us now turn to two-third filling, where we recall that the Peierls' mechanism gives rise to a threefold degenerate ground state with a trimerization of the $\mathbb{Z}_2$ fields (see Fig. 5.8). The resulting phases are insulators that can either be topologically trivial or non-trivial, depending on the strength of the Hubbard interactions, as described in chapter 4. Figure 5.8**(b)** depicts the different ground state configurations for $U = 10t$ (trivial) and $U = 15t$ (topological): the trivial phase has a BOW pattern with two strong bonds and one weak bond (A), whereas the topological phase has a BOW pattern with two weak bonds and one strong bond ($\bar{\text{A}}$). The topology of these ground states can be characterized with the help of the inter-cell local Berry phase, which is equal to $\gamma = 0$ in the trivial phases A, B and C, but non-zero $\gamma = \pi$ in the topological phases $\bar{\text{A}}$, $\bar{\text{B}}$ and $\bar{\text{C}}$. We note that the three degenerate ground states A, B and C (resp. $\bar{\text{A}}$, $\bar{\text{B}}$ and $\bar{\text{A}}$) are related to each other by a translation of one site, and are thus equivalent in the thermodynamic limit.

We emphasize here that the three ground states have the same topology, unlike the half-filled case, where B = $\bar{\text{A}}$ has a different topology with respect to A (Fig. 5.8).

We now move away from the commensurate fillings, and address the topological characterization of the bound quasi-particles that appear when doping the system with one particle above the two-third filled ground state, which would correspond to the trivial BOW phase for $U = 10t$. As discussed in previous sections, three topological solitons arise leading to the A-B-C-A configuration (Fig. 5.8**(b)**), each of which hosts a localized bosonic quasi-particle with a fractional charge of 1/3. Notice that, in contrast to half-filling, the defects are no longer separating regions with different topological bulk properties. According to the theory of SPT-d, since the solitons do not interpolate between topologically-distinct regions, there is no reason to expect that a quasi-particle will be bound to the soliton. Nonetheless, such bound quasi-particles do appear, carry fractionalized charges, and we would like to understand if they have some generalized topological origin. In the next section, we show that these quasi-particles can be understood as remnants of topologically protected defect modes of an extended 2D system, even if this cannot be inferred a priori in the 1D system.

5.3.2 Quantized inter-soliton pumping

In chapter 1, we show how a generalized bulk-defect correspondence can be established by extending topological defects to higher dimension through a Thouless pumping argument [Tho83]. Here move away from the single-particle scenario, and explore the pumping of bosons between the topological solitons in the strongly-correlated $\mathbb{Z}_2$BHM. We shall use this pumping to discuss a generalized bound-defect correspondence that shines light on the topological origin of the bound fractional bosons. In this case, we implement the adiabatic pumping by modifying the $\mathbb{Z}_2$BH model (3.32) as follows

$$\begin{aligned} H = &- \sum_i \left[b_i^\dagger (t + \alpha \sigma^z_{i,i+1}) b_{i+1} + \text{H.c.} \right] + \frac{U}{2} \sum_i n_i (n_i - 1) \\ &+ \sum_i \frac{\Delta_{\varphi,i}}{2} \sigma^z_{i,i+1} + \sum_i \beta_{\varphi,i} \sigma^x_{i,i+1}, \end{aligned} \tag{5.11}$$

where $\Delta_{\varphi,i} = 2(-1)^i \delta \cos(\varphi)$ and $\beta_{\varphi,i} = (-1)^i \delta \sin(\varphi)$. By choosing $\delta \gg t$, we guarantee that the spins rotate periodically, effectively generating a superlattice modulation similar to the one we considered in the non-interacting Rice-Mele model (1.49). In practice, it is enough to fix $\delta = t$.

In this case, one must consider the many-body ground-state due to the presence of interactions. Therefore, the notion of the Chern number of the band must be generalized to that of an interacting system. The latter can be done by defining the Chern number in a 2D finite size system with the help of twisted boundary

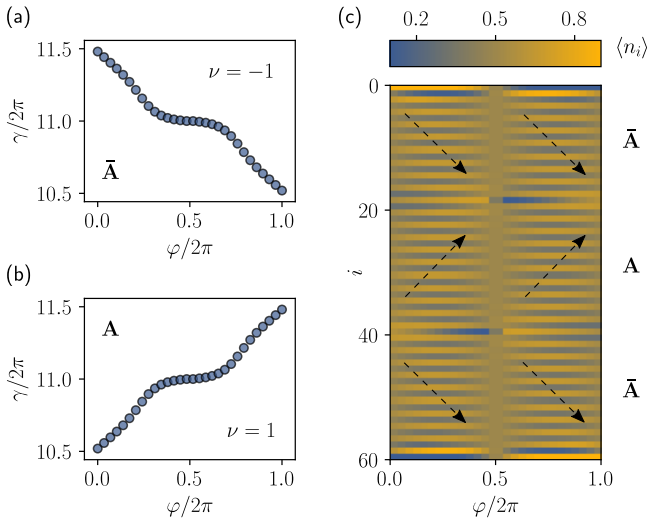

Fig. 5.10 Inter-soliton pumping with $\mathbb{Z}_2$ solitons: **(a)** and **(b)** show the local Berry phase γ calculated at the middle of a finite chain with $L = 42$ sites as a function of the pumping parameter φ. Both correspond to half filling, but starting from the homogeneous configurations $\bar{\mathrm{A}}$ and A, respectively. Using Eq. (5.12) we can calculate the corresponding Chern numbers, obtaining $\nu_{\bar{\mathrm{A}}} = -1$ and $\nu_{\mathrm{A}} = +1$, respectively. The sign of the Chern number gives us the direction of the transport, $\Delta n = -\nu$. This can be observed in **(c)**, where we represent the real-space bosonic occupation $\langle n_i \rangle$ through the pumping cycle of a system with two domain walls, starting from the $\bar{\mathrm{A}}\mathrm{A}\bar{\mathrm{A}}$ configuration at $\varphi = 0$. Each region transports a quantized charge in the bulk, but the direction (dashed arrows) is different in each of them.

conditions [NTW85a]. Alternatively, the Chern number can also be computed for a cylinder as the change of the Berry phase $\gamma(\varphi)$ during the pumping cycle [ZMP14, AHB11]

$$\nu = \frac{1}{2\pi} \int_0^{2\pi} \mathrm{d}\varphi \, \partial_\varphi \gamma(\varphi). \tag{5.12}$$

We use the latter definition to infer the Chern number and characterize the topology of our pumping cycle.

We first consider the case of solitons around half filling. Figure 5.10**(a)** shows the change in the many-body Berry phase during the pumping, which starts from the configuration B= $\bar{\mathrm{A}}$ at $\varphi = 0$. We note that the many-body Chern number can be calculated from the finite changes of this quantity, which yield $\nu_{\bar{\mathrm{A}}} \approx -1$. The Chern number associated to the reversed pumping starting from the configuration A is $\nu_{\mathrm{A}} \approx 1$, as shown in Fig. 5.10**(b)**. These results allow us to draw an alternative

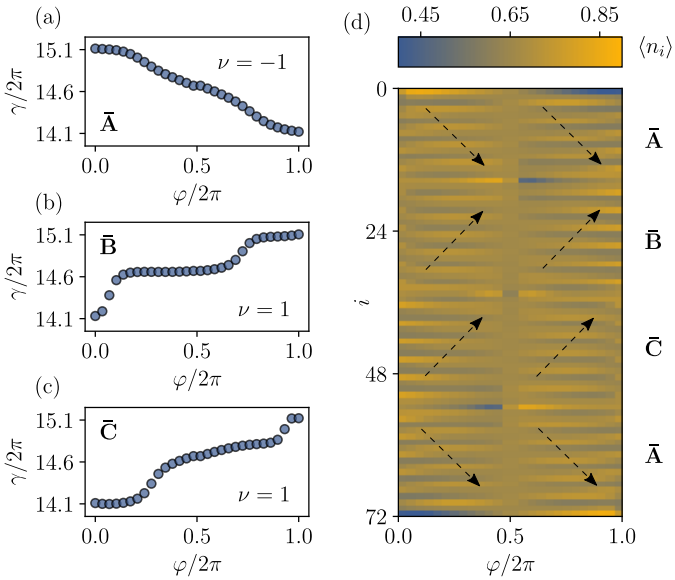

Fig. 5.11 Inter-soliton pumping with $\mathbb{Z}_4$ solitons: **(a)**, **(b)** and **(c)** show the local Berry phase γ calculated at the middle of a finite chain with $L = 42$ sites as a function of the pumping parameter φ. They correspond to $\rho = 2/3$, but starting from the homogeneous configurations $\bar{\mathrm{A}}$, $\bar{\mathrm{B}}$ and $\bar{\mathrm{C}}$, respectively. Using eq. (5.12) we obtain Chern numbers equal to **(a)** $\nu_{\bar{\mathrm{A}}} = -1$, **(b)** $\nu_{\bar{\mathrm{B}}} = 1$ and **(c)** $\nu_{\bar{\mathrm{C}}} = 1$. **(d)** Real space bosonic occupation $\langle n_i \rangle$ through the pumping cycle of a system with three domain walls, starting from the $\bar{\mathrm{A}}\bar{\mathrm{B}}\bar{\mathrm{C}}\bar{\mathrm{A}}$ configuration. At the edges of the system, one particle is transported during the cycle, since the former act as boundaries between the region $\bar{\mathrm{A}}$ and the vacuum, with a the difference in Chern numbers of -1. Two of the defects separate regions where this difference is ± 2, and the charge pumped through these defects is two, while it is zero across the trivial soliton (center). The direction of the transport (dashed arrows) depends on the sign of the Chern number, with $\Delta n = -\nu$.

picture of the topological origin of the fractionalized bound quasi-particles that appear in the $\mathbb{Z}_2$-BHM above/below half filling. Similarly to the non-interacting case, the fractional bosons bound to the defects can be understood as remnants of the conducting states localized at the 1D cylindrical interfaces that separate synthetic 2D regions with different Chern numbers. The difference between the Chern numbers of these regions predicts the number of bound modes, and its sign is related to the direction of the particle flow [IZH19]. Figure 5.10**(c)** shows how the real-space bosonic occupation evolves for a finite chain with two domain walls. This figure clearly supports the above prediction: as a consequence of the different topological invariants, quantised charge is transported between the two existing

solitons. The latter separate regions with different Chern numbers in the extended 2D system, and the direction of the transport is different for each one.

As stated above, this pumping offers an alternative take on the topological origin of the fractionalized bosons. However, for the half-filled case, it is not essential as the topological solitons always separate regions with a different Berry phase, and one can develop a topological characterization based solely on the equilibrium properties of the 1D model. Let us now move the case of two-third filling, where solitons interpolate between regions with the same Berry phase, and pumping becomes essential to unravel the topological aspects of the fractionalized bosons. We first compute the Chern numbers associated to the three degenerate configurations $\bar{\mathrm{A}}$, $\bar{\mathrm{B}}$ and $\bar{\mathrm{C}}$. Figures 5.11 **(a)**, **(b)** and **(c)** show the Berry phases for the three configurations $\bar{\mathrm{A}}$, $\bar{\mathrm{B}}$ and $\bar{\mathrm{C}}$, the change of which as a function of the pumping phase leads to Chern numbers $\nu_{\bar{\mathrm{A}}} = -1$, $\nu_{\bar{\mathrm{B}}} = 1$ and $\nu_{\bar{\mathrm{C}}} = 1$ respectively. Two configurations have therefore the same Chern number, which means that one of the solitons does not host a topologically-protected conducting state in the extended 2D system. As a consequence, the in-gap state of the corresponding defect does not connect the valence and conduction bands, and can be thus removed without closing the gap.

In the full many-body $\mathbb{Z}_2$BHM (5.11), the aforementioned absence of spectral flow means that the $\bar{\mathrm{B}}\bar{\mathrm{C}}$ soliton will not accumulate an integer pumped charge during the adiabatic cycle. In Figure 5.11**(d)**, we represent the time evolution of the bosonic density through the cycle for a system with three solitons. It can be observed how the bosonic density is pumped along distinct directions in the the three different regions, and that no particle number is being pumped in one of the defects, which is consistent with the above argument. In the contrary, for the other $\bar{\mathrm{A}}\bar{\mathrm{B}}$ and $\bar{\mathrm{C}}\bar{\mathrm{A}}$ solitons, the extended interfaces have a different Chern number, and the quantization of the adiabatic pumping can be thus used for the topological characterization of the SPTd. Let us highlight once more, that the Berry phase of all these composite defects are all the same $\gamma_{\bar{\mathrm{A}}} = \gamma_{\bar{\mathrm{B}}} = \gamma_{\bar{\mathrm{C}}} = \pi$. Therefore, although the fractionalized bound states do not arise in the interface of two topologically distinct regions in the equilibrium situation, we see that the extended regions via the pumping do indeed interpolate between regions with a different Chern number, guaranteeing thus the topological robustness of the pumping between these SPT-d.

It is important to notice that the Chern number, defined here through the Thouless pumping, is not unique. This is because the Chern number is associated to an extended 2D system, and there are different 2D systems for the same 1D topological phase, which depend on the details of the pumping protocol. For example, one could reverse the direction of the pumping and the sign of the Chern numbers will change. For the proposed protocol, the resulting Chern numbers associated to $\bar{\mathrm{B}}$ and $\bar{\mathrm{C}}$ are the same. This is why there is no charge accumulation in the soliton separating both, as opposed to the other ones. Again, one could devise a different protocol and the transport properties would be different. The impor-

tant point is then that for any of the three possible solitons one can always find an appropriate pumping protocol such that the soliton corresponds to a 1D defect in the associated 2D system, separating regions with different Chern numbers, and thus topologically protected.

As a summary, the pumping argument has allowed us to uncover the topological origin of the localized bosonic states associated to the $\mathbb{Z}_4$ solitons. As opposed to the case of $\mathbb{Z}_2$ solitons, in the later this origin could not be inferred from the topological properties of the different SSB sectors in 1D, as they all belong to the same topological phase. We note that, in these simulations, we have pinned down the defects since everything is computed in the ground state of the system, which coincides with the time-dependent calculation for an adiabatic evolution. In a cold-atom experiment, however, the defects are expected to move during the cycle. The results for the transported charge, however, should hold also in this situation.

5.4 Summary

In this chapter, we have explored the existence of symmetry-protected topological defects in intertwined topological phases, where both spontaneous symmetry breaking and topological symmetry protection cooperate, giving rise to exotic states of matter. We have analyzed how the topological solitons, which interpolate between different symmetry-broken sectors, can host fractionalized matter quasi-particles, and how the back action of the matter sector on the topological solitons is crucial to encounter this phenomenon directly in the ground state. We have presented a thorough analysis of the $\mathbb{Z}_2$ Bose-Hubbard model, where such interesting effects appear via a bosonic version of the Peielrs' mechanism. This leads to different types of $\mathbb{Z}_n$ solitons, showing distinct fractionalized bosonic densities bound to the solitons, and organized according to a rich variety of layouts: from pinned configurations with few topological defects, to solitonic lattices with corresponding crystalline densities of fractionalized bosons. The experimental realization of the $\mathbb{Z}_2$ Bose-Hubbard model, motivated by the remarkable progress in cold-atom quantum simulators, would allow for the first direct observation of dynamic topological solitons with bound fractionalized quasi-particles, overcoming past difficulties in conjugate-polymer science, and giving novel insights in genuinely quantum-mechanical topological defects.

In addition to the aforementioned static phenomena, we have also explored the quantization of particle transport in adiabatic pumping protocols. As a consequence of the topological solitons and bound quasi-particles, we have observed that an integer number of bosons can be pumped between the topological solitons, and that this phenomenon can be used to derive a generalized bulk-defect correspondence. Given the variety of intertwined topological phases in the $\mathbb{Z}_2$ Bose-Hubbard model, it turns out that one can find fractionalized quasi-particles bound to solitons

that separate regions with the same topological Berry phase. It is only through the adiabatic inter-soliton pumping of bosons, and the connection to extended 2D system with the adiabatic parameter playing the role of an extra synthetic dimension, that the topological origin of the bound quasi-particles can be neatly understood. We have shown that, despite appearing at the interface of SSB sectors with the same topological Berry phase, these quasi-particles bound to the solitons can be understood, via the pumping scheme, as remnants of protected edge states in 2D that are bound to the boundaries separating synthetic regions with different Chern numbers. This generalized bulk-defect correspondence thus clarifies the topological origin of these quasi-particles via a Kaluza-Klein dimension reduction.

Part III

High-energy physics at ultracold temperatures

Chapter 6

A cold-atom approach to quark confinement

6.1 Introduction: quantum simulation of quantum field theories

Quantum field theory (QFT) provides a unifying framework to understand many-body systems at widely different scales. At the highest energies reached so far, the standard model of particle physics explains all observed phenomena by means of a relativistic QFT of fermions coupled to scalar and gauge bosons [PS95]. At lower energies, non-relativistic QFTs of interacting fermionic and bosonic particles form the core of the standard model of condensed-matter physics [Wen07], which explains a wide variety of phases via Landau's seminal contributions of spontaneous symmetry-breaking (SSB) [Lan37] and quasi-particle renormalization [Lan56]. In the vicinity of certain SSB phase transitions, the quasi-particles governing the long-wavelength phenomena can be completely different from the original non-relativistic constituents [And72], and even be described by relativistic models analogous to those of particle physics. In fact, it is the careful understanding of this quasi-particle renormalization, which yields the very definition of a relativistic QFT [WK74, Wil75, Hol13], and sets the basis for the non-perturbative approach to lattice gauge theories [Wil74, Kog79].

More recently, the range of applications of relativistic theories has been extended to much lower energies, as they also appear in experiments dealing with the coldest type of quantum matter controlled in a laboratory: ultracold neutral atoms [TGU+12, DLR+15, FRT+16, SGB+19, MZH+20, YSO+20] and trapped atomic ions [GKZ+10, GLK+11, MMS+16]. As we introduced in chapter 2, in con-

trast to the case of condensed matter and high-energy physics, cold-atom/trapped-ion experiments deal with quantum many-body systems that can be accurately initialized, controlled, and measured, even at the single-particle level, turning Feynman's idea of a quantum simulator (QS) [Fey82, LSA+07] into a practical reality [BDN12, BR12]. One of the unique properties of cold-atom QSs is the possibility of controlling the effective dimensionality of the model in an experiment. This is particularly important in a QFT context, where interactions tend to be more relevant as the dimensionality is lowered [WK74], bringing in an increased richness in the form of non-perturbative effects. Moreover, the reduced dimensionality sometimes captures the essence of these non-perturbative effects, characteristic of higher-dimensional non-Abelian gauge theories, in a much simpler arena. Some paradigmatic examples of this trend are the axial anomaly of the Schwinger model [Sch62, Man85], the strong-weak duality of the Thirring model [Thi58, Col75], asymptotic freedom and dynamical mass generation in the Gross-Neveu model [GN74], and the fractionalization of charge by solitons in the Jackiw-Rebbi model [JR76]. Therefore, the first QSs of QFTs are targeting models in low dimensions [BC19, ZCR15, DM16, Wie13, BC20, KJL+20].

We note that the flexibility of these platforms offers an exceptional alternative: rather than using the QS to target a QFT already studied in the realm of high-energy physics or condensed matter, one can design the QS to realize new QFTs which, although inspired by phenomena first considered in these disciplines, lead to partially-uncharted territory and give an alternative take on long-standing open problems in these fields. For instance, despite the huge success of the standard model of particle physics, the absence of fractionally-charged quarks from the spectrum still presents unsolved questions in quantum chromodynamics (QCD), such as understanding the specific microscopic mechanism for the confinement of quarks into mesons/hadrons with integer electric charges [Gre20]. One related problem that remains open is the nature of the confinement-deconfinement transitions at finite temperatures/densities [KS03] that lead to phases with isolated quarks and gluons—as well as its relation with the restoration of chiral symmetry [BDH+19]. Unfortunately, gauge theories in (1+1) dimensions are all confining regardless of the Abelian or non-Abelian nature of the gauge group. In higher dimensions, deconfinement is usually driven by four-body plaquette interactions, which are challenging to implement in cold-atom experiments [DYR+17, BBC+20].

In this third part of the thesis, we follow two different approaches to investigate open problems in high-energy physics using cold-atom QSs based on current technology. Similarly to the condensed matter models studied in part II, here we also consider mixtures of ultracold atoms in optical lattices to simulate the relevant phenomena. Once again, topology will play an important role to describe many of these effects, as we will see for the case of quark confinement. In this chapter, rather than looking for QSs of gauge theories, we exploit the aforementioned flexibility of QSs to design new QFTs where characteristic phenomena of higher-dimensional

non-Abelian gauge theories emerge in strongly-correlated phases. In particular, identify a simple lattice model in (1+1) dimensions that regularizes a relativistic Jackiw-Rebbi-type QFT [JR76] where the interplay between dynamical mass generation and charge fractionalization leads to confinement-deconfinement transitions of quark-like quasi-particles, the mechanism of which can be neatly understood at the microscopic level. Although various mechanisms of confinement in QSs have been discussed in the literature [ZR11, ZCR12, TCZL13, TCO+13, BPR+16, RDZ+18, PKI19, LLT+19, TBL+19, BVGM20, NCM20, SMG+20, MDF+20, GCTLB20, CZLT20, LWB+20], to the best of our knowledge, our work identifies for the first time a confinement-deconfinement transition between fractionally-charged quasi-particles. Moreover, the feasibility of our QS proposal with state-of-the-art cold-atom experiments indicates the possibility of experimentally observing this transition, together with other QCD-like phenomena, such as chiral symmetry restoration at finite densities.

In chapter 7.6, we focus instead on a simple gauge theory where spinless fermions are coupled to $\mathbb{Z}_2$ gauge fields on a quasi-one-dimensional geometry. We demonstrate how, even in the absence of a plaquette term, the ground state is in a deconfined phase, that survives, moreover, to large quantum fluctuations due to a frustration phenomenon. This phase presents topological order, that intertwines also with SPT features, giving rise to novel topological effects. These results indicate new paths to access the physics of two-dimensional gauge theories using near-term quantum simulators, offering also the possibility to prepare strongly-correlated phases of matter with interesting topological properties.

The rest of this chapter is organized as follows. In Sec. 6.2, we introduce the Jackiw-Rebbi model and summarize our main results. Starting from a discretized spin-fermion Hamiltonian on a one-dimensional lattice, we show how the continuum quantum field theory emerges in the long-wavelength limit. Moreover, we propose a quantum simulation scheme of this theory using a mixture of ultracold atoms in an optical lattice. In Sec. 6.3, we study the spontaneous breaking of chiral symmetry in the vacuum of the theory, and the corresponding generation of a dynamical mass for the fermionic fields. We derive analytically the phase diagram of the continuum model in the large-spin limit. We then extend these results numerically to the lattice, as well as in the presence of quantum and thermal fluctuations, and show how the latter can restore chiral symmetry. In Sec. 6.4, we analyze the different regimes of quasi-particles that appear on top of the symmetry-broken vacuum. In particular, we calculate the static potential between them, finding how fermionic quasi-particles with fractional charge modify their interactions from repulsive to attractive as we vary one microscopic parameter. The latter corresponds to a deconfinement-confinement transition, as we confirm in the case of non-zero chemical potentials in the thermodynamic limit. Finally, we show how, in the deconfined phase, chiral symmetry is restored even at zero temperature.

6.2 The rotor Jackiw-Rebbi model

In this section, we construct the Jackiw-Rebbi model by first introducing a discretized lattice model, where movable spinless fermions are coupled to spins located on the lattice sites. In Sec. 6.2.1 we describe the main elements of the corresponding Hamiltonian and we compare it to other models used in high-energy physics such as lattice gauge theories. We finish by summarizing the phase diagram of the model, both in the vacuum as well as for finite densities. In Sec. 6.2.2, we present a detailed quantum simulation scheme for the spin-fermion model using a Bose-Fermi mixture of ultracold atoms on a single optical lattice, and show how its whole phase diagram is experimentally accessible. Finally, in Sec. 6.2.3, we take the continuum limit of the lattice model in the long-wavelength regime, establishing a precise connection between the atomic system and the Jackiw-Rebbi quantum field theory.

6.2.1 Lattice discretization

To motivate the nature of our model, we note that imposing non-linear constraints in QFTs is also a source of non-perturbative phenomena that resemble the phenomenology of non-Abelian gauge theories. The $O(N)$ non-linear sigma model, where a vector field is constrained to take values on the $(N-1)$-sphere, also displays asymptotic freedom and dynamical mass generation [Pol75, Kog79], although the latter cannot be accompanied by SSB in (1+1) dimensions [Col73]. Remarkably, the $O(3)$ non-linear sigma model with an additional topological term arises as the long-wavelength description of Heisenberg antiferromagnetic spin chains [Hal83, Aff85]. For leading antiferromagnetic correlations, these systems are effectively described by quantum rotor models, which consist of particles rotating in the surface of a sphere, such that their angular momentum competes with the interactions that favor a collective orientation [Hal83, Aff85, Sac11]. This motivates our study of constrained QFTs involving rotors as mediators of interactions between Dirac fermions.

Let us introduce a (1+1)-dimensional lattice model that can display SSB of a chiral symmetry, leading to dynamical mass generation, which allows, as we will see, the emergence of confinement. We consider a Hamiltonian lattice field theory of fermions $c_i, c_i^\dagger$ and spins $\boldsymbol{S}_i$, both residing at the sites $x_i = ia$ of a 1D chain of N_s sites and length $L = N_\mathrm{s} a$ (see Fig. 6.1). The fermions hop between neighboring sites with tunneling strength t across a potential landscape set by a spin-fermion coupling $\boldsymbol{g} = g\mathbf{e}_z$, and determined by the spin along the quantization axis

$$H = \sum_i \left(-t \left(c_i^\dagger c_{i+1} + c_{i+1}^\dagger c_i \right) + \boldsymbol{g} \cdot \boldsymbol{S}_i \, c_i^\dagger c_i - \boldsymbol{h} \cdot \boldsymbol{S}_i \right). \tag{6.1}$$

Additionally, the spins precess under an external field with both longitudinal and transverse components $\boldsymbol{h} = h_\ell \mathbf{e}_z + h_\mathrm{t} \mathbf{e}_x$, the latter controlling the quantum fluctu-

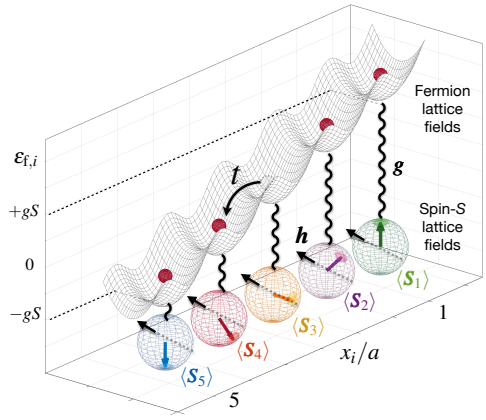

Fig. 6.1 Discretized rotor Jackiw-Rebbi model: Fermions tunnel with strength t against an energy landscape set by the lattice spins $\epsilon_{f,i} = \boldsymbol{g} \cdot \langle \boldsymbol{S}_i \rangle$, which additionally precess under a magnetic field $\boldsymbol{h}$. In the figure, we show a possible configuration of the spins that lead to an energy landscape with a simple gradient. In the text, we show that other configurations that break translational symmetry appear directly in the equilibrium states of the model.

ations of the spins. Although Eq. (6.1) bares a certain resemblance to the Kondo model of fermions coupled to magnetic impurities [Kon64, Kog79], the fermions are spinless in the present case, and there is no continuous $SU(2)$ symmetry in the coupling.

Let us briefly summarize our findings. Dispensing with the continuous O(3) symmetry of the non-linear sigma model [Hal83, Aff85], we show that long-range antiferromagnetic order can take place even in (1+1) dimensions, as it is the result of the breakdown of a discrete chiral symmetry (Fig. 6.2**(a)**). These properties can be neatly understood in the long-wavelength limit, where we find an effective Jackiw-Rebbi-type QFT with rotor fields playing the role of the self-interacting scalar field: a *rotor Jackiw-Rebbi model*. Interestingly, in contrast to the standard Jackiw-Rebbi model [JR76], the SSB does not take place at the classical level, but requires genuine quantum effects that lead to the non-perturbative dynamical generation of a fermion mass. We also explore how different rotor profiles can arise in the ground state by varying the fermion density, which either leads to fractionally-charged or fermion-bag quasi-particles, and proof their stability even in the ultimate quantum limit of spin $S = 1/2$. In fact, we show that the fermion-bag quasi-particles can be understood as confined pairs of fractional charges, resembling the confinement of fractionally-charged quarks in mesons that occurs in the standard model of particle physics (Fig. 6.2**(b)**). Interestingly, we find that

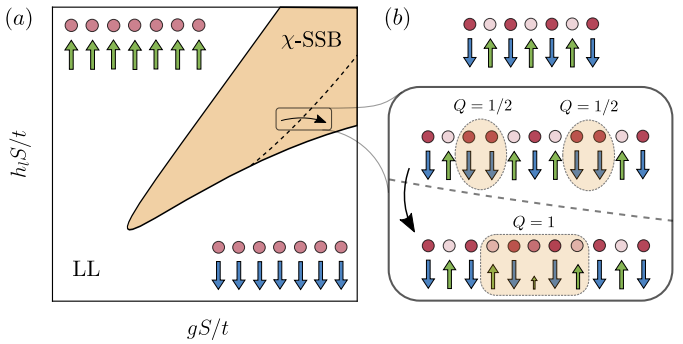

Fig. 6.2 Phase diagram of the rotor Jackiw-Rebbi model: (a) In the figure, we represent qualitatively the different phases that appear in the half-filled vacuum in terms of the interaction g and the longitudinal field h_ℓ, for fixed values of the transverse field h_t and temperature T. Chiral symmetry is spontaneously broken in the shaded region (χ-SSB), where the fermions develop a dynamical mass and the spins display Néel long-range order, as depicted in the upper panel of **(b)**. This region is surrounded by a chiral-symmetric phase with a longitudinal paramagnet for the spins, such that the interacting massless fermions form a Luttinger liquid (LL). **(b)** Within the ordered region, we find two different quasi-particle regimes, separated in the figure by a dashed line. In the first one, deconfined topological defects in the spins bound repulsive quark-like fermions with fractional charges. In the second one, the quasi-particles attract each other, forming meson-like fermion bags with integer charge. For a finite doping density, the two regimes are separated by a first-order confinement-deconfinement phase transition, which coincides with a chiral symmetry restoration due to the proliferation of defects.

a confinement-deconfinement transition can be controlled by tuning a single microscopic parameter, and that this quantum phase transition is associated to the restoration of chiral symmetry by soliton proliferation.

Similarly to lattice gauge theories, in our lattice model (6.1), fermion-fermion interactions are mediated by bosonic fields. However, contrary to the former, our model does not possess gauge invariance, a challenging feature to simulate with atomic resources [BC19]. We show how this simplification allows one to implement the lattice model using state-of-the-art cold-atom QSs in a large regime of realistic experimental parameters. Our results thus show how non-perturbative high energy phenomena, such as charge confinement, could be investigated using minimal experimental resources. Let us start with the proposed scheme for the cold-atom QS.

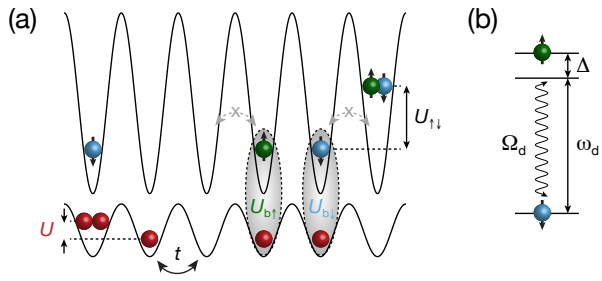

Fig. 6.3 Bose-Fermi quantum simulator: (a) Optical lattice potentials for both the bosonic atoms, here represented by red spheres, and the two-state fermionic atoms, here represented by green (blue) spheres for the $\uparrow$ ($\downarrow$) states. The bosons have a tunneling amplitude t, and the Bose-Hubbard on-site interaction U. Conversely, the fermionic tunneling is suppressed by the very deep lattice, and the Fermi-Hubbard ons-site interaction strength is $U_{\uparrow\downarrow}$. When residing on the same lattice site, bosons and fermions interact with different strengths $U_{b\uparrow} \neq U_{b\downarrow}$. **(b)** Driving that induces Rabi oscillations between the fermionic states with Rabi frequency Ω_d and detuning Δ_d.

6.2.2 Cold-atom quantum simulation

The lattice Hamiltonian (6.1) can be realized with a Bose-Fermi mixture of ultracold atoms confined in spin-independent optical lattices. We focus on the $S = \frac{1}{2}$ case, as it presents fewer requirements and, moreover, all the relevant phenomena already appear in this limit of maximal quantum fluctuations. Notice that the roles of bosonic and fermion degrees of freedom are interchanged here. In particular, we propose to use hard-core bosons to simulate the dynamical fermionic matter, while the fermionic atoms will be used to implement the rotor fields. As will become clear below, this approach is motivated by the specific choice of bosonic and fermionic species, which presents a well-characterized Feshbach resonance that will allow an accurate experimental control of the inter-species scattering, the crucial ingredient in our scheme.

Bose-Fermi Hamiltonian.– We aim at realizing the following grand-canonical Hamiltonian for the Bose-Fermi mixture (Fig. 6.3)

$$H = H_b + H_f + H_{bf}, \tag{6.2}$$

where H_b describes the dynamics of the bosonic atoms of mass m_b, H_f the one of the fermionic atoms of mass m_f, and H_{bf} the interaction between the two species. The bosonic part of the Hamiltonian is defined as follows

$$H_b = -t \sum_i \left(b_i^\dagger b_{i+1} + \text{h.c.} \right) + \frac{U}{2} \sum_i b_i^\dagger b_i^\dagger b_i b_i - \sum_i \mu_i b_i^\dagger b_i ,$$

where b_i and $b_i^\dagger$ are the bosonic creation and annihilation operators acting on lattice site i. This grand-canonical Hamiltonian describes the tunneling of bosonic atoms in a 1D lattice with strength t, and the Hubbard interactions with energy U. Here, $\mu_i = \mu - V_{b,i}$ is expressed in terms of the chemical potential μ and the on-site optical trapping potential $V_{b,i}$, and controls the bosonic filling in the local density approximation. The fermionic contribution can be divided in two parts $H_f = H_f^m + H_f^i$, where the first term describes the external motional degrees of freedom

$$H_f^m = -t_f \sum_{i,\sigma} \left(f_{i,\sigma}^\dagger f_{i+1,\sigma} + \text{H.c.} \right) + U_{\uparrow\downarrow} \sum_i f_{i,\downarrow}^\dagger f_{i,\uparrow}^\dagger f_{i,\uparrow} f_{i,\downarrow} - \sum_i \mu_{i,\uparrow} f_{i,\uparrow}^\dagger f_{i,\uparrow} - \sum_i \mu_{i\downarrow} f_{i,\downarrow}^\dagger f_{i,\downarrow}. \tag{6.3}$$

Here, $f_{i\sigma}$ and $f_{i\sigma}^\dagger$ are the fermionic creation/annihilation operators acting on lattice site i with internal state $\sigma = \{\uparrow, \downarrow\}$. Fermions are trapped in a very deep optical lattice, such that $t_f \ll t$, and we can neglect their tunneling along the 1D lattice during the timescale of interest. They interact with Hubbard interaction $U_{\uparrow\downarrow}$, and their filling is controlled by the local chemical potentials $\mu_{i\sigma} = \mu_\sigma - V_{f,i}$, where μ_σ is the chemical potential for the fermionic atoms in each internal state, and $V_{f,i}$ is an optical trapping potential. In addition, the internal degrees of freedom shall be described by

$$H_f^i = \sum_{i,\sigma} \epsilon_\sigma f_{i,\sigma}^\dagger f_{i,\sigma} + \sum_i \left(\Omega_\text{d} \cos \omega_\text{d} t f_{i,\uparrow}^\dagger f_{i,\downarrow} + \text{H.c.} \right), \tag{6.4}$$

where we have introduced the atomic energy levels $\epsilon_\uparrow, \epsilon_\downarrow$ for the two states of the fermionic species, and a local driving of frequency ω_d that induces local oscillations between these two states with a Rabi frequency Ω_d, where $\hbar = 1$ henceforth. As will become clear below, this driving stems from radio-frequency radiation, which has a negligible momentum, and one can thus neglect recoil effects that would couple the internal and external degrees of freedom. Finally, the interaction between the two species is

$$\hat{H}_{bf} = \sum_i b_i^\dagger b_i \left(U_{b\uparrow} f_{i,\uparrow}^\dagger f_{i,\uparrow} + U_{b\downarrow} f_{i,\downarrow}^\dagger f_{i,\downarrow} \right), \tag{6.5}$$

which describes the on-site interaction between bosonic and fermionic atoms, and depends on the internal spin state of the fermions, i.e. in general $U_{b\uparrow} \neq U_{b\downarrow}$. As will be clear for the particular Bose-Fermi mixture discussed below, there are also boson-fermion scattering processes where the internal states of the fermions is changed by populating other bosonic states such that the total angular momentum along the quantization axis is conserved. Nonetheless, these so-called spin-flipping collisions of strength U_sf are negligible for a sufficiently-large difference of the on-site energies $U_\text{sf} \ll |\epsilon_\uparrow - \epsilon_\downarrow|$.

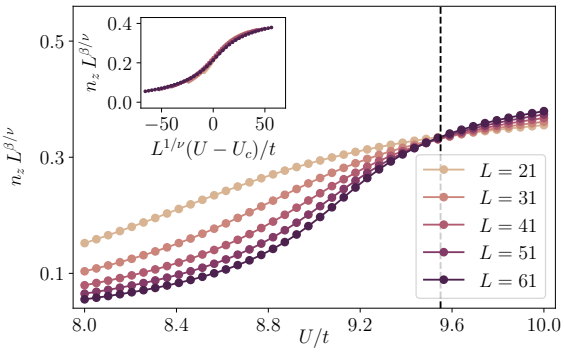

Fig. 6.4 Bosonic mass generation: Order parameter n_z in terms of U/t for the ground state of a finite chain of different lengths L, with $gS/t = 1.0$, $h_\ell S = 0.5t$ and $h_t S/t = 0.05$. The different lines cross at the critical point, consistent with a phase transition in the Ising universality class ($\nu = 1$, $\beta = 1/8$). The inset shows how the rescaled lines collapse into a single one.

Let us now discuss the steps to arrive at the desired model (6.1), and find the relation between the model microscopic couplings and the cold-atom experimental parameters. Using two internal states $|\uparrow\rangle$ and $|\downarrow\rangle$ with different magnetic moments, the energy splitting corresponds to the Zeeman energy and can be tuned via an external magnetic. The driving frequency will be near-resonant and fulfills $\omega_d = (\epsilon_\uparrow - \epsilon_\downarrow) - \Delta_d$, where Δ_d is the so-called detuning. Let us note at this point that the optical trapping potential $V_{f,i}$ of Eq. (6.3) is assumed to be state-independent, which is generally the case, such that it does not modify the above resonance condition, and need not be included in the present discussion. Moving to an interaction picture with respect to

$$H^i_{f,0} = \sum_{i,\sigma} \epsilon_\sigma f^\dagger_{i,\sigma} f_{i,\sigma}, \tag{6.6}$$

the fermionic operators become $f_{i,\sigma} \to f_{i,\sigma}(t) = f_{i,\sigma} e^{-i\epsilon_\sigma t}$. Furthermore, assuming that $|\Omega_d|, |\Delta_d| \ll \omega_d$, we can perform a rotating-wave approximation such that

$$H^i_f(t) \approx \sum_i \left(\frac{\Omega_d}{2} e^{i\Delta_d t} f^\dagger_{i,\uparrow} f_{i,\downarrow} + \text{H.c.} \right). \tag{6.7}$$

Finally, by moving to a frame that rotates with the drive frequency, this Hamiltonian can be written as the following time-independent term

$$\hat{H}^i_f = \sum_i \left(\frac{\Delta_d}{2} \left(\hat{f}^\dagger_{i,\uparrow} \hat{f}_{i,\uparrow} - \hat{f}^\dagger_{i,\downarrow} \hat{f}_{i,\downarrow} \right) + \frac{\Omega_d}{2} \left(\hat{f}^\dagger_{i,\uparrow} \hat{f}_{i,\downarrow} + \hat{f}^\dagger_{i,\downarrow} \hat{f}_{i,\uparrow} \right) \right). \tag{6.8}$$

where we define the Bloch sphere in a way that $\Omega_{\rm d} \in \mathbb{R}$, i.e. we use the phase of the driving as a reference for subsequent measurements. Here, we have introduced the following relation between the fermionic operators in the original Schrödinger picture $f_{i,\sigma}$, and those $\hat{f}_{i,\sigma}$ in the rotating frame

$$\begin{aligned} \hat{f}_{i,\uparrow} &= f_{i,\uparrow} \mathrm{e}^{-\mathrm{i}\left(\epsilon_\uparrow - \frac{\Delta_{\rm d}}{2}\right)t}, \\ \hat{f}_{i,\downarrow} &= f_{i,\downarrow} \mathrm{e}^{-\mathrm{i}\left(\epsilon_\downarrow + \frac{\Delta_{\rm d}}{2}\right)t}, \end{aligned} \tag{6.9}$$

We can now define the following spin-$\frac{1}{2}$ operators in terms of these fermionic annihilation and creation operators

$$\begin{aligned} S_i^z &= \tfrac{1}{2}(\hat{f}_{i,\uparrow}^\dagger \hat{f}_{i,\uparrow} - \hat{f}_{i\downarrow}^\dagger \hat{f}_{i,\downarrow}) = \tfrac{1}{2}(f_{i,\uparrow}^\dagger f_{i,\uparrow} - f_{i,\downarrow}^\dagger f_{i,\downarrow}), \\ S_i^x &= \tfrac{1}{2}(\hat{f}_{i,\uparrow}^\dagger \hat{f}_{i,\downarrow} + \hat{f}_{i,\downarrow}^\dagger \hat{f}_{i,\uparrow}) = \tfrac{1}{2}(f_{i,\uparrow}^\dagger f_{i,\downarrow} \mathrm{e}^{\mathrm{i}\omega_{\rm d} t} + \text{H.c.}). \end{aligned} \tag{6.10}$$

Therefore, to measure the spin operators discussed in the main text, one would have to lock the phase evolution to the one set by the source that drives the transition.

After these derivations, we should enforce that only 1 fermion resides at each lattice site, which can be adjusted by the filling, and maintained by working in the regime where $t_f \ll t$, thus suppressing double occupancies. In this case, we obtain the desired $S = \langle S_i^z \rangle = \frac{1}{2}$ limit. Moreover, since the fermion tunneling t_f is negligible, super-exchange processes stemming from virtual double occupancies occurring at order $t_f^2/U_{\uparrow\downarrow}$ are also negligible, and we can finally arrive at an effective description according to the following grand-canonical Hamiltonian

$$\begin{aligned} \hat{H} = &- t \sum_i \left(\hat{b}_i^\dagger \hat{b}_{i+1} + \text{h.c.} \right) + \frac{U}{2} \sum_i \hat{n}_i(\hat{n}_i - 1) - \sum_i \mu_i \hat{b}_i^\dagger \hat{b}_i, \\ &+ g \sum_i \hat{n}_i S_i^z - \sum_i (h_\ell S_i^z + h_{\mathfrak{t}} S_i^x), \end{aligned} \tag{6.11}$$

where the boson operators are not altered by moving to the rotating frame $\hat{b}_i = b_i$. In the Hamiltonian above, the coupling constant is defined as

$$g = 2(U_{b\uparrow} - U_{b\downarrow}), \tag{6.12}$$

and the external field given by the driving term

$$h_\ell = -\Delta_{\rm d}, \quad h_{\mathfrak{t}} = -\Omega_{\rm d}, \tag{6.13}$$

the specifics of which are discussed below. The local chemical potential μ_i will be adjusted to vary the filling of the bosonic atoms, which is homogeneous in the central region of the trap. The variation of the filling will allow to explore the different quasi-particle regimes discussed in the main text.

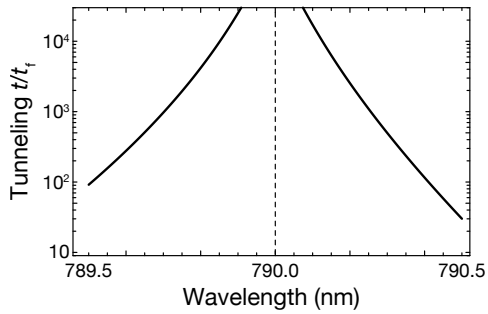

Fig. 6.5 Tunneling ratio t/t_f as a function of the lattice wavelength. The zero crossing of the polarizability of Rb at λ_{bz} is indicated by the dashed vertical line. For the numerical calculation, we have chosen a fixed laser intensity for the lattice, and have tuned it to a regime where $t_f/h \simeq 5\,\mathrm{mHz}$. Since t_f is more or less constant throughout the whole regime, t/t_f illustrates the range of available tunneling couplings for t. This can be optimized further by going to shallower lattice depths.

Softcore bosons.– We can now address the final step in the derivation. Dispensing with the chemical potential, and working in the central region of the trap to neglect the residual on-site potentials, the Hamiltonian associated to Eq. (6.11) coincides with the lattice model (6.1) in the hardcore limit, $U/t \to \infty$, where bosons can be mapped to fermions via the Jordan-Wigner transformation. Nevertheless, we emphasize that the phases investigated in the main text appear also away from this singular point, i.e. for finite values of U/t, provided that the Hubbard interactions are sufficiently strong. This is true in particular for the AF phase found in the fermionic case, which survives away from the hardcore limit, giving rise to the generation of a dynamical mass for strongly-correlated bosons. In Fig. 6.4, we represent the finite-size scaling for the Néel order parameter, and find that the disorder-order transitions occurs for interactions of the order $U_c \approx 10t$. Below this value the soft-core bosons are in a superfluid state, while the spins form a longitudinal paramagnet, similar to the disorder phase in the hardcore limit. Moreover, we find the the phase transition is also in the Ising universality class.

Once all the steps for the derivation of the target model (6.11) have been discussed for a generic cold-atom setting, let us estimate the specific parameters for a mixture of bosonic ^{87}Rb and spinfull fermionic ^{40}K atoms, and discuss the viability of the experimental realization. The following main ingredients are relevant for the implementation:

Optical lattice potential.– The dominant transitions of the two alkali atoms, bosonic ^{87}Rb and fermionic ^{40}K are

$$\begin{aligned} \lambda_{\mathrm{Rb,D2}} &\simeq 780\,\mathrm{nm}, \quad \lambda_{\mathrm{Rb,D1}} \simeq 795\,\mathrm{nm} \\ \lambda_{\mathrm{K,D2}} &\simeq 767\,\mathrm{nm}, \quad \lambda_{\mathrm{K,D1}} \simeq 770\,\mathrm{nm} \end{aligned} \tag{6.14}$$

which allows for widely tunable polarizabilities and optical-lattice potentials. In order to achieve a large separation of timescales, it is desirable to achieve a large ratio of the tunneling couplings t/t_f, where t is the strength of the tunnel coupling for the bosonic species, and t_f denotes the spin-independent tunneling amplitude of the fermionic species. In essence, this means that the lattice potential experienced by the bosonic species should be much weaker compared to the one seen by the fermionic atoms. In order to reduce off-resonant photon scattering, which would result in additional heating, at the same time the detuning from any internal transition has to be maximized. Due to the large fine-structure splitting of Rb, there is a convenient tuning range around the zero crossing of the polarizability at $\lambda_{bz} = 790\,\mathrm{nm}$. This range offers both a wide tunability of the tunneling ratio t/t_f (Fig. 6.5) and a large detuning from all resonances to minimize heating. Notice that a similar strategy was used in chapter 3 to simulate the rotor SSH model with a Bose-Bose mixture. Contrary to that case, here the periodic potential for both species is not shifted, so they reside on the same lattice sites.

Tunable interspecies interactions.– In order to provide good control over the parameter g (6.12) that appears in the effective Hamiltonian (6.11), we propose to make use of the well-calibrated and easily-accessible interspecies Feshbach resonance between the absolute ground states $|F = 1, m_F = 1\rangle$ of ^{87}Rb and $|\uparrow\rangle \equiv |F = 9/2, m_F = -9/2\rangle$ of ^{40}K [SZD+08]. Although there does not seem to be a Feshbach resonance nearby to tune the scattering length between the ground state of Rubidium and $|\downarrow\rangle \equiv |F = 9/2, m_F = -7/2\rangle$ of ^{40}K, the interaction parameter g can still be fully tuned over a wide range of values as shown in Fig. 6.6, as it depends on the difference of scattering lengths. In this figure, we have plotted the scattering length $a_{b\uparrow}$ according to

$$a_{b\uparrow}(B) = a_{bg}\left(1 - \frac{\Delta}{B - B_0}\right) \tag{6.15}$$

based on the theoretical values reported in Ref. [SZD+08], i.e. $B_0 = 546.75(6)\,\mathrm{G}$, $\Delta = -3.1\,\mathrm{G}$ and $a_{bg} = -189\,a_0$, where a_0 is the Bohr radius.The on-site interspecies interaction energy is determined by

$$U_{b\sigma} = \frac{2\pi\hbar^2 a_{b\sigma}}{\mu_{b\sigma}} \int |w_b(\mathbf{r})|^2 |w_f(\mathbf{r})|^2 \mathrm{d}^3\mathbf{r}, \tag{6.16}$$

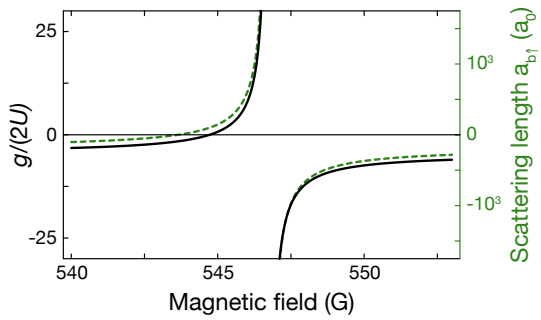

Fig. 6.6 Ratio of interactions strengths gS/U as a function of magnetic field. The tunability here stems from the tunability of the interspecies scattering length $a_{b\uparrow}$, here shown in green and defined in Eq. (6.15).

where $\mu_{b\sigma} = m_{\mathrm{Rb}} m_{\mathrm{K}}/(m_{\mathrm{Rb}} + m_{\mathrm{K}})$ is the reduced mass and $m_{\mathrm{Rb}} = 86.9\,u$ is the mass of one ^{87}Rb atom and $m_{\mathrm{K}} = 39.96\,u$ the mass of one ^{40}K atom; u is the atomic mass unit. The functions $w_b(\mathbf{r})$ and $w_f(\mathbf{r})$ denote the Wannier functions of Rb and K respectively, which are different because the two species see a lattice potential of different depth. Through these expressions, we can obtain the parameter g, as discussed below.

Interaction ratio gS/U.– Rubidium in its absolute ground state has a scattering length of $a_b \simeq 100.4\,a_0$, and the on-site Hubbard interaction is defined as

$$U = \frac{4\pi\hbar^2 a_b}{m_{\mathrm{Rb}}} \int |w_b(\mathbf{r})|^4 \mathrm{d}^3\mathbf{r}, \tag{6.17}$$

Neglecting the contribution from the Wannier functions, which is dependent on the lattice depth, we can achieve a wide tunability as illustrated in Fig. 6.6, where we plot $gS/U \approx \frac{a_{b\uparrow}(m_{\mathrm{Rb}}+m_{\mathrm{K}})}{2a_b m_{\mathrm{K}}}$ as a function of the external magnetic field.

Coupling between spin states.– Let us now discuss the specifics of the driving term discussed previously. The external fields $h_\ell, h_{\mathfrak{t}}$ can be realized with a radio-frequency or two-photon microwave transitions at frequency ω_{d} almost resonant with the Zeeman energy difference $\Delta E^Z_{\uparrow,\downarrow} = \epsilon_{i,\uparrow} - \epsilon_{i,\downarrow}$ between $|\uparrow\rangle$ and $|\downarrow\rangle$ atoms. For the Feshbach resonance shown in Fig. 6.6, the resonance occurs at B_0, which corresponds to $\Delta E^Z_{\uparrow,\downarrow}/h \approx 80\,\mathrm{MHz}$, where h denotes Planck's constant. The energy offset h_ℓ is then realized by detuning the coupling frequency from resonance, i.e. $h_\ell = \Delta E^Z_{\uparrow,\downarrow}/\hbar - \omega_{\mathrm{d}}$. With single-photon transitions, Rabi frequencies $\Omega_{\mathrm{d}}/2\pi$ of several 10 kHz can be easily achieved, which corresponds to the regime $|h_{\mathfrak{t}}| = |\Omega_{\mathrm{d}}| \gg t$. Moreover, the pair of states $|\uparrow\rangle$ and $|\downarrow\rangle$ is well isolated from the other

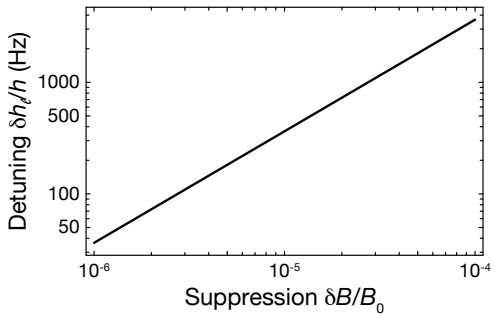

Fig. 6.7 Detuning of the microwave transition δh_ℓ**.** The residual detuning is technically limited by magnetic field fluctuations δB. Estimating the residual detuning serves as a lower bound for the coupling strength ω and the control over the detuning h_ℓ.

internal states, even in the presence of this coupling. The energetically closest transition is between the levels $|\downarrow\rangle$ and $|F = 9/2, m_F = -5/2\rangle$, which is detuned by $\sim 5\,\mathrm{MHz} \gg \Omega_\mathrm{d}/h$.

For some of the proposed phenomena, it is desirable to tune the coupling in order to enter the regime where h_t is on the order of the tunnel coupling t. The level of control one can achieve is limited by the stability of the magnetic field that defines the Zeeman shift $\Delta E^Z_{\uparrow,\downarrow}$. We have calculated the detuning from resonance δh_ℓ that occurs due to an imperfect control of the external magnetic field (Fig. 6.7). It has been demonstrated that the fluctuations in the external field can be suppressed below 3×10^{-6}, as reported in Ref. [JDPC17]. The most sensitive regime occurs for $h_\ell = 0$, where the lower bound for h_t would be on the order of a few 100 Hz, which coincides with typical experimental values for t. Note, that the typical timescale for these fluctuations is large compared to the duration of the experiment, hence, the detuning δh_ℓ can be assumed constant but will fluctuate between individual experimental realizations.

To summarize, we have presented detailed calculations of all the relevant parameters for the Rb-K mixture, demonstrating a wide range of experimentally tunability. We would like to emphasize that the above ingredients have been realized in current cold-atom experiments, and the QS of the model (6.1) is thus realistic. We believe that the main experimental challenge will likely be the preparation of extended regions in the lattice with the proper filling for the bosons and fermions. In the sections below, we give a detailed account of the results summarized above about the equilibrium states and low-energy quasi-particles of the Hamiltonian (6.1). When discussing these particular phenomena, we will comment on specific probing techniques and the temperatures that would be required to observe them. Let us start by describing these effects by means of an effective

long-wavelength theory.

6.2.3 Continuum limit

We now derive the continuum Hamiltonian QFT that captures the low-energy properties of the lattice model (6.1) at half filling, this is, with fermionic density $\rho = \frac{1}{N_s}\sum_i \langle c_i^\dagger c_i\rangle = 1/2$, which will be considered as the vacuum state in the following. As customary in various (1+1)-dimensional systems [Hal81], one starts by linearizing the dispersion relation to obtain a Tomonaga-Luttinger model [Tom50, Lut63]. In this case, this amounts to a long-wavelength approximation around the Fermi points $\pm k_F = \pm\pi/2a$, such that $c_i \approx \mathrm{e}^{-\mathrm{i}k_F x_i}\sqrt{a}\psi_+(x) + \mathrm{e}^{+\mathrm{i}k_F x_i}\sqrt{a}\psi_-(x)$ is expressed in terms of slowly-varying right- and left-moving fermion fields $\psi_\pm(x)$. As detailed in Appendix B.1, this can be recast in terms of the staggered-fermion discretization of lattice gauge theories [KS75], where one identifies the Fermi velocity $v_\mathrm{F} = 2ta$ as the effective speed of light $c = v_\mathrm{F}$. To proceed with the continuum limit, the spin operators are also expressed in terms of slowly-varying fields $\boldsymbol{S}_i \approx \cos(k_\mathrm{N} x_i) S\boldsymbol{n}(x) + a\boldsymbol{\ell}(x)$ with $k_N = \pi/a$, corresponding to the Néel $\boldsymbol{n}(x)$ and canting $\boldsymbol{\ell}(x)$ fields [Hal83, Aff85]. Performing a gradient expansion and neglecting rapidly-oscillating terms yields $H = \int \mathrm{d}x \mathcal{H}(x)$ with

$$\mathcal{H} = \overline{\Psi}(x)\left(-\mathrm{i}c\gamma^1\partial_1 + \boldsymbol{g}_s\cdot\boldsymbol{n}(x)\right)\Psi(x) + (\boldsymbol{g}j_0(x) - \boldsymbol{h})\cdot\boldsymbol{\ell}(x), \tag{6.18}$$

where $\overline{\Psi}(x) = \Psi^\dagger(x)\gamma^0$ is the adjoint for the spinor $\Psi(x) = (\psi_+(x), \psi_-(x))^\mathrm{t}$, the gamma matrices are $\gamma^0 = \sigma^x$, $\gamma^1 = -\mathrm{i}\sigma^y$, and the charge-density is $j_0(x) = \overline{\Psi}(x)\gamma_0\Psi(x)$. Additionally, we have introduced the coupling $\boldsymbol{g}_s = gS\mathbf{e}_z$, and $\partial_1 = \partial/\partial x$.

This relativistic QFT (6.18) can be understood as a Jackiw-Rebbi-type of model [JR76], in which a Yukawa term couples the fermion-mass bi-linear $\overline{\Psi}(x)\Psi(x)$ to the Néel field $\boldsymbol{n}(x)$, instead of the standard Yukawa coupling to a scalar field $\phi(x)$. Additionally, the rotor dynamics is determined by the precession of the canting field under $\boldsymbol{g}_s j_0(x)/S - \boldsymbol{h}$, instead of the more familiar $\lambda\phi^4$ term of the Jackiw-Rebbi QFT. Hence, this precession includes the back-action of the matter field onto the mediating fields via the charge density. In the large-S limit, and in phases dominated by Néel correlations, $\boldsymbol{n}(x)$ and $\boldsymbol{\ell}(x)$ represent, respectively, the orientation and angular momentum of a quantum rotor lying on the unit sphere, such that this QFT (6.18) can be understood as a rotor Jackiw-Rebbi (rJR) model. In contrast to the standard rotor model [Sac11], neighboring rotor fields are not coupled via $O(N)$-symmetric interactions, but rotor-rotor couplings will instead be generated through their coupling to the Dirac fields, and vice versa. As shown below, the lack of a continuous symmetry in Eq. (6.18) plays a crucial role, and makes the physics of the rJR model very different form these $O(N)$ counterparts.

If the spins order according to a Néel pattern $\langle n_z(x)\rangle \neq 0$, fermions will acquire a mass by the SSB of the discrete chiral symmetry $\Psi(x) \to \gamma^5\Psi(x)$ with $\gamma^5 = \sigma^z$,

and $n_z(x) \to -n_z(x)$. However, in contrast to the JR model [JR76], this chiral SSB cannot be predicted classically by looking at the symmetry-broken sectors of the scalar field, i.e. the double-well minima of the classical potential in the $\lambda\phi^4$ theory. In our case, the bare rotor term only describes precession of the rotor angular momentum, and does not include a collective coupling of the rotors that would induce Néel order already classically. Instead, in closer similarity to the Gross-Neveu model [GN74], chiral SSB shall occur by a *dynamical mass generation* that can only be accounted for by including quantum effects (i.e. rotor-fermion loops). On the other hand, there are important differences, as the Gross-Neveu model uses an auxiliary Hubbard-Stratonovich field [Col85], whereas our rotor fields represent real degrees of freedom with their intrinsic quantum dynamics. As discussed below, this will lead to crucial differences for the chiral SSB, the quasi-particle spectrum, and confinement.

6.3 Dynamical mass generation

In this section, we study the phenomenon of dynamical mass generation associated to the spontaneous breaking of chiral symmetry in the theory's vacuum. In Sec. 6.3.1, we show how this SSB takes place in a region of the quantum field theory phase diagram, and uncover the non-perturbative character of this process using a large-S expansion. In Sec. 6.3.2, we study the effect of quantum fluctuations, and calculate numerically the phase diagram of the lattice model for various values of S. Finally, in Sec. 6.3.3, we include thermal fluctuations, and show how the restoration of chiral symmetry shrinks the region in parameter space where the fermion fields have a non-zero mass.

6.3.1 Large-S limit

Using a coherent-state basis [Rad71, Fra13], as discussed in App. B.2, the partition function $\mathsf{Z} = \int \mathrm{D}[\overline{\Psi}, \Psi, \boldsymbol{n}, \boldsymbol{\ell}] \mathrm{e}^{-\mathsf{S}_\mathrm{E}}$ can be expressed in terms of an action $\mathsf{S}_\mathrm{E} = \int \mathrm{d}^2x \mathcal{L}(\boldsymbol{x})$ with the Lagrangian

$$\mathcal{L} = \overline{\Psi}(\boldsymbol{x}) \left(\hat{\gamma}^\mu \partial_\mu + \boldsymbol{g}_s \cdot \boldsymbol{n}(\boldsymbol{x})\right) \Psi(\boldsymbol{x}) + (\boldsymbol{g} j_0(\boldsymbol{x}) - \boldsymbol{h}) \cdot \boldsymbol{\ell}(\boldsymbol{x}). \tag{6.19}$$

Here, $\boldsymbol{x}$ is a 2-dimensional Euclidean space with imaginary time $x^0 = c\tau = c(\mathrm{i}t)$, and $x^1 = x$, and the Euclidean gamma matrices are $\hat{\gamma}^0 = \gamma^0, \hat{\gamma}^1 = -\mathrm{i}\gamma^1$. The Dirac and adjoint spinors are Grassmann-valued fields $\Psi(\boldsymbol{x}) = (\psi_+(\tau, x), \psi_-(\tau, x))^\mathrm{t}$, $\overline{\Psi}(\boldsymbol{x}) = (\psi_-(\tau, x), \psi_+(\tau, x))$, and the charge density is the Grassmann bi-linear $j_0(\boldsymbol{x}) = \overline{\Psi}(\tau, x)\hat{\gamma}_0\Psi(\tau, x)$. Likewise, the spins lead to constrained vector fields which, in the large-S and Néel-dominated limits, correspond to the position $\boldsymbol{n}(\boldsymbol{x})$ and angular momentum $\boldsymbol{\ell}(\boldsymbol{x})$ of a collection of rotors with

$$\boldsymbol{n}(\boldsymbol{x}) \cdot \boldsymbol{n}(\boldsymbol{x}) = 1, \quad \boldsymbol{n}(\boldsymbol{x}) \cdot \boldsymbol{\ell}(\boldsymbol{x}) = 0. \tag{6.20}$$

Since the Lagrangian (6.19) is quadratic in Grassmann fields, the fermions can be integrated out to obtain an effective action for the rotor fields $\mathsf{S}_{\text{eff}} = -\log\left(\int \mathrm{D}[\overline{\Psi},\Psi]\mathrm{e}^{-\mathsf{S}_{\text{E}}}\right)$. In analogy to the Gross-Neveu model [GN74], where dynamical mass generation can be derived by assuming a homogeneous auxiliary field, we consider $\boldsymbol{n}(\boldsymbol{x}) = \boldsymbol{n}$, $\boldsymbol{\ell}(\boldsymbol{x}) = \boldsymbol{\ell}$, $\forall \boldsymbol{x} \in (0,\beta] \times (0,L]$. As shown in App. B.3, the functional integral leads to

$$\mathsf{S}_{\text{eff}} = \beta L\left(\left(\frac{\boldsymbol{g}}{2} - \boldsymbol{h}\right)\cdot\boldsymbol{\ell} - \frac{(\boldsymbol{g}_s\cdot\boldsymbol{n})^2}{4\pi c}\left(\log\left(\frac{\Lambda_{\text{c}}}{\boldsymbol{g}_s\cdot\boldsymbol{n}}\right)^2 + 1\right)\right), \tag{6.21}$$

where we have introduced the UV cutoff $\Lambda_{\text{c}} = 2t$ set by the bandwith of the bare fermion dispersion on the lattice (6.1).

Exploiting the analogy to the Gross-Neveu model [GN74], where one deals with N flavors of Dirac fermions and finds the non-perturbative dynamical mass generation in the $N \to \infty$ limit, we will send $S \to \infty$ to determine the non-perturbative phase diagram quantitatively. Since phases not governed by Néel correlations can also appear, and we are interested in possible quantum phase transitions transitions thereof, we must relax the first constraint in Eq. (6.20). By considering the explicit construction of the rotor fields in terms of the spin coherent states, we find the Néel and canting fields

$$\begin{aligned}\boldsymbol{n} &= \frac{1}{2}(\sin\theta_A - \sin\theta_B)\mathbf{e}_z - \frac{1}{2}(\cos\theta_A - \cos\theta_B)\mathbf{e}_x,\\ \boldsymbol{\ell} &= \frac{S}{2a}(\sin\theta_A + \sin\theta_B)\mathbf{e}_z - \frac{S}{2a}(\cos\theta_A + \cos\theta_B)\mathbf{e}_x.\end{aligned} \tag{6.22}$$

The fields are thus parametrized by $\theta_A, \theta_B \in [0,\pi]$, each of which represents the angle of the spin coherent state associated to the A (odd sites) and B (even sites) sub-lattice, pointing along the great circle contained in the xz plane (see Fig. 6.1). One can check that the second constraint in Eq. (6.20) is readily satisfied $\boldsymbol{n}\cdot\boldsymbol{\ell} = 0$, whereas the first one will only be recovered in Néel-dominated phases $\theta_A \approx -\theta_B = \pm\pi/2$, where $\boldsymbol{n}\cdot\boldsymbol{n} \approx 1$.

By inspecting the effective action (6.21), one finds that it is proportional to $\mathsf{S}_{\text{eff}} = \beta L S \mathsf{V}_{\text{eff}}(\theta_A,\theta_B)$, such that the large-$S$ limit is obtained through the saddle-point equations $\boldsymbol{\nabla}_\theta \mathsf{V}_{\text{eff}}|_{\boldsymbol{\theta}^\star} = \mathbf{0}$. The features of the phase diagram can be understood in two complementary regimes: *(a)* For $h_{\mathsf{t}}/t \gg h_\ell/t, g/t$, the saddle-point equations will be solved by $\theta_A^\star = \theta_{\text{B}}^\star = \pi$, such that all spins are maximally polarised in the direction of the leading transverse field $|\mathsf{g}_{\mathsf{tP}}\rangle = \otimes_i |S,S\rangle_{x,i}$, where $|S,m\rangle_{\alpha,i}$ is the common eigenstate of $\boldsymbol{S}_i^2, S_i^\alpha$ with eigenvalues $S(S+1)$, and $m \in \{-S,-S+1,\cdots,S\}$, respectively. This state can thus be understood as a disordered *transverse paramagnet*, with all spins aligned along the equator of Fig. 6.1. Since $\langle n_z\rangle = 0$, there is no mass generation, and the chiral symmetry remains intact. Therefore, the fermionic sector will correspond to a *metallic Luttinger liquid*.

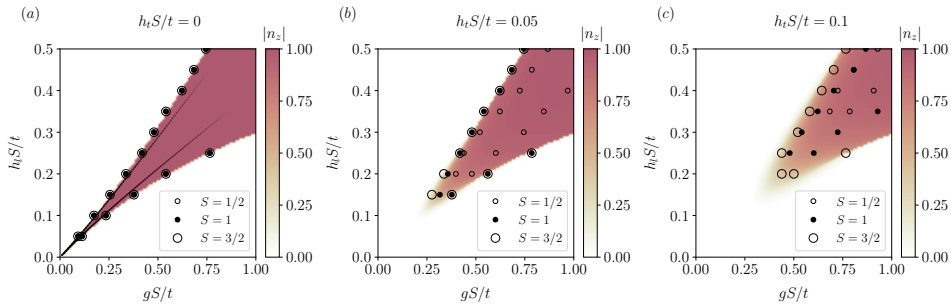

Fig. 6.8 Dynamical mass generation at finite S: In the background of the different phase diagrams represented in the figure, we show the absolute value of n_z calculated with the HF method for a periodic chain of $N_s = 64$ sites and $N_f = 32$ fermions. The different dots correspond to the critical points separating the AF from the LL phase, obtained using iDMRG for various values of S. **(a)** When quantum fluctuations are absent, all the points coincide with the HF solution and the large-S predictions for the whole phase diagram. The solid lines correspond to the solution obtained using the large-S expansion in the continuum model (6.23), agreeing with the lattice critical lines for small values of gS/t. **(b)** In the presence of finite quantum fluctuations, the HF solution departs from the correct ground state, although it provides a good approximation even for small values of S in the case of small fluctuations. **(c)** The AF region shrinks as $h_t S/t$ increases, and it does it faster for smaller values of S. However, this phase can always be found, even in the limit $S = 1/2$, provided that gS/t and $h_\ell S/t$ are sufficiently large.

(b) For $h_t/t \ll h_\ell/t, g/t$, we find a competition between two distinct phases. If $h_\ell > h_\ell^+$ or $h_\ell < h_\ell^-$, where we have introduced

$$h_\ell^\pm = \frac{g}{2} \pm \frac{t}{\pi S}\left(\frac{gS}{2t}\right)^2\left(\log\left(\frac{2t}{gS}\right) + \frac{1}{2}\right), \tag{6.23}$$

the saddle-point equations are solved by $\theta_A^\star = \theta_B^\star = \pi/2$ or $\theta_A^\star = \theta_B^\star = -\pi/2$, respectively. These correspond to disordered *longitudinal paramagnets* with ground states $\left|\mathsf{g}_{\ell\mathsf{P}}^+\right\rangle = \otimes_i \left|S, S\right\rangle_{z,i}$, or $\left|\mathsf{g}_{\ell\mathsf{P}}^-\right\rangle = \otimes_i \left|S, -S\right\rangle_{z,i}$, with all spins pointing towards the north or south poles of Fig. 6.1, respectively. Once again, since $\left\langle \mathsf{g}_{\ell\mathsf{P}}^\pm \right| n_z \left|\mathsf{g}_{\ell\mathsf{P}}^\pm\right\rangle = 0$, there is no mass generation and the fermions are described by a massless Luttinger liquid. If $h_\ell^- < h_\ell < h_\ell^+$, the saddle points correspond to $\theta_A^\star = -\theta_B^\star = \pm\pi/2$, which yields two *Néel antiferromagnets* $\left|\mathsf{g}_{\mathsf{N}}^\pm\right\rangle = \otimes_{i\in A} \left|S, \pm S\right\rangle_{z,i} \otimes_{i\in B} \left|S, \mp S\right\rangle_{z,i}$, in which chiral symmetry is spontaneously broken, yielding $\left\langle \mathsf{g}_{\mathsf{N}}^\pm \right| n_z \left|\mathsf{g}_{\mathsf{N}}^\pm\right\rangle = \pm 1$ respectively. In both cases, the spins of Fig. 6.1 alternate between the north and south poles, and the Dirac fermions acquire a mass dynamically, accompanied by a so-called scalar condensate

$$\langle \overline{\Psi}\Psi \rangle = \langle \psi_+^\dagger(x)\psi_-(x) + \psi_-^\dagger(x)\psi_+(x)\rangle = \Sigma_0. \tag{6.24}$$

Since the spinor components $\psi_\pm(x)$ correspond to the long-wavelength excitations around momenta $\pm k_\mathrm{F} = \pm\pi/2a$, the scalar condensate of the continuum QFT leads to a periodic modulation of the lattice density $\langle c_i^\dagger c_i \rangle = \frac{1}{2} + (-1)^i \Sigma_0 a$. This phase is reminiscent of a charge-density wave insulator in electron-phonon systems. However, in these systems, Peierls' argument shows that the 1D metal is always unstable towards the insulator [Pei55], instead of showing different phases separated by quantum critical lines, as occurs for our rotor Jackiw-Rebbi QFT (6.23). Let us remark once more that, while in the standard JR model [JR76] chiral SSB can be understood by means of perturbation theory about the classically SSB sectors in $g \ll 1$, the mass is dynamically generated in our case, and cannot be understood perturbatively, which can be appreciated by the fact that the $\log(St/g)$ dependence in Eq. (6.23) cannot be Taylor expanded for small g.

6.3.2 Quantum fluctuations and Ising universality class

Let us now benchmark the above large-S calculations with numerical results based on a Hartree-Fock (HF) [GV08] self-consistent mean-field method, and a matrix-product-state (MPS) [Sch11, HP18] formulation of the density-matrix renormalization group (DMRG) [Whi92]. This serves a two-fold purpose: on the one hand, both methods are directly applied to the discretized model on the lattice (6.1), and can thus be used to identify the parameter regime where the continuum QFT predictions (6.21) are recovered. On the other hand, the quasi-exact MPS method gives direct access to corrections of the large-S predictions for finite values of $S \in \{\frac{3}{2}, 1, \frac{1}{2}\}$, testing the dynamical mass generation in the regime of large quantum fluctuations. Likewise, we can adapt the HF method to non-zero temperatures T and chemical potentials μ in order to explore the role of thermal fluctuations and finite densities (see Appendix A.2).

Figure 6.8 contains our results for the zero-temperature half-filling phase diagram as a function of $(gS/t, h_\ell S/t)$ for various values of the transverse field $h_\mathrm{t} S/t$. In the background, we represent the Néel order parameter, $n_z = \frac{2}{N_\mathrm{s}} \sum_x \mathbf{e}_z \cdot \boldsymbol{n}(x)$, obtained by averaging over the Néel field $\boldsymbol{n}(x) = \frac{1}{2S} (\langle \boldsymbol{S}_{2i} \rangle - \langle \boldsymbol{S}_{2i-1} \rangle)$. In Fig. 6.8**(a)**, one can see how the HF predicts an intermediate region, here depicted in red, displaying antiferromagnetic long-range order $n_z \approx 1$ due to the SSB of the discrete chiral symmetry. In order to test the validity of our QFT predictions based on the phenomenon of dynamical mass generation, we benchmark these numerical results against the critical lines of Eq. (6.23), which are depicted as solid black lines in Fig. 6.8**(a)**. In analogy to the large-N limit of other strongly-coupled QFTs [Col85], we must rescale the coupling to obtain physical results for $S \to \infty$, such that gS remains finite. From the comparison of the HF and large-S results, we understand that it is the regime of $gS \ll t$ (i.e. couplings much smaller than the UV cutoff), where we can recover the continuum QFT from the lattice discretization, as

typically occurs in asymptotically-free lattice field theories.

Note that, in fact, the lattice theory already agrees with the continuum predictions for intermediate couplings $gS \sim 0.25t$, which is a sensible fraction of the UV cutoff, and signals the wide validity of the aforementioned scheme of dynamical mass generation. It is worth mentioning, however, that the SSB mechanism that yields the Néel phase is valid for an even wider range of parameters. Indeed, around any of the critical lines of Fig. 6.8**(a)**, there will be an effective continuum QFT, albeit with different renormalized parameters that require us to rely on numerical methods or experimental QSs. This wider parameter regime is useful in light of the cold-atom realization presented above, which will be able to probe antiferromagnetic correlations in a regime more favorable than the one set by super-exchange mechanisms [DDL03, TCF+08, GUJ+13, BHS+16, MCJ+17, DJB+20]. In particular, for larger values of gS, the order survives to larger temperatures, as we will also show below.

The generation of a dynamical mass described in this section can be implemented following the previous cold-atom scheme, and experimentally probed using standard detection techniques. In particular, the scalar condensate (i.e. charge-density-wave ordering) can be readily probed by measuring the imbalance $I = (n_A - n_B)/(n_A + n_B)$ between the occupation of Rb atoms on A- and B-sublattices by using superlattices [SSAJP06, FTC+07, TCF+12] or via noise correlations [FGW+05, RBvO+06, YSO+20]. The antiferromagnetic Néel ordering can be further revealed by evaluating the imbalance observable, or the noise correlations, for the fermionic K atoms in a spin-resolved manner, which requires separating the two hyperfine states during the detection by means of a Stern-Gerlach sequence [TCF+08], or other similar techniques [TCS+10, GUJ+13]. Since in the SBB phase, however, there are two energetically-degenerate configurations shifted by one lattice site, and the experiment will consist of many independent copies of the one-dimensional chains, the ensemble-averaged observables may fail to signal the phase transition without an additional term that weakly breaks the symmetry between the configurations. If a small symmetry-breaking field cannot be globally introduced in all these copies, one may resort to a combination with quantum gas microscopy [BPT+10, SWE+10, MCJ+17, KHB+20, HOJZ20], which now also enables full spin and charge read-out.

Let us now explore the effect of finite S and non-zero h_{t}. In Fig. 6.8**(a)**, the circles represent the critical values of the SSB phase transition for different values of S, and are obtained with the MPS method based on the iDMRG scheme for an infinite chain [HP18]. These critical points are estimated by localizing the divergence of the spin susceptibility, $\chi_S = \partial n_z/\partial(gS/t)$, where we use bond dimension $D = 200$ and a four-sites repeating unit cell. As can be observed in the figure, for a vanishing transverse field, the critical points for different S are all arranged along the same critical line which, furthermore, delimits the Néel-ordered phase obtained with the HF method, and agrees with the large-S predictions (6.23) in

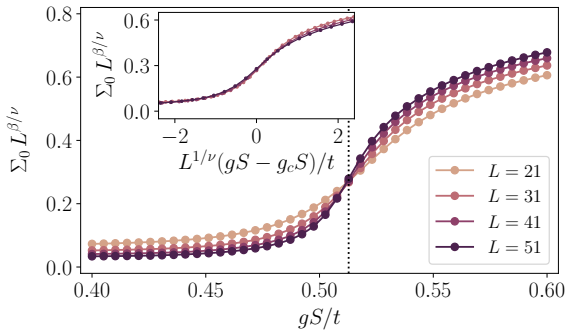

Fig. 6.9 Scalar condensate and chiral SSB: We represent the scalar fermion condensate $\Sigma_0 = \langle\overline{\Psi}\Psi\rangle$ in terms of gS/t for the ground state of a half-filled chain of different lengths N_s, with $h_\ell S = 0.3t$ and $h_t S = 0.05t$. The results are obtained using DMRG for $S = 1/2$. Using the critical exponents of the 2D Ising universality class ($\nu = 1$, $\beta = 1/8$), the lines cross at the critical point obtained for the infinite system with iDMRG, and collapse for an appropriate rescaling (inset).

the regime where we expect to recover the continuum QFT from the lattice regularization. We note that, in our model, changing the value of the spin S for a vanishing $h_t = 0$, does not modify the quantum fluctuations, such that the large-S prediction works equally well for any value of S. This contrasts the typical situation in models with $O(3)$ symmetry, where the the classical limit is associated with $S \to \infty$, and quantum fluctuations appear as soon as S is finite. Moreover, as outlined in the appendix, we confirm that there is no qualitative distinction in the underlying physics for integer or half-integer spins, as occurs for models with a continuous $O(3)$ rotational symmetry.

In Figs. 6.8**(b)** and **(c)**, we represent the phase diagram as the transverse field is switched on, which introduces quantum fluctuations on the spins. In this limit, we observe how the long-range Néel phase shrinks as a result of the competing quantum fluctuations. We also observe that, as the value of S increases, a better agreement with the HF and QFT predictions is obtained, confirming the generic expectation. Note that this agreement is remarkable, given that the considered values of the spins S are still very far away from the large-S limit.

So far, our numerical benchmark has focused on the SSB captured by the Néel field. Let us note, however, that the dynamical mass generation refers to the fermionic sector, and the gap opening is associated to an underlying non-zero scalar condensate $\Sigma_0 = \langle\overline{\Psi}\Psi\rangle$. In order to extract the value of this condensate from the lattice simulations, we use $\Sigma_0 = \frac{1}{N_s}\sum_i (-1)^i \langle c_i^\dagger c_i\rangle$, where the expectation value is calculated with the MPS ground state obtained using a DMRG algorithm with bond dimension $D = 200$ for finite chains of variable length $L = N_s a$ and unit

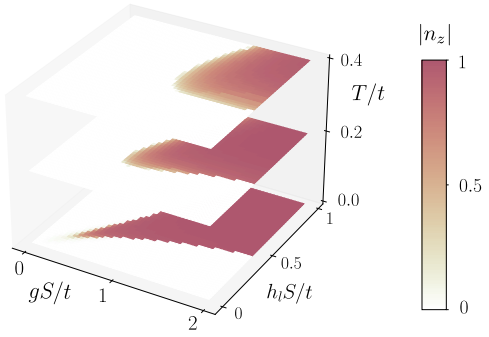

Fig. 6.10 Chiral symmetry restoration at finite temperatures: Phase diagram for different T/t and $h_tS = 0.05t$, where we represent the Néel order parameter n_z calculated in the HF approximation. The AF phase, where chiral symmetry is spontaneously broken, shrinks as the temperature increases. In the high-energy-physics lore, one says that chiral symmetry is restored at high temperatures.

lattice spacing $a = 1$. In Fig. 6.9, we represent the finite-size scaling for the scalar condensate of the $S = 1/2$ model. The crossing of the lines in the main panel serve to locate the critical point of the model gS_c/t, which agrees with our previous iDMRG results based on the Néel order parameter. Hence, this shows that the chiral-SSB occurs via the simultaneous onset of a Néel antiferromagnet and a scalar fermion condensate, which corresponds to a charge density wave as seen from the lattice perspective. Moreover, these results allow us to identify the universality class of the corresponding chiral phase transition. As proved by the data collapse shown in the inset of Fig. 6.9, the critical exponents correspond to those of the (1+1) Ising universality class.

6.3.3 Thermal fluctuations and chiral symmetry restoration

Let us now move on to the study of the corrections due to thermal fluctuations. In Fig. 6.10, we represent sections of the phase diagram as a function of $(gS/t, h_\ell S/t)$ for several values of the temperature T obtained with the HF method. One can observe how the area that encloses a dynamically-generated mass, characterized by the Néel order parameter n_z, shrinks with increasing T. Therefore, for sufficiently high temperatures, the chiral SSB phase would eventually disappear in favor of the disordered paramagnet and the massless Dirac fermions, both of which respect the chiral symmetry.

As shown in Fig. 6.10, the required temperature scale for a robust observation of the different phases may lie above that of the tunnel coupling t, which is a very promising feature of our QS scheme. Using state-of-the-art cooling techniques,

temperatures as low as $T/t = 0.2$ have been reported for two-component Fermi gases [MCJ+17] and $T/U = 0.05$ for bosonic atoms [YSH+20]. As displayed in Fig. 6.10, the dynamical mass generation leading to the anti-ferromagnetic order and the scalar condensate can be accessed at larger temperatures $T/t \sim 0.4$. The underlying reason is that the onset of antiferromagnetic correlations does not rest on the super-exchange mechanism, the scale of which is $t^2/U \ll U$. In our case, the mechanism is the dynamical breaking of chiral symmetry, the scale /gap of which is directly set by the interaction coupling $g \sim U_{bf}$, which can be on the order of the Rb-K interactions U_{bf}.

Let us now interpret these results in light of *thermal chiral symmetry restoration* in the standard model. In particular, for a large region of its phase diagram, the vacuum of QCD is expected to break spontaneously a chiral symmetry associated to the quarks' flavor [CW80]. This mechanism is confirmed experimentally by the measured mass of light baryons, such as protons and neutrons, where chiral symmetry breaking yields the largest contribution to their masses [Wil99], while only a small part comes from the masses of their constituent quarks. On the other hand, at very high temperatures or densities, corresponding to the first instants after the Big Bang or to the dense core of neutron stars, respectively, chiral symmetry is restored and quarks become massless, as shown in experiments involving heavy-ion collisions [RW00]. This phenomenon is captured by several effective theories of nucleons, such as the Nambu-Jona-Lasinio quantum field theory [NJL61a] and, as discussed above, also occurs in our model.

There are, however, several unsolved questions in QCD regarding the restoration of chiral symmetry. One is whether a phase transition at finite T_c or a crossover exists for intermediate values of the baryon chemical potential μ_B [BEF+14]. Another one and is the relation to the deconfinement of quarks where, instead of forming hadronic bound states, deconfinement gives rise to a so-called quark-gluon plasma [KS03]. For large values of μ_B, it is not known if both transitions occur simultaneously or, alternatively, intermediate phases exist [MP07]. Many effective theories, however, fail to address these questions, since they do not include any confinement mechanism even if they correctly capture the essence of dynamical mass generation. As we show in the next section, our model presents such confinement-deconfinement phase transition between fractionally-charged quasi-particles, allowing for the investigation of the interplay between the latter and chiral symmetry restoration in a simple setup.

6.4 Emergent quarks and mesons

In this section, we departure from the half-filled vacuum of the Jackiw-Rebbi model, and study the properties of the system when extra particles are added. In Sec. 6.4.1, we dope the system in the ordered phase with one fermion, and find a regime

where the latter fractionalised into two deconfined fermionic quasi-particles bound to topological defects of the rotor field. We calculate the static potential between them, and show how it changes from repulsive to attractive in a different parameter region. This attractive potential confine the quark-like emergent quasi-particles, forming mesons with integer charge. In Sec. 6.4.2, we investigate these two regimes for a finite density of extra particles, establishing well-defined deconfined and confined phases in the thermodynamic limit. Finally, in Sec. 6.4.3, we show how these are separated by a first-order phase transition, associated also to the restoration of chiral symmetry, and how these effects could be investigated by modifying a single experimental parameter.

6.4.1 Confinement of fractionally-charged quasi-particles

As mentioned before, the fundamental fields of the QCD sector of the standard model correspond to fractionally-charged fermion fields, the so-called quarks, coupled to bosonic Yang-Mills fields, the so-called gluons [PS95]. In contrast, the fundamental fields of our model (6.18) are fermion fields with integer charges coupled to the constrained Néel and canting fields. As noted in the introduction, however, the renormalised quasi-particles of a strongly-coupled QFT may sometimes differ completely from its fundamental constituents. As shown below, our QFT (6.18) displays a Jackiw-Rebbi-like mechanism of fractionalisation [JR76], whereby soliton configurations of the Néel field host localized fermions with a fractional charge $q = \pm e/2$, which will play the role of quarks, allowing us to discuss various aspects of a confinement mechanism.

In Figs. 6.11**(a)-(b)**, we present the MPS numerical results for the real-space configurations of the Néel lattice field $n_z(j) = \frac{1}{2S}(\langle S^z_{2j}\rangle - \langle S^z_{2j-1}\rangle)$, and the integrated fermion charge above the half-filled vacuum $N(j) = Q(j)/e = \sum_{i<j}(\langle c^\dagger_i c_i\rangle - \frac{1}{2})$ when one extra fermion is introduced above half filling. These figures show that the Néel field presents a kink-antikink pair that interpolates between the different SSB sectors, and that each of these topological solitons hosts a localized fermionic excitation with charge $q = e/2$, henceforth referred to as a 'quark' by the analogy with the fractionally-charged fundamental fermion fields of QCD. We note that similar quasi-particles with charges $q = -e/2$ would appear for dopings below half filling, playing the role of 'anti-quarks', and that quark-antiquark pairs could appear in the vacuum due to thermal fluctuations, as they correspond to higher-energy states of the theory.

Contrary to the general situation in (1+1) lattice gauge theories, which can only host confining phases [Gre20], we can find regimes where quarks/anti-quarks can be confined/deconfined depending on the microscopic parameters. In order to explore this phenomenon, let us remark that the distance of the pair of quarks of Fig. 6.11**(b)** is determined by the external pinning of the Néel solitons of

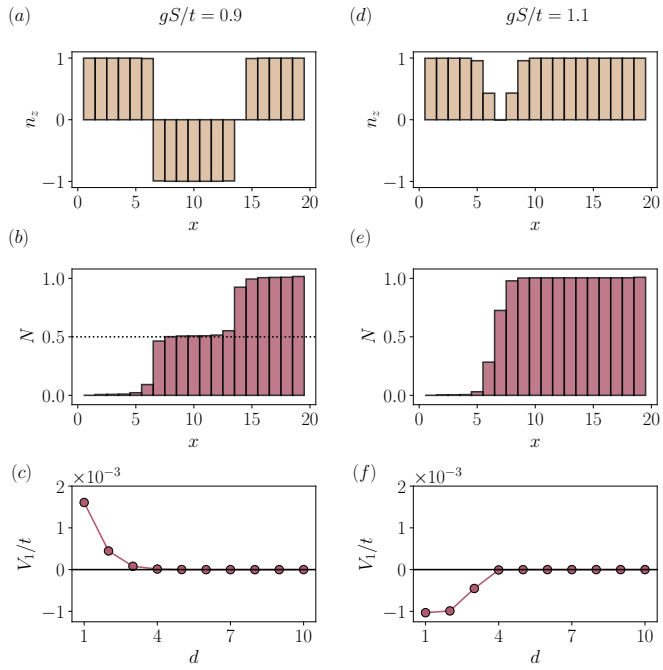

Fig. 6.11 Fractionalization and confinement: (a) Space dependence of n_z in the ground state of a chain with $N_\mathrm{s} = 41$ sites and $N_\mathrm{f} = 22$ fermions, for $gS/t = 0.9$, $h_\ell S/t = 0.4$ and $h_\mathrm{t} S/t = 0.01$. Two solitons appear on the otherwise homogeneous configuration found at half filling. **(b)** The accumulated particle density shows how each defect carries a fermion with fractional charge $e/2$. **(c)** The solitons repel each other at short distances, implying that the composite soliton-charge quasi-particles are deconfined. **(d)** At larger values of gS/t, solitons merge forming a quark-bag quasi-particle with integer charge **(e)**. **(f)** In this case, the potential energy between the solitons is attractive, indicating a transition to a confined phase.

Fig. 6.11**(a)**. We introduce an external potential that breaks explicitly the translational invariance and localizes the solitons, which would otherwise travel freely through the chain, at the desired positions,

$$H_\epsilon = -\sum_i \epsilon_i(d) S_i^z, \tag{6.25}$$

with

$$\epsilon_i(d) = \begin{cases} \epsilon(-1)^i & 1 \le i < i_0 \\ \epsilon(-1)^{i+1} & i_0 \le i < i_0 + d \\ \epsilon(-1)^i & i_0 + d \le i \le N_s. \end{cases} \tag{6.26}$$

This field breaks translational invariance and pins two solitons, and the associated fractional fermionic charges, to positions i_0 and $i_0 + d$. This pinning makes our fractionally-charged quasi-particles static, such that we can discuss the analogue of the static quark potential [Bal01]. We note that it is a standard practice in lattice gauge theories to use this terminology whether or not the charges actually correspond to dynamical quarks [Gre20]. Therefore, the static quark potential quantifies the interaction energy between any pair of static charges as their distance is modified, giving information about confinement not only in QCD, but in other effective models.

In our model, the static quark potential $V_1(d) = E_1(d) - E_0$ can be obtained using the MPS numerics by calculating the energy $E_1(d)$ of the doped system with an extra fermion that fractionalizes into a pair of quarks pinned at a distance d, measured in unit cells $(2a)$, with respect to the energy E_0 of a pair pinned far apart $(d \gg 1)$. We note that the standard situation of (1+1) lattice gauge theories, such as the Schwinger model [Sch62], is that the preservation of gauge symmetry requires that the static charges must be connected through an intermediate electric-field string, such that the energy increases with the separation d and leads to a linearly-increasing static quark potential [CJS75, BHV+16]. In our case, the situation is completely different, as the energy of the deformed Néel field that connects the two quarks in Fig. 6.11**(c)** is independent of the pinning distance, and confinement is thus not enforced a priori. As argued below, there exists a competing mechanism that either favors confinement or deconfinement depending on the microscopic parameters of the model.

In Fig. 6.11**(c)**, we depict the distance-dependence of the static quark potential for the $S = 1/2$ rotor Jackiw-Rebbi model for coupling $gS/t = 0.9$, and setting the other parameters such that we lie in the chiral-SSB phase. As can be observed in this figure, the potential decreases with the distance for small soliton separations, which means that the quarks repel each other. Hence, in the absence of the external pinning, the fractionally-charged quasi-particles would move freely at large distances from each other, and thus appear as asymptotic excitations in the spectrum of the rJR QFT. As we increase the coupling to $gS/t = 1.1$, Figs. 6.11**(d)-(e)** show that a completely-different quasi-particle emerges. In this case, the Néel field no longer interpolates between the two SSB sectors, but is instead suppressed within a small region of space where, as shown in Fig. 6.11**(e)**, an integer-charged fermion is localised. This situation is reminiscent of the so-called quark bag models [CJJ+74, BCD+75], where quarks and gluons are locked within a finite region of space, in which a phenomenological term that compresses the bag compensates the outward pressure of the quarks that are held inside, and confinement results from the competition of these two terms. The present situation is closer in spirit to the soliton quark model [FL77a, FL77b], where the fermions deplete a SSB condensate in a finite region of space, gaining kinetic energy at the expense of the cost of deforming the condensate. In our case, as the Néel field vanishes in the inner

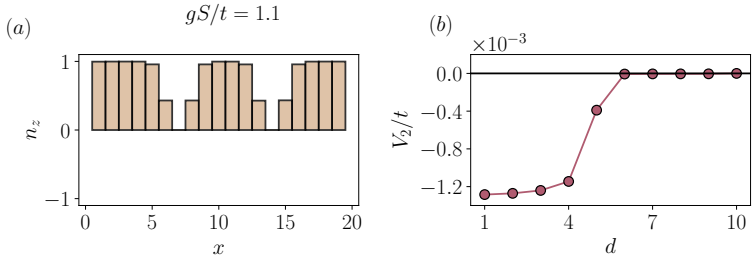

Fig. 6.12 Static quark-bag potential: (a) Real-space configuration of the Néel field $n_z(x)$ in the ground state of a chain with $N_\mathrm{s} = 41$ sites and $N_\mathrm{f} = 23$ fermions, this is, two fermions above half filling, for $gS/t = 1.1$, $h_\ell S/t = 0.4$ and $h_\mathrm{t} S/t = 0.01$. The two quark-bag quasi-particles are pinned at a certain distance d (see main text). **(b)** The potential energy between them decreases with the distance, and the minimum is reached when they are located at neighbouring sites.

region, there scalar condensate will become zero $\Sigma_0(x) = 0, \forall x \in [x_0 - \xi, x_0 + \xi]$, such that the bound fermions have a vanishing dynamically-generated mass, increasing their kinetic energy and the outward pressure. As mentioned above, this is compensated by the energy cost due to the inhomogeneous layout of the Néel field and the accompanying scalar condensate.

To substantiate this neat picture and connect it to the quark confinement, we should provide evidence that the integer-valued charges shown in Fig. 6.11**(e)** are the result of an attractive force between the fractionally-charged quasi-particles of Figs. 6.11**(a)-(b)**. This evidence of confinement is supported by the numerical results presented in Fig. 6.11**(f)**, where we show that the static quark potential increases with the inter-quark distance in this case. Hence, as advanced in the introduction, it is possible to understand the microscopic confinement mechanism in our model. In the regime $g < g_\mathrm{c}$, the outward pressure of the quarks overcomes the inner force that tends to re-establish the homogeneity of the condensate, such that the quarks get deconfined and can move synchronous with the kin/antikink. This changes for $g > g_\mathrm{c}$, where the inward force to reestablish condensate homogeneity prevails, and the quarks get confined within the so-called quark bag. For $h_\ell S/t = 0.4$ and $h_\mathrm{t} S/t = 0.01$, we estimate a critical value of this confinement-deconfinement phase transition to be $g_\mathrm{c} S/t \approx 1.01$ (see Fig. 6.13).

We note that similar integer-charged excitations occur in other QFT with a non-classical scalar condensate due to chiral-SSB, such as the Gross-Neveu model [CJJ+74]. However, to the best of our knowledge, there is no deconfinement transition where they become a pair of fractionally-charged fermions and, additionally, they require at least two fermion flavors to exist, which anyway masks the occurrence of fractionalization as happens for polyacetilene [SSH79, CB82].

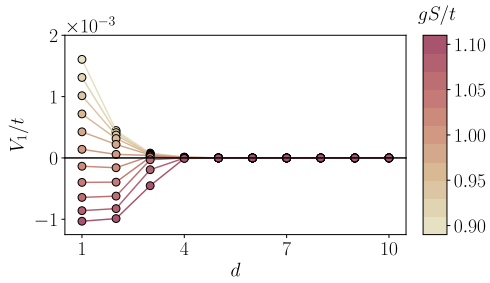

Fig. 6.13 Deconfinement transition and quark-bag instability: (a) Potential energy between two defects pinned at a distance d (see main text) for a chain with $N_\mathrm{s} = 41$ sites and $N_\mathrm{f} = 22$, at $h_\ell S = 0.4t$, $h_\mathrm{t} S = 0.01t$ and $\epsilon S = 0.02t$. As gS/t is increased, the repulsive potential between two solitons turns into an attractive one, signaling a deconfinement-confinement transition.

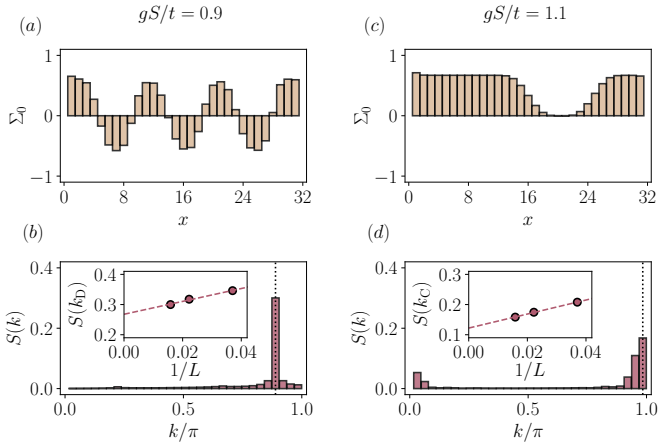

Fig. 6.14 Quark crystal and phase separation: (a) Space dependence of the scalar condensate Σ_0 in the ground state of a chain with $N_\mathrm{s} = 63$ sites and $N_\mathrm{f} = 35$ fermions, for $gS/t = 0.9$, $h_\ell S/t = 0.4$ and $h_\mathrm{t} S/t = 0.01$. For a finite density of particles above half filling, the deconfined quarks rearrange forming an ordered structure. **(b)** Long-range order can be detected using the structure factor $S(k)$, which shows a peak at a momentum commensurate with the fermionic density, $k_\mathrm{D}/\pi = 2N_\mathrm{f}/N_\mathrm{s}$. **(c)** In the confined phase, the attractive quark bags create an extensive region where the dynamical fermionic mass is screened to zero. **(d)** In this case, the peak at k_D disappears, while $S(k)$ is non-zero around $k_\mathrm{C} = \pi$, signaling a reduced but non-vanishing AF order. The insets show the finite-size scaling of the peak in $S(k)$ for each case, where the density is kept fixed.

6.4.2 Quark crystals and chiral symmetry restoration

Let us now move towards finite densities, and explore the rJR ground state properties in the confined and deconfined regimes. In the deconfined regime, we have shown that the isolated quarks repel each other, such that they will maximize the inter-quark distance and broaden the density profiles if left unpinned. Accordingly, for finite fermion densities above the half-filled vacuum, one would expect the formation of a crystalline structure of equidistant kinks and anti-kinks with the corresponding periodic distribution of fractionally-charged fermions, namely a *quark crystal*.

On the other hand, in the confined regime, we have no a priori intuition of the possible ground state ordering. To gain such intuition, let us first calculate the static potential between two distant quark-bag excitations, each of which contains a pair of confined quarks and thus an integer-charged fermion. The static bag potential can be obtained using the MPS numerics by considering in this case the energy of the system doped with a pair of fermions that are held inside the bags $E_2(d)$, and pinned at a distance d, $V_2(d) = E_2(d) - E_0$, where E_0 is again the energy of two quark bags pinned far apart. In order to fix the quark-bag distance as depicted in Fig. 6.12**(a)**, we impose again an external potential that localises them at two given locations, this is, using now a parallel field (6.25) with

$$\epsilon_i = \epsilon \left[(-1)^i - 2\delta_{i,i_0} - 2\delta_{i,i_0+d}\right]. \tag{6.27}$$

Our numerical results show that the static fermion-bag potential of Fig. 6.12**(b)** increases with the inter-bag distance, proving that the quark-bags attract each other. Therefore, if left unpinned, we expect that the two bags will merge yielding a wider depletion region of the condensate that can accommodate two integer-charged fermions, each of which can be thought of being composed of two confined quarks. This trend can be generalized to finite density regimes, where we expect the appearance of an extensive quark bag that is sufficiently wide to host all of the extra fermions. In the context of ultracold atoms, this phase can be understood as a phase separation phenomenon.

Let us now confirm this intuition by presenting the MPS numerics for the finite-density regime. In Fig. 6.14**(a)** and **(c)**, we display the real-space dependence of the scalar condensate for the deconfined and confined regimes without the pinning potentials. As can be clearly observed, Fig. 6.14**(a)** presents a periodic sequence of kinks and antikinks, each of which hosts a single localized quark, giving rise to the aforementioned quark crystal. On the other hand, as we increase the coupling strength, Fig. 6.14**(c)** displays an extensive region where the Néel field vanishes, and the dynamical fermionic mass is screened to zero. This wide bag accommodates for all the extra fermions, leading to a phase separation with respect to the region where the vacuum displays a large dynamically-generated mass inhibiting the penetration of the massless confined quarks.

We note that the corresponding phases can be quantitatively distinguished by means of the static spin structure factor $S(k) = \frac{1}{N_s^2}\sum_{i,j}\langle S_i^z S_j^z\rangle e^{ik(i-j)}$, which will peak at different momenta k_D, k_C for the deconfined/confined phases. For the deconfined quark crystal, Fig. 6.14**(b)** shows that the corresponding peak of the structure factor occurs for a momentum that is commensurate with the fermionic density modulation of the scalar condensate $k_D = 2\pi N_f/N_s$. Conversely, for the confined phase-separated bag phase, Fig. 6.14**(d)** shows that the peak at k_D vanishes, and one gets instead a non-zero structure factor around $k_C = \pi$, signaling Néel order, which is partially broadened by the condensate deformation due to the quark bag. The inset of both figures displays the finite-size scaling of each peak, where we increase both the size N_s and the number of fermions N_f, such that the density $\rho = N_f/N_s$ remains fixed. The extrapolated non-zero values of the corresponding peaks for $1/L \to 0$ show that the quark-crystal and phase-separated bag phases are both stable in the thermodynamic limit.

The vanishing value of of the structure factor at momentum $k = \pi$ in the quark crystal suggests the possibility of a zero-temperature *quantum chiral symmetry restoration* for finite dopings—since this quantity is equivalent to the Néel order parameter n_z used in our discussion of thermal chiral symmetry restoration for the rJR vacuum. This is confirmed by calculating the average value of the fermionic condensate $\overline{\Sigma}_0 = \frac{1}{N_s}\sum_i \Sigma_0(i)$, where we get $\overline{\Sigma}_0 = 0.06$ and $\overline{\Sigma}_0 = 0.48$ for the parameters used in Fig. 6.14**(a)** and Fig. 6.14**(b)**, respectively. In this case, it is not the thermal fluctuations, but instead the finite density of topological solitons, which reduces the average value of the fermionic condensate to zero (up to finite-size effects), indicating that chiral symmetry is restored in the quark-crystal phase. In this phase, therefore, chiral symmetry coexists with deconfinement. The situation is analogous in QCD, where both properties appear in the quark-gluon plasma. The presence of a single transition from this phase to a confined symmetry-broken phase, or the possibility of intermediate phases with only one of these properties, is still an open question in particles physics [MP07]. The investigation of such interplay in simple models could help to gain a better understanding of it in more complicated theories, specially in regimes where the chemical potential is large and Monte Carlo simulations suffer from the sign problem [BEF+14].

Let us thus explore this interplay in the presence of thermal fluctuations. Figure 6.15 depicts the HF phase diagram for a finite density of fermions over the half-filled vacuum for different values of T/t. To distinguish the two phases, we use as an order parameter the difference between the structure factor at the two different momenta of the confined and deconfined phases, $\mathcal{O} = S(k_C) - S(k_D)$. This quantity is zero in the disordered paramagnetic phase, which corresponds to a Luttinger liquid, as in the case of half filling. Positive and negative finite values of $\mathcal{O}$ corresponds, on the other hand, to the quark-bag and quark-crystal phases, respectively. For $T/t = 0$, we can clearly distinguished these three phases.

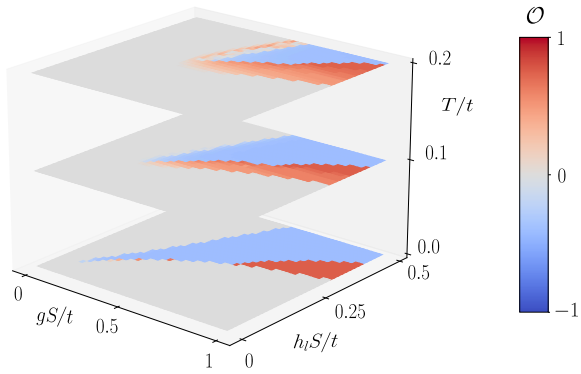

Fig. 6.15 Deconfinement and chiral symmetry restoration: Phase diagram for different values of T/t obtained in the HF approximation for a periodic chain with $N_s = 64$ sites and $N_f = 35$ fermions, with $h_t S = 0.01t$. The order parameter $\mathcal{O}$ (see main text) allows us to distinguish between the three different phases that appear for a finite doping. As the temperature increases, the phase transition line between the quark-bag and the quark-crystal phases gets modified, until both of them disappear at a sufficiently high value of T/t.

Note that, it is only in the ordered phases, surrounded by a disorder LL, where the notion of confinement and deconfinement of fractionally-charged quasi-particles is well defined. Within this region, we observe that both the quark-bag and the quark-crystal phases have a finite extension, with a phase transition line separating them. The ordered region shrinks as the temperature increases (Fig. 6.15). It is interesting to notice that, in our model, the quark crystal disappears more rapidly than the quark-bag phase.

6.4.3 Confinement-deconfinement phase transition

As we have shown in the previous sections, a characteristic feature of our (1+1)-dimensional QFT (6.18) is the possibility to understand the mechanism of confinement microscopically and, moreover, the existence of a deconfinement quantum phase transition as we vary the microscopic parameters. In order to study the latter in more detail, we make use again of the static structure factor peaks, which serve as order parameters to detect the corresponding phase transitions. In this section, we study two different types of phase transitions occurring at finite densities with DMRG, confirming the results obtained above using the HF method. The first one, corresponding to Fig. 6.16**(a)**, describes the transition between the quark crystal and a longitudinal paramagnetic phase. As shown in this figure, following the the spin structure factor at the two characteristic momenta k_D and k_C, one can see that

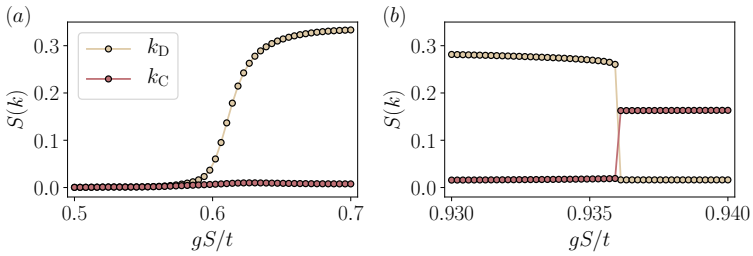

Fig. 6.16 Deconfinement phase transitions: Structure factor at $k_D = 2\pi N_f/N_s$ and $k_C = \pi$ as a function of gS/t for a chain with $N_s = 63$ sites and $N_f = 35$ particles, at $h_\ell S = 0.4t$ and $h_t S = 0.01t$. **(a)** In this case, $S(k_D)$ serves as an order parameter, signaling a direct transition between a disorder LL and an ordered quark crystal, while $S(k_C)$ remains zero all the way. **(b)** At higher values of gS/t, we observe a deconfinement-confinement transition between the two ordered phases, the quark crystal and the quark bag, where both $S(k_D)$ and $S(k_C)$ are the respective order parameters.

we start from a disordered phase at small interactions, where both $S(k_D)$ and $S(k_C)$ are zero. As gS/t increases, the quark crystal order parameter reaches a non-zero value $S(k_D) > 0$, while $S(k_C)$ remains zero. This phase transition is continuous, similarly to the direct order-disorder transition we found for half filling. For larger values of gS/t, we find another phase transition, again in correspondence with the HF results. Fig. 6.16**(b)** shows the transition between the deconfined quark crystal $S(k_D) > 0, S(k_C) = 0$ towards the confined quark-bag phase $S(k_D) = 0, S(k_C) > 0$. In this case, this deconfinement transition is a first-order phase transition. This is believed to be the case also for the confinement-deconfinement transition in QCD at finite chemical potential. For $h_\ell S/t = 0.4$ and $h_t S/t = 0.01$, this transition is located at $g_c S/t = 0.94$, which roughly agrees with the prediction we obtained using the static quark potential (i.e. $g_c S/t = 1.01$). The difference shows the presence of many-body effects in the case of a quark crystal, where the interaction between two quarks is influenced by the presence of a finite density of them. This agreement supports our claim that the mechanism behind the transition between a quark crystal and a quark-bag phase is the confinement of quark-like fractional quasi-particles.

6.5 Summary

In this chapter, we have studied several high-energy non-perturbative phenomena using a neat (1+1) quantum field theory, the rotor Jackiw-Rebbi model, and proposed a quantum simulation scheme using a Fermi-Bose mixture of ultracold atoms in an optical lattice. Dirac fermions, whose interactions are mediated by spin-S ro-

tors in this model, acquire a dynamical mass through the spontaneous breaking of chiral symmetry. The generation of a mass term in the theory is accompanied here by antiferromagnetic order in the rotors, that we predict analytically in the large-S limit of the continuum model. Using a lattice model that regularizes the theory, we study the phase diagram at half filling in the presence of quantum and thermal fluctuation, showing how dynamical mass generation, in particular, survives in the ultimate quantum limit of $S = 1/2$. We have also shown how, in this limit, the chiral symmetry breaking quantum phase transition lies in the Ising universality class and, moreover, we observed chiral symmetry restoration at sufficiently high temperatures.

We then focused on the regime of finite chemical potentials, where we find a confinement-deconfinement phase transition between quark bags and a crystal of fractional quark-like quasi-particles. This transition is characterized using the spin structure factor, and its microscopic origin is uncovered by means of the static quark potential. We have also shown how deconfinement coexists with a restoration of chiral symmetry, even in the absence of thermal fluctuations. In this case, the latter occurs due to a proliferation of topological solitons at finite densities, drawing an interesting analogy to the quark-gluon plasma of QCD. Our results indicate how confinement between fractional charges could be further investigated in atomic experiments, shedding light into one of the long-standing questions of particle physics.

In the future, it would also be interesting to use matrix-product-state simulations to study real-time dynamics, serving as alternative benchmark for quantum simulations in addition to the finite-density regime hereby studied, where Monte Carlo simulations for a single flavor of fermion fields are expected to suffer from the sign problem. The model can also be easily extended to higher dimensions, where the simulation proposal can be generalized in a straightforward manner by using higher-dimensional optical lattices, which would also reach the limits of efficient tensor-network numerical techniques. It is precisely in the cases where numerical simulations show limitations where cold atoms represent an efficient alternative to provide a full solution of the quantum many-body problem.

Chapter 7

Near-term gauge-theory quantum simulators

7.1 Introduction: topological order and gauge invariance

As we have emphasized in different occasions along this thesis, understanding quantum many-body systems is generally a hard problem, as their complexity increases exponentially with the number of constituents. However, as we have seen, exotic collective phenomena may arise from this large complexity. A prominent example are the so-called spin liquids, phases of matter that evade spontaneous symmetry breaking, and thus long-range order [Lan37], down to the lowest possible temperatures [And87, Mis10, Bal10]. In spite of this, spin liquids can be characterized by a different notion of order: topological order [Wen17]. As we reviewed in chapter 2, systems with topological order have degenerate ground-states, the number of which depends on the underlying topology. Each ground-state is a strongly-correlated state, as witnessed by the multipartite long-range entanglement among the constituents [KP06, LW06]. Besides, the ground-state manifold is separated from the rest of the spectrum by a finite energy gap and, more importantly, only non-local perturbations can act non-trivially within it. It is thus a natural subspace to encode quantum information, and a promising route for fault-tolerant quantum computers [Kit03, NSS+08].

Unfortunately, topological order is very elusive and tends to be fragile, as witnessed by the few materials where it has been observed, requiring in many cases extremely low temperatures and very high purity in the samples [HHC+12, WYL+19]. In this chapter, we identify a promising route to prepare robust topologically-

ordered states in cold-atom systems using gauge invariance.

Gauge theories, used to describe strong, weak and electromagnetic interactions [Kog79], have local symmetries that cannot be broken spontaneously [Eli75], evading thus the standard form of ordering. For this reason [Fra13], emergent gauge theories also play an important role in long-wavelength descriptions of non-standard phases of matter, such as high-T_c superconductors [BA88] and frustrated magnets [RS91]. Formally, gauge theories can be described through Hamiltonians that commute with an extensive number of local symmetry operators forming a group, the gauge group [KS75].

Pure gauge theories describe the physics of gauge bosons, the generalization of photons to arbitrary gauge groups [YM54], and host different phases that can be characterized by the potential that the bosons mediate between test charges [Kog79, Gre11]. In a deconfined phase, as we saw in chapter 6, particles generated in pairs of opposite charge can be separated arbitrarily far away with a finite energy cost. Conversely, there can also exist confined phases where this potential energy increases linearly with the distance. In chapter 6 we studied these phases from an emergent point of view. Here we look directly at gauge theories where these phases also appear. At the end of chapter 1, we introduced the $\mathbb{Z}_2$ or Ising gauge theory (IGT) [Wil74], the simplest gauge theory on the lattice. This theory already gives rise to a confined-deconfined phase transition without spontaneous symmetry breaking [Weg71], where the very nature of this deconfined phase is the key underlying Kitaev's toric code [Kit03], a spin-liquid phase allowing for topological quantum error correction and fault-tolerant quantum computing [Ter15]. It is thus important, both from fundamental and applied perspectives, to study the fate of the IGT deconfined phase and, more generally, its full phase diagram as perturbations are introduced [Kit03, TWT+07, HL08, VDS09, TV11]. Understanding such phase diagrams when the gauge fields interact with matter fields, either bosonic or fermionic, is generally a very hard problem with longstanding open questions [Kog79]. In the simplest case, the topologically-ordered deconfined phase of the IGT coupled to dynamical $\mathbb{Z}_2$ matter can be understood through the toric code perturbed by both parallel and transverse fields [FS79, Kit03, VTSD09, TKPS10]. While the corresponding phase diagram is known since the late 70s [FS79], exchanging $\mathbb{Z}_2$ for fermionic matter leads to a much richer scenario, which is only beginning to be explored [AG16, GRV17, PLM17, GAS+18, KCT19].

These connections have fueled a multi-disciplinary effort towards, not only improving our understanding of these lattice gauge theories (LGTs), but also realizing them experimentally, either in natural or in synthetic quantum materials, such as cold atoms in optical lattices [LSA17]. In these systems, atoms are very dilute and primarily interact by s-wave scattering. Trapping the atoms by an optical lattice allows to reach the strongly-interacting regime, but the interactions are still limited to be on-site [BDZ08]. This fact constitutes a major hurdle when trying to realize lattice gauge theories with ultra-cold atoms [BC19, Wie13, ZCR15, DM16], as they

require interactions between all the atoms connected through elementary loops of the lattice (i.e. plaquettes) [BHH+05, BY06, ZR11, ZCR12, ZCR13a, BBD+13, TCO+13, TCZL13, ZFRC17]. Aside from this point, the implementation of the tunneling of matter dressed by the gauge fields is also far from trivial. Floquet engineering in strongly-interacting gases [BP15, DTLZ17, BSA+19], and spin-changing collisions in atomic mixtures [ZCR13b, KHJ+17, GCZC17, MVE+19], have identified neat directions towards this goal, which are particularly promising in light of recent experiments [SGB+19, GSM+19, MZH+20, YSO+20]. Since the realization of plaquette terms is currently the major experimental bottleneck to simulate gauge theories beyond 1D, a timely question would be: is it possible to find characteristic features, such as deconfinement and topological order, in lattice gauge theories without plaquette terms?

In this chapter, we show that this is indeed possible. By studying a cross-linked lattice connectivity (see Fig. 7.1), we identify a new avenue for the interplay of local symmetries and topology in LGTs, as an Aharonov-Bohm instability can induce a magnetic flux in the absence of plaquette terms, giving rise to topological order, that, in this case, coexists with a symmetry-protected topological (SPT) phase [Sen15]. The crucial role that gauge symmetry plays in the topological properties of the system extends to large quantum fluctuations through a frustration mechanism, allowing deconfinement to survive to the whole phase diagram.

The chapter is organized as follows. In Sec. 7.2, we introduce the *Creutz-Ising ladder*, a quasi-1D $\mathbb{Z}_2$ LGT where the Ising fields are coupled to spinless fermions hopping in a cross-linked ladder, and summarize our main findings. In Sec. 7.3, we describe the Aharonov-Bohm instability and the emergence of a magnetic flux, which gives rise to an SPT phase. We study this phenomenon in the presence of quantum fluctuations of the gauge fields, and provide a full discussion of the phase diagram. In Sec. 7.4, we demonstrate that the cross-linked ladder can be understood as the thin-cylinder limit of a 2D LGT, providing a practical scenario where the ground-state degeneracy is related to the topology of the underlying manifold. In Sec. 7.5, we explore the mechanism of fermionic deconfinement mediated by topological solitons, which can be neatly understood in the limit of large quantum fluctuations through a gauge frustration effect.

7.2 The Creutz-Ising ladder

7.2.1 The model

The Creutz ladder, which describes spinless fermions on a cross-linked ladder [Cre99], is a lattice model hosting an SPT phase. The tunneling of fermions is dressed by a static magnetic field that pierces the ladder, which is described by a gauge-invariant flux that pierces the elementary plaquettes. For a static π flux, the

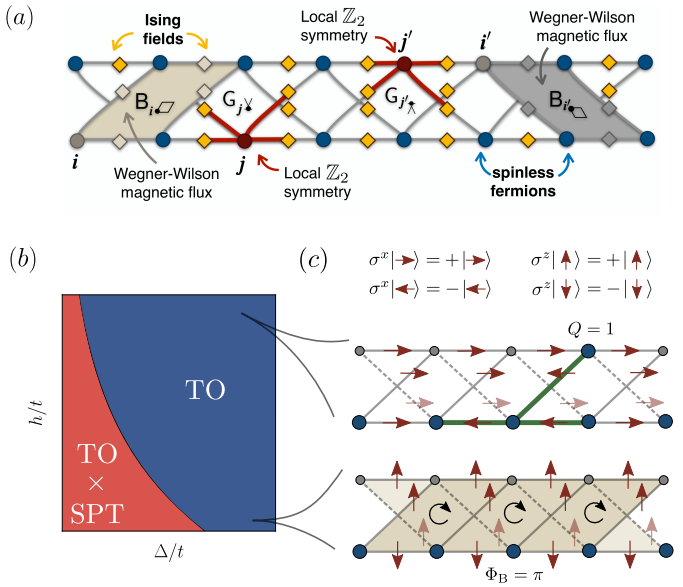

Fig. 7.1 The Creutz-Ising ladder: (a) Spinless fermions reside on the sites of a two-leg ladder (filled circles), and can tunnel along and across the legs forming a cross-linked pattern. These tunnelings are minimally dressed by Ising spin-1/2 fields, which sit on the corresponding links (filled rhombi). We represent the Wegner-Wilson fluxes across the two minimal plaquettes (titled trapezes in grey), and the generators of the local $\mathbb{Z}_2$ symmetries (red graphs). **(b)** Sketch of the phase diagram at half filling in terms of the electric field h and the imbalance Δ. We found two phases, both with topological order (TO). In one case, the latter coexists with a symmetry-protected topological phase (SPT) in the matter sector. **(c)** For $\Delta \gg t$, the fermions populate the lower leg of the ladder. At $h \ll t$, the Ising fields rearranged to spontaneously generate a π flux per plaquette through an Aharonov-Bohm instability, giving rise to TO. For $h \gg t$, the latter survives due to a gauge frustration mechanism. Fermions delocalize by forming bound quasi-particles with topological defects created in an otherwise dimerized electric field background.

ground-state of this model may correspond to either the BDI, or the AIII class of topological insulators [CTSR16], a free-fermion insulating SPT phase. Interestingly, the physics of cross-linked ladders has already been explored in experiments of ultracold atoms by exploiting Floquet engineering in two-orbital optical lattices [KHS18, KHS20]. To go beyond this free-fermion scenario, a natural possibility is to include Hubbard-type interactions [JPR+17], which leads to correlated SPT phases with interesting connections to relativistic quantum field theories of self-interacting fermions [BTR+18, TRS+19].

We hereby follow a different, and yet unexplored, route: we upgrade the back-

ground magnetic fields to a $\mathbb{Z}_2$ LGT by introducing Ising fields on the links (see Fig. 7.1**(a)**). This IGT is described by the following Hamiltonian

$$\mathsf{H}_{\rm CI}(t,\Delta,h)=\sum_{\boldsymbol{i}}\sum_{(\boldsymbol{i},\boldsymbol{j})}\left(-tc_{\boldsymbol{i}}^{\dagger}\sigma_{(\boldsymbol{i},\boldsymbol{j})}^{z}c_{\boldsymbol{j}}-h\sigma_{(\boldsymbol{i},\boldsymbol{j})}^{x}\right)+\frac{\Delta}{2}\sum_{\boldsymbol{i}}s_{\boldsymbol{i}}c_{\boldsymbol{i}}^{\dagger}c_{\boldsymbol{i}}, \tag{7.1}$$

where $c_{\boldsymbol{i}}^{\dagger}(c_{\boldsymbol{i}})$ creates (annihilates) a fermion at site $\boldsymbol{i}=(i_1,i_2)$. Here, $i_2\in\mathbb{Z}_2=\{0,1\}$ labels the lower and upper legs of the ladder, and $i_1\in\mathbb{Z}_{N_{\rm s}}=\{0,\cdots,N_{\rm s}-1\}$ labels the sites of each of these legs. At the horizontal or diagonal links $(\boldsymbol{i},\boldsymbol{j})$ adjacent to $\boldsymbol{i}$, we introduce the Pauli matrices $\sigma_{(\boldsymbol{i},\boldsymbol{j})}^{z},\sigma_{(\boldsymbol{i},\boldsymbol{j})}^{x}$ as the corresponding Ising link operators. The first term of Eq. (7.1) describes the tunneling of fermions dressed by the Ising gauge fields, which has tunneling strength t. The second term introduces an electric transverse field of strength h. Finally, the third term describes an energy imbalance of magnitude Δ for the fermions sitting on the upper $s_{\boldsymbol{i}}=+1$,or lower leg $s_{\boldsymbol{i}}=-1$.

The above Hamiltonian (7.1) displays a local $\mathbb{Z}_2$ symmetry $[\mathsf{H}_{\rm CI},\mathsf{G}_{\boldsymbol{i}}]=0,\forall\boldsymbol{i}\in\mathbb{Z}_{N_{\rm s}}\times\mathbb{Z}_2$, with the generators

$$\mathsf{G}_{\boldsymbol{i}}=(-1)^{c_{\boldsymbol{i}}^{\dagger}c_{\boldsymbol{i}}}\prod_{(\boldsymbol{i},\boldsymbol{j})\in s_{\boldsymbol{i}}}\sigma_{(\boldsymbol{i},\boldsymbol{j})}^{x} \tag{7.2}$$

displayed in Fig. 7.1**(a)**, where $s_{\boldsymbol{i}}$ denote the set of links connected to site $\boldsymbol{i}$. In addition, we also depict in this figure the smallest Wegner-Wilson loops, corresponding to gauge-invariant magnetic fields across two types of trapezia

$$\mathsf{B}_{\boldsymbol{i}\blacktriangleleft}=\prod_{(\boldsymbol{i},\boldsymbol{j})\in\boldsymbol{i}\blacktriangleleft}\sigma_{(\boldsymbol{i},\boldsymbol{j})}^{z},\qquad \mathsf{B}_{\boldsymbol{i}\blacktriangleright}=\prod_{(\boldsymbol{i},\boldsymbol{j})\in\boldsymbol{i}\blacktriangleright}\sigma_{(\boldsymbol{i},\boldsymbol{j})}^{z}, \tag{7.3}$$

with corresponding magnetic fluxes

$$\Phi_{\mathsf{B}}^{\boldsymbol{i}\blacktriangleleft}=\arccos(\langle\mathsf{B}_{\boldsymbol{i}\blacktriangleleft}\rangle),\qquad \Phi_{\mathsf{B}}^{\boldsymbol{i}\blacktriangleright}=\arccos(\langle\mathsf{B}_{\boldsymbol{i}\blacktriangleright}\rangle). \tag{7.4}$$

The magnetic flux that threads a plaquette corresponds to the phase accumulated by a particle that encircles that plaquette. Using this picture, we can write down the spin operators present in the gauge-invariant tunneling terms of (7.1) as dynamical $\mathbb{Z}_2$ Peierls phases, $\sigma_{(\boldsymbol{i},\boldsymbol{j})}^{z}=e^{i\varphi_{(\boldsymbol{i},\boldsymbol{j})}}$, where $\varphi_{(\boldsymbol{i},\boldsymbol{j})}$ has eigenvalues 0 and π.

We note that, in the standard formulation of IGTs [Kog79], one also introduces an additional magnetic-field term

$$\tilde{\mathsf{H}}_{\rm CI}(t,\Delta,h,J)=\mathsf{H}_{\rm CI}(t,\Delta,h)-J\sum_{\boldsymbol{i}}\left(\mathsf{B}_{\boldsymbol{i}\blacktriangleleft}+\mathsf{B}_{\boldsymbol{i}\blacktriangleright}\right), \tag{7.5}$$

such that the magnetic plaquette coupling J competes with the electric transverse field h. In the (2+1) pure IGT, this competition leads to a quantum phase transition between deconfined $h/J<h/J|_{\rm c}$ and confined $h/J>h/J|_{\rm c}$ phases [Weg71].

These phases are not characterized by a local order parameter, but instead display Wegner-Wilson loops that scale either with the perimeter ($h/J < h/J|_c$) or with the encircled area ($h/J < h/J|_c$) of a closed loop, i.e. perimeter or area law.

The $\mathbb{Z}_2$ symmetry generators (7.2) can be used to define different charge sectors of the Hilbert space, as the eigenstates of the Hamiltonian $|\psi\rangle$ must also fulfill

$$\mathsf{G}_{\boldsymbol{i}} |\psi\rangle = (-1)^{q_{\boldsymbol{i}}} |\psi\rangle \,, \tag{7.6}$$

where $q_{\boldsymbol{i}} \in \{0, 1\}$ are the so-called static $\mathbb{Z}_2$ charges. Typically, one considers the vacuum/even sector $\{q_{\boldsymbol{i}}\} = \{0, 0, \cdots, 0\}$, introducing a few static charges on top of it. For instance, $\{q_{\boldsymbol{i}}\} = \{\delta_{\boldsymbol{i},(i_0,0)}, \delta_{\boldsymbol{i},(i_0+L,0)}\}$ describes a pair of static $\mathbb{Z}_2$ charges separated by a distance L. In the (2+1) pure IGT [Kog79], these test charges are subjected to a potential $V(L) = E_{\rm gs}(L) - E_{\rm gs}(0)$ that either remains constant in the deconfined phase $V(L) \propto V_0$, or increases with the distance in the confined phase $V(L) \propto L$. We note that (2+1) is the lower critical dimension, since the (1+1) IGT can only display an area law [Kog79], hosting solely a confined phase. In the presence of fermionic matter, rather than through the aforementioned area law, the (1+1) confined phase can be characterized through the appearance of chargeless bound dimers [BVGM20].

In this chapter, we argue that fermionic $\mathbb{Z}_2$ gauge theories in quasi-1D geometries, such as the ladder structure of Fig. 7.1, lead to a much richer playground in comparison to the strict 1D limit (Fig. 7.1**(b)**). Let us summarize our main findings.

7.2.2 Summary of our results

In the pure gauge sector, which is obtained from Eq. (7.5) by setting $t = \Delta = 0$, we show that $\tilde{\mathsf{H}}_{\rm CI}(0, 0, h, J)$ still hosts a quantum phase transition at a critical $h/J|_c$, separating confined and deconfined phases. We characterize this phase transition quantitatively using matrix-product-state (MPS) numerical simulations [Sch11], which allow us to extract the critical behavior of the Ising magnetic fluxes, and their susceptibilities. We note that the ladder geometry plays a key role to go beyond the (1+1) lower critical dimension [Kog79]. By switching on the coupling to the dynamical fermions, we show that the aforementioned Aharonov-Bohm instability takes place, and results in an emerging π-flux deconfined phase even in the absence of the magnetic plaquette term (Fig. 7.1**(c)**), namely setting $J = 0$ in the Creutz-Ising Hamiltonian $\tilde{\mathsf{H}}_{\rm CI}(t, \Delta, h, 0)$. We explicitly demonstrate the presence of topological order by calculating the topological entanglement entropy associated to the ground-state wavefunction [KP06, LW06]. As opposed to the pure gauge theory, we show how the accompanying deconfinement survives in the limit of arbitrary quantum fluctuations set by large transverse fields h (Fig. 7.1**(c)**). Here, single $\mathbb{Z}_2$ charges can be localized within topological solitons that interpolate between two different symmetry-breaking orders. We believe that this is a generic

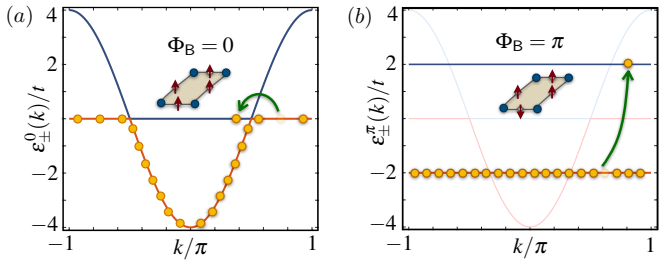

Fig. 7.2 Aharonov-Bohm instability: Band structure of the Creutz-Ising gauge theory for $J = h = \Delta = 0$, and corresponding filling of the fermionic sector. The green arrows depict the lowest-energy particle-hole excitations of the half-filled ladder. **(a)** For an Ising background with a vanishing flux $\Phi_B = 0$, the ground-state corresponds to a gapless state with macroscopic degeneracy. **(b)** For $\Phi_B = \pi$, there is destructive Aharonov-Bohm interference that opens a gap, forming two flat bands, and lowering the ground-state energy (the semi-transparent lines serve to compare to the $\Phi_B = 0$ case).

feature of IGTs in the particular charge sector considered here. To the best of our knowledge, this study provides the first quantitative analysis of such deconfinement mechanism.

Moreover, as a result of the cross-linked geometry, we also show that the matter sector may lie in an SPT phase characterized by a non-zero topological invariant. From the perspective of the fermions, the corresponding topological edge states can be understood as domain-wall fermions [Kap92, JS92, GJK93] with the novelty that, instead of requiring fine tuning to incorporate chiral symmetry on the lattice, they are spontaneously generated by the Ising-matter coupling. The fact that a plaquette term $J \neq 0$ is not required to host this exotic behavior is particularly interesting in light of current developments in cold-atom quantum simulations. Interestingly, the interplay between geometry and gauge-invariant interactions allows us to obtain a topological phase for gauge fields without introducing four-body plaquette terms, simplifying enormously the experimental implementation. This point is important since the main building blocks of the model have already been realized in cold-atom experiments [SGB+19]. Therefore, future quantum simulations of this fermionic IGT will be capable of testing the non-trivial equilibrium properties described in this chapter.

7.3 Aharonov-Bohm Instability

We start by exploring the limit of zero electric-field strength $h = 0$. In the following, and unless stated otherwise, we fix $J = 0$. Here, the Ising fields have vanishing quantum fluctuations, and the fermions tunnel in a classical $\mathbb{Z}_2$ back-

ground $\big|\{\sigma_{(\boldsymbol{i},\boldsymbol{j})}\}\big\rangle$, where $\sigma_{(\boldsymbol{i},\boldsymbol{j})} = \pm 1$ are the eigenvalues of the σ^z link operator. In this limit, there are only two translationally-invariant ground-states corresponding to the 0- or π-flux configurations, namely $\langle \mathsf{B}_{\boldsymbol{i}\square} \rangle = \langle \mathsf{B}_{\boldsymbol{i}\bullet\!\square} \rangle = \pm 1$. The fermions minimize their energy in these backgrounds by partially filling the corresponding energy bands $\epsilon^0_\pm(k)$ or $\epsilon^\pi_\pm(k)$.

For vanishing imbalance $\Delta = 0$, and considering periodic boundary conditions, these band structures read

$$\epsilon^0_\pm(k) = -2t\cos k \pm 2t|\cos k|, \qquad \epsilon^\pi_\pm(k) = \pm 2t, \tag{7.7}$$

where $k \in [-\pi, \pi)$. As depicted in Fig. 7.2**(a)**, for magnetic flux $\Phi_{\mathsf{B}} = 0$, the half-filled ground-state corresponds to a gapless state. Conversely, for $\Phi_{\mathsf{B}} = \pi$ flux (Fig. 7.2**(b)**), the band structure consists of two flat bands, such that the half-filled ground-state is a single gapped state with a fully-occupied lowest band. By direct inspection of Fig. 7.2, it is apparent that the π-flux case is energetically favorable. This is indeed the case, as one finds that $E^\pi_{\rm gs} = -2tN_{\rm s} < -(4t/\pi)N_{\rm s} = E^0_{\rm gs}$. Recalling the Peierls instability in 1D metals [Pei55], where the underlying lattice adopts a dimerized configuration and a gap is opened in the metallic band; here, it is the Ising fields which adopt a π-flux configuration leading to a gap opening in the fermionic sector. This spontaneous generation of a π-flux is in accordance with Lieb's result for bipartite lattices [Lie94] but, in contrast to the square lattice [AG16, GRV17, GAS+18], it does not lead to a semi-metallic phase with emergent Dirac fermions [WZ89]. In this case, it is an insulator with complete band flattening caused by destructive Aharonov-Bohm interference at $\Phi_{\mathsf{B}} = \pi$ [AB59], which can result in many-body localization [KOI20]. Due to the remarkable similarities with the Peierls effect, we call this effect the Aharonov-Bohm instability.

This flux instability is actually generic for any imbalance $\Delta > 0$, in spite of the fact that the bands gain curvature. In this case, the corresponding ground-state energies are

$$\begin{aligned} E^0_{\rm gs} &= -\frac{4t}{\pi}\Big(\big(1+\xi^2\big)^{1/2}\, \mathsf{E}\big(\theta_0\big)\Big) N_{\rm s}, \\ E^\pi_{\rm gs} &= -\frac{2t}{\pi}\Big(|1+\xi|\, \mathsf{E}\big(\theta_\pi\big) + |1-\xi|\, \mathsf{E}\big(\tilde{\theta}_\pi\big)\Big) N_{\rm s}, \end{aligned} \tag{7.8}$$

where we have introduced the parameters $\xi = \Delta/4t$, $\theta_0 = 1/(1+\xi^2)$, $\theta_\pi = 4\xi/(1+\xi)^2$, and $\tilde{\theta}_\pi = -4\xi/(1-\xi)^2$. Additionally, we have used the complete elliptic integral of the second kind $\mathsf{E}(x) = \int_0^{\pi/2} \mathrm{d}\alpha \, \big(1 - x\sin^2\alpha\big)^{1/2}$. Once again, one can readily confirm that $E^\pi_{\rm gs} < E^0_{\rm gs}$, such that it is energetically favorable for the ground-state to lie in the π-flux phase, which is generally gapped except for $\xi = 1$, namely $\Delta = 4t$.

7.3.1 Emerging Wilson fermions and SPT phases

By exploring the imbalanced case at long wavelengths, we can understand the insulating π-flux phase from a different perspective. Rather than the massless Dirac fermions that emerge in the square-lattice π-flux phase [AG16, GRV17, GAS+18], we get the following long-wavelength dispersion around $k_\pm = \pm\pi/2$

$$\epsilon^\pi_\pm(k_\pm + p) \approx \pm\sqrt{(m_\pm c^2)^2 + (cp)^2}, \qquad m_\pm = (\xi \pm 1)/2t \tag{7.9}$$

where $c = 2t$ is the propagation speed, and $m_\pm$ are two mass parameters. Except for $\xi = 1$, we get two massive relativistic fermions characterised by a different mass, which are known as Wilson fermions in a LGT context [Wil77].

The fact that the Wilson masses are different $m_+ \neq m_-$ turns out to be crucial in connection to the spontaneous generation of an SPT phase. The Chern-Simons form $\mathsf{Q}^\pi_1 = \frac{\mathrm{i}}{2\pi}\left\langle \epsilon^\pi_-(k)\right| \partial_k \left|\epsilon^\pi_-(k)\right\rangle \mathrm{d}k$ [RSFL10], equivalent to the Zak phase in 1D [Zak89], leads to a Chern-Simons invariant after integrating over all occupied quasi-momenta

$$\mathsf{CS}^\pi_1 = \int_{-\pi}^{\pi} \mathsf{Q}^\pi_1 = \frac{1}{4}\Big(\mathrm{sgn}(m_+) - \mathrm{sgn}(m_-)\Big). \tag{7.10}$$

One can define a gauge-invariant Wilson loop $\mathsf{W}^\pi_1 = \mathrm{e}^{\mathrm{i}2\pi\mathsf{CS}^\pi_1}$ that detects the non-trivial topology when $\mathsf{W}^\pi_1 = -1$. This occurs when the pair of Wilson fermions have masses with opposite signs. Accordingly, if $|\xi| < 1$ (i.e. $-4t < \Delta < 4t$), the topological Wilson loop is non trivial $\mathsf{W}^\pi_1 = -1$, and the emerging π-flux phase is an insulating SPT phase.

This result draws a further analogy between the Peierls and Aharonov-Bohm instabilities. As we saw throughout part II, in the former, when the instability is triggered by an electron-lattice coupling that modulates the tunneling [SSH79], one of the dimerization patterns of the lattice leads to a non-zero topological invariant and an SPT phase [AOP16]. In our case, there is no dimerization due to SSB since the local $\mathbb{Z}_2$ symmetry cannot be spontaneously broken. However, there are two gauge-invariant fluxes at $h = 0$, and it is only the π-flux configuration that leads to a non-zero topological invariant when $|\Delta| < 4t$. We can thus conclude that, as a consequence of the Aharonov-Bohm instability, the fermions intertwine with the Ising fields in such a way that a gap is opened in the fermion sector with non-trivial topology.

7.3.2 Gauge-matter edge states and fractionalisation

So far, our discussion has revolved around the zero electric field limit $h = 0$, and assumed periodic boundary conditions. From now onwards, we abandon this limit and explore the effect of quantum fluctuations in open Creutz-Ising ladders (i.e. Dirichlet/hard-wall boundary conditions). Due to the bulk-boundary correspondence, when the bulk of the spontaneously-generated π-flux phase is characterized

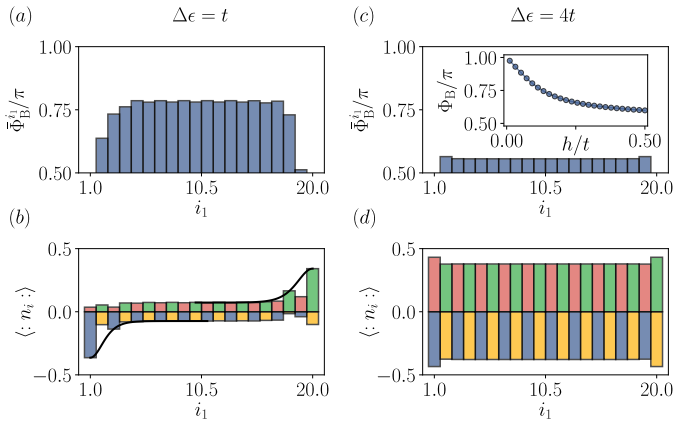

Fig. 7.3 Gauge-matter edge states: **(a)** Average Ising flux $\bar{\Phi}_{\rm B}^{i_1}$ in the ground-state of the Creutz-Ising ladder for $\Delta = t$ and $h = 0.1t$, for a ladder of length $N_s = 20$ filled with $N = 20$ particles. Due to the quantum fluctuations, the bulk flux gets lowered $\bar{\Phi}_{\rm B}^{\rm bulk} < \pi$. **(b)** Fermionic occupation $\langle : n_{\boldsymbol{i}} : \rangle$ showing boundary peaks that can be identified with the topologically-protected edge modes. We use red and green to represent odd and even sites, respectively, of the lower leg, and blue and yellow for the upper one. The solid black lines are obtained by fitting the latter to eq. (7.13), showing that the excess and defect of charge is due to the presence of edge states at zero energy. In **(c)** and **(d)** we can observe how, for a higher value of the imbalance ($\Delta = 4t$), the edge states disappear. The inset shows the flux in an infinite ladder as a function of h/t for $\Delta = 0.1t$.

by a non-zero topological invariant (7.10), one expects that edge states will appear at the boundaries of the ladder. In the context of LGTs, these states are lower-dimensional domain-wall fermions [Kap92] with the key difference that, in our case, they are generated via the Aharonov-Bohm instability.

In Fig. 7.3, we show the real-space configuration of both matter and Ising fields. We use a MPS-based algorithm [HP18] of the density-matrix renormalization group (DMRG) [Whi92], setting the bond dimension to $D = 200$ for a ladder of leg length $N_{\rm s} = 20$ at half-filling, and introduce quantum fluctuations through $h = 0.1t$. In these figures, we display the Ising flux

$$\bar{\Phi}_{\rm B}^{i_1} = \frac{\Phi_{\rm B}^{\boldsymbol{i}\swarrow} + \Phi_{\rm B}^{\boldsymbol{i}\nwarrow}}{2} \tag{7.11}$$

averaged over the two trapezoidal plaquettes, and the normal-ordered fermionic occupation

$$\langle : n_{\boldsymbol{i}} : \rangle = \langle c_{\boldsymbol{i}}^\dagger c_{\boldsymbol{i}} \rangle - \rho, \tag{7.12}$$

where $\rho = 1/2$ at half-filling. As shown in Fig. 7.3**(a)** and **(c)**, due to the quantum fluctuations, the Ising flux is no longer fixed at π. As the transverse field increases,

$\bar{\Phi}_{\mathsf{B}} \to \pi/2$, which amounts to an electric-field dominated phase with a vanishing expectation values of the magnetic plaquettes $\langle \mathsf{B}_{i\square} \rangle = \langle \mathsf{B}_{i\square} \rangle = 0$. In the inset we show how the flux Φ_{B} changes with h in an infinite ladder, where the ground state was obtained using the iDMRG algorithm with $D = 200$ [HP18]. This change is continuous from $h = 0$, suggesting that the flux-dominated phase found in the absence of quantum fluctuations with $\Phi_{\mathsf{B}} = \pi$ extends to finite values of h. In the next section, we will argue that this flux-dominated phase actually extends to the whole phase diagram, as in the case of $h = 0$.

In Fig. 7.3**(b)**, we show that the corresponding fermion distribution is not translationally invariant, but displays an excess/deficit of charge around the boundaries of the ladder. This real-space distribution is consistent with the existence of two topological edge states in the SPT phase, one of them being filled while the other one remains empty at half filling. We note that, in analogy with the phenomenon of charge-fractionalization put forth by Jackiw and Rebbi [JR76], when these zero modes are occupied/empty, an excess/deficit of 1/2 fermion is formed around the boundaries. This fractionalization can be readily observed in Fig. 7.3**(b)**, where we also show that the excess/defect of charge with respect to the bulk density on each leg of the ladder ρ_{i_2} follows

$$\langle n_{(j,i_2)} \rangle - \rho_{i_2} = \pm \frac{1}{4\xi_\ell} \mathrm{sech}^2 \left(\frac{j - j_{\mathrm{p}}}{\xi_\ell} \right). \tag{7.13}$$

Here, $j = 2i_1$ (resp. $j = 2i_1 - 1$) is the sublattice index for the lower (resp. upper) leg of the ladder, with $j_{\mathrm{p}} = L$ (resp. $j_{\mathrm{p}} = 0$), and ξ_ℓ is the localization length of the corresponding edge state. This behavior is a universal feature of zero modes in relativistic quantum field theories and condensed-matter models [CB81], and we show that it also holds for LGTs. In Fig. 7.3**(b)** we observe how the edge states disappear for higher values of the imbalance Δ, signaling a transition towards a trivial phase.

The presence of edge states points towards the robustness of the SPT flux-dominated phase described in the previous section, which thus persists as one introduces non-zero quantum fluctuations. Therefore, the SPT phase should extend to a larger region in parameter space. Let us also highlight that, by looking at the enlarged fluctuations of the Ising flux close to the boundaries (Fig. 7.3**(a)**), one realizes that the edge states are indeed composite objects where both the matter and gauge degrees of freedom are intertwined. We will unveil a very interesting consequence of this intertwining below.

7.3.3 Topological phase transitions

We explore the extent of this SPT phase in parameter space $(\Delta/t, h/t)$. The topological invariant (7.10) is related to the Berry phase γ acquired by the ground-state $|E_{\mathrm{gs}}(\theta)\rangle$ along an adiabatic Hamiltonian cycle $\mathsf{H}(\theta) = \mathsf{H}(\theta + 2\pi)$ [Ber84],

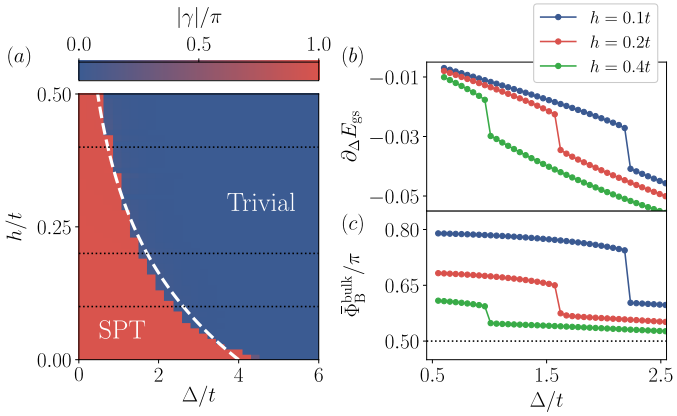

Fig. 7.4 Topological phase transitions: **(a)** Contour plot of the many-body Berry phase, which allows differentiating between the SPT with $\gamma = \pi$ and the trivial band insulator (TBI) with $\gamma = 0$. The dashed line is obtained by fitting the critical points to an exponential (see main text). **(b)** First derivative of the ground-state energy $\partial_\Delta E_{\rm gs} = (E_{\rm gs}(\Delta_1) - E_{\rm gs}(\Delta_2))/(\Delta_1 - \Delta_2)$ with respect to the imbalance Δ/t for different values of h/t. **(c)** Average Ising flux $\Phi_{\rm B}^{\rm bulk}$ as a function of the imbalance Δ/t. The calculations were performed directly in the thermodynamic limit for a half-filled ladder.

namely

$$\gamma = \mathrm{i}\int_0^{2\pi} \mathrm{d}\theta \, \langle E_{\rm gs}(\theta)| \, \partial_\theta \, |E_{\rm gs}(\theta)\rangle \tag{7.14}$$

For non-interacting fermions in a classical $\mathbb{Z}_2$ background, one can use quasi-momentum as the adiabatic parameter $\theta = k$, such that $\gamma = 2\pi \mathsf{CS}_1^\pi$ (7.10). However, as the electric field is switched on, the Ising fields fluctuate quantum-mechanically mediating interactions between the fermions, and the quasi-momentum is no longer an appropriate adiabatic parameter. Building on ideas of quantized charge pumping [NT84] and Hall conduction [NTW85b], one can obtain a many-body Berry phase by twisting the tunneling $t \to te^{\mathrm{i}\theta}$ that connects the boundaries, and integrating over the twisting angle θ. Interestingly, this concept can be generalized to systems with hard-wall boundary conditions [Hat06], since the twisting can actually be placed locally in any link that respects the underlying symmetry that protects the SPT phase, e.g. inversion symmetry in this case.

We have computed the many-body Berry phase (7.14) for an infinite Creutz-Ising ladder using iDMRG [HP18], yielding the phase diagram of Fig. 7.4**(a)**. The SPT phase is characterized by $\gamma = \pi$ in the red region, and is separated from a trivial band insulator (TBI) with $\gamma = 0$ in the blue region by a critical line that reaches $\Delta \approx 4t$ for $h = 0$. This corroborates our previous interpretation (7.10) in terms of the mass-inversion point of the emergent Wilson fermions at $\xi = \Delta/4t = 1$.

As the electric field h increases, this inversion point flows towards smaller values of the imbalance Δ, which can be interpreted as a renormalization of the Wilson masses due to the interactions mediated by the gauge fields.

In this figure, we also show that the numerical critical line can be fitted to an exponential $\xi_c = \xi_0 \exp\{-h/h_\xi\}$, where h_ξ is a fitting parameter, and $\xi_0 = 1$ is fixed by setting the critical point at $\Delta/4t = 1$ for $h = 0$. Let us remark that this exponential behavior is consistent with the claim that the SPT phase and, in general, the Aharonov-Bohm instability and the flux-dominated phase, persists to arbitrarily-large values of the transverse h when the imbalance is $\Delta = 0$. For zero imbalance, the appearance of the flat bands described previously endows the SPT phase with an intrinsic robustness to the interactions mediated by the fluctuating gauge field.

Let us note that the critical line describes first-order topological phase transitions, as can be appreciated in Fig. 7.4**(b)**, where we display the derivative of the ground-state energy $\partial_\Delta E_{\text{gs}}$ for three different values of electric field strength (dotted lines of Fig. 7.4**(a)**). The discontinuous jumps account for the first-order nature of the phase transitions. A similar discontinuity can be observed in the average magnetic flux (7.11), evaluated at the bulk of the ladder (Fig. 7.4**(c)**).

7.4 Topology from Connectivity

The topological properties described in the previous section are associated, loosely speaking, to the matter degrees of freedom, since they are adiabatically connected to the static gauge field limit at $h = 0$—although matter and gauge are intertwined for any finite value of h. In this section, we focus on different topological effects that arise due to the dynamical nature of the gauge field. In particular, we provide quantitative evidence supporting the equivalence between the cross-linked ladder and a cylindrical geometry. This allows us to interpret our model as the thin-cylinder limit of a 2D IGT, and to identify various topological properties such as the ground-state degeneracy or the presence of topological order throughout the whole phase diagram. We also show that the intertwining of the matter and gauge fields in the SPT phase leads to a topological flux threading of the cylinder, and give further arguments for its survival to arbitrary transverse fields.

7.4.1 The effective Creutz-Ising cylinder

Let us, momentarily, switch off the gauge-matter coupling and focus on the pure gauge theory $\tilde{\mathsf{H}}_{\text{CI}}(0, 0, h, J)$ in Eq. (7.5). For $h/J \to 0$ (with $J > 0$), and for the sake of the argument, we assume that $|\mathrm{g}\rangle$ is the single ground-state in a flux-dominated phase with zero flux per plaquette $\Phi_{\mathsf{B}} = 0$. We note that the following argument, first applied to the IGT on a square ladder [Fra13], is also valid for

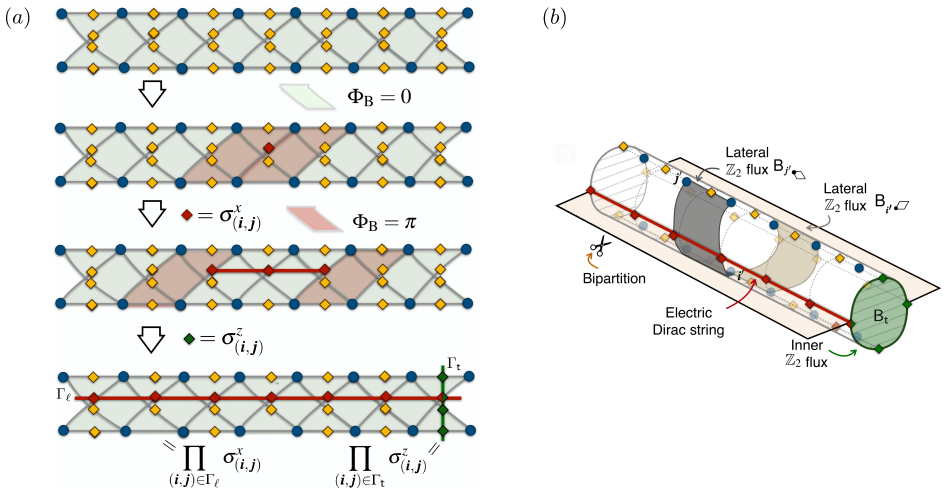

Fig. 7.5 Ground-state degeneracy of the Creutz-Ising cylinder: (a) In the $h/J \to 0$ limit, the ground-state corresponds to the zero-flux state (green plaquettes), and excitations correspond to π-flux plaquettes (red) connected by a electric-field string (red line). By extending the string to the ladder edges, one recovers a different zero-flux ground-state state. **(b)** By considering the crossed-link tunnelings of the ladder as two different paths enclosing an area, the Creutz ladder can be represented as a thin-cylinder limit of a 2D LGT.

$\Phi_B = \pi$ in the case $J < 0$. As shown in Fig. 7.5**(a)**, flipping the Ising fields via $\sigma^x_{(i,j)}$ creates a pair of $\Phi_B = \pi$ excitations at neighboring plaquettes, which can be separated at the expense of flipping additional Ising fields along a path Γ_ℓ. By extending this path towards the boundaries of the ladder, the π fluxes get expelled, and one recovers a state $|\tilde{g}\rangle = D_\ell |g\rangle$ with vanishing flux a $\Phi_B = 0$, where

$$D_\ell = \prod_{(i,j)\in\Gamma_L} \sigma^x_{(i,j)} \tag{7.15}$$

is the so-called Dirac string. Similarly to those in Eq. (7.3), one can define a 4-point correlator involving Ising fields

$$B_t = \prod_{(i,j)\in\Gamma_t} \sigma^z_{(i,j)}, \tag{7.16}$$

where Γ_t is a vertical path that connects the two legs of the ladder. As demonstrated below, Γ_t is equivalent to a path that wraps around a non-trivial cycle of a cylinder, such that the correlator (7.16) can be interpreted as a Wegner-Wilson loop operator measuring the flux threading the hole of the cylinder.

In the lowest panel of Fig. 7.5**(a)**, one can see that the Dirac string shares only one common link with the 4-point correlator, and thus anti-commutes $\{\mathsf{D}_\ell, \mathsf{B}_\mathsf{t}\} = 0$. Conversely, the Dirac string shares a pair of links with the trapezoidal plaquettes (7.3). and thus commutes with the Hamiltonian $[\tilde{\mathsf{H}}_{\mathrm{CI}}(0,0,h,J), \mathsf{D}_\ell] = 0$. As a consequence, if we assume that $\mathsf{B}_\mathsf{t}|\mathrm{g}\rangle = +|\mathrm{g}\rangle$, we immediately obtain $\mathsf{B}_\mathsf{t}|\tilde{\mathrm{g}}\rangle = -|\tilde{\mathrm{g}}\rangle$, whereas $\tilde{\mathsf{H}}_{\mathrm{CI}}(0,0,h,J)|\tilde{\mathrm{g}}\rangle = E_{\mathrm{gs}}|\tilde{\mathrm{g}}\rangle$, $\tilde{\mathsf{H}}_{\mathrm{CI}}(0,0,h,J)|\mathrm{g}\rangle = E_{\mathrm{gs}}|\mathrm{g}\rangle$. Accordingly, the two states are orthogonal and have the same energy E_{gs}. Our original assumption of a single ground-state thus needs to be dropped in favor of the existence of a two dimensional ground-state manifold spanned by $\{|\mathrm{g}\rangle, |\tilde{\mathrm{g}}\rangle\}$.

The presence of such ground-state manifold can be a manifestation of topological order. As outlined in the introduction, spin-liquid states with topological order can be characterized by a ground-state degeneracy that depends on the genus of the manifold in which they are defined [Wen17]. The deconfined phase of the (2+1) IGT does indeed display this property, which is crucial in studies of fractionalisation in high-T_c superconductors [SF00, SF01]. In our case, the cross-linked tunnelings of Fig. 7.1 can be understood as a planar projection of the two paths that traverse the different faces of a thin cylinder (see Fig. 7.5**(b)**). From this perspective, the 4-point correlator (7.16) is actually Wegner-Wilson loop that measured the inner $\mathbb{Z}_2$ flux through the hole of the cylinder. As a consequence, the two-fold degeneracy follows from the non-trivial topology of the manifold: the two states that span the ground-state manifold $|\mathrm{g}\rangle, |\tilde{\mathrm{g}}\rangle$ have a vanishing flux $\Phi_\mathsf{B} = 0$ through the lateral surface of the cylinder, but only one of them $|\tilde{\mathrm{g}}\rangle$ has a π flux through the cylinder's hole. This ground-state $|\tilde{\mathrm{g}}\rangle$ is sometimes described as a state with a vison (i.e. vortex excitation) trapped within the hole of the cylinder.

In a finite-size system, at any small but non-zero h/J, the ground-state degeneracy is lifted and the manifold splits into two eigenstates of D_ℓ that amount to the symmetric and anti-symmetric superpositions of $|\mathrm{g}\rangle$ and $|\tilde{\mathrm{g}}\rangle$. In the thermodynamic limit, the gap in the ground-state manifold closes exponentially, and any small perturbation tends to select one of the two eigenstates of B_t, either $|\mathrm{g}\rangle$ or $|\tilde{\mathrm{g}}\rangle$, which have a lower entanglement [ZGT+12]. In particular, we note that MPS simulations with finite bond dimension favor $|\mathrm{g}\rangle, |\tilde{\mathrm{g}}\rangle$ as ground-states with respect to any other choice. Having less entanglement, their approximation for a fixed value of the bond dimension is more accurate, and thus their energy lower than the one of any other linear combination. Below, we show that this effect is also manifest in the presence of dynamical fermions, and that the specific intertwining of gauge and matter fields in the SPT phase induce well-defined magnetic fluxes inside the cylinder.

7.4.2 Magnetic fluxes and Ising susceptibility

We explore now the properties of the ground state as we departure from the limit $h/J \to 0$. For the pure-gauge case described above, in particular, a phase transition

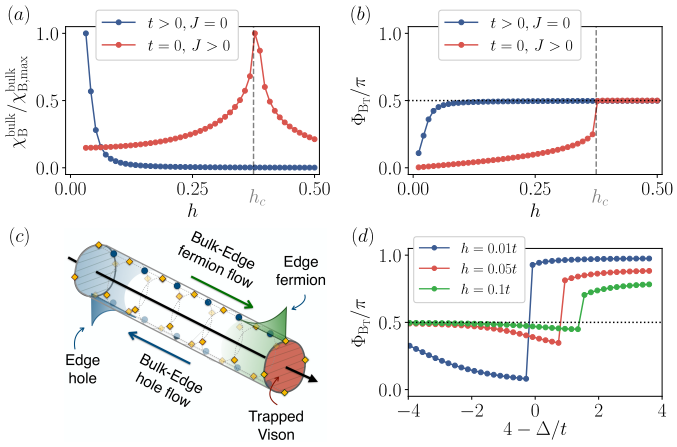

Fig. 7.6 $\mathbb{Z}_2$ **magnetic fluxes in the infinite Creutz-Ising cylinder: (a)** $\mathbb{Z}_2$-flux susceptibility as a function of the electric field strength. We compare the pure-gauge case, setting $t = 0$ and $J = 1$ (red circles) with the case in which the gauge fields interact with the fermionic matter, setting $t = 1$, $\Delta = 5t$ and $J = 0$ (blue circles). In the first case, the susceptibility shows a diverging peak, signaling a quantum phase transition between deconfined and confined phases. In the presence of dynamical matter, however, there is no apparent divergence hinting at the absence of such a transition. **(b)** $\mathbb{Z}_2$ inner flux piercing the cylinder Φ_{B_t}. In the pure-gauge case (red circles), this inner flux displays non-analytical behavior across a critical transverse field h_c. For dynamical matter (blue circles), this tendency is not abrupt, and the inner flux only attains the value $\Phi_{B_t} \approx \pi/2$ asymptotically without any non-analyticity. **(c)** Topological flux threading relating the existence of edge states to a trapped vison inside the cylinder. **(d)** Similarly to the Berry phase γ, the inner flux Φ_{B_t} changes from 0 to π as one crosses the critical point separating TBI and SPT. The deviations from those precise are due to quantum fluctuations.

takes place at a finite value of h/J. As announced in Sec 7.2.2, the cross-linked ladder geometry allows for a confinement-deconfinement phase transition akin to the (2+1) IGT [Weg71]. This phase transition can be probed by the $\mathbb{Z}_2$-flux susceptibility $\chi_B^{bulk} = \partial \bar{\Phi}_B^{bulk}/\partial h$, evaluated through the magnetic flux (7.11) at the bulk of the ladder. It can be show that, after a duality transformation, the pure-gauge Ising gauge theory is equivalent to the quantum Ising model in a transverse field [Weg71]. In this picture, the $\mathbb{Z}_2$-flux susceptibility is equivalent to the susceptibility of the magnetization, which acts as an order parameter in the Ising model. We use iDMRG to obtain the approximation of the ground-state of the system defined on an infinitely-long ladder as an MPS. The system is thus equivalent to a $2 \times \infty$ cylinder: the thin-cylinder limit of a 2+1 fermionic IGT. The maximum bond dimension we have used is $D = 200$, testing that it is sufficient to achieve a good convergence. As clearly evidenced by the iDMRG results of Fig. 7.6**(a)**(red

circles) , there is a peak in the $\mathbb{Z}_2$ susceptibility, whose height actually diverges with the ladder size at the critical coupling $h/J|_c$. In Fig. 7.6**(b)**, we plot the value of the inner flux $\Phi_{\mathsf{B}_t} = \arccos(\langle \mathsf{B}_t \rangle)$ through the hole of the effective cylinder as a function of the transverse field h (red circles). The plot shows that, in the $h/J \to 0$ limit, the cylinder has zero inner flux $\Phi_{\mathsf{B}_t} = 0$, and the ground-state is $|g\rangle$ as anticipated. By increasing the transverse field, quantum fluctuations change the inner flux, which acts as a non-local order parameter for the transition to the confined phase displaying a non-analytical behavior as we cross $h/J|_c$.

Let us now switch on the gauge-matter coupling, and see how this picture gets modified by the inclusion of dynamical fermions governed by $\tilde{\mathsf{H}}_{\mathrm{CI}}(t, \Delta, h, 0)$ in Eq. (7.5). First of all, we find that there is no peak in the $\mathbb{Z}_2$ susceptibility for any value of h (see blue circles of Fig. 7.6**(a)**), which suggests the absence of a phase transition. Furthermore, we plot the value of the inner flux in Fig. 7.6**(b)**, which again attains the value $\Phi_{\mathsf{B}_t} = 0$ in the $h/t \to 0$ limit (blue circles). The zero inner-flux state can be understood as the generalization of the $|g\rangle$ ground-state to a situation that encompasses dynamical fermions intertwining with the Ising fields. As neatly depicted, the $\mathbb{Z}_2$ flux changes smoothly from $\Phi_{\mathsf{B}_t} = 0 \to \pi/2$ as the electric field strength is increased. Therefore, the absence of non-analyticities again suggests that there is a single flux-dominated phase for arbitrary transverse fields. Although we did not show here that, for a cylindrical geometry and in the presence of fermionic matter, this phase exhibits a degenerate ground-state manifold, we will argue at the end of the section that this is indeed the case using the topological entanglement entropy. Moreover, in the last section we will demonstrate that, in this phase, fermionic matter is deconfined.

7.4.3 Trapped Visons from topological flux threading

As discussed above for the pure-gauge limit, topological order becomes manifest through the two-fold ground-state degeneracy $\{|\mathrm{g}\rangle, |\tilde{\mathrm{g}}\rangle\}$, and the absence/presence of a trapped vison. Yet, in the previous section (see Fig. 7.6**(b)**), we have only found the dynamical-fermion generalization of $|g\rangle$. As described in Sec. 7.3, the Aharonov-Bohm instability can lead to an SPT ground-state or to a trivial band insulator (see Fig. 7.4**(a)**). We now discuss the difference of the intertwining of the gauge and matter fields in these two cases, and unveil a very interesting interplay between the topological degeneracy and the existence of edge states in the SPT phase.

To understand this interplay, let us recall Laughlin's argument for the quantum Hall effect [Lau81], which states that a single charge is transferred between the edges of a quantum Hall cylinder when a magnetic flux quantum is threaded through its hole. In the Creutz-Ising ladder, one can move from the TBI onto the SPT ground-state by gradually decreasing the imbalance Δ. As the system crosses the critical point, topological edge states will appear at the boundaries of the ladder, which

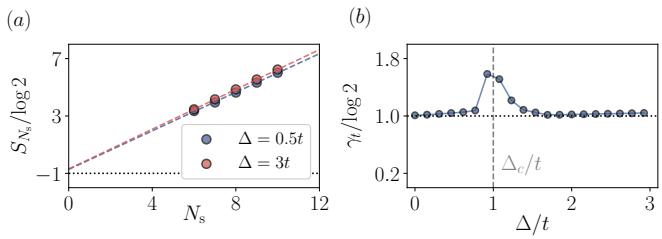

Fig. 7.7 Topological entanglement in the Creutz-Ising ladder: **(a)** Scaling of the entanglement entropy S_{N_s} with N_s setting $h = 0.02t$, and for different imbalances corresponding to the SPT ($\Delta = 0.5t$) and TBI ($\Delta = 3t$) phases. In both cases, the topological correction to the entanglement entropy is $\gamma_t = \log 2$, signaling topological order. In **(b)** we represent this quantity as a function of Δ/t. The grey dashed line denotes the position of the first-order transition for a finite cylinder of length $N_s = 10$.

can be seen as the result of charge being transferred from the bulk to the edges (see Fig. 7.6**(c)**). In contrast to Laughlin's pumping, where it is the external variation of the flux which leads to charge transport, here it is the transition into a topological phase and the associated charge transfer which should generate a non-vanishing $\mathbb{Z}_2$ inner flux. In Fig. 7.6**(d)**, we confirm this behavior, and show that the $\mathbb{Z}_2$ inner flux changes from $\Phi_{\mathsf{B}_t} \approx 0$ (TBI) to $\Phi_{\mathsf{B}_t} \approx \pi$ (SPT) at fixed $h = 0.01t$.

This effect can be understood as a *topological flux threading*, where the existence of edge states gets intertwined with the trapping of a vison through the cylinder's hole, giving access to the dynamical-fermion generalization of $|\tilde{g}\rangle$. We note that this phenomenon cannot be observed with a background static field, such as the magnetic field of the quantum Hall effect, but is instead characteristic of LGTs with fermionic matter, unveiling an interesting interplay between the Berry phase and the inner $\mathbb{Z}_2$ flux. This offers a neat alternative to the numerical demonstration of the two-fold ground-state degeneracy, typically hindered by finite-size effects. As the quantum fluctuations are increased by raising h, we see that one tends smoothly to the electric-field dominated phase $\Phi_{\mathsf{B}_t} = \pi/2$, but the first-order topological phase transition between SPT and TBI, and the intertwining of the edge and vison states is still captured by the discontinuity of the inner flux.

7.4.4 Topological entanglement entropy

As argued in the previous section, the ground-state degeneracy and the flux threading are topological phenomena related to the underlying cylindrical manifold. This raises the possibility that this quasi-1D IGT (7.5) displays topological order, as occurs for Kitaev's toric code [Kit03]. This is indeed the case in other quasi-1D geometries, such as the thin-torus limit of two-dimensional fractional quantum

Hall states [BK05, GH14, CSCR+17]. In recent years, quantum-information tools that quantify the entanglement of the ground-state have turned out to be extremely useful to characterise various many-body properties [Laf16]. In particular, the Von Neumann entanglement entropy for a bi-partition of the ground-state $|g\rangle$ into two blocks A-B of equal sizes is defined as $S(\rho_A) = -\mathrm{Tr}\{\rho_A \log \rho_A\}$, where $\rho_A = \mathrm{Tr}_B\{|g\rangle\langle g|\}$ is the reduced density matrix. For a (2+1) topologically-ordered ground-state, this entanglement entropy scales as

$$S(\rho_\mathrm{r}) = \alpha|\partial A| - \gamma_\mathrm{t}, \tag{7.17}$$

where $|\partial A|$ is the number of sites that belong to the boundary separating the A-B regions, α is a constant that characterizes this entanglement area law, while γ_t is a universal sub-leading constant that quantifies the topological corrections [KP06, **?**]. Although in a gapped phase the value of γ_t is constant, it has already been obseverd that close to a QPT there are strong finite size effects, and from numerical simulation it is very hard to extract a reliable determination of it [TCL14]. Furthermore, the value of γ_t for bipartitions that are not contractible to a point depends on both the choice of the bipartition and the choice of the ground-state in the ground-state manifold [ZGT+12].

In order to reliably extract γ_t, we turn to study finite-size Creutz-Ising ladders, interpreted through the mapping to the thin cylinder of length $2\times N_\mathrm{s}$ of Fig. 7.5**(b)**. We consider a bipartition separating the two legs, such that $|\partial A| = N_\mathrm{s}$. In the effective manifold, this corresponds to a longitudinal bipartition of the cylinder (see Fig. 7.5**(b)**), such that the entropy (7.17) should scale with the length of the cylinder. In this finite-size regime, the ground-state is an eigenstate of D_ℓ, and thus has minimal entropy. γ_t should thus get saturated at its maximum value, namely $\gamma_\mathrm{t} = \log(2)$. Our numerical analysis is limited to short ladders, as the particular bipartition limits the efficiency of the MPS routines. In Fig. 7.7**(a)**, we plot the entanglement entropy as a function of the ladder length for two points deep in the SPT and the TBI. The fit of the data allows to confirm that $\gamma_\mathrm{t} \approx \log 2$ in both the SPT and TBI phases. After repeating the same analysis for several values of the imbalance, we obtain Fig. 7.7**(b)**. In this figure, γ_t is constantly very close to the expected $\log(2)$ within both SPT and TBI phases. It only departs significantly from that value close to the phase transition, where the larger correlation length increases the finite-size effects [TCL14]. The presence of a non-zero topological entropy is a further indication that the complete gauge-matter system is topologically ordered both in the SPT phase and in the TBI. Due to the lack of signature of criticality in our numerical results about the fluxes threading the cylinder and the bulk susceptibility of Figs. 7.6**(a)** and **(b)** (blue circles), we are thus confident that the topologically-ordered phase survives for large values of the electric-field.

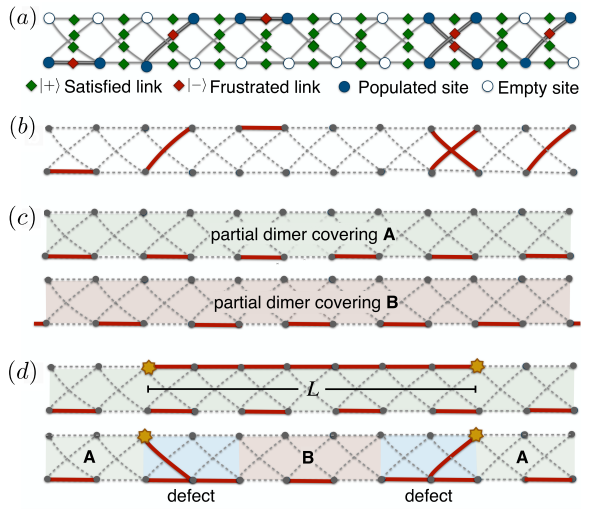

Fig. 7.8 Dimer coverings and soliton deconfinement: (a) In the $h \gg t, J$ and $\Delta = 0$ limit, Gauss law requires that some of the Ising fields will be frustrated due to the distribution of fermionic matter in the ladder. **(b)** The frustrated Ising fields can be identified with dimers (red bonds) that partially cover the lattice. **(c)** Switching on $\Delta > 0$ selects only the A and B dimer coverings. **(d)** Adding two fermions changes the dimer covering, and it becomes energetically favorable to create topological defects in the dimer configurations, which can accommodate for the deconfined charges.

7.5 $\mathbb{Z}_2$ Fermionic Deconfinement

In this section, we argue that the topologically-ordered flux-dominated phase described above shows fermionic deconfinement for any value of the transverse field. We first introduce the notion of gauge frustration, and how it generates deconfined topological defects when the system is doped above or below half filling. We then quantitatively characterize the absence of confinement using static charges, and we compare it with the more standard case involving string breaking.

7.5.1 Gauge frustration and topological defects

Paralleling the situation in the standard (2+1) IGT [Fra13], the existence of topological order in the Creutz-Ising ladder suggests that the ground-state lies in a deconfined phase despite the lack of plaquette interactions $J = 0$. As outlined above, the absence of criticality for large h suggests that this deconfinement may survive to arbitrarily-large electric-field strengths, which contrasts to the standard IGT [Kog79].

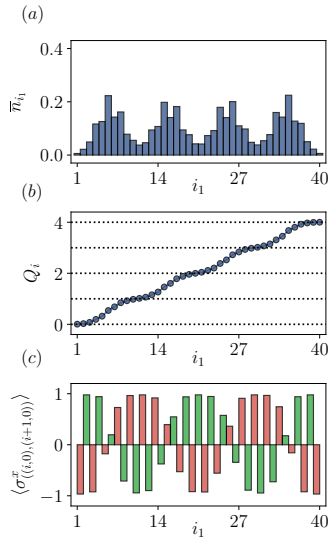

Fig. 7.9 Finite doping and soliton-induced deconfinement: **(a)** Real-space fermionic occupation for a ladder of length $N_s = 40$ filled with $N = 44$ particles for $\Delta = 4t$, $h = 0.2t$ and $J = 0$, where the formation of a periodic crystalline structure can be appreciated. **(b)** Integrated charge Q_i along the ladder, showing that each peak of excess charge with respect to half filling contains a fermionic number of one. **(c)** Corresponding electric field configuration $\langle\sigma^x_{((i,0),(i+1,0))}\rangle$ in the lower leg of the ladder, odd links are red and even are green. Topological solitons between the two degenerate electric field configurations appear, and the peaks of excess charge are located at the position of the defects.

Let us start by discussing the half-filled regime of the Hamiltonian (7.5) for $h \gg t$ and $\Delta = 0$. In this case, the link lsing fields minimize their energy for $|+\rangle = (|\uparrow\rangle + |\downarrow\rangle)/\sqrt{2}$. However, the presence of fermions can frustrate some links in order to satisfy the constraints (7.6), forcing the Ising fields to lie in $|-\rangle = (|\uparrow\rangle - |\downarrow\rangle)/\sqrt{2}$. We call this *gauge frustration*, namely the impossibility of simultaneously minimizing all the individual Hamiltonian terms due to the Gauss constraint.

In contrast to pure gauge theories, this type of frustration can occur in the even sector $q_i = 0$, as some of the sites might be occupied by a dynamical fermion (see Fig. 7.8**(a)**). By plotting only the frustrated links/bonds, one understands that the ground-state corresponds to a partial covering of the ladder with a single restriction: each site can be touched by one bond at most (see Fig. 7.8**(b)**). This is precisely the definition of a dimer, with the peculiarity that dimer models typically consider the complete covering of the lattice [Fis61, RK88], whereas in our half-filled case

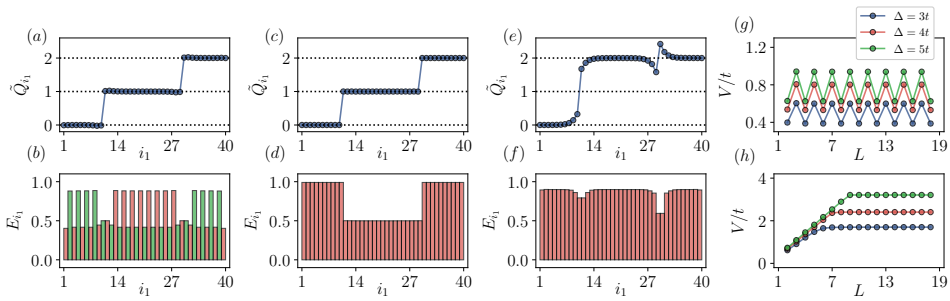

Fig. 7.10 Deconfinement versus string breaking : From **(a)** to **(f)** we represent the ground-state configuration corresponding to a ladder of length $N_s = 40$ at half filling with two extra static charges located in the upper leg and separated by $L = 20$ sites, with $h = 0.2t$. **(a)** Integrated total charge Q_i in the even charge sector for $\Delta = 3t$, showing two jumps of height one at the location of the static charges. **(b)** Each static charge creates a defect electric field to satisfy Gauss law. **(c)** Same as before but for the imbalanced sector with $\Delta = 10t$. **(d)** In this case, an electric string develops between the charges. **(e)** and **(f)** depicts how, for $\Delta = 3t$ and in the imbalanced sector, a particle-antiparticle pair is created in the vacuum to screen the static charges, breaking the original string between them. **(g)** Potential energy V/t between the two static charges as a function of the distance x between them, for different values of Δ, in the even charge sector. **(h)** A similar calculation in the imbalanced sector.

the ground-state will be a linear superposition of all partial dimer coverings. We note that, in the absence of dynamical fermions, the original connection of an IGT to a quantum dimer model in the large-h limit was put forth by R. Moessner et *al.* by introducing a static background $\mathbb{Z}_2$ charge $q_i = 1$ at every site (i.e. odd charge sector) [MSF01]. In our case, the dynamical fermions allow for this dimer limit even in the absence of static charges, albeit only with partial coverings.

So far, the imbalance has been fixed to zero. If we now allow for $\Delta > 0$, the fermions will preferably occupy the lower leg, such that only two degenerate coverings are relevant for the large-h ground-state (see Fig. 7.8**(c)**). These two coverings, which we label as A and B, are related by a simple lattice translation and, yet, they are essential for the deconfinement of the Creutz-Ising ladder. If one adds a pair of fermions at a distance L above half-filling, these must be accommodated in the upper leg, such that the Ising fields change to comply with the Gauss constraints. As depicted in Fig. 7.8**(d)**, if we insist on maintaining one of the dimer coverings, say A, an electric field string must connect the fermions in the upper leg, such that the energy is $E(L) - E_0 = hL$, and the charges are confined $V(L) \propto L$. This is the standard situation in the (2+1) IGT in the even sector [Kog79]. In our case, however, the two-fold coverings allow for a different situation: one can interpolate

between the A and B configurations, such that $E(L) - E_0 = 3h$, and the charges are deconfined $V(L) \propto V_0$. The charges, which are no longer confined in pairs but localized at the topological soliton that interpolates between A and B, carry a non-zero $\mathbb{Z}_2$ charge, which is at the very heart of the notion of deconfinement.

To assess the validity of these arguments, and extend them beyond the $h \gg t$ limit, we explore the Creutz-Ising ladder for finite doping using the MPS numerics. In Fig. 7.9**(a)**, we depict the occupation $\overline{n}_{i_1} = \langle : n_{(i_1,0)} : \rangle + \langle : n_{(i_1,1)} : \rangle$ summed over the pair of sites in the upper and lower legs. This density displays an inversion-symmetric distribution of the extra doped charges, which are localized around distant centers maximizing their corresponding distances. In Fig. 7.9**(b)**, we represent the integrated $\mathbb{Z}_2$ charge from the left boundary of the ladder $Q_{i_1} = \sum_{j_1 \leq i_1} \overline{n}_{j_1}$. Comparing this profile to Fig. 7.9**(c)**, where we represent the electric-field configuration, it becomes manifest that each of the doped fermions is localised within a topological soliton of the gauge fields. The bound fermion-soliton quasi-particles are deconfined, as they carry a unit $\mathbb{Z}_2$ charge (Fig. 7.9**(b)**), and can interact among each other forming a crystalline structure (Fig. 7.9**(a)**). To be best of our knowledge, our results confirm quantitatively this mechanism for the first time, and show that it can also appear in fermionic LGTs that combine topological order and SPT phases. We note that a similar deconfinement mechanism has been suggested for the odd sector of a pure IGT in (1+1) dimensions [MSF01], based on an analogy to the Peierls solitons in polymers [SSH79]. Our detailed analysis shows that, in our case, this type of solitons characterised by charge fractionalization [**?**, GDG+20, GDG+19] are not the underlying mechanism explaining the deconfinement for the $h \gg t$ limit of IGTs. As discussed above, the integrated charge around the solitons is quantized in units of the $\mathbb{Z}_2$ charge, but there is no signature of charge fractionalization (Fig. 7.9**(b)**). This result points to a different nature of topological defects in the magnetic- and electric-dominated phases, which will be the subject of detailed future studies.

7.5.2 Deconfinement versus string breaking

In this last section, we argue that the appearance of the mechanism of soliton deconfinement depends on the particular charge sector (7.6). So far, we have focused on the even sector, which is characterized by the absence of background $\mathbb{Z}_2$ charges $q_{\boldsymbol{i}} = 0, \forall \boldsymbol{i} \in \mathbb{Z}_{N_s} \times \mathbb{Z}_2$. We now make a full comparison with a different sector, hereby referred to as the *imbalanced sector*, where there is a static $\mathbb{Z}_2$ charge at each site of the lower leg, namely $q_{(i,0)} = 1$, $q_{(i,1)} = 0$ $\forall i \in \mathbb{Z}_{N_s}$. In this case, there are neither frustrated bonds in the ground-state, nor partial dimer coverings or solitons as in Fig. 7.8. Accordingly, the situation and the confinement properties change completely. To quantify these differences, we introduce two additional background charges on the upper leg of the ladder that are separated by a distance L, namely we add $q_{(i_0,1)} = q_{(i_0+L,1)} = 1$ to the two different charge sectors.

In Figs. 7.10**(a)-(b)**, we represent the total integrated charge $\tilde{Q}_{i_1} = Q_{i_1} + \sum_{j_1<i_1}(q_{(j_1,0)} + q_{(j_1,1)})$, which includes both the dynamical fermions and the background charges above the even charge sector. We also depict the underlying averaged electric field, $E_{i_1} = \sum_{i_2,i_2'} \langle \sigma^x_{((i_1,i_2),(i_1+1,i_2'))} \rangle / 4$. The situation is analogous to the soliton-induced deconfinement discussed in the previous section, but the location of each solitons is now pinned to the position of the extra static charge, while in Fig. 7.9 the unpinned solitons tend to maximize their spread and distance forming a soliton lattice. In Figs. 7.10**(c)-(d)**, we depict the same observables for the imbalanced sector. It is clear that an electric field line connecting the static charges is established, which leads to the aforementioned confinement. The new aspect brought by the dynamical matter is that, by lowering the energy imbalance Δ, it can become energetically favorable to create a particle-antiparticle pair that breaks this string and screens the static $\mathbb{Z}_2$ charges, as can be observed in Figs. 7.10 **(e)-(f)**. In these figures, one sees that the electric fields are restricted to the regions around the static charges, and that the $\mathbb{Z}_2$ charges are no longer unity, but get screened to $\tilde{Q}_i \bmod 2 = 0$, signaling the aforementioned string breaking.

We can make a quantitative study of the difference in the confinement properties of the two charge sectors by calculating the dependence of the effective potential with the distance between the static charges $V(L)$. In Fig. 7.10 **(g)**, we present the results for the even charge sector and different values of Δ. In all cases, apart from an even-odd effect due to the so-called Peierls-Nabarro barriers associated with the defects [Pei40, Nab47], the energy does not grow with the distance, signaling deconfinement. In contrast, in the imbalanced sector of Fig. 7.10 **(h)**, the potential grows linearly with the distance until the string breaks at a certain length, signaling confinement.

7.6 Summary

In this chapter, we have identified novel topological effects in fermionic gauge theories. In particular, we have introduced a minimal fermionic $\mathbb{Z}_2$ lattice gauge theory, the Creutz-Ising ladder, which allows investigating the interplay between topology and gauge invariance. We have shown how, even in the absence of a plaquette term, the system presents a magnetic-flux dominated phase, in which a dynamical π flux appears in the ground state as a consequence of an Aharonov-Bohm instability. This phenomenon results from the interplay between gauge-invariant interactions and the particular connectivity of the model, which also gives rise to SPT phases in the fermionic sector. We have characterized the properties of these phases, including the presence of protected gauge-matter edge states, through MPS-based numerical calculations, and use a topological invariant to find first-order phase transitions between the topological and trivial phases.

Our model can also be interpreted as a thin-cylinder limit of a (2+1) $\mathbb{Z}_2$ LGT.

This equivalence allows us to uncover the presence of topological order by calculating the topological correction to the entanglement entropy. Topological order is also associated with the degeneracy of the ground-state, which can be characterized by two different fluxes threading the hole of the cylinder (i.e. presence or absence of a trapped vison). We have shown that, in the Creutz-Ising ladder, the topological order intertwines with topological symmetry protection, and this connection manifests in the change of the inner flux, and thus the trapping of a vison, when crossing phase transition lines towards the SPT phase such that edge states emerge from the bulk and localize within the ladder boundaries. This feature could facilitate the detection of topological order in future experiments.

Finally, we have shown how fermionic deconfinement, which accompanies topological order, survives for the whole parameter space considered. This occurs due to the presence of deconfined topological defects associated to the fermionic quasiparticles, that appear on a frustrated background of electric fields imposed by gauge invariance. We have investigated this mechanism using both static and dynamical charges, and compare it to the more standard confining case where string breaking usually takes place.

We believe that our results advance substantially the understanding of topological phenomena in lattice gauge theories. Moreover, we have shown that the inclusion of dynamical fermions can stabilize a magnetic-dominated deconfined phase even in the absence of plaquette interactions. Therefore, the results identify a new avenue for the realization of spin-liquid physics in LGTs, relevant for both condensed matter and high-energy physics, in cold-atom experiments based on state-of-the-art building blocks that have already been used for quantum simulation purposes. This would allow to investigate complex phenomena, such as topological order and deconfinement, using minimal resources. The methods applied here can be used to further explore the static and dynamical properties of $\mathbb{Z}_2$ fermionic gauge theories, including the phase diagram at different fillings or the non-equilibrium quench dynamics.

Conclusions and perspectives

Throughout this thesis, we have studied a range of strongly-correlated topological effects that appear in mixtures of ultracold atoms in optical lattices. We have shown, in particular, how these atomic systems can be employed as quantum simulators to investigate several quantum many-body phenomena characteristic of condensed matter and high-energy physics.

The interest in this approach is two fold. First, cold-atom quantum simulators allow to experimentally verify certain phenomena that are harder to access in natural systems. This is the case for charge fractionalization, induced in particular by topological solitons, that, although predicted decades ago by Su, Schrieffer and Heeger in polyacetylene, still lacks a direct experimental confirmation. We have shown that both topological solitons and fractionalization take place in the ground state of the doped $\mathbb{Z}_2$ Bose-Hubbard (chapter 3) and the rotor Jackiw-Rebbi model (chapter 6), and proposed how these can be implemented using Bose-Bose and Bose-Fermi mixtures, respectively. Thanks to their remarkable control properties, ultracold atoms could provide a cleaner observation of these effects compared to their solid-state counterparts.

Second, quantum simulators promise to overcome the limitations associated to classical computers in their task to solve relevant mathematical models that describe physical systems. In this thesis, we have focused on quark confinement which, although a central concept in particle physics, remains poorly understood. Our approach consists on addressing this problem by studying simpler systems, that can be more easily simulated with cold atoms, where a confinement-deconfinement transition appears for the emergent quasi-particles in strongly-correlated phases (chapter 6).

Moreover, we have also considered the possibilities that cold-atom simulators offer beyond quantum simulations. More precisely, we have extended charge fractionalization to bosonic matter (chapter 5), and uncover various topological phases

where the interplay between symmetry breaking and symmetry protection gives rise to novel topological effects (chapter 4). Finally, we have explored near-term quantum simulators for gauge theories, where we found a gauge-frustration mechanism that could allow to prepare robust topological order in cold-atomic systems (chapter 7), as well as to explore other two-dimensional gauge theory phenomena such as fermionic deconfinement.

Our results thus establish new connections between atomic, condensed-matter and high-energy physics that could prove beneficial for further investigations on topological quantum matter, both from a theoretical and experimental point of view.

Appendices

Appendix A

Mean-field approach

In this appendix, we include more detailed calculations performed to obtain some of the results included in the thesis. We present, in particular, the mean-field approach considered in chapters 4 and 6, including both a Born-Oppenheimer ansatz (Sec. A.1) and a self-consistent Hartree-Fock method (Sec. A.2).

A.1 Born-Oppenheimer ansatz

In this section, we present various details of the Born-Oppenheimer-type variational ansatz for the ground-state and low-energy excitations of the $\mathbb{Z}_2$BH model used in chapter 4. In the hard-core limit, we consider the Hamiltonian

$$H^{U\to\infty}_{\mathsf{Z_2BH}} = \sum_i \Big(-(t+\alpha\sigma^z_{i,i+1})c^\dagger_i c_{i+1} + \frac{\beta}{2}\sigma^x_{i,i+1} + \frac{\Delta}{4}\sigma^z_{i,i+1} + \text{H.c.} \Big). \tag{A.1}$$

For the groundstate, the family of variational states is defined in Eq. (4.2),

$$|\Psi_{\text{gs}}(\{d_{\boldsymbol{n}},\boldsymbol{\theta}\})\rangle = |\psi_{\text{f}}(\{d_{\boldsymbol{n}}\})\rangle \bigotimes \mathrm{e}^{-\mathrm{i}\sum_i \frac{\theta_{i,i+1}}{2}\sigma^y_{i,i+1}} |-\rangle_{\text{s}} \,. \tag{A.2}$$

The set of variational parameters $\{d_{\boldsymbol{n}},\boldsymbol{\theta}\}$ can be fully determined by the minimization of

$$\epsilon_{\text{gs}}(\{d_{\boldsymbol{n}},\boldsymbol{\theta}\}) = \frac{1}{L}\langle\Psi_{\text{gs}}(\{d_{\boldsymbol{n}},\boldsymbol{\theta}\})| H^{U\to\infty}_{\mathsf{Z_2BH}} |\Psi_{\text{gs}}(\{d_{\boldsymbol{n}},\boldsymbol{\theta}\})\rangle \,. \tag{A.3}$$

Since the $\mathbb{Z}_2$ fields are quasi-static with respect to bosons, averaging over the former in Eq. (A.3) leads to an effective Hamiltonian $H_{\text{f}}(\boldsymbol{\theta})$ acting on the state of the latter, with $|\psi_{\text{f}}(\{d_{\boldsymbol{n}}\}\rangle$ as its ground state. Accordingly, the fermionic variational parameters are fully determined by the $\mathbb{Z}_2$-field variational angles $d_{\boldsymbol{n}} = d_{\boldsymbol{n}}(\boldsymbol{\theta})$ (i.e. the fermions adapt instantaneously to the slow spins). As discussed in chapter 4,

for periodic boundary conditions, it suffices to consider only two variational angles, namely $\boldsymbol{\theta} = (\theta_A, \theta_B)$ for the links joining odd-even (even-odd) lattice sites. In such a case, the effective Hamiltonian $H_{\mathrm{f}}(\boldsymbol{\theta})$ turns out to be the static SSH Hamiltonian introduced in chapter 1 through Eq. (1.47),

$$\hat{H}_{\mathrm{SSH}}(\boldsymbol{\theta}) = t_1(\boldsymbol{\theta}) \sum_i \hat{c}_{2i}^\dagger \left(\hat{c}_{2i+1} + \mathrm{H.c.} \right) + t_2(\boldsymbol{\theta}) \sum_i \left(\hat{c}_{2i+1}^\dagger \hat{c}_{2i+2} + \mathrm{H.c.} \right), \tag{A.4}$$

parametrized by the variational fields $t_1(\boldsymbol{\theta}) = t(\boldsymbol{\theta})(1 + \delta(\boldsymbol{\theta}))$ and $t_2(\boldsymbol{\theta}) = t(\boldsymbol{\theta})(1 - \delta(\boldsymbol{\theta}))$, where

$$\begin{aligned} t(\boldsymbol{\theta}) &= t + \frac{\alpha}{2} \big(\sin\theta_A + \sin\theta_B \big), \\ \delta(\boldsymbol{\theta}) &= \frac{\alpha(\sin\theta_A - \sin\theta_B)}{2t + \alpha(\sin\theta_A + \sin\theta_B)}. \end{aligned} \tag{A.5}$$

For such Hamiltonian, the variational ground-state energy (A.3) takes analytical form. To set the notation, and introduce concepts that are also used for the variational ansatz of excitations, let us present the diagonalization of $H_{\mathrm{SSH}}(\boldsymbol{\theta})$. We define Bogoliubov-type fermionic operators as

$$\begin{aligned} \gamma_{k,+} &= u_k(\boldsymbol{\theta}) c_k + v_k(\boldsymbol{\theta}) c_{k+\pi}, \\ \gamma_{k,-} &= v_k(\boldsymbol{\theta}) c_k + u_k(\boldsymbol{\theta}) c_{k+\pi}, \end{aligned} \tag{A.6}$$

where we have used the Fourier transformed operators $c_k = \sum_i \mathrm{e}^{-\mathrm{i}ki} c_i / \sqrt{L}$, and $c_{k+\pi} = \sum_i (-1)^i \mathrm{e}^{-\mathrm{i}ki} c_i / \sqrt{L}$, the quasi-momenta $k \in [-\frac{\pi}{2}, \frac{\pi}{2})$. By using the following functions

$$\begin{aligned} u_k(\boldsymbol{\theta}) &= \frac{\mathrm{i}\, s}{\sqrt{2}} \sqrt{1 - \frac{2t(\boldsymbol{\theta}) \cos k}{\epsilon_k^{\mathrm{f}}(\boldsymbol{\theta})}}, \\ v_k(\boldsymbol{\theta}) &= \frac{1}{\sqrt{2}} \sqrt{1 + \frac{2t(\boldsymbol{\theta}) \cos k}{\epsilon_k^{\mathrm{f}}(\boldsymbol{\theta})}}, \end{aligned} \tag{A.7}$$

where $s = \mathrm{sgn}\{\delta(\boldsymbol{\theta}) k\}$ and

$$\epsilon_k^{\mathrm{f}}(\boldsymbol{\theta}) = 2t(\boldsymbol{\theta}) \sqrt{\cos^2 k + \delta^2(\boldsymbol{\theta}) \sin^2 k}, \tag{A.8}$$

one can rewrite the static SSH Hamiltonian in terms of these $\gamma_{k,+}$ and $\gamma_{k,-}$ operators in diagonal form

$$H_{\mathrm{SSH}}(\boldsymbol{\theta}) = \sum_k \epsilon_k^{\mathrm{f}}(\boldsymbol{\theta}) \left(\gamma_{k,+}^\dagger \gamma_{k,+} - \gamma_{k,-}^\dagger \gamma_{k,-} \right), \tag{A.9}$$

Accordingly, the fermionic part of the variational groundstate can be written as follows

$$|\psi_{\rm f}(\{d_{\boldsymbol{n}}\})\rangle = \sum_{\boldsymbol{n}} d_{\boldsymbol{n}}(\boldsymbol{\theta}^\star)\,|\boldsymbol{n}\rangle_{\rm f} = \prod_{|k|\leq\pi/2} \gamma^\dagger_{k,-}\,|0\rangle\,, \tag{A.10}$$

where $|0\rangle$ is the fermionic vaccum, and the variational constants $d_{\boldsymbol{n}} = d_{\boldsymbol{n}}(\boldsymbol{\theta})$ only depend on the spin variational angles via Eqs. (A.7). As advanced below, the fermions adapt instantaneoulsy to the background $\mathbb{Z}_2$ fields, and the variational angles can be found by minimizing the groundstate energy of Eq. (A.2), where the first term stems from the addition of the fermionic single-particle energies in Eq. (A.8), while the remaining terms are straightforward expectation values over the spin coherent states.

Let us now turn into the variational ansatz for the low-energy excitations introduced in Eq. (4.5),

$$|\Psi_{\rm exc}(\boldsymbol{\eta})\rangle = \left(\sum_{k\in{\rm BZ}} \eta_{{\rm f},k}\gamma^\dagger_{k,+} + \sum_{i=1}^{N}\eta_{{\rm s},i}a_i^\dagger\right)|\Psi_{\rm gs}(\{d_{\boldsymbol{n}},\boldsymbol{\theta}^\star\})\rangle\,. \tag{A.11}$$

The excitation energies are then derived from the minimization of

$$\epsilon_{\rm exc}(\boldsymbol{\theta}^\star) = \min_{\boldsymbol{\eta}}\left(\mathcal{E}[\boldsymbol{\eta}]/\mathcal{N}[\boldsymbol{\eta}]\right), \tag{A.12}$$

where we have introduced the norm functional $\mathcal{N}[\boldsymbol{\eta}] = \langle\Psi_{\rm exc}(\boldsymbol{\eta})|\Psi_{\rm exc}(\boldsymbol{\eta})\rangle$ and the excitation energy functional $\mathcal{E}[\boldsymbol{\eta}] = \langle\Psi_{\rm exc}(\boldsymbol{\eta})|\,H^{U\to\infty}_{\mathsf{Z_2BH}} - \epsilon_{\rm gs}(\boldsymbol{\theta}^\star)|\Psi_{\rm exc}(\boldsymbol{\eta})\rangle$. In this part, the Hamiltonian (A.1) is treated within the spin-wave approximation (4.4) for the $\mathbb{Z}_2$ fields up to quadratic order,

$$\begin{aligned}
\sigma^z_{i,i+1} &\approx \cos\theta^\star_{i,i+1}\left(a_i + a_i^\dagger\right) - \sin\theta^\star_{i,i+1}\left(2a_i^\dagger a_i - 1\right),\\
\sigma^x_{i,i+1} &\approx \sin\theta^\star_{i,i+1}\left(a_i + a_i^\dagger\right) + \cos\theta^\star_{i,i+1}\left(2a_i^\dagger a_i - 1\right),
\end{aligned} \tag{A.13}$$

such that

$$\begin{aligned}
\mathcal{N}[\boldsymbol{\eta}] &= \sum_k \eta^*_{{\rm f},k}\eta_{{\rm f},k} + \sum_i \eta^*_{{\rm s},i}\eta_{{\rm s},i},\\
\mathcal{E}[\boldsymbol{\eta}] &= \sum_k \epsilon^{\rm f}_k(\boldsymbol{\theta}^\star)\eta^*_{{\rm f},k}\eta_{{\rm f},k} + \sum_i \epsilon^{\rm s}_i(\boldsymbol{\theta}^\star)\eta^*_{{\rm s},i}\eta_{{\rm s},i}.
\end{aligned} \tag{A.14}$$

By solving $\partial_{\boldsymbol{\eta}^*}(\mathcal{E}[\boldsymbol{\eta}]/\mathcal{N}[\boldsymbol{\eta}]) = 0$ using $\epsilon_{\rm exc}(\boldsymbol{\theta}^\star) = \min_{\boldsymbol{\eta}}\{\mathcal{E}[\boldsymbol{\eta}]/\mathcal{N}[\boldsymbol{\eta}]\}$, one can see that in the hardcore boson limit, the low-energy excitations can be: *(i)* delocalized fermion-like excitations with $\epsilon_{\rm exc}(\boldsymbol{\theta}^\star) = \epsilon^{\rm f}_k(\boldsymbol{\theta}^\star)\ \forall k \in [-\frac{\pi}{2},\frac{\pi}{2})$, or *(ii)* localized spin-wave-type excitations with $\epsilon_{\rm exc}(\boldsymbol{\theta}^\star) = \epsilon^{\rm s}_i(\boldsymbol{\theta}^\star)\ \forall i \in \{1,\cdots N\}$, as discussed in chapter 4.

Let us now give some details on how the calculation can be generalized for softcore bosons. To leading order in a $0 < \max\{t/U, \alpha/U\} \ll 1$ expansion, the $\mathbb{Z}_2$BHM (3.32) can be expressed as $H_{\mathsf{Z}_2\mathsf{BH}} \approx H^{U\to\infty}_{\mathsf{Z}_2\mathsf{BH}} + \Delta H$, with

$$\Delta H = -\frac{4t^2}{U}\sum_i \left(1 + 2\tilde{\delta}\sigma^z_{i,i+1} + \tilde{\delta}^2\right) n_i n_{i+1} + \frac{2t^2}{U}\sum_i \left(1 + \tilde{\delta}\left(\sigma^z_{i,i+1} + \sigma^z_{i+1,i+2}\right) + \tilde{\delta}^2\sigma^z_{i,i+1}\sigma^z_{i+1,i+2}\right)\left(c_i^\dagger n_{i+1} c_{i+2} + \text{H.c.}\right). \tag{A.15}$$

Considering the leading-order corrections to the ground-state energy $\epsilon_{\text{gs}}(\boldsymbol{\theta}^\star) + \delta\epsilon_{\text{gs}}(\boldsymbol{\theta}^\star)$, where $\delta\epsilon_{\text{gs}}(\boldsymbol{\theta}^\star) = \langle\Psi_{\text{gs}}(\boldsymbol{\theta}^\star)|\,\Delta H\,|\Psi_{\text{gs}}(\boldsymbol{\theta}^\star)\rangle$, the excitation energy (A.12) will be given by $\epsilon_{\text{exc}}(\boldsymbol{\theta}^\star) + \delta\epsilon_{\text{exc}}(\boldsymbol{\theta}^\star)$, where

$$\delta\epsilon_{\text{exc}}(\boldsymbol{\theta}^\star) = \min_{\{\eta\}}\left(\delta\mathcal{E}[\eta]/\mathcal{N}[\eta]\right), \tag{A.16}$$

and where the we have introduced the functional

$$\delta\mathcal{E}(\boldsymbol{\eta}) = \langle\Psi_{\text{exc}}(\boldsymbol{\eta})|\,\Delta H - \delta\epsilon_{\text{gs}}(\boldsymbol{\theta}^\star)|\Psi_{\text{exc}}(\boldsymbol{\eta})\rangle \tag{A.17}$$

in terms of the excited-state ansatz (A.11). We can evaluate these corrections by applying Wick's theorem, as the variational ansatz is built with free spinless fermions. Several of the possible Wick contractions will be canceled by the substraction of the ground-state energy shift $\delta\epsilon_{\text{gs}}(\boldsymbol{\theta}^\star)$. For the evaluation of the energy gap protecting the TBOW phase, the non-vanishing contributions will arise from Wick contractions that include single-particle correlations between the excited fermion and the lattice operators, e.g. $\langle\gamma_{k,+}c_i^\dagger\rangle_{\text{gs}}\langle c_i c_{i+1}^\dagger\rangle_{\text{gs}}\langle c_i\gamma_{k,+}^\dagger\rangle_{\text{gs}}$. By performing the corresponding calculations in detail, we find the particular correction to the energy gap expressed in Eq. (4.13),

$$\Delta\epsilon \approx 2t(\boldsymbol{\theta}^\star)|\delta(\boldsymbol{\theta}^\star)| - \frac{4t^2}{U}\left(1 + \frac{1}{\pi}\mathsf{E}(1-\tilde{\delta}^2)\right)\left(1 + \tilde{\delta}\left(\sin\theta_A^\star + \sin\theta_B^\star\right)\right), \tag{A.18}$$

to leading order in $\tilde{\delta} \ll 1$.

A.2 Self-consistent Hartree-Fock method

In this section, we discuss more in depth the details of the derivation of the self-consistent mean-field theory used in chapter 6. We start from the Hamiltonian

$$H = \sum_i \left(-t\left(c_i^\dagger c_{i+1} + c_{i+1}^\dagger c_i\right) + \boldsymbol{g}\cdot\boldsymbol{S}_i\, c_i^\dagger c_i - \boldsymbol{h}\cdot\boldsymbol{S}_i\right), \tag{A.19}$$

and perform a Hartree-Fock decoupling of the spin-fermion coupling

$$\boldsymbol{g}\cdot\boldsymbol{S}_i\, n_i \simeq \boldsymbol{g}\cdot\langle\boldsymbol{S}_i\rangle n_i + \boldsymbol{g}\cdot\boldsymbol{S}_i\langle n_i\rangle - \boldsymbol{g}\cdot\langle\boldsymbol{S}_i\rangle\langle n_i\rangle, \tag{A.20}$$

where we have introduced the number operator $n_i = c_i^\dagger c_i$. After the Hartree-Fock decoupling, the Hamiltonian can be expressed as the sum of non-interacting Hamiltonians for the fermion/spin sectors

$$H_\mathrm{f} = -\sum_i t c_i^\dagger c_{i+1} + \sum_i \epsilon_{\mathrm{f},i} n_i, \quad \epsilon_{\mathrm{f},i} = \boldsymbol{g}\cdot\langle\boldsymbol{S}_i\rangle \tag{A.21}$$

$$H_\mathrm{s} = -\sum_i \boldsymbol{h}_{\mathrm{s},i}\cdot\boldsymbol{S}_i\,, \qquad \boldsymbol{h}_{\mathrm{s},i} = \boldsymbol{h} - \boldsymbol{g}\langle n_i\rangle \tag{A.22}$$

where f (s) stands for fermions (spins). Accordingly, the fermion tunnel in a potential-energy landscape $\epsilon_{\mathrm{f},i}$ set by the expectation value of the spins, while the spins precess in an effective external field, which becomes inhomogeneous depending on the average distribution of fermions.

This mean-field approximation requires the obsrevables $\{\langle\boldsymbol{S}_i\rangle, \langle n_i\rangle\}_{i=1}^{N_\mathrm{s}}$ to be determined self-consistently, and we must deal with a number of self-consistency equations that grows linearly with the number of sites. The self-consistent loop consists in the following steps: We start by setting an initial spin configuration $\langle\boldsymbol{S}_i\rangle$, and compute the expectations values $\langle n_i\rangle$ by solving the fermionic tight-biding model (A.21) for a given temperature $T = \beta^{-1}$. These mean-field parameters are then used as input to determine the effective external field in the spin Hamiltonian (A.22), which is subsequently diagonalised, such that we can calculate the corresponding spin expectation values $\langle\boldsymbol{S}_i\rangle$ for a given temperature T.

This process must be iterated until reaching convergence for the free energy, which can be expressed as $\mathsf{F}_\mathrm{MF} = \mathsf{F}_\mathrm{f} + \mathsf{F}_\mathrm{s} + C$, where F_f (F_s) is the free energy of the fermions (spins) and C is the constant term appearing in the Hartree-Fock decoupling (A.20). The free energy for the system of fermions can be expressed in terms of the grand partition function

$$\mathsf{Z}_\mathrm{f} = \mathrm{Tr}\left\{\mathrm{e}^{-\beta(H_\mathrm{f}-\mu N_\mathrm{f})}\right\}, \tag{A.23}$$

where we have introduced the chemical potential μ, and the total fermion number $N_\mathrm{f} = \sum_i n_i$. For the mean-field decoupled model, this partition function can be readily expressed as

$$\mathsf{Z}_\mathrm{f} = \prod_{n=1}^{N_\mathrm{s}} \mathsf{Z}_{\mathrm{f},n}, \quad \mathsf{Z}_{\mathrm{f},n} = 1 + \mathrm{e}^{-\beta(E_{\mathrm{f},n}-\mu)}, \tag{A.24}$$

where $E_{\mathrm{f},n}$ are the eigenvalues of the quadratic fermionic Hamiltonian (A.21). The

free energy, which can be expressed as $\mathsf{F}_\mathrm{f} = -\frac{1}{\beta}\log \mathsf{Z}_\mathrm{f} + \frac{\mu}{\beta}\frac{\partial}{\partial\mu}\log \mathsf{Z}_\mathrm{f}$, thus becomes

$$\mathsf{F}_\mathrm{f} = -\frac{1}{\beta}\sum_n \log \mathsf{Z}_{\mathrm{f},n} + \mu \sum_n n_\mathrm{FD}(\mu,\beta), \tag{A.25}$$

where $n_\mathrm{FD}(\mu,\beta) = \frac{\mu\partial_\mu \mathsf{Z}_{\mathrm{f},n}}{\beta \mathsf{Z}_{\mathrm{f},n}} = 1/(\mathrm{e}^{\beta(E_{\mathrm{f},n}-\mu)}+1)$ is the so-called Fermi-Dirac distribution. For the spins, the number of which is conserved, the free energy can be written in terms of the canonical partition function

$$\mathsf{Z}_\mathrm{s} = \mathrm{Tr}\left\{\mathrm{e}^{-\beta H_\mathrm{s}}\right\}, \tag{A.26}$$

For the mean-field decoupled system, the Hamiltonian (A.22) can be diagonalised for each spin independently

$$\mathsf{Z}_\mathrm{s} = \prod_{i=1}^{N_\mathrm{s}} \mathsf{Z}_{\mathrm{s},i}, \quad \mathsf{Z}_{\mathrm{s},i} = \sum_{n=1}^{2S+1} \mathrm{e}^{-\beta E_{\mathrm{s},n}}, \tag{A.27}$$

where $E_{\mathrm{s},n}$ are the the $(2S+1)$ energies of the spins, which are identical for all sites of the chain. The corresponding free energy is

$$\mathsf{F}_s = -\frac{1}{\beta}\sum_i \log \mathsf{Z}_{\mathrm{s},i}. \tag{A.28}$$

Appendix B

Quantum field theory tools

This appendix contains further detailes on the quantum field theory tools used in chapter 6, including the continuum limit of the lattice Hamiltonian (Sec. B.1), the path integral formulation of the corresponding quantum field theory (Sec. B.2) and the effective action in the large-S limit (Sec. B.3).

B.1 Continuum limit of the lattice Hamiltonian

In this section, we present the details for the derivation of the continuum Hamiltonian field theory for the rotor-Jackiw-Rebbi (rJR) model. Splitting the Hamiltonian in Eq. (A.19) as $H = H_\mathrm{f} + H_\mathrm{sf} + H_\mathrm{s}$, the bare fermion tunnelling H_f leads to a periodic band structure with a pair of Fermi points at $\pm k_F = \pm\pi/2a$. Making the long-wavelength approximation

$$c_i \approx \mathrm{e}^{-\mathrm{i}k_F x_i}\sqrt{a}\psi_+(x) + \mathrm{e}^{+\mathrm{i}k_F x_i}\sqrt{a}\psi_-(x), \tag{B.1}$$

yields a pair of slowly-varying fields with the correct canonical algebra in the continuum limit $a \to 0$

$$\{\psi_\eta(x), \psi_{\eta'}(x')\} = \delta_{\eta,\eta'}\frac{\delta_{x,x'}}{a} \to \delta_{\eta,\eta'}\delta(x-x'). \tag{B.2}$$

By making a gradient expansion on the slowly-varying fields $\psi_\eta(x+a) = \psi_\eta(x) + a\partial_x\psi_\eta(x) + \mathcal{O}(a^2)$, neglecting rapidly oscillating terms, and setting $a\sum_j \to \int \mathrm{d}x$ in the continuum limit, the tunnelling term becomes

$$H_\mathrm{f} = \int \mathrm{d}x \sum_{\eta=\pm} \psi^\dagger_\eta(x)(-\mathrm{i}\eta c\partial_x)\psi_\eta(x), \quad c = 2ta, \tag{B.3}$$

where $c = 2ta$ plays the role of an effective speed of light. Defining the two-component spinors $\Psi(x) = (\psi_+(x), \psi_-(x))^{\mathrm{t}}$, $\overline{\Psi}(x) = (\psi_-^\dagger(x), \psi_+^\dagger(x))$, one readily sees that the Hamiltonian corresponds to a relativistic QFT of massless Dirac spinors

$$H_{\mathrm{f}} = \int \mathrm{d}x \overline{\Psi}(x) \left(-\mathrm{i}c\gamma^1 \partial_1\right) \Psi(x) \tag{B.4}$$

in a (1+1) Minkowski spacetime $x^0 = ct, x^1 = x$ of metric $g_{\mu\nu} = \mathrm{diag}(1, -1)$, where $\gamma^0 = \sigma^x$, $\gamma^1 = -\mathrm{i}\sigma^y$ are the gamma matrices $\{\gamma_\mu, \gamma_\nu\} = 2\delta_{\mu,\nu}$ in the so-called Weyl basis, and $\overline{\Psi}(x) = \Psi^\dagger(x)\gamma^0$. In the context of lattice gauge theories, the tunnelling Hamiltonian corresponds to the staggered-fermion discretization of the Dirac equation [KS75] by setting $t = 1/2a$ and applying a Kawamoto-Smit rotation $c_j \to \mathrm{e}^{\mathrm{i}\pi j/2} c_j$ [KS81].

Let us now turn our attention to the spin operators, which yield a $(2S+1)$-dimensional representation of the $\mathfrak{su}(2)$ algebra $\boldsymbol{S}_i \times \boldsymbol{S}_j = \mathrm{i}\delta_{i,j}\boldsymbol{S}_i$. We introduce the so-called Néel $\boldsymbol{n}(x)$ and canting $\boldsymbol{\ell}(x)$ slowly-varying fields

$$\boldsymbol{S}_i \approx \cos(k_N x_i) S\, \boldsymbol{n}(x) + a\boldsymbol{\ell}(x), \tag{B.5}$$

where the wave-vector $k_N = \pi/a$ captures the Néel alternation of antiferromagnetic ordering. These operators satisfy the following algebra in the continuum limit

$$\begin{aligned} \boldsymbol{\ell}(x) \times \boldsymbol{n}(x') &= \mathrm{i}\delta(x - x')\boldsymbol{n}(x), \\ \boldsymbol{\ell}(x) \times \boldsymbol{\ell}(x') &= \mathrm{i}\delta(x - x')\boldsymbol{\ell}(x), \\ \boldsymbol{n}(x) \times \boldsymbol{n}(x') &= \mathrm{i}\delta(x - x')\boldsymbol{\ell}(x)(a/S)^2, \end{aligned} \tag{B.6}$$

where one must consider that there is a two-site unit cell, such that the continuum limit yields $\delta_{x,x'}/2a \to \delta(x - x')$ in this case. In situations dominated by the Néel field, the contribution of the canting field will be negligible $\langle \boldsymbol{\ell}(a/S)^2 \rangle \to \boldsymbol{0}$, and one obtains the algebra of position $\boldsymbol{n}$ and angular momentum $\boldsymbol{\ell} = \boldsymbol{n} \times (-\mathrm{i}\boldsymbol{\nabla}_{\boldsymbol{n}})$ of a quantum-mechanical particle [Hal83, Aff85]. Moreover, in this limit, one also finds that

$$\boldsymbol{n}(x) \cdot \boldsymbol{n}(x) = 1 + 1/S \tag{B.7}$$

such that the particle will be confined to a unit sphere in the large-spin limit $S \gg 1$. Therefore, in the large-S limit, the Néel and canting fields represent a the orientation of a quantum rotor and its angular momentum, respectively.

Combining the expressions for the Dirac (B.1) and rotor (B.5) fields, and neglecting again rapidly-oscillating terms, we find that the spin-fermion coupling can be expressed as

$$H_{\mathrm{sf}} = \int \mathrm{d}x \overline{\Psi}(x) \boldsymbol{g}_s \cdot \left(\boldsymbol{n}(x) + \boldsymbol{\ell}(x)\gamma^0/S\right) \Psi(x), \quad \boldsymbol{g}_s = gS\mathbf{e}_z. \tag{B.8}$$

The first term can be understood as a Yukawa-like term that couples the fermion bilinear $\overline{\Psi}(x)\Psi(x)$ to the rotor projection $n_z(x)$ instead of the standard scalar field in a Yukawa theory [PS95]. The second term couples the time-like component of the fermion current $j^0(x) = \overline{\Psi}(x)\gamma^0\Psi(x)$, i.e. the charge density, to the projection of the rotor angular angular $\ell_z(x)$.

Finally, the continuum limit of the spin precession yields

$$H_{\mathrm{s}} = -\int \mathrm{d}x \;\boldsymbol{h}\cdot\boldsymbol{\ell}(x). \tag{B.9}$$

In analogy to the original situation (A.19), the rotor angular momentum is subjected to a magnetic field with both longitudinal and transverse components, being the latter responsible for introducing quantum fluctuations since $[\ell_x(x), n_z(x)] \neq 0$. Altogether, the continuum limit of the lattice model (A.19) corresponds to the quantum field theory of Eq. (6.18), $H = \int \mathrm{d}x \mathcal{H}(x)$, with

$$\mathcal{H} = \overline{\Psi}(x)\left(-\mathrm{i}c\gamma^1\partial_1 + \boldsymbol{g}_s\cdot\boldsymbol{n}(x)\right)\Psi(x) + (\boldsymbol{g}j_0(x) - \boldsymbol{h})\cdot\boldsymbol{\ell}(x), \tag{B.10}$$

B.2 Path integral formulation

In this section, we provide a path-integral derivation of the continuum-limit rotor-fermion QFT (B.10). This derivation serves for two purposes: one the one hand, it allows to clarify the absence of a topological θ term for any spin S, differing markedly from $O(N)$ non-linear sigma models arising from Heisenberg models [Hal83]; on the other hand, it sets the stage for a large-S limit approach to dynamical mass generation.

We are interested in the partition function $\mathsf{Z} = \mathrm{Tr}\{\mathrm{e}^{-\beta H}\}$, where H is the spin-fermion lattice Hamiltonian (A.19). In the $\beta \to \infty$ limit of zero temperature, this partition function contains all the relevant information about quantum phase transitions related to the chiral SSB and dynamical mass generation we are seeking. Using fermionic and spin coherent states in Euclidean time $\tau = \mathrm{i}t \in (0, \beta)$ [Fra13], this partition function can be expressed as a functional integral in terms of anti-commuting Grassmann fields for the fermions $\psi(\tau, x_i), \psi^\star(\tau, x_i)$ and commuting vector fields for the spins $\boldsymbol{\Omega}(\tau, x_i)$ lying in a 2-sphere of radius S, which can be rescaled in terms of unit vector fields $\boldsymbol{\Omega}(\tau, x_i) = S\boldsymbol{\omega}_i(\tau)$. Using the resolution of the identity in terms of both types of fields [Fra13], one finds that

$$\mathsf{Z} = \int \mathrm{D}[\psi^\star, \psi, \boldsymbol{\omega}]\mathrm{e}^{-\mathsf{S}_{\mathrm{E}}[\psi^\star, \psi, S\boldsymbol{\omega}]} \tag{B.11}$$

where the Euclidean action $\mathsf{S}_{\mathrm{E}} = \mathsf{S}_{\mathrm{sf}} - \mathrm{i}S\mathsf{A}_{\mathrm{WZ}}$ can be expressed as a functional over the fermion and spin fields

$$\mathsf{S}_{\mathrm{E}} = \int_0^\beta \mathrm{d}\tau \left(\sum_i \psi^\star(\tau, x_i)\partial_\tau\psi(\tau, x_i) + H(\psi^\star, \psi, S\boldsymbol{\omega})\right), \tag{B.12}$$

where $H(\psi^\star, \psi, S\boldsymbol{\omega})$ is obtained by substituting the fermion and spin operators in the normal-ordered Hamiltonian (A.19) by the Grassmann and vector fields. One also finds the so-called Wess-Zumino term, which corresponds to the area enclosed by the trajectory of the spin field in the unit 2-sphere

$$\mathsf{A}_{\mathrm{WZ}} = \int_0^\beta \mathrm{d}\tau \int_0^1 \mathrm{d}s \sum_i \boldsymbol{\omega}_i(s,\tau) \cdot (\partial_s \boldsymbol{\omega}_i(s,\tau) \times \partial_\tau \boldsymbol{\omega}_i(s,\tau)). \tag{B.13}$$

Here, this area is parametrized by $s \in [0,1]$, such that $\boldsymbol{\omega}_i(s,0) = \boldsymbol{\omega}_i(s,\beta)$ correspond to the closed trajectories that cover a spherical cap Σ between $\boldsymbol{\omega}_i(0,\tau) = \omega_i(\tau)$ and the north pole $\boldsymbol{\omega}_i(1,\tau) = \mathbf{e}_z$, which is used as the fiducial state in Bloch's sphere to define the spin coherent states (see Fig. 6.1).

In $O(3)$-symmetric situations, such as those arising in antiferromagnetic Heisenberg models, this Wess-Zumino term plays a crucial role as it is responsible for the mapping to a non-linear sigma model with an additional topological θ term that depends on the integer or half-integer nature of the spins [Hal83]. In the present case, however, there is no rotational symmetry in the classical Hamiltonian $H(\psi^\star, \psi, S\boldsymbol{\omega})$, and one can see from the particular form of the spin-fermion coupling and the external field that it will suffice to use coherent states pointing along the meridian at vanishing longitude

$$\boldsymbol{\omega}_i(\tau) = \omega_i^x(s,\tau)\mathbf{e}_x + \omega_i^z(s,\tau)\mathbf{e}_z, \tag{B.14}$$

which correspond to the great circle in the xz plane of Fig. 6.1. Accordingly, $\boldsymbol{\omega}_i \cdot (\partial_s \boldsymbol{\omega}_i \times \partial_\tau \boldsymbol{\omega}_i) = 0$ and there is no enclosed area by the precession of the spins, such that the Wess-Zumino term vanishes $\mathsf{A}_{\mathrm{WZ}} = 0$.

We can now introduce the equivalent of the slowly-varying quantum fields in Eqs. (B.1) and (B.5) in terms of the Grasmmann fermion fields

$$\psi(\tau, x_i) \approx \mathrm{e}^{-\mathrm{i}k_F x_i}\sqrt{a}\psi_+(\tau,x) + \mathrm{e}^{+\mathrm{i}k_F x_i}\sqrt{a}\psi_-(\tau,x), \tag{B.15}$$

and the spin vector fields

$$\omega_i(\tau) \approx \cos(k_N x_i)\,\boldsymbol{n}(\tau,x) + \frac{a}{S}\boldsymbol{\ell}(\tau,x). \tag{B.16}$$

Proceeding in analogy to App. B.1, we perform the gradient expansion in the continuum limit $a \to 0$, neglect rapidly-oscillating terms, and find $\mathsf{S}_{\mathrm{E}} \approx \int \mathrm{d}^2x\, \mathcal{L}(\boldsymbol{x})$ with the following Lagrangian density

$$\mathcal{L}(\boldsymbol{x}) = \overline{\Psi}(\boldsymbol{x})\left(\hat{\gamma}^\mu\partial_\mu + \boldsymbol{g}_s \cdot \boldsymbol{n}(\boldsymbol{x})\right)\Psi(\boldsymbol{x}) + (\boldsymbol{g}j_0(x) - \boldsymbol{h}) \cdot \boldsymbol{\ell}(\boldsymbol{x}), \tag{B.17}$$

with coupling $\boldsymbol{g}_{\mathrm{s}}$ and external field $\boldsymbol{h}$ defined in Eqs. (B.8) and (B.9), respectively. Here, $\boldsymbol{x} = (c\tau, x)$ is a 2-dimensional Euclidean space with metric $g^{\mathrm{E}}_{\mu,\nu} =$

diag(1, 1), and the Euclidean gamma matrices are $\hat{\gamma}^0 = \gamma^0, \hat{\gamma}^1 = -\mathrm{i}\gamma^1$. The Dirac spinor is composed of the right- and left-moving continuum Grassmann fields $\Psi(\boldsymbol{x}) = (\psi_+(\tau, x), \psi_-(\tau, x))^{\mathrm{t}}$, such that the adjoint becomes $\overline{\Psi}(\boldsymbol{x}) = \Psi^\dagger(\boldsymbol{x})\hat{\gamma}^0 = (\psi_-(\tau, x), \psi_+(\tau, x))$. Likewise, the Néel and canting fields are the vector fields

$$\begin{aligned} \boldsymbol{n}(\tau, x) &= \frac{1}{2}\left(\boldsymbol{\omega}_{2i}(\tau) - \boldsymbol{\omega}_{2i-1}(\tau)\right), \\ \boldsymbol{\ell}(\tau, x) &= \frac{S}{2a}\left(\boldsymbol{\omega}_{2i}(\tau) + \boldsymbol{\omega}_{2i-1}(\tau)\right). \end{aligned} \tag{B.18}$$

In the large-S limit, and in situations dominated by Néel correlations $|\boldsymbol{\ell}(a/S)^2| \to 0$, these fields are additionally subjected to the rotor constraints

$$\boldsymbol{n}(\boldsymbol{x}) \cdot \boldsymbol{n}(\boldsymbol{x}) = 1, \quad \boldsymbol{n}(\boldsymbol{x}) \cdot \boldsymbol{\ell}(\boldsymbol{x}) = 0, \tag{B.19}$$

which can be included in the partition function

$$Z = \int \mathrm{D}[\overline{\Psi}, \Psi, \boldsymbol{n}, \boldsymbol{\ell}] \mathrm{e}^{-\int \mathrm{d}^2 x \mathcal{L}(\boldsymbol{x})}, \tag{B.20}$$

through the functional integral measure

$$\mathrm{D}[\overline{\Psi}, \Psi, \boldsymbol{n}, \boldsymbol{\ell}] = \frac{(2S+1)}{4\pi} \prod_{\boldsymbol{x}} \mathrm{d}\overline{\Psi}(\boldsymbol{x}) \mathrm{d}\Psi(\boldsymbol{x}) \mathrm{d}^3 n(\boldsymbol{x}) \mathrm{d}^3 \ell(\boldsymbol{x}) \delta(\boldsymbol{n}^2 - 1) \delta(\boldsymbol{n} \cdot \boldsymbol{\ell}). \tag{B.21}$$

B.3 Effective rotor action and large-S limit

In this section, we give a detailed derivation of the effective rotor action (6.21). As outlined in chapter 6, one can integrate out the Grassmann fields from the partition function

$$\mathsf{Z} = \int \mathrm{D}[\boldsymbol{n}, \boldsymbol{\ell}] \left(\int \mathrm{D}[\overline{\Psi}, \Psi] \mathrm{e}^{-\int \mathrm{d}^2 x \mathcal{L}(\boldsymbol{x})} \right), \tag{B.22}$$

since the corresponding functional integral reduces to a product of Gaussian integrals. These integrals are obtained after transforming the fields in terms of Matsubara frequencies $\omega_n = \frac{\pi}{\beta}(2n+1)$, and quasi-momentum $qa \in [-\pi, \pi)$, according to

$$\begin{aligned} \Psi(\tau, x_i) &= \frac{1}{\sqrt{\beta L}} \sum_{n \in \mathbb{Z}} \sum_{q \in \mathrm{BZ}} \mathrm{e}^{\mathrm{i}(\omega_n \tau + q x_i)} \Psi(\omega_n, q), \\ \overline{\Psi}(\tau, x_i) &= \frac{1}{\sqrt{\beta L}} \sum_{n \in \mathbb{Z}} \sum_{q \in \mathrm{BZ}} \mathrm{e}^{-\mathrm{i}(\omega_n \tau + q x_i)} \overline{\Psi}(\omega_n, q). \end{aligned} \tag{B.23}$$

The corresponding integrals lead to

$$\int \mathrm{D}[\overline{\Psi},\Psi]\mathrm{e}^{-\int \mathrm{d}^2x\mathcal{L}} = \mathrm{e}^{-\int \mathrm{d}^2x\mathcal{L}_\mathrm{r}} \prod_{n,q} \det\left(-\mathrm{i}\omega_n + h_\mathrm{D}(q, \boldsymbol{g}_s\cdot\boldsymbol{n})\right), \tag{B.24}$$

where we have introduced a renormalised rotor Lagrangian

$$\mathcal{L}_\mathrm{r} = \left(\frac{\boldsymbol{g}}{2} - \boldsymbol{h}\right)\cdot\boldsymbol{\ell}, \tag{B.25}$$

for a homogeneous canting field $\boldsymbol{\ell}(\boldsymbol{x}) = \boldsymbol{\ell}$. This term (B.25), which contains the original precession under the external field $-\boldsymbol{h}$, gets a contribution from the back-action of the fermion current (B.17). For a homogeneous canting field, and at half-filling conditions $\int \mathrm{d}x j_0(x) = N_\mathrm{s}/2$, this back-action renormalizes the external field to $-(\boldsymbol{h} - \boldsymbol{g}/2)$.

In Eq. (B.24), we have introduced the single-particle Hamiltonian of a (1+1)-dimensional Dirac fermion

$$h_\mathrm{D}(q,m) = cq\gamma^5 + m\gamma^0, \tag{B.26}$$

with a Dirac mass proportional to the homogeneous Néel field $m = \boldsymbol{g}_s\cdot\boldsymbol{n}$. In the continuum and $T = 0$ limits, the product of determinants involving these Dirac Hamiltonians can be expressed in terms of momentum integrals

$$\prod_{n,q} \det\left(-\mathrm{i}\omega_n + h_\mathrm{D}(q, \boldsymbol{g}_s\cdot\boldsymbol{n})\right) = \mathrm{e}^{\frac{1}{4\pi^2 c}\int \mathrm{d}^2k \log\left(\boldsymbol{k}^2 + (\boldsymbol{g}_s\cdot\boldsymbol{n})^2\right)} \tag{B.27}$$

where we have introduced Euclidean momentum $\boldsymbol{k} = (\omega_n, cq)$.

This expression, together with Eq. (B.24), leads to an effective action which, up to an irrelevant term independent of the Néel and canting fields, reads as follows

$$\mathsf{S}_\mathrm{eff} = \int \mathrm{d}^2x \left(\left(\frac{\boldsymbol{g}}{2} - \boldsymbol{h}\right)\cdot\boldsymbol{\ell} - \frac{(\boldsymbol{g}_s\cdot\boldsymbol{n})^2}{4\pi c}\left(\log\left(\frac{\Lambda_\mathrm{c}}{\boldsymbol{g}_s\cdot\boldsymbol{n}}\right)^2 + 1\right)\right), \tag{B.28}$$

where the UV cutoff $\Lambda_\mathrm{c} = 2t$ appears in the integrals over the Euclidean momentum $\int \mathrm{d}^2k = \frac{2\pi}{c}\int_0^{\Lambda_\mathrm{c}} k\mathrm{d}k$. Since the fields are homogeneous, this equation leads directly to the result (6.21) used in chapter 6. This type of effective action, which contains a non-perturbative contribution $\sigma^2\log\sigma^2$, is a characteristic of the dynamical mass generation of the Gross-Neveu model [GN74], where σ is an auxiliary field. In that case, the above calculation is equivalent to a large-N limit summation of the leading Feynman diagrams, which contain a single fermion loop and all possible even numbers of legs for the σ field [GN74]. This contributes to an effective potential that develops a double-well structure as soon as $g \neq 0$, and thus induces the dynamical mass generation and chiral SSB. As noted in chapter 6, this SSB is

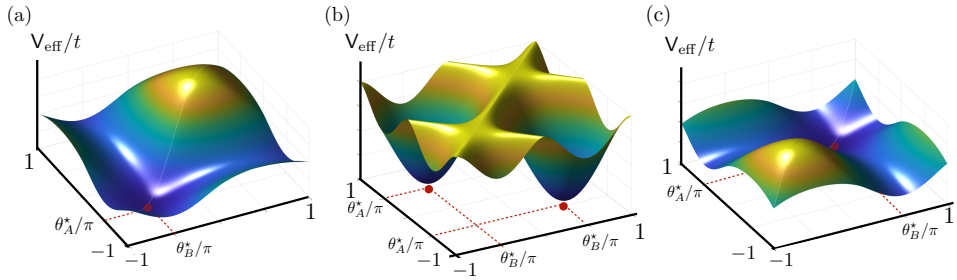

Fig. B.1 Saddle points of the effective potential (a) Effective potential for the south-pole paramagnetic regime $h_\ell = h_\ell^- - \delta/2$, where $\delta = h_\ell^+ - h_\ell^-$. **(b)** Effective potential for the Néel anti-ferromagnetic regime $h_\ell = h_\ell^- + \delta/2$. **(c)** Effective potential for the north-pole paramagnetic regime $h_\ell = h_\ell^- + 3\delta/2$.

dynamical as it requires quantum-mechanical effects via the fermion loops in order to take place, which makes it different from the classical SSB in the Jackiw-Rebbi model [**?**]. In the present case (B.28), the situation is different as the Néel and canting fields are not auxiliary, but have their own quantum dynamics that results from the non-commutativity of the rotor position and angular momentum. In particular, as a result of this competition, the dynamical SSB does not take place for an arbitrarily small g regardless of the other microscopic parameters, but there will be critical lines that delimit the phase with a dynamically generated mass, as discussed in chapter 6.

Let us now describe the large-S limit in more detail. Expressing the Néel and canting fields in the coherent-state basis (6.22),

$$\begin{aligned} \boldsymbol{n} &= \frac{1}{2}(\sin\theta_A - \sin\theta_B)\mathbf{e}_z - \frac{1}{2}(\cos\theta_A - \cos\theta_B)\mathbf{e}_x, \\ \boldsymbol{\ell} &= \frac{S}{2a}(\sin\theta_A + \sin\theta_B)\mathbf{e}_z - \frac{S}{2a}(\cos\theta_A + \cos\theta_B)\mathbf{e}_x. \end{aligned} \tag{B.29}$$

one finds that the effective action (B.28) can be expressed in terms of an effective potential $\mathsf{S}_{\rm eff} = \beta L S \mathsf{V}_{\rm eff}(\theta_A, \theta_B)$, as there are no time derivatives of the fields. By letting $S \to \infty$, the solutions correspond to the saddle point equations $\partial_{\theta_A} \mathsf{V}_{\rm eff}|_{\boldsymbol{\theta}^\star} =$

$\partial_{\theta_B}\mathsf{V}_{\rm eff}|_{\boldsymbol{\theta}^\star}=0$, which lead to the following system of non-linear equations

$$\begin{aligned}&\left(\left(\frac{g}{2}-h_\ell\right)-\frac{t}{\pi S}\left(\frac{gS}{2t}\right)^2(\sin\theta_A^\star-\sin\theta_B^\star)\log\left(\frac{4t}{gS(\sin\theta_A^\star-\sin\theta_B^\star)}\right)^2\right)\cos\theta_A^\star\\&=-h_{\mathsf{t}}\sin\theta_A^\star,\\&\left(\left(\frac{g}{2}-h_\ell\right)+\frac{t}{\pi S}\left(\frac{gS}{2t}\right)^2(\sin\theta_A^\star-\sin\theta_B^\star)\log\left(\frac{4t}{gS(\sin\theta_A^\star-\sin\theta_B^\star)}\right)^2\right)\cos\theta_B^\star\\&=-h_{\mathsf{t}}\sin\theta_B^\star,\end{aligned}\tag{B.30}$$

Despite the non-linearity, one can readily find an exact analytical solution to these saddle-point equations in the limit of vanishing transverse fields $h_{\mathsf{t}}=0$, where the only possible solutions correspond to $\cos\theta_A^\star=\cos\theta_B^\star=0$. There are four possible solutions within $\boldsymbol{\theta}^\star\in[-\pi,\pi)\times[-\pi,\pi)$, namely

(i) North-pole paramagnet: This solution is $\theta_A^\star=\theta_B^\star=\pi/2$, where the canting field points towards the north pole $\boldsymbol{\ell}(\boldsymbol{x})=(S/a)\boldsymbol{e}_z,\forall\boldsymbol{x}$. The corresponding spin coherent state is

$$\left|\mathsf{g}_{\ell\mathsf{P}}^{+}\right\rangle=|S,S\rangle_{z,1}\otimes|S,S\rangle_{z,2}\otimes\cdots\otimes|S,S\rangle_{z,N_{\rm s}}\,,\tag{B.31}$$

where $|S,m\rangle_{\alpha,i}$ is the common eigenstate of $\boldsymbol{S}_i^2,S_i^\alpha$ with eigenvalues $S(S+1)$ and $m\in\{-S,-S+1,\cdots,S-1,S\}$. Hence, all spin-$S$ particles are aligned towards the north pole. We note that this ordering is not caused by collective effects, but induced by the external longitudinal field, and that is why we refer to this state as a spin paramagnet.

(ii) South-pole paramagnet: This solution is $\theta_A^\star=\theta_B^\star=-\pi/2$, where the canting field points towards the south pole $\boldsymbol{\ell}(\boldsymbol{x})=-(S/a)\boldsymbol{e}_z,\forall\boldsymbol{x}$. The corresponding coherent state is

$$\left|\mathsf{g}_{\ell\mathsf{P}}^{-}\right\rangle=|S,-S\rangle_{z,1}\otimes|S,-S\rangle_{z,2}\otimes\cdots\otimes|S,-S\rangle_{z,N_{\rm s}}\,.\tag{B.32}$$

Hence, all spin-S particles are aligned towards the south pole.

(iii) Néel anti-ferromagnets: These solutions are $\theta_A^\star=-\theta_B^\star=\pi/2$, or $\theta_A^\star=-\theta_B^\star=-\pi/2$. In this case, and it is the Néel field which points towards the north $\boldsymbol{n}(\boldsymbol{x})=\boldsymbol{e}_z,\forall\boldsymbol{x}$ and south pole $\boldsymbol{n}(\boldsymbol{x})=-\boldsymbol{e}_z,\forall\boldsymbol{x}$, respectively. The corresponding spin coherent states are

$$\begin{aligned}\left|\mathsf{g}_{\mathsf{N}}^{+}\right\rangle&=|S,S\rangle_{z,1}\otimes|S,-S\rangle_{z,2}\otimes\cdots\otimes|S,S\rangle_{z,N_{\rm s}-1}\otimes|S,-S\rangle_{z,N_{\rm s}}\,,\\\left|\mathsf{g}_{\mathsf{N}}^{-}\right\rangle&=|S,-S\rangle_{z,1}\otimes|S,S\rangle_{z,2}\otimes\cdots\otimes|S,-S\rangle_{z,N_{\rm s}-1}\otimes|S,S\rangle_{z,N_{\rm s}}\,,\end{aligned}\tag{B.33}$$

Hence, all neighbouring spin-S particles are aligned in an anti-parallel manner. We note that, in this case, this ordering is caused by collective effects, and the north-

or south-pole solutions occur via the spontaneous symmetry breaking of the $\mathbb{Z}_2$ chiral symmetry $\boldsymbol{n}(\boldsymbol{x}) \to -\boldsymbol{n}(\boldsymbol{x})$ mentioned in chapter 6. This is why we refer to these states as anti-ferromagnets.

In order to decide which of the above orderings occurs in the system, we can compare the corresponding free energies per unit length $\mathsf{f}(\theta_A^\star, \theta_B^\star) = \frac{1}{L}\mathsf{F}(\theta_A^\star, \theta_B^\star) = -\frac{1}{L\beta}\log \mathsf{Z}(\theta_A^\star, \theta_B^\star)$, namely

$$\begin{aligned} \mathsf{f}\left(\pm\frac{\pi}{2}, \pm\frac{\pi}{2}\right) &= \pm\left(\frac{g}{2} - h_\ell\right)\frac{S}{a}, \\ \mathsf{f}\left(\pm\frac{\pi}{2}, \mp\frac{\pi}{2}\right) &= -\frac{t}{2\pi a}\left(\frac{gS}{2t}\right)^2\left(\log\left(\frac{2t}{gS}\right)^2 + 1\right). \end{aligned} \tag{B.34}$$

Comparing these energies, we find two critical lines $h_\ell^\pm$ that separate the Néel anti-ferromagnet from the two longitudinal paramagnets. The first one

$$h_\ell^- = \frac{g}{2} - \frac{t}{\pi S}\left(\frac{gS}{2t}\right)^2\left(\log\left(\frac{2t}{gS}\right) + \frac{1}{2}\right), \tag{B.35}$$

is obtained from $\mathsf{f}(-\pi/2, -\pi/2) = \mathsf{f}(+\pi/2, -\pi/2)$. Accordingly, for $h_\ell < h_\ell^-$, the groundstate corresponds to the south-pole longitudinal paramagnet. Conversely, for $h_\ell > h_\ell^-$, we enter into the Néel anti-ferromagnet. The second line is

$$h_\ell^+ = \frac{g}{2} + \frac{t}{\pi S}\left(\frac{gS}{2t}\right)^2\left(\log\left(\frac{2t}{gS}\right) + \frac{1}{2}\right), \tag{B.36}$$

and is obtained from $\mathsf{f}(+\pi/2, -\pi/2) = \mathsf{f}(+\pi/2, +\pi/2)$. In this case, for $h_\ell < h_\ell^+$, the groundstate corresponds to the Néel anti-ferromagnet, while or $h_\ell > h_\ell^+$, we enter into the north-pole longitudinal paramagnet. Both critical lines correspond to a situation where the effective potential changes from a single minimum into a double well, as represented in Fig. B.1.

(iv) Equator paramagnet: Finally, before concluding this section, let us discuss the other limit where one can find a different saddle-point solution. This corresponds to the $h_\ell = g = 0$ and $h_\mathsf{t} > 0$ limit, where both equations (B.30) are solved when $\sin\theta_A^\star = \sin\theta_B^\star = 0$. In this case, by comparing the corresponding free energies, one readily sees that there is a unique groundstate corresponding to $\theta_A^\star = \theta_B^\star = \pi$, where the canting field points along the equator $\boldsymbol{\ell}(\boldsymbol{x}) = (S/a)\boldsymbol{e}_x, \forall \boldsymbol{x}$. In terms of the spins, this phase corresponds to

$$|\mathsf{g}_{\mathsf{tP}}\rangle = |S, S\rangle_{x,1} \otimes |S, S\rangle_{x,2} \otimes \cdots \otimes |S, S\rangle_{x,N_\mathrm{s}}, \tag{B.37}$$

where all spins align parallel to the external transverse field. Since the ordering is not due to collective effects, we refer to this phase as a transverse paramagnet.

Bibliography

[AAL+13] M. Aidelsburger, M. Atala, M. Lohse, J. T. Barreiro, B. Paredes, and I. Bloch. Realization of the hofstadter hamiltonian with ultracold atoms in optical lattices. *Phys. Rev. Lett.*, 111:185301, Oct 2013.

[AAN+11] M. Aidelsburger, M. Atala, S. Nascimbène, S. Trotzky, Y.-A. Chen, and I. Bloch. Experimental realization of strong effective magnetic fields in an optical lattice. *Phys. Rev. Lett.*, 107:255301, Dec 2011.

[AB59] Y. Aharonov and D. Bohm. Significance of electromagnetic potentials in the quantum theory. *Phys. Rev.*, 115:485–491, Aug 1959.

[ABC+15] A. Amaricci, J. C. Budich, M. Capone, B. Trauzettel, and G. Sangiovanni. First-order character and observable signatures of topological quantum phase transitions. *Phys. Rev. Lett.*, 114:185701, May 2015.

[AEM+95] M. H. Anderson, J. R. Ensher, M. R. Matthews, C. E. Wieman, and E. A. Cornell. Observation of Bose-Einstein Condensation in a Dilute Atomic Vapor. *Science*, 269:198–201, 1995.

[Aff85] Ian Affleck. The quantum hall effects, σ-models at $\theta = \pi$ and quantum spin chains. *Nuclear Physics B*, 257:397 – 406, 1985.

[AG16] F. F. Assaad and Tarun Grover. Simple fermionic model of deconfined phases and phase transitions. *Phys. Rev. X*, 6:041049, Dec 2016.

[AGW12] Alán Aspuru-Guzik and Philip Walther. Photonic quantum simulators. *Nature Physics*, 8(4):285–291, 2012.

[AHB11] A. Alexandradinata, Taylor L. Hughes, and B. Andrei Bernevig. Trace index and spectral flow in the entanglement spectrum of topological insulators. *Phys. Rev. B*, 84:195103, Nov 2011.

[AM76] N.W. Ashcroft and N.D. Mermin. *Solid State Physics*. Saunders College, Philadelphia, 1976.

[And59] P. W. Anderson. New approach to the theory of superexchange interactions. *Phys. Rev.*, 115:2–13, Jul 1959.

[And63] P. W. Anderson. Plasmons, gauge invariance, and mass. *Phys. Rev.*, 130:439–442, Apr 1963.

[And72] P. W. Anderson. More is different. *Science*, 177(4047):393–396, 1972.

[And87] P. W. Anderson. The Resonating Valence Bond State in La2CuO4 and Superconductivity. *Science*, 235(4793):1196–1198, March 1987.

[AOP16] János K. Asbóth, László Oroszlány, and András Pályi. *A Short Course on Topological Insulators*, volume 919. Springer, 2016.

[AS06] Alexander Altland and Ben Simons. *Condensed Matter Field Theory*. Cambridge University Press, 2006.

[AZ97] Alexander Altland and Martin R. Zirnbauer. Nonstandard symmetry classes in mesoscopic normal-superconducting hybrid structures. *Phys. Rev. B*, 55:1142–1161, Jan 1997.

[BA88] G. Baskaran and P. W. Anderson. Gauge theory of high-temperature superconductors and strongly correlated fermi systems. *Phys. Rev. B*, 37:580–583, Jan 1988.

[BA13] Jan Carl Budich and Eddy Ardonne. Fractional topological phase in one-dimensional flat bands with nontrivial topology. *Phys. Rev. B*, 88:035139, 2013.

[BAH17] D. N. Basov, R. D. Averitt, and D. Hsieh. Towards properties on demand in quantum materials. *Nature Materials*, 16(11):1077–1088, Nov 2017.

[Bal01] Gunnar S. Bali. Qcd forces and heavy quark bound states. *Physics Reports*, 343(1):1 – 136, 2001.

[Bal10] Leon Balents. Spin liquids in frustrated magnets. *Nature*, 464(7286):199–208, March 2010.

[BBC+20] Mari Carmen Bañuls, Rainer Blatt, Jacopo Catani, Alessio Celi, Juan Ignacio Cirac, Marcello Dalmonte, Leonardo Fallani, Karl Jansen, Maciej Lewenstein, Simone Montangero, Christine A. Muschik, Benni Reznik, Enrique Rico, Luca Tagliacozzo, Karel Van Acoleyen, Frank Verstraete, Uwe-Jens Wiese, Matthew Wingate, Jakub Zakrzewski, and Peter Zoller. Simulating lattice gauge theories within quantum technologies. *The European Physical Journal D*, 74(8):165, Aug 2020.

[BBD+13] D. Banerjee, M. Bögli, M. Dalmonte, E. Rico, P. Stebler, U.-J. Wiese, and P. Zoller. Atomic quantum simulation of $\mathbf{U}(n)$ and $\mathrm{SU}(n)$ non-abelian lattice gauge theories. *Phys. Rev. Lett.*, 110:125303, Mar 2013.

[BBM+02] K. Bernardet, G. G. Batrouni, J.-L. Meunier, G. Schmid, M. Troyer, and A. Dorneich. Analytical and numerical study of hardcore bosons in two dimensions. *Phys. Rev. B*, 65:104519, Feb 2002.

[BC19] Mari Carmen BaÃśuls and Krzysztof Cichy. Review on novel methods for lattice gauge theories. *Reports on Progress in Physics*, dec 2019.

[BC20] Mari Carmen Bañuls and Krzysztof Cichy. Review on novel methods for lattice gauge theories. *Reports on Progress in Physics*, 83(2):024401, jan 2020.

[BCD+75] W. A. Bardeen, M. S. Chanowitz, S. D. Drell, M. Weinstein, and T. M. Yan. Heavy quarks and strong binding: A field theory of hadron structure. *Phys. Rev. D*, 11:1094–1136, Mar 1975.

[BCN+13] U. Bissbort, D. Cocks, A. Negretti, Z. Idziaszek, T. Calarco, F. Schmidt-Kaler, W. Hofstetter, and R. Gerritsma. Emulating solid-state physics with a hybrid system of ultracold ions and atoms. *Phys. Rev. Lett.*, 111:080501, Aug 2013.

[BDH+19] A. Bazavov, H.-T. Ding, P. Hegde, O. Kaczmarek, F. Karsch, N. Karthik, E. Laermann, Anirban Lahiri, R. Larsen, S.-T. Li, Swagato Mukherjee, H. Ohno, P. Petreczky, H. Sandmeyer, C. Schmidt, S. Sharma, and P. Steinbrecher. Chiral crossover in qcd at zero and non-zero chemical potentials. *Physics Letters B*, 795:15 – 21, 2019.

[BDN12] Immanuel Bloch, Jean Dalibard, and Sylvain Nascimbène. Quantum simulations with ultracold quantum gases. *Nature Physics*, 8(4):267–276, 2012.

[BDZ08] I. Bloch, J. Dalibard, and W. Zwerger. Many-body physics with ultracold gases. *Rev. Mod. Phys.*, 80:885, 2008.

[BEF+14] N. Brambilla, S. Eidelman, P. Foka, S. Gardner, A. S. Kronfeld, M. G. Alford, R. Alkofer, M. Butenschoen, T. D. Cohen, J. Erdmenger, L. Fabbietti, M. Faber, J. L. Goity, B. Ketzer, H. W. Lin, F. J. Llanes-Estrada, H. B. Meyer, P. Pakhlov, E. Pallante, M. I. Polikarpov, H. Sazdjian, A. Schmitt, W. M. Snow, A. Vairo, R. Vogt, A. Vuorinen, H. Wittig, P. Arnold, P. Christakoglou, P. Di Nezza, Z. Fodor, X. Garcia i Tormo, R. Höllwieser, M. A. Janik, A. Kalweit, D. Keane, E. Kiritsis, A. Mischke, R. Mizuk, G. Odyniec, K. Papadodimas, A. Pich, R. Pittau, J.-W. Qiu, G. Ricciardi, C. A. Salgado, K. Schwenzer, N. G. Stefanis, G. M. von Hippel, and V. I. Zakharov. Qcd and strongly coupled gauge theories: challenges and perspectives. *The European Physical Journal C*, 74(10):2981, Oct 2014.

[Ber84] Michael Victor Berry. Quantal phase factors accompanying adiabatic changes. *Proceedings of the Royal Society of London. A. Mathematical and Physical Sciences*, 392(1802):45–57, 1984.

[BGBE10] Kristian Baumann, Christine Guerlin, Ferdinand Brennecke, and Tilman Esslinger. Dicke quantum phase transition with a superfluid gas in an optical cavity. *Nature*, 464(7293):1301, 2010.

[BHH+05] H. P. Büchler, M. Hermele, S. D. Huber, Matthew P. A. Fisher, and P. Zoller. Atomic quantum simulator for lattice gauge theories and ring exchange models. *Phys. Rev. Lett.*, 95:040402, Jul 2005.

[BHS06] G. G. Batrouni, F. Hébert, and R. T. Scalettar. Supersolid phases in the one-dimensional extended soft-core bosonic hubbard model. *Phys. Rev. Lett.*, 97:087209, Aug 2006.

[BHS+16] Martin Boll, Timon A. Hilker, Guillaume Salomon, Ahmed Omran, Jacopo Nespolo, Lode Pollet, Immanuel Bloch, and Christian Gross. Spin- and density-resolved microscopy of antiferromagnetic correlations in fermi-hubbard chains. *Science*, 353(6305):1257–1260, 2016.

[BHV+16] Boye Buyens, Jutho Haegeman, Henri Verschelde, Frank Verstraete, and Karel Van Acoleyen. Confinement and string breaking for qed_2 in the hamiltonian picture. *Phys. Rev. X*, 6:041040, Nov 2016.

[BHZ06] B. Andrei Bernevig, Taylor L. Hughes, and Shou-Cheng Zhang. Quantum spin hall effect and topological phase transition in hgte quantum wells. *Science*, 314(5806):1757–1761, 2006.

[BK81] S Brazovskii and Natasa Kirova. Excitons, polarons, and bipolarons in conducting polymers. *Sov. Phys. JET Lett.*, 33:4, 01 1981.

[BK05] Emil J. Bergholtz and Anders Karlhede. Half-filled lowest landau level on a thin torus. *Phys. Rev. Lett.*, 94:026802, Jan 2005.

[BK08] E. J. Bergholtz and A. Karlhede. Quantum hall system in tao-thouless limit. *Phys. Rev. B*, 77:155308, Apr 2008.

[BKKY08] Tim Byrnes, Na Young Kim, Kenichiro Kusudo, and Yoshihisa Yamamoto. Quantum simulation of fermi-hubbard models in semiconductor quantum-dot arrays. *Phys. Rev. B*, 78:075320, Aug 2008.

[BLA11] Erez Berg, Michael Levin, and Ehud Altman. Quantized pumping and topology of the phase diagram for a system of interacting bosons. *Phys. Rev. Lett.*, 106:110405, Mar 2011.

[Blo05] Immanuel Bloch. Ultracold quantum gases in optical lattices. *Nat. Phys.*, 1(1):23, 2005.

[BmcD08] Gök çe Başar and Gerald V. Dunne. Self-consistent crystalline condensate in chiral gross-neveu and bogoliubov–de gennes systems. *Phys. Rev. Lett.*, 100:200404, May 2008.

[BN09] Iulia Buluta and Franco Nori. Quantum simulators. *Science*, 326(5949):108–111, 2009.

[BP15] Alejandro Bermudez and Diego Porras. Interaction-dependent photon-assisted tunneling in optical lattices: A quantum simulator of strongly-correlated electrons and dynamical Gauge fields. *New J. Phys.*, 17(10):103021, October 2015.

[BPR+16] G. K. Brennen, G. Pupillo, E. Rico, T. M. Stace, and D. Vodola. Loops and strings in a superconducting lattice gauge simulator. *Phys. Rev. Lett.*, 117:240504, Dec 2016.

[BPT+10] W. S. Bakr, A. Peng, M. E. Tai, R. Ma, J. Simon, J. I. Gillen, S. Fölling, L. Pollet, and M. Greiner. Probing the Superfluid–to–Mott Insulator Transition at the Single-Atom Level. *Science*, 329(5991):547–550, July 2010. Publisher: American Association for the Advancement of Science Section: Report.

[BPV04] P. Buonsante, V. Penna, and A. Vezzani. Fractional-filling loophole insulator domains for ultracold bosons in optical superlattices. *Phys. Rev. A*, 70:061603, Dec 2004.

[BR12] R. Blatt and C. F. Roos. Quantum simulations with trapped ions. *Nature Physics*, 8(4):277–284, Apr 2012.

[BRvdS18] Wit Busza, Krishna Rajagopal, and Wilke van der Schee. Heavy ion collisions: The big picture and the big questions. *Annual Review of Nuclear and Particle Science*, 68(1):339–376, 2018.

[BRvW19] Aron J. Beekman, Louk Rademaker, and Jasper van Wezel. An Introduction to Spontaneous Symmetry Breaking. *SciPost Phys. Lect. Notes*, page 11, 2019.

[BSA+19] Luca Barbiero, Christian Schweizer, Monika Aidelsburger, Eugene Demler, Nathan Goldman, and Fabian Grusdt. Coupling ultracold matter to dynamical gauge fields in optical lattices: From flux attachment to âĎď2 lattice gauge theories. *Science Advances*, 5(10), 2019.

[BSB19] Simone Barbarino, Giorgio Sangiovanni, and Jan Carl Budich. First-order topological quantum phase transition in a strongly correlated ladder. *Phys. Rev. B*, 99:075158, Feb 2019.

[BTR+18] A. Bermudez, E. Tirrito, M. Rizzi, M. Lewenstein, and S. Hands. GrossâĂŞneveuâĂŞwilson model and correlated symmetry-protected topological phases. *Annals of Physics*, 399:149 – 180, 2018.

[BVGM20] Umberto Borla, Ruben Verresen, Fabian Grusdt, and Sergej Moroz. Confined phases of one-dimensional spinless fermions coupled to Z_2 gauge theory. *Phys. Rev. Lett.*, 124:120503, Mar 2020.

[BY06] Tim Byrnes and Yoshihisa Yamamoto. Simulating lattice gauge theories on a quantum computer. *Phys. Rev. A*, 73:022328, Feb 2006.

[Caz03] M. A. Cazalilla. One-dimensional optical lattices and impenetrable bosons. *Phys. Rev. A*, 67:053606, May 2003.

[CB81] D. K. Campbell and A. R. Bishop. Solitons in polyacetylene and relativistic-field-theory models. *Phys. Rev. B*, 24:4859–4862, Oct 1981.

[CB82] D.K. Campbell and A.R. Bishop. Soliton excitations in polyacetylene and relativistic field theory models. *Nuclear Physics B*, 200(2):297 – 328, 1982.

[CC04] Pasquale Calabrese and John Cardy. Entanglement entropy and quantum field theory. *Journal of Statistical Mechanics: Theory and Experiment*, 2004(06):P06002, 2004.

[CCG+11] M. A. Cazalilla, R. Citro, T. Giamarchi, E. Orignac, and M. Rigol. One dimensional bosons: From condensed matter systems to ultracold gases. *Rev. Mod. Phys.*, 83:1405–1466, Dec 2011.

[CGW11] Xie Chen, Zheng-Cheng Gu, and Xiao-Gang Wen. Classification of gapped symmetric phases in one-dimensional spin systems. *Phys. Rev. B*, 83:035107, Jan 2011.

[Cha60] R. G. Chambers. Shift of an electron interference pattern by enclosed magnetic flux. *Phys. Rev. Lett.*, 5:3–5, Jul 1960.

[CJJ+74] A. Chodos, R. L. Jaffe, K. Johnson, C. B. Thorn, and V. F. Weisskopf. New extended model of hadrons. *Phys. Rev. D*, 9:3471–3495, Jun 1974.

[CJS75] Sidney Coleman, R Jackiw, and Leonard Susskind. Charge shielding and quark confinement in the massive schwinger model. *Annals of Physics*, 93(1):267 – 275, 1975.

[Col73] Sidney Coleman. There are no goldstone bosons in two dimensions. *Communications in Mathematical Physics*, 31(4):259–264, Dec 1973.

[Col75] Sidney Coleman. Quantum sine-gordon equation as the massive thirring model. *Phys. Rev. D*, 11:2088–2097, Apr 1975.

[Col85] Sidney Coleman. *Aspects of Symmetry: Selected Erice Lectures*. Cambridge University Press, 1985.

[Cor97] John F Cornwell. *Group theory in physics: An introduction*, volume 1 of *Techniques of Physics*. Academic press, San Diego, 1997.

[Cre99] Michael Creutz. End states, ladder compounds, and domain-wall fermions. *Phys. Rev. Lett.*, 83:2636–2639, Sep 1999.

[CSCR+17] Marcello Calvanese Strinati, Eyal Cornfeld, Davide Rossini, Simone Barbarino, Marcello Dalmonte, Rosario Fazio, Eran Sela, and Leonardo Mazza. Laughlin-like states in bosonic and fermionic atomic synthetic ladders. *Phys. Rev. X*, 7:021033, Jun 2017.

[CT98] Claude N. Cohen-Tannoudji. Nobel Lecture: Manipulating atoms with photons. *Rev. Mod. Phys.*, 70(3):707–719, 1998.

[CTSR16] Ching-Kai Chiu, Jeffrey C. Y. Teo, Andreas P. Schnyder, and Shinsei Ryu. Classification of topological quantum matter with symmetries. *Rev. Mod. Phys.*, 88:035005, Aug 2016.

[CW80] Sidney Coleman and Edward Witten. Chiral-symmetry breakdown in large-n chromodynamics. *Phys. Rev. Lett.*, 45:100–102, Jul 1980.

[CZ95] J. I. Cirac and P. Zoller. Quantum computations with cold trapped ions. *Phys. Rev. Lett.*, 74:4091–4094, May 1995.

[CZ12] J Ignacio Cirac and Peter Zoller. Goals and opportunities in quantum simulation. *Nat. Phys.*, 8(4):264–266, 2012.

[CZLT20] Titas Chanda, Jakub Zakrzewski, Maciej Lewenstein, and Luca Tagliacozzo. Confinement and lack of thermalization after quenches in the bosonic schwinger model. *Phys. Rev. Lett.*, 124:180602, May 2020.

[Dav77] A.S. Davydov. Solitons and energy transfer along protein molecules. *Journal of Theoretical Biology*, 66(2):379, 1977.

[DDL03] L.-M. Duan, E. Demler, and M. D. Lukin. Controlling spin exchange interactions of ultracold atoms in optical lattices. *Phys. Rev. Lett.*, 91:090402, Aug 2003.

[DGH+15] Omjyoti Dutta, Mariusz Gajda, Philipp Hauke, Maciej Lewenstein, Dirk-Sören Lühmann, Boris A Malomed, Tomasz Sowiński, and Jakub Zakrzewski. Non-standard hubbard models in optical lattices: a review. *Rep. Prog. Phys.*, 78(6):066001, 2015.

[DGJbuO11] Jean Dalibard, Fabrice Gerbier, Gediminas Juzeliūnas, and Patrik Öhberg. Colloquium. *Rev. Mod. Phys.*, 83:1523–1543, Nov 2011.

[DHN74] Roger F. Dashen, Brosl Hasslacher, and André Neveu. Nonperturbative methods and extended-hadron models in field theory. ii. two-dimensional models and extended hadrons. *Phys. Rev. D*, 10:4130–4138, Dec 1974.

[Dir31] Paul Adrien Maurice Dirac. Quantised singularities in the electromagnetic field,. *Proceedings of the Royal Society of London. Series A, Containing Papers of a Mathematical and Physical Character*, 133(821):60–72, 1931.

[DJB+20] Ivana Dimitrova, Niklas Jepsen, Anton Buyskikh, Araceli Venegas-Gomez, Jesse Amato-Grill, Andrew Daley, and Wolfgang Ketterle. Enhanced superexchange in a tilted mott insulator. *Phys. Rev. Lett.*, 124:043204, Jan 2020.

[DKSV04] A J Daley, C Kollath, U SchollwÃűck, and G Vidal. Time-dependent density-matrix renormalization-group using adaptive effective hilbert spaces. *Journal of Statistical Mechanics: Theory and Experiment*, 2004(04):P04005, 2004.

[DLR+15] L. Duca, T. Li, M. Reitter, I. Bloch, M. Schleier-Smith, and U. Schneider. An aharonov-bohm interferometer for determining bloch band topology. *Science*, 347(6219):288–292, 2015.

[DM16] M. Dalmonte and S. Montangero. Lattice gauge theory simulations in the quantum information era. *Contemporary Physics*, 57(3):388–412, 2016.

[DMA+95] K.B. Davis, M.-O. Mewes, M. R. Andrews, N. J. van Druten, D. S. Durfee, D. M. Kurn, and W. Ketterle. Bose-Einstein Condensation in a Gas of Sodium Atoms. *Physical Review Letters*, 75(22):3969–3973, 1995.

[DTBA06] Emanuele G. Dalla Torre, Erez Berg, and Ehud Altman. Hidden order in 1d bose insulators. *Phys. Rev. Lett.*, 97:260401, Dec 2006.

[DTLZ17] Omjyoti Dutta, Luca Tagliacozzo, Maciej Lewenstein, and Jakub Zakrzewski. Toolbox for Abelian lattice gauge theories with synthetic matter. *Phys. Rev. A*, 95(5):053608, May 2017.

[DV80] M. Daniel and C. M. Viallet. The geometrical setting of gauge theories of the yang-mills type. *Rev. Mod. Phys.*, 52:175–197, Jan 1980.

[DYR+17] Han-Ning Dai, Bing Yang, Andreas Reingruber, Hui Sun, Xiao-Fan Xu, Yu-Ao Chen, Zhen-Sheng Yuan, and Jian-Wei Pan. Four-body ring-exchange interactions and anyonic statistics within a minimal toric-code Hamiltonian. *Nature Physics*, 13(12):1195–1200, December 2017.

[EB64] F. Englert and R. Brout. Broken symmetry and the mass of gauge vector mesons. *Phys. Rev. Lett.*, 13:321–323, Aug 1964.

[ECP10] J. Eisert, M. Cramer, and M. B. Plenio. Colloquium. *Rev. Mod. Phys.*, 82:277–306, Feb 2010.

[Eli75] S. Elitzur. Impossibility of spontaneously breaking local symmetries. *Phys. Rev. D*, 12:3978–3982, Dec 1975.

[Eme87] V. J. Emery. Theory of high-t_c superconductivity in oxides. *Phys. Rev. Lett.*, 58:2794–2797, Jun 1987.

[Emi12] David Emin. *Polarons*. Cambridge University Press, 2012.

[Fey82] R. P. Feynman. Simulating physics with computers. *Int. J. Theor. Phys.*, 21:467, 1982.

[FGW+05] Simon Fölling, Fabrice Gerbier, Artur Widera, Olaf Mandel, Tatjana Gericke, and Immanuel Bloch. Spatial quantum noise interferometry in expanding ultracold atom clouds. *Nature*, 434(7032):481–484, March 2005.

[FH83] Eduardo Fradkin and Jorge E. Hirsch. Phase diagram of one-dimensional electron-phonon systems. i. the su-schrieffer-heeger model. *Phys. Rev. B*, 27:1680–1697, Feb 1983.

[FHS05] Takahiro Fukui, Yasuhiro Hatsugai, and Hiroshi Suzuki. Chern numbers in discretized brillouin zone: Efficient method of computing (spin) hall conductances. *Journal of the Physical Society of Japan*, 74(6):1674–1677, 2005.

[Fis61] Michael E. Fisher. Statistical mechanics of dimers on a plane lattice. *Phys. Rev.*, 124:1664–1672, Dec 1961.

[FK10] Lukasz Fidkowski and Alexei Kitaev. Effects of interactions on the topological classification of free fermion systems. *Phys. Rev. B*, 81:134509, Apr 2010.

[FK11] Lukasz Fidkowski and Alexei Kitaev. Topological phases of fermions in one dimension. *Phys. Rev. B*, 83:075103, Feb 2011.

[FKT15] Eduardo Fradkin, Steven A. Kivelson, and John M. Tranquada. Colloquium: Theory of intertwined orders in high temperature superconductors. *Rev. Mod. Phys.*, 87:457–482, May 2015.

[FL77a] R. Friedberg and T. D. Lee. Fermion-field nontopological solitons. *Phys. Rev. D*, 15:1694–1711, Mar 1977.

[FL77b] R. Friedberg and T. D. Lee. Fermion-field nontopological solitons. ii. models for hadrons. *Phys. Rev. D*, 16:1096–1118, Aug 1977.

[FNW92] M. Fannes, B. Nachtergaele, and R. F. Werner. Finitely correlated states on quantum spin chains. *Communications in Mathematical Physics*, 144(3):443–490, Mar 1992.

[FP19] Kieran A Fraser and Francesco Piazza. Topological soliton-polaritons in 1d systems of light and fermionic matter. *Communications Physics*, 2(1):48, 2019.

[Fra13] Eduardo Fradkin. *Field Theories of Condensed Matter Physics*. Cambridge University Press, 2 edition, 2013.

[FRT+16] N. Fläschner, B. S. Rem, M. Tarnowski, D. Vogel, D.-S. Lühmann, K. Sengstock, and Christof Weitenberg. Experimental reconstruction of the Berry curvature in a Floquet Bloch band. *Science*, 352(6289):1091–1094, 2016.

[FS79] Eduardo Fradkin and Stephen H. Shenker. Phase diagrams of lattice gauge theories with Higgs fields. *Phys. Rev. D*, 19(12):3682–3697, June 1979.

[FSG+08] Axel Friedenauer, Hector Schmitz, Jan Tibor Glueckert, Diego Porras, and Tobias Schätz. Simulating a quantum magnet with trapped ions. *Nature Physics*, 4(10):757–761, 2008.

[FTC+07] S. Fölling, S. Trotzky, P. Cheinet, M. Feld, R. Saers, A. Widera, T. Müller, and I. Bloch. Direct observation of second-order atom tunnelling. *Nature*, 448(7157):1029–1032, August 2007.

[Fu11] Liang Fu. Topological crystalline insulators. *Phys. Rev. Lett.*, 106:106802, Mar 2011.

[FWGF89] Matthew P. A. Fisher, Peter B. Weichman, G. Grinstein, and Daniel S. Fisher. Boson localization and the superfluid-insulator transition. *Phys. Rev. B*, 40:546–570, Jul 1989.

[GAS+18] Snir Gazit, Fakher F. Assaad, Subir Sachdev, Ashvin Vishwanath, and Chong Wang. Confinement transition of âĎď2 gauge theories coupled to massless fermions: Emergent quantum chromodynamics and so(5) symmetry. *Proc. Nat. Acad. Sci.*, 115(30):E6987–E6995, 2018.

[GBZ16] N. Goldman, J. C. Budich, and P. Zoller. Topological quantum matter with ultracold gases in optical lattices. *Nature Physics*, 12(7):639–645, Jul 2016.

[GC15] Huaiming Guo and Shu Chen. Kaleidoscope of symmetry-protected topological phases in one-dimensional periodically modulated lattices. *Phys. Rev. B*, 91:041402, Jan 2015.

[GCBG+19] Daniel González-Cuadra, Alejandro Bermudez, Przemyslaw R. Grzybowski, Maciej Lewenstein, and Alexandre Dauphin. Intertwined topological phases induced by emergent symmetry protection. *Nature Communications*, 10(1):2694, 2019.

[GCDA+20] Daniel González-Cuadra, Alexandre Dauphin, Monika Aidelsburger, Maciej Lewenstein, and Alejandro Bermudez. The rotor jackiw-rebbi model: a cold-atom approach to chiral symmetry restoration and quark confinement, 2020.

[GCDG+19] Daniel González-Cuadra, Alexandre Dauphin, Przemysław R. Grzybowski, Paweł Wójcik, Maciej Lewenstein, and Alejandro Bermudez. Symmetry-breaking topological insulators in the $\mathbb{Z}_2$ bose-hubbard model. *Phys. Rev. B*, 99:045139, Jan 2019.

[GCGDL18] Daniel González-Cuadra, Przemysław R. Grzybowski, Alexandre Dauphin, and Maciej Lewenstein. Strongly correlated bosons on a dynamical lattice. *Phys. Rev. Lett.*, 121:090402, Aug 2018.

[GCOcvacVac09] Andrew T. Grier, Marko Cetina, Fedja Oručević, and Vladan Vuletić. Observation of cold collisions between trapped ions and trapped atoms. *Phys. Rev. Lett.*, 102:223201, Jun 2009.

[GCTLB20] Daniel González-Cuadra, Luca Tagliacozzo, Maciej Lewenstein, and Alejandro Bermudez. Aharonov-bohm instability in fermionic $\mathbb{Z}_2$ gauge theories: topological order and soliton-induced deconfinement, 2020.

[GCZC17] Daniel González-Cuadra, Erez Zohar, and J Ignacio Cirac. Quantum simulation of the abelian-higgs lattice gauge theory with ultracold atoms. *New Journal of Physics*, 19(6):063038, jun 2017.

[GDG+19] Daniel González-Cuadra, Alexandre Dauphin, Przemysław R. Grzybowski, Maciej Lewenstein, and Alejandro Bermudez. $\mathbb{Z}_n$ solitons in intertwined topological phases. *arXiv e-prints*, page arXiv:1908.02186, August 2019.

[GDG+20] Daniel González-Cuadra, Alexandre Dauphin, Przemysław R. Grzybowski, Maciej Lewenstein, and Alejandro Bermudez. Dynamical solitons and boson fractionalization in cold-atom topological insulators. *arXiv e-prints*, page arXiv:2003.10994, March 2020.

[GH14] Fabian Grusdt and Michael Höning. Realization of fractional chern insulators in the thin-torus limit with ultracold bosons. *Phys. Rev. A*, 90:053623, Nov 2014.

[GHF13] Fabian Grusdt, Michael Höning, and Michael Fleischhauer. Topological edge states in the one-dimensional superlattice bose-hubbard model. *Phys. Rev. Lett.*, 110:260405, Jun 2013.

[GHK64] G. S. Guralnik, C. R. Hagen, and T. W. B. Kibble. Global conservation laws and massless particles. *Phys. Rev. Lett.*, 13:585–587, Nov 1964.

[GJK93] Maarten F.L. Golterman, Karl Jansen, and David B. Kaplan. Chern-simons currents and chiral fermions on the lattice. *Physics Letters B*, 301(2):219 – 223, 1993.

[GJOS14] N Goldman, G Juzeliūnas, P Öhberg, and I B Spielman. Light-induced gauge fields for ultracold atoms. *Rep. Prog. Phys.*, 77(12):126401, 2014.

[GKZ+10] R. Gerritsma, G. Kirchmair, F. Zähringer, E. Solano, R. Blatt, and C. F. Roos. Quantum simulation of the dirac equation. *Nature*, 463(7277):68–71, Jan 2010.

[GL16] Christof Gattringer and Kurt Langfeld. Approaches to the sign problem in lattice field theory. *International Journal of Modern Physics A*, 31(22):1643007, 2016.

[GLK+11] R. Gerritsma, B. P. Lanyon, G. Kirchmair, F. Zähringer, C. Hempel, J. Casanova, J. J. García-Ripoll, E. Solano, R. Blatt, and C. F. Roos. Quantum simulation of the klein paradox with trapped ions. *Phys. Rev. Lett.*, 106:060503, Feb 2011.

[GME+02] Markus Greiner, Olaf Mandel, Tilman Esslinger, Theodor W. Hänsch, and Immanuel Bloch. Quantum phase transition from a superfluid to a mott insulator in a gas of ultracold atoms. *Nature*, 415(6867):39, 2002.

[GMZP15] Adolfo G. Grushin, Johannes Motruk, Michael P. Zaletel, and Frank Pollmann. Characterization and stability of a fermionic $\nu = 1/3$ fractional chern insulator. *Phys. Rev. B*, 91:035136, 2015.

[GN74] David J. Gross and André Neveu. Dynamical symmetry breaking in asymptotically free field theories. *Phys. Rev. D*, 10:3235–3253, Nov 1974.

[GND+12] R. Gerritsma, A. Negretti, H. Doerk, Z. Idziaszek, T. Calarco, and F. Schmidt-Kaler. Bosonic josephson junction controlled by a single trapped ion. *Phys. Rev. Lett.*, 109:080402, Aug 2012.

[Gre11] J. Greensite. *An Introduction to the Confinement Problem*. Lecture Notes in Physics. Springer Berlin Heidelberg, 2011.

[Gre20] Jeff Greensite. *Introduction to the confinement problem*. Springer Nature, 2020.

[Gro96] David J. Gross. The role of symmetry in fundamental physics. *Proceedings of the National Academy of Sciences*, 93(25):14256–14259, 1996.

[GRV17] Snir Gazit, Mohit Randeria, and Ashvin Vishwanath. Emergent dirac fermions and broken symmetries in confined and deconfined phases of z2 gauge?theories. *Nat. Phys.*, 13:484 EP –, Feb 2017.

[GSF12] Huaiming Guo, Shun-Qing Shen, and Shiping Feng. Fractional topological phase in one-dimensional flat bands with nontrivial topology. *Phys. Rev. B*, 86:085124, Aug 2012.

[GSM+19] Frederik Görg, Kilian Sandholzer, Joaquín Minguzzi, Rémi Desbuquois, Michael Messer, and Tilman Esslinger. Realization of density-dependent peierls phases to engineer quantized gauge fields coupled to ultracold matter. *Nature Physics*, 15(11):1161–1167, 2019.

[GSN+10] N. Goldman, I. Satija, P. Nikolic, A. Bermudez, M. A. Martin-Delgado, M. Lewenstein, and I. B. Spielman. Realistic time-reversal invariant topological insulators with neutral atoms. *Phys. Rev. Lett.*, 105:255302, Dec 2010.

[GTC+12] M. Gullans, T. G. Tiecke, D. E. Chang, J. Feist, J. D. Thompson, J. I. Cirac, P. Zoller, and M. D. Lukin. Nanoplasmonic lattices for ultracold atoms. *Phys. Rev. Lett.*, 109:235309, Dec 2012.

[GU10] SHI-JIAN GU. Fidelity approach to quantum phase transitions. *International Journal of Modern Physics B*, 24(23):4371–4458, 2010.

[GUJ+13] Daniel Greif, Thomas Uehlinger, Gregor Jotzu, Leticia Tarruell, and Tilman Esslinger. Short-range quantum magnetism of ultracold fermions in an optical lattice. *Science*, 340(6138):1307–1310, 2013.

[GV08] Grabiele Giuliani and Giovani Vignale. *Quantum theory of the electron liquid*. Cambridge University Press, 2008.

[GW09] Zheng-Cheng Gu and Xiao-Gang Wen. Tensor-entanglement-filtering renormalization approach and symmetry-protected topological order. *Phys. Rev. B*, 80:155131, Oct 2009.

[GWO00] Rudolf Grimm, Matthias WeidemÃijller, and Yurii B. Ovchinnikov. Optical dipole traps for neutral atoms. volume 42 of *Advances In Atomic, Molecular, and Optical Physics*, pages 95 – 170. Academic Press, 2000.

[Hal81] F. D. M. Haldane. Luttinger liquid theory of one-dimensional quantum fluids. i. properties of the luttinger model and their extension to the general 1d interacting spinless fermi gas. *Journal of Physics C: Solid State Physics*, 14(19):2585–2609, jul 1981.

[Hal83] F. D. M. Haldane. Continuum dynamics of the 1-d heisenberg antiferromagnet: Identification with the o(3) nonlinear sigma model. *Physics Letters A*, 93(9):464 – 468, 1983.

[Hal88] F. D. M. Haldane. Model for a quantum hall effect without landau levels: Condensed-matter realization of the "parity anomaly". *Phys. Rev. Lett.*, 61:2015–2018, Oct 1988.

[Hal17] F. D. M. Haldane. Nobel lecture: Topological quantum matter. *Rev. Mod. Phys.*, 89:040502, Oct 2017.

[Har55] P G Harper. The general motion of conduction electrons in a uniform magnetic field, with application to the diamagnetism of metals. *Proceedings of the Physical Society. Section A*, 68(10):879–892, oct 1955.

[Has06] M. B. Hastings. Solving gapped hamiltonians locally. *Phys. Rev. B*, 73:085115, Feb 2006.

[Has07] M B Hastings. An area law for one-dimensional quantum systems. *Journal of Statistical Mechanics: Theory and Experiment*, 2007(08):P08024, 2007.

[Hat93a] Y Hatsugai. Edge states in the integer quantum Hall effect and the Riemann surface of the Bloch function. *Physical Review B*, 48(16):11851, 1993.

[Hat93b] Yasuhiro Hatsugai. Chern number and edge states in the integer quantum hall effect. *Phys. Rev. Lett.*, 71:3697–3700, Nov 1993.

[Hat06] Yasuhiro Hatsugai. Quantized berry phases as a local order parameter of a quantum liquid. *Journal of the Physical Society of Japan*, 75:123601, 2006.

[HCZ+02] W. Hofstetter, J. I. Cirac, P. Zoller, E. Demler, and M. D. Lukin. High-temperature superfluidity of fermionic atoms in optical lattices. *Phys. Rev. Lett.*, 89:220407, Nov 2002.

[HD14] A. Härter and J. Hecker Denschlag. Cold atom–ion experiments in hybrid traps. *Contemporary Physics*, 55(1):33–45, 2014.

[HDY+15] Russell A Hart, Pedro M Duarte, Tsung-Lin Yang, Xinxing Liu, Thereza Paiva, Ehsan Khatami, Richard T Scalettar, Nandini Trivedi, David A Huse, and Randall G Hulet. Observation of antiferromagnetic correlations in the hubbard model with ultracold atoms. *Nature*, 519(7542):211, 2015.

[HF63] J. Hubbard and Brian Hilton Flowers. Electron correlations in narrow energy bands. *Proceedings of the Royal Society of London. Series A. Mathematical and Physical Sciences*, 276(1365):238–257, 1963.

[HF16] Y. Hatsugai and T. Fukui. Bulk-edge correspondence in topological pumping. *Phys. Rev. B*, 94:041102, Jul 2016.

[HHC+12] Tian-Heng Han, Joel S. Helton, Shaoyan Chu, Daniel G. Nocera, Jose A. Rodriguez-Rivera, Collin Broholm, and Young S. Lee. Fractionalized excitations in the spin-liquid state of a kagome-lattice antiferromagnet. *Nature*, 492(7429):406–410, December 2012.

[Hig64] Peter W. Higgs. Broken symmetries and the masses of gauge bosons. *Phys. Rev. Lett.*, 13:508–509, Oct 1964.

[HK90] Y. Hatsugai and M. Kohmoto. Energy spectrum and the quantum hall effect on the square lattice with next-nearest-neighbor hopping. *Phys. Rev. B*, 42:8282–8294, Nov 1990.

[HK10] M. Z. Hasan and C. L. Kane. Colloquium: Topological insulators. *Rev. Mod. Phys.*, 82:3045–3067, Nov 2010.

[HKSS88] A. J. Heeger, S. Kivelson, J. R. Schrieffer, and W. P. Su. Solitons in conducting polymers. *Rev. Mod. Phys.*, 60:781–850, Jul 1988.

[HL08] Alioscia Hamma and Daniel A. Lidar. Adiabatic Preparation of Topological Order. *Phys. Rev. Lett.*, 100(3):030502, January 2008.

[Ho98] Tin-Lun Ho. Spinor Bose Condensates in Optical Traps. *Physical Review Letters*, 81(4):742–745, 1998.

[Hof76] Douglas R. Hofstadter. Energy levels and wave functions of bloch electrons in rational and irrational magnetic fields. *Phys. Rev. B*, 14:2239–2249, Sep 1976.

[HOJZ20] Thomas Hartke, Botond Oreg, Ningyuan Jia, and Martin Zwierlein. Measuring total density correlations in a Fermi-Hubbard gas via bilayer microscopy. *arXiv e-prints*, page arXiv:2003.11669, March 2020.

[Hol59] T Holstein. Studies of polaron motion: Part i. the molecular-crystal model. *Annals of Physics*, 8(3):325 – 342, 1959.

[Hol13] Timothy J. Hollowood. *Renormalization Group and Fixed Points in Quantum Field Theory.* Springer, 2013.

[Hoo81] G.'t Hooft. Topology of the gauge condition and new confinement phases in non-abelian gauge theories. *Nuclear Physics B*, 190(3):455 – 478, 1981.

[Hor81] Baruch Horovitz. Soliton lattice in polyacetylene, spin-peierls systems, and two-dimensional sine-gordon systems. *Phys. Rev. Lett.*, 46:742–745, Mar 1981.

[Hor87] Baruch Horovitz. Solitons in the peierls condensate. ii. amplitude solitons. *Phys. Rev. B*, 35:734–745, Jan 1987.

[HP40] T. Holstein and H. Primakoff. Field dependence of the intrinsic domain magnetization of a ferromagnet. *Phys. Rev.*, 58:1098–1113, Dec 1940.

[HP18] Johannes Hauschild and Frank Pollmann. Efficient numerical simulations with Tensor Networks: Tensor Network Python (TeNPy). *SciPost Phys. Lect. Notes*, page 5, 2018.

[HPB11] Taylor L. Hughes, Emil Prodan, and B. Andrei Bernevig. Inversion-symmetric topological insulators. *Phys. Rev. B*, 83:245132, Jun 2011.

[HQW+08] D. Hsieh, D. Qian, L. Wray, Y. Xia, Y. S. Hor, R. J. Cava, and M. Z. Hasan. A topological dirac insulator in a quantum spin hall phase. *Nature*, 452:970 EP –, Apr 2008.

[HT73] Akira Hasegawa and Frederick Tappert. Transmission of stationary nonlinear optical pulses in dispersive dielectric fibers. i. anomalous dispersion. *Applied Physics Letters*, 23(3):142–144, 1973.

[HVAS+15] Jutho Haegeman, Karel Van Acoleyen, Norbert Schuch, J. Ignacio Cirac, and Frank Verstraete. Gauging quantum states: From global to local symmetries in many-body systems. *Phys. Rev. X*, 5:011024, Feb 2015.

[IZH19] Bernhard Irsigler, Jun-Hui Zheng, and Walter Hofstetter. Interacting hofstadter interface. *Phys. Rev. Lett.*, 122:010406, Jan 2019.

[Jac77] R. Jackiw. Quantum meaning of classical field theory. *Rev. Mod. Phys.*, 49:681–706, Jul 1977.

[JBC+98] D. Jaksch, C. Bruder, J. I. Cirac, C. W. Gardiner, and P. Zoller. Cold bosonic atoms in optical lattices. *Phys. Rev. Lett.*, 81:3108–3111, 1998.

[JBC+99] D. Jaksch, H.-J. Briegel, J. I. Cirac, C. W. Gardiner, and P. Zoller. Entanglement of atoms via cold controlled collisions. *Phys. Rev. Lett.*, 82:1975–1978, Mar 1999.

[JcvacAB17] Vladimir Juričić, D. S. L. Abergel, and A. V. Balatsky. First-order quantum phase transition in three-dimensional topological band insulators. *Phys. Rev. B*, 95:161403, Apr 2017.

[JCZ+00] D. Jaksch, J. I. Cirac, P. Zoller, S. L. Rolston, R. Côté, and M. D. Lukin. Fast quantum gates for neutral atoms. *Phys. Rev. Lett.*, 85:2208–2211, Sep 2000.

[JDPC17] Jacob Johansen, B. J. DeSalvo, Krutik Patel, and Cheng Chin. Testing universality of Efimov physics across broad and narrow Feshbach resonances. *Nature Physics*, 13(8):731–735, August 2017.

[JNG14] J. Joger, A. Negretti, and R. Gerritsma. Quantum dynamics of an atomic double-well system interacting with a trapped ion. *Phys. Rev. A*, 89:063621, Jun 2014.

[JPR+17] J. Jünemann, A. Piga, S.-J. Ran, M. Lewenstein, M. Rizzi, and A. Bermudez. Exploring interacting topological insulators with ultracold atoms: The synthetic creutz-hubbard model. *Phys. Rev. X*, 7:031057, Sep 2017.

[JR76] R. Jackiw and C. Rebbi. Solitons with fermion number 1/2. *Phys. Rev. D*, 13:3398–3409, Jun 1976.

[JR81] R. Jackiw and P. Rossi. Zero modes of the vortex-fermion system. *Nuclear Physics B*, 190(4):681 – 691, 1981.

[JS92] Karl Jansen and Martin Schmaltz. Critical momenta of lattice chiral fermions. *Physics Letters B*, 296(3):374 – 378, 1992.

[JSG+08] Robert Jördens, Niels Strohmaier, Kenneth Günter, Henning Moritz, and Tilman Esslinger. A mott insulator of fermionic atoms in an optical lattice. *Nature*, 455(7210):204–207, Sep 2008.

[JVW09] Michael Johanning, Andrés F Varón, and Christof Wunderlich. Quantum simulations with cold trapped ions. *J. Phys. B: At. Mol. Opt. Phys.*, 42(15):154009, 2009.

[JW28] P. Jordan and E. Wigner. Über das paulische äquivalenzverbot. *Zeitschrift für Physik*, 47(9):631–651, Sep 1928.

[JZ05] D. Jaksch and P. Zoller. The cold atom hubbard toolbox. *Annals of Physics*, 315(1):52 – 79, 2005.

[Kap92] David B. Kaplan. A method for simulating chiral fermions on the lattice. *Physics Letters B*, 288(3):342 – 347, 1992.

[KCT19] Elio J. König, Piers Coleman, and Alexei M. Tsvelik. Soluble limit and criticality of fermions in $\mathbb{Z}_2$ gauge theories, 2019.

[KD14] Stefanos Kourtis and Maria Daghofer. Combined topological and landau order from strong correlations in chern bands. *Phys. Rev. Lett.*, 113:216404, Nov 2014.

[KDP80] K. v. Klitzing, G. Dorda, and M. Pepper. New method for high-accuracy determination of the fine-structure constant based on quantized hall resistance. *Phys. Rev. Lett.*, 45:494–497, Aug 1980.

[KHB+20] Joannis Koepsell, Sarah Hirthe, Dominik Bourgund, Pimonpan Sompet, Jayadev Vijayan, Guillaume Salomon, Christian Gross, and Immanuel Bloch. Robust bilayer charge pumping for spin- and density-resolved quantum gas microscopy. *Phys. Rev. Lett.*, 125:010403, Jul 2020.

[KHJ+17] V Kasper, F Hebenstreit, F Jendrzejewski, M K Oberthaler, and J Berges. Implementing quantum electrodynamics with ultracold atomic systems. *New Journal of Physics*, 19(2):023030, feb 2017.

[KHS18] Jin Hyoun Kang, Jeong Ho Han, and Y. Shin. Realization of a cross-linked chiral ladder with neutral fermions in a 1d optical lattice by orbital-momentum coupling. *Phys. Rev. Lett.*, 121:150403, Oct 2018.

[KHS20] Jin Hyoun Kang, Jeong Ho Han, and Y Shin. Creutz ladder in a resonantly shaken 1d optical lattice. *New Journal of Physics*, 22(1):013023, jan 2020.

[Kib76] T W B Kibble. Topology of cosmic domains and strings. *Journal of Physics A: Mathematical and General*, 9(8):1387, 1976.

[Kit03] A.Yu. Kitaev. Fault-tolerant quantum computation by anyons. *Annals of Physics*, 303(1):2 – 30, 2003.

[Kit09] Alexei Kitaev. Periodic table for topological insulators and superconductors. *AIP Conference Proceedings*, 1134(1):22–30, 2009.

[Kiv86] S. Kivelson. Chapter 6 - soliton model of polyacetylene. In S.E. Trullinger, V.E. Zakharoov, and V.L. Pokrovsky, editors, *Solitons*, volume 17 of *Modern Problems in Condensed Matter Sciences*, pages 301 – 387. Elsevier, 1986.

[Kiv01] S.A. Kivelson. Electron fractionalization. *Synthetic Metals*, 125(1):99 – 106, 2001.

[KJL+20] Valentin Kasper, Gediminas Juzeliunas, Maciej Lewenstein, Fred Jendrzejewski, and Erez Zohar. From the Jaynes-Cummings model to non-Abelian gauge theories: a guided tour for the quantum engineer. *arXiv e-prints*, page arXiv:2006.01258, June 2020.

[KL87] V. Kalmeyer and R. B. Laughlin. Equivalence of the resonating-valence-bond and fractional quantum hall states. *Phys. Rev. Lett.*, 59:2095–2098, Nov 1987.

[KLR+12] Yaacov E. Kraus, Yoav Lahini, Zohar Ringel, Mor Verbin, and Oded Zilberberg. Topological states and adiabatic pumping in quasicrystals. *Phys. Rev. Lett.*, 109:106402, Sep 2012.

[KM05] C. L. Kane and E. J. Mele. Z_2 topological order and the quantum spin hall effect. *Phys. Rev. Lett.*, 95:146802, Sep 2005.

[Kog79] John B. Kogut. An introduction to lattice gauge theory and spin systems. *Rev. Mod. Phys.*, 51:659–713, Oct 1979.

[KOI20] Yoshihito Kuno, Takahiro Orito, and Ikuo Ichinose. Flat-band many-body localization and ergodicity breaking in the creutz ladder. *New Journal of Physics*, 22(1):013032, jan 2020.

[Kon64] Jun Kondo. Resistance Minimum in Dilute Magnetic Alloys. *Progress of Theoretical Physics*, 32(1):37–49, 07 1964.

[Kos17] John Michael Kosterlitz. Nobel lecture: Topological defects and phase transitions. *Rev. Mod. Phys.*, 89:040501, Oct 2017.

[KP06] Alexei Kitaev and John Preskill. Topological entanglement entropy. *Phys. Rev. Lett.*, 96:110404, Mar 2006.

[KS75] John Kogut and Leonard Susskind. Hamiltonian formulation of wilson's lattice gauge theories. *Phys. Rev. D*, 11:395–408, Jan 1975.

[KS81] N. Kawamoto and J. Smit. Effective lagrangian and dynamical symmetry breaking in strongly coupled lattice qcd. *Nuclear Physics B*, 192(1):100 – 124, 1981.

[KS03] John B. Kogut and Mikhail A. Stephanov. *The Phases of Quantum Chromodynamics: From Confinement to Extreme Environments.* Cambridge Monographs on Particle Physics, Nuclear Physics and Cosmology. Cambridge University Press, 2003.

[KWB+07] Markus König, Steffen Wiedmann, Christoph Brüne, Andreas Roth, Hartmut Buhmann, Laurens W. Molenkamp, Xiao-Liang Qi, and Shou-Cheng Zhang. Quantum spin hall insulator state in hgte quantum wells. *Science*, 318(5851):766–770, 2007.

[Laf16] Nicolas Laflorencie. Quantum entanglement in condensed matter systems. *Physics Reports*, 646:1 – 59, 2016. Quantum entanglement in condensed matter systems.

[Lan37] L. Landau. On the theory of phase transitions. *Zh. Eksp. Teor. Fiz*, 11:26, 1937.

[Lan56] L. Landau. The theory of a fermi liquid. *Sov. Phys. JETP*, 30:1058, 1956.

[Lau81] R. B. Laughlin. Quantized hall conductivity in two dimensions. *Phys. Rev. B*, 23:5632–5633, May 1981.

[Lau83] R. B. Laughlin. Anomalous quantum hall effect: An incompressible quantum fluid with fractionally charged excitations. *Phys. Rev. Lett.*, 50:1395–1398, May 1983.

[Lau99] R. B. Laughlin. Nobel lecture: Fractional quantization. *Rev. Mod. Phys.*, 71:863–874, Jul 1999.

[LBMW03] D. Leibfried, R. Blatt, C. Monroe, and D. Wineland. Quantum dynamics of single trapped ions. *Rev. Mod. Phys.*, 75:281–324, Mar 2003.

[LD98] Daniel Loss and David P. DiVincenzo. Quantum computation with quantum dots. *Phys. Rev. A*, 57:120–126, Jan 1998.

[LDML08] Jonas Larson, Bogdan Damski, Giovanna Morigi, and Maciej Lewenstein. Mott-insulator states of ultracold atoms in optical resonators. *Phys. Rev. Lett.*, 100:050401, Feb 2008.

[LF17] Rui Li and Michael Fleischhauer. Finite-size corrections to quantized particle transport in topological charge pumps. *Phys. Rev. B*, 96:085444, 2017.

[LGS+90] E. Y. Loh, J. E. Gubernatis, R. T. Scalettar, S. R. White, D. J. Scalapino, and R. L. Sugar. Sign problem in the numerical simulation of many-electron systems. *Phys. Rev. B*, 41:9301–9307, May 1990.

[LH08] Hui Li and F. D. M. Haldane. Entanglement spectrum as a generalization of entanglement entropy: Identification of topological order in non-abelian fractional quantum hall effect states. *Phys. Rev. Lett.*, 101:010504, Jul 2008.

[LHD+16] Renate Landig, Lorenz Hruby, Nishant Dogra, Manuele Landini, Rafael Mottl, Tobias Donner, and Tilman Esslinger. Quantum phases from competing short-and long-range interactions in an optical lattice. *Nature*, 532(7600):476, 2016.

[LHN+11] Ben P Lanyon, C Hempel, D Nigg, Markus Müller, R Gerritsma, F Zähringer, P Schindler, JT Barreiro, M Rambach, G Kirchmair, et al. Universal digital quantum simulation with trapped ions. *Science*, 334(6052):57–61, 2011.

[LIB+10] Oren Lahav, Amir Itah, Alex Blumkin, Carmit Gordon, Shahar Rinott, Alona Zayats, and Jeff Steinhauer. Realization of a sonic black hole analog in a bose-einstein condensate. *Physical review letters*, 105(24):240401, 2010.

[Lie94] Elliott H. Lieb. Flux phase of the half-filled band. *Phys. Rev. Lett.*, 73:2158–2161, Oct 1994.

[LLH+17] Jun-Ru Li, Jeongwon Lee, Wujie Huang, Sean Burchesky, Boris Shteynas, Furkan Çağrı Top, Alan O Jamison, and Wolfgang Ketterle. A stripe phase with supersolid properties in spin–orbit-coupled bose–einstein condensates. *Nature*, 543(7643):91–94, 2017.

[LLT+19] Fangli Liu, Rex Lundgren, Paraj Titum, Guido Pagano, Jiehang Zhang, Christopher Monroe, and Alexey V. Gorshkov. Confined quasiparticle dynamics in long-range interacting quantum spin chains. *Phys. Rev. Lett.*, 122:150601, Apr 2019.

[LNW06] Patrick A. Lee, Naoto Nagaosa, and Xiao-Gang Wen. Doping a mott insulator: Physics of high-temperature superconductivity. *Rev. Mod. Phys.*, 78:17–85, Jan 2006.

[LS09] Michael Levin and Ady Stern. Fractional topological insulators. *Phys. Rev. Lett.*, 103:196803, Nov 2009.

[LSA+07] Maciej Lewenstein, Anna Sanpera, Veronica Ahufinger, Bogdan Damski, Aditi Sen(De), and Ujjwal Sen. Ultracold atomic gases in optical lattices: mimicking condensed matter physics and beyond. *Advances in Physics*, 56(2):243–379, 2007.

[LSA17] M. Lewenstein, A. Sanpera, and V. Ahufinger. *Ultracold Atoms in Optical Lattices: Simulating Quantum Many-body Systems*. Oxford University Press, Oxford, 2017.

[LSZ+16] M. Lohse, C. Schweizer, O. Zilberberg, M. Aidelsburger, and I. Bloch. A Thouless quantum pump with ultracold bosonic atoms in an optical superlattice. *Nature Physics*, 12(4):350–354, 2016.

[Lut63] J. M. Luttinger. An exactly soluble model of a many–fermion system. *Journal of Mathematical Physics*, 4(9):1154–1162, 1963.

[LW06] Michael Levin and Xiao-Gang Wen. Detecting topological order in a ground state wave function. *Phys. Rev. Lett.*, 96:110405, Mar 2006.

[LWB+20] Fangli Liu, Seth Whitsitt, Przemyslaw Bienias, Rex Lundgren, and Alexey V. Gorshkov. Realizing and probing baryonic excitations in rydberg atom arrays, 2020.

[LYB+12] Li Liu, Hong Yao, Erez Berg, Steven R. White, and Steven A. Kivelson. Phases of the infinite u hubbard model on square lattices. *Phys. Rev. Lett.*, 108:126406, Mar 2012.

[M+16] E. A. Martinez et al. Real-time dynamics of lattice gauge theories with a few-qubit quantum computer. *Nature*, 534:516–519, 2016.

[Man85] N.S Manton. The schwinger model and its axial anomaly. *Annals of Physics*, 159(1):220 – 251, 1985.

[Man02] Efstratios Manousakis. A quantum-dot array as model for copper-oxide superconductors: A dedicated quantum simulator for the many-fermion problem. *Journal of low temperature physics*, 126(5-6):1501–1513, 2002.

[MCJ+17] Anton Mazurenko, Christie S Chiu, Geoffrey Ji, Maxwell F Parsons, Márton Kanász-Nagy, Richard Schmidt, Fabian Grusdt, Eugene Demler, Daniel Greif, and Markus Greiner. A cold-atom fermi–hubbard antiferromagnet. *Nature*, 545(7655):462, 2017.

[MCO15] Pasquale Marra, Roberta Citro, and Carmine Ortix. Fractional quantization of the topological charge pumping in a one-dimensional superlattice. *Phys. Rev. B*, 91:125411, Mar 2015.

[MDF+20] Giuseppe Magnifico, Marcello Dalmonte, Paolo Facchi, Saverio Pascazio, Francesco V. Pepe, and Elisa Ercolessi. Real Time Dynamics and Confinement in the $\mathbb{Z}_n$ Schwinger-Weyl lattice model for 1+1 QED. *Quantum*, 4:281, June 2020.

[Mer79] N. D. Mermin. The topological theory of defects in ordered media. *Rev. Mod. Phys.*, 51:591–648, Jul 1979.

[MGY88] A. H. MacDonald, S. M. Girvin, and D. Yoshioka. $\frac{t}{U}$ expansion for the hubbard model. *Phys. Rev. B*, 37:9753–9756, Jun 1988.

[Mis10] Gregoire Misguich. Quantum spin liquids. *Exact Methods in Low-dimensional Statistical Physics and Quantum Computing: Lecture Notes of the Les Houches Summer School: Volume 89, July 2008*, page 431, 2010.

[MMR07] Igor B Mekhov, Christoph Maschler, and Helmut Ritsch. Probing quantum phases of ultracold atoms in optical lattices by transmission spectra in cavity quantum electrodynamics. *Nature Physics*, 3(5):319, 2007.

[MMS+16] Esteban A. Martinez, Christine A. Muschik, Philipp Schindler, Daniel Nigg, Alexander Erhard, Markus Heyl, Philipp Hauke, Marcello Dalmonte, Thomas Monz, Peter Zoller, and Rainer Blatt. Real-time dynamics of lattice gauge theories with a few-qubit quantum computer. *Nature*, 534(7608):516–519, Jun 2016.

[MO06] Oliver Morsch and Markus Oberthaler. Dynamics of bose-einstein condensates in optical lattices. *Rev. Mod. Phys.*, 78:179–215, Feb 2006.

[MP07] Larry McLerran and Robert D. Pisarski. Phases of dense quarks at large nc. *Nuclear Physics A*, 796(1):83 – 100, 2007.

[MRP17] Farokh Mivehvar, Helmut Ritsch, and Francesco Piazza. Superradiant topological peierls insulator inside an optical cavity. *Phys. Rev. Lett.*, 118:073602, Feb 2017.

[MSF01] R. Moessner, S. L. Sondhi, and Eduardo Fradkin. Short-ranged resonating valence bond physics, quantum dimer models, and ising gauge theories. *Phys. Rev. B*, 65:024504, Dec 2001.

[MSK+13] Hirokazu Miyake, Georgios A. Siviloglou, Colin J. Kennedy, William Cody Burton, and Wolfgang Ketterle. Realizing the harper hamiltonian with laser-assisted tunneling in optical lattices. *Phys. Rev. Lett.*, 111:185302, Oct 2013.

[MVE+19] G. Magnifico, D. Vodola, E. Ercolessi, S. P. Kumar, M. Müller, and A. Bermudez. $\mathcal{F}_N$ gauge theories coupled to topological fermions: qed_2 with a quantum mechanical θ angle. *Phys. Rev. B*, 100:115152, Sep 2019.

[MW97] John Milnor and David W Weaver. *Topology from the differentiable viewpoint*. Princeton university press, 1997.

[MZH+20] Alexander Mil, Torsten V. Zache, Apoorva Hegde, Andy Xia, Rohit P. Bhatt, Markus K. Oberthaler, Philipp Hauke, Jürgen Berges, and Fred Jendrzejewski. A scalable realization of local u(1) gauge invariance in cold atomic mixtures. *Science*, 367(6482):1128–1130, 2020.

[Nab47] F R N Nabarro. Dislocations in a simple cubic lattice. *Proceedings of the Physical Society*, 59(2):256–272, mar 1947.

[Nag66] Yosuke Nagaoka. Ferromagnetism in a narrow, almost half-filled s band. *Phys. Rev.*, 147:392–405, Jul 1966.

[Nak03] Mikio Nakahara. *Geometry, topology and physics*. CRC Press, 2003.

[NCM20] Simone Notarnicola, Mario Collura, and Simone Montangero. Real-time-dynamics quantum simulation of $(1 + 1)$-dimensional lattice qed with rydberg atoms. *Phys. Rev. Research*, 2:013288, Mar 2020.

[NGI+14] A. Negretti, R. Gerritsma, Z. Idziaszek, F. Schmidt-Kaler, and T. Calarco. Generalized kronig-penney model for ultracold atomic quantum systems. *Phys. Rev. B*, 90:155426, Oct 2014.

[NJL61a] Y. Nambu and G. Jona-Lasinio. Dynamical model of elementary particles based on an analogy with superconductivity. i. *Phys. Rev.*, 122:345–358, Apr 1961.

[NJL61b] Y. Nambu and G. Jona-Lasinio. Dynamical model of elementary particles based on an analogy with superconductivity. ii. *Phys. Rev.*, 124:246–254, Oct 1961.

[NS86] A.J. Niemi and G.W. Semenoff. Fermion number fractionization in quantum field theory. *Physics Reports*, 135(3):99 – 193, 1986.

[NSS+08] Chetan Nayak, Steven H. Simon, Ady Stern, Michael Freedman, and Sankar Das Sarma. Non-abelian anyons and topological quantum computation. *Rev. Mod. Phys.*, 80:1083–1159, Sep 2008.

[NT84] Q Niu and D J Thouless. Quantised adiabatic charge transport in the presence of substrate disorder and many-body interaction. *Journal of Physics A: Mathematical and General*, 17(12):2453–2462, 1984.

[NTT+16] Shuta Nakajima, Takafumi Tomita, Shintaro Taie, Tomohiro Ichinose, Hideki Ozawa, Lei Wang, Matthias Troyer, and Yoshiro Takahashi. Topological Thouless pumping of ultracold fermions. *Nature Physics*, 12(4):296–300, 2016.

[NTW85a] Qian Niu, D. J. Thouless, and Yong-Shi Wu. Quantized hall conductance as a topological invariant. *Phys. Rev. B*, 31:3372, 1985.

[NTW85b] Qian Niu, D. J. Thouless, and Yong-Shi Wu. Quantized hall conductance as a topological invariant. *Phys. Rev. B*, 31:3372–3377, Mar 1985.

[OR95] Stellan Östlund and Stefan Rommer. Thermodynamic limit of density matrix renormalization. *Phys. Rev. Lett.*, 75:3537–3540, Nov 1995.

[Oru14] Roman Orus. A practical introduction to tensor networks: Matrix product states and projected entangled pair states. *Annals of Physics*, 349(Supplement C):117 – 158, 2014.

[PB10] Dmytro Pesin and Leon Balents. Mott physics and band topology in materials with strong spin–orbit interaction. *Nature Physics*, 6(5):376–381, May 2010.

[PC04] D. Porras and J. I. Cirac. Effective quantum spin systems with trapped ions. *Phys. Rev. Lett.*, 92:207901, May 2004.

[PDZ15] Anna Przysikezna, Omjyoti Dutta, and Jakub Zakrzewski. Rice–mele model with topological solitons in an optical lattice. *New Journal of Physics*, 17:013018, 2015.

[Pei40] R Peierls. The size of a dislocation. *Proceedings of the Physical Society*, 52(1):34–37, jan 1940.

[Pei55] R.E. Peierls. *Quantum Theory of Solids*. International series of monographs on physics. Clarendon Press, 1955.

[PGM+08] G. Pupillo, A. Griessner, A. Micheli, M. Ortner, D.-W. Wang, and P. Zoller. Cold atoms and molecules in self-assembled dipolar lattices. *Phys. Rev. Lett.*, 100:050402, Feb 2008.

[Phi98] William D. Phillips. Nobel Lecture: Laser cooling and trapping of neutral atoms. *Rev. Mod. Phys.*, 70(3):721–741, 1998.

[PKI19] Jonghoon Park, Yoshihito Kuno, and Ikuo Ichinose. Glassy dynamics from quark confinement: Atomic quantum simulation of the gauge-higgs model on a lattice. *Phys. Rev. A*, 100:013629, Jul 2019.

[PLM17] Christian Prosko, Shu-Ping Lee, and Joseph Maciejko. Simple $\mathbb{Z}_2$ lattice gauge theories at finite fermion density. *Phys. Rev. B*, 96:205104, Nov 2017.

[PMC+16] Maxwell F. Parsons, Anton Mazurenko, Christie S. Chiu, Geoffrey Ji, Daniel Greif, and Markus Greiner. Site-resolved measurement of the spin-correlation function in the fermi-hubbard model. *Science*, 353(6305):1253–1256, 2016.

[Pol75] A.M. Polyakov. Interaction of goldstone particles in two dimensions. applications to ferromagnets and massive yang-mills fields. *Physics Letters B*, 59(1):79 – 81, 1975.

[Pol77] A.M. Polyakov. Quark confinement and topology of gauge theories. *Nuclear Physics B*, 120(3):429 – 458, 1977.

[PQSV11] David Poulin, Angie Qarry, Rolando Somma, and Frank Verstraete. Quantum simulation of time-dependent hamiltonians and the convenient illusion of hilbert space. *Phys. Rev. Lett.*, 106:170501, Apr 2011.

[PS95] Michael E. Peskin and Daniel V. Schroeder. *An Introduction to quantum field theory*. Addison-Wesley, Reading, USA, 1995.

[PS08] C. J. Pethick and H. Smith. *Bose–Einstein Condensation in Dilute Gases*. Cambridge University Press, 2 edition, 2008.

[PS14] Francesco Piazza and Philipp Strack. Umklapp superradiance with a collisionless quantum degenerate fermi gas. *Phys. Rev. Lett.*, 112:143003, Apr 2014.

[PTBO10] Frank Pollmann, Ari M. Turner, Erez Berg, and Masaki Oshikawa. Entanglement spectrum of a topological phase in one dimension. *Phys. Rev. B*, 81:064439, Feb 2010.

[PWM+04] Belén Paredes, Artur Widera, Valentin Murg, Olaf Mandel, Simon FÃűlling, Ignacio Cirac, Gora V. Shlyapnikov, Theodor W. HÃďnsch, and Immanuel Bloch. Tonks–girardeau gas of ultracold atoms in an optical lattice. *Nature*, 429:277–281, 2004.

[QZ11] Xiao-Liang Qi and Shou-Cheng Zhang. Topological insulators and superconductors. *Rev. Mod. Phys.*, 83:1057–1110, Oct 2011.

[Rac18] Stephan Rachel. Interacting topological insulators: a review. *Reports on Progress in Physics*, 81(11):116501, oct 2018.

[Rad71] J M Radcliffe. Some properties of coherent spin states. *Journal of Physics A: General Physics*, 4(3):313–323, may 1971.

[Raj82] R. Rajaraman. *Solitons and Instantons. An introduction to solitons and instants in quantum field theory.* North-holland, 1982.

[RBH01] J. M. Raimond, M. Brune, and S. Haroche. Manipulating quantum entanglement with atoms and photons in a cavity. *Rev. Mod. Phys.*, 73:565–582, Aug 2001.

[RBvO+06] T. Rom, Th Best, D. van Oosten, U. Schneider, S. Fölling, B. Paredes, and I. Bloch. Free fermion antibunching in a degenerate atomic Fermi gas released from an optical lattice. *Nature*, 444(7120):733–736, December 2006.

[RDZ+18] E. Rico, M. Dalmonte, P. Zoller, D. Banerjee, and M. B˙ So(3) nuclear physics with ultracold gases. *Annals of Physics*, 393:466 – 483, 2018.

[RG00] N. Read and Dmitry Green. Paired states of fermions in two dimensions with breaking of parity and time-reversal symmetries and the fractional quantum hall effect. *Phys. Rev. B*, 61:10267–10297, Apr 2000.

[RGS16] Bitan Roy, Pallab Goswami, and Jay D. Sau. Continuous and discontinuous topological quantum phase transitions. *Phys. Rev. B*, 94:041101, Jul 2016.

[RH02] Shinsei Ryu and Yasuhiro Hatsugai. Topological origin of zero-energy edge states in particle-hole symmetric systems. *Phys. Rev. Lett.*, 89:077002, Jul 2002.

[RK88] Daniel S. Rokhsar and Steven A. Kivelson. Superconductivity and the quantum hard-core dimer gas. *Phys. Rev. Lett.*, 61:2376–2379, Nov 1988.

[RM82] M. J. Rice and E. J. Mele. Elementary excitations of a linearly conjugated diatomic polymer. *Phys. Rev. Lett.*, 49:1455–1459, Nov 1982.

[RQHZ08] S. Raghu, Xiao-Liang Qi, C. Honerkamp, and Shou-Cheng Zhang. Topological mott insulators. *Phys. Rev. Lett.*, 100:156401, Apr 2008.

[RS91] N. Read and Subir Sachdev. Large-n expansion for frustrated quantum antiferromagnets. *Phys. Rev. Lett.*, 66:1773–1776, Apr 1991.

[RSFL10] Shinsei Ryu, Andreas P Schnyder, Akira Furusaki, and Andreas W W Ludwig. Topological insulators and superconductors: ten-fold way and dimensional hierarchy. *New Journal of Physics*, 12(6):065010, jun 2010.

[RW00] R. Rapp and J. Wambach. *Chiral Symmetry Restoration and Dileptons in Relativistic Heavy-Ion Collisions*, pages 1–205. Springer US, Boston, MA, 2000.

[Sac11] Subir Sachdev. *Quantum Phase Transitions*. Cambridge University Press, 2 edition, 2011.

[Sac18] Subir Sachdev. Topological order, emergent gauge fields, and fermi surface reconstruction. *Reports on Progress in Physics*, 82(1):014001, nov 2018.

[Sch62] Julian Schwinger. Gauge invariance and mass. ii. *Phys. Rev.*, 128:2425–2429, Dec 1962.

[Sch11] Ulrich Schollwöck. The density-matrix renormalization group in the age of matrix product states. *Annals of Physics*, 326(1):96 – 192, 2011.

[Sch14] Matthew D. Schwartz. *Quantum Field Theory and the Standard Model*. Cambridge University Press, 3 2014.

[SDL05] Anders S Sørensen, Eugene Demler, and Mikhail D Lukin. Fractional quantum hall states of atoms in optical lattices. *Physical review letters*, 94(8):086803, 2005.

[SDS05] V. W. Scarola and S. Das Sarma. Quantum phases of the extended bose-hubbard hamiltonian: Possibility of a supersolid state of cold atoms in optical lattices. *Phys. Rev. Lett.*, 95:033003, Jul 2005.

[Sen15] T. Senthil. Symmetry-protected topological phases of quantum matter. *Annual Review of Condensed Matter Physics*, 6(1):299–324, 2015.

[SF00] T. Senthil and Matthew P. A. Fisher. Z_2 gauge theory of electron fractionalization in strongly correlated systems. *Phys. Rev. B*, 62:7850–7881, Sep 2000.

[SF01] T. Senthil and Matthew P. A. Fisher. Fractionalization, topological order, and cuprate superconductivity. *Phys. Rev. B*, 63:134521, Mar 2001.

[SGB+19] Christian Schweizer, Fabian Grusdt, Moritz Berngruber, Luca Barbiero, Eugene Demler, Nathan Goldman, Immanuel Bloch, and Monika Aidelsburger. Floquet approach to $\mathbb{Z}_2$ lattice gauge theories with ultracold atoms in optical lattices. page Preprint at https://arxiv.org/abs/1901.07103, Jan 2019.

[SGDS10] Tudor D. Stanescu, Victor Galitski, and S. Das Sarma. Topological states in two-dimensional optical lattices. *Phys. Rev. A*, 82:013608, Jul 2010.

[SHD10] Stefan Schmid, Arne Härter, and Johannes Hecker Denschlag. Dynamics of a cold trapped ion in a bose-einstein condensate. *Phys. Rev. Lett.*, 105:133202, Sep 2010.

[SHW+08] U. Schneider, L. Hackermüller, S. Will, Th. Best, I. Bloch, T. A. Costi, R. W. Helmes, D. Rasch, and A. Rosch. Metallic and insulating phases of repulsively interacting fermions in a 3d optical lattice. *Science*, 322(5907):1520–1525, 2008.

[Sim83] Barry Simon. Holonomy, the quantum adiabatic theorem, and berry's phase. *Phys. Rev. Lett.*, 51:2167–2170, Dec 1983.

[SKA90] B. S. Shastry, H. R. Krishnamurthy, and P. W. Anderson. Instability of the nagaoka ferromagnetic state of the u=∞ hubbard model. *Phys. Rev. B*, 41:2375–2379, Feb 1990.

[SKK01] D. M. Stamper-Kurn and W. Ketterle. *Spinor Condensates and Light Scattering from Bose- Einstein Condensates.* Springer, New York, 2001.

[SMG+20] Federica M. Surace, Paolo P. Mazza, Giuliano Giudici, Alessio Lerose, Andrea Gambassi, and Marcello Dalmonte. Lattice gauge theories and string dynamics in rydberg atom quantum simulators. *Phys. Rev. X*, 10:021041, May 2020.

[SPGC11] Norbert Schuch, David Pérez-García, and Ignacio Cirac. Classifying quantum phases using matrix product states and projected entangled pair states. *Phys. Rev. B*, 84:165139, Oct 2011.

[SPOT09] V. W. Scarola, L. Pollet, J. Oitmaa, and M. Troyer. Discerning incompressible and compressible phases of cold atoms in optical lattices. *Phys. Rev. Lett.*, 102:135302, Mar 2009.

[SPS12] Ch Schneider, Diego Porras, and Tobias Schätz. Experimental quantum simulations of many-body physics with trapped ions. *Rep. Prog. Phys.*, 75(2):024401, 2012.

[SR44] J Scott Russell. Report on waves. *Proc. R. Soc. Edinburgh,.*, page 319, 1844.

[Sre93] Mark Srednicki. Entropy and area. *Phys. Rev. Lett.*, 71:666–669, Aug 1993.

[SS80] W. P. Su and J. R. Schrieffer. Soliton dynamics in polyacetylene. *Proceedings of the National Academy of Sciences*, 77(10):5626–5629, 1980.

[SS81] W. P. Su and J. R. Schrieffer. Fractionally charged excitations in charge-density-wave systems with commensurability 3. *Phys. Rev. Lett.*, 46:738–741, Mar 1981.

[SSAJP06] J. Sebby-Strabley, M. Anderlini, P. S. Jessen, and J. V. Porto. Lattice of double wells for manipulating pairs of cold atoms. *Phys. Rev. A*, 73(3):033605, March 2006.

[SSC03] Pinaki Sengupta, Anders W. Sandvik, and David K. Campbell. Peierls transition in the presence of finite-frequency phonons in the one-dimensional extended peierls-hubbard model at half-filling. *Phys. Rev. B*, 67:245103, Jun 2003.

[SSH79] W. P. Su, J. R. Schrieffer, and A. J. Heeger. Solitons in polyacetylene. *Phys. Rev. Lett.*, 42:1698–1701, Jun 1979.

[Su83] W. P. Su. Fractionally charged kinks in a 1: 3 peierls system. *Phys. Rev. B*, 27:370–379, Jan 1983.

[SWE+10] Jacob F. Sherson, Christof Weitenberg, Manuel Endres, Marc Cheneau, Immanuel Bloch, and Stefan Kuhr. Single-atom-resolved fluorescence imaging of an atomic Mott insulator. *Nature*, 467(7311):68–72, September 2010.

[SYFK09] Kai Sun, Hong Yao, Eduardo Fradkin, and Steven A. Kivelson. Topological insulators and nematic phases from spontaneous symmetry breaking in 2d fermi systems with a quadratic band crossing. *Phys. Rev. Lett.*, 103:046811, Jul 2009.

[SZD+08] Andrea Simoni, Matteo Zaccanti, Chiara D'Errico, Marco Fattori, Giacomo Roati, Massimo Inguscio, and Giovanni Modugno. Near-threshold model for ultracold KRb dimers from interisotope Feshbach spectroscopy. *Phys. Rev. A*, 77, 2008.

[TBL+19] W. L. Tan, P. Becker, F. Liu, G. Pagano, K. S. Collins, A. De, L. Feng, H. B. Kaplan, A. Kyprianidis, R. Lundgren, W. Morong, S. Whitsitt, A. V. Gorshkov, and C. Monroe. Observation of domain wall confinement and dynamics in a quantum simulator, 2019.

[TCF+08] S. Trotzky, P. Cheinet, S. Fölling, M. Feld, U. Schnorrberger, A. M. Rey, A. Polkovnikov, E. A. Demler, M. D. Lukin, and I. Bloch. Time-resolved observation and control of superexchange interactions with ultracold atoms in optical lattices. *Science*, 319(5861):295–299, 2008.

[TCF+12] S. Trotzky, Y-A. Chen, A. Flesch, I. P. McCulloch, U. Schollwöck, J. Eisert, and I. Bloch. Probing the relaxation towards equilibrium in an isolated strongly correlated one-dimensional Bose gas. *Nature Phys*, 8(4):325–330, April 2012.

[TCL14] L. Tagliacozzo, A. Celi, and M. Lewenstein. Tensor Networks for Lattice Gauge Theories with Continuous Groups. *Phys. Rev. X*, 4(4):041024, November 2014.

[TCO+13] L. Tagliacozzo, A. Celi, P. Orland, M. W. Mitchell, and M. Lewenstein. Simulation of non-abelian gauge theories with optical lattices. *Nature Communications*, 4(1):2615, 2013.

[TCR+17] Luca Taddia, Eyal Cornfeld, Davide Rossini, Leonardo Mazza, Eran Sela, and Rosario Fazio. Topological fractional pumping with alkaline-earth-like atoms in synthetic lattices. *Phys. Rev. Lett.*, 118:230402, 2017.

[TCS+10] Stefan Trotzky, Yu-Ao Chen, Ute Schnorrberger, Patrick Cheinet, and Immanuel Bloch. Controlling and Detecting Spin Correlations of Ultracold Atoms in Optical Lattices. *Phys. Rev. Lett.*, 105(26):265303, December 2010.

[TCZL13] L. Tagliacozzo, A. Celi, A. Zamora, and M. Lewenstein. Optical abelian lattice gauge theories. *Annals of Physics*, 330:160 – 191, 2013.

[TdOIL08] L. Tagliacozzo, Thiago. R. de Oliveira, S. Iblisdir, and J. I. Latorre. Scaling of entanglement support for matrix product states. *Phys. Rev. B*, 78:024410, Jul 2008.

[Ter15] Barbara M. Terhal. Quantum error correction for quantum memories. *Rev. Mod. Phys.*, 87:307–346, Apr 2015.

[TGU+12] Leticia Tarruell, Daniel Greif, Thomas Uehlinger, Gregor Jotzu, and Tilman Esslinger. Creating, moving and merging dirac points with a fermi gas in a tunable honeycomb lattice. *Nature*, 483(7389):302–305, Mar 2012.

[TH17] Jeffrey C.Y. Teo and Taylor L. Hughes. Topological defects in symmetry-protected topological phases. *Annual Review of Condensed Matter Physics*, 8(1):211–237, 2017.

[Thi58] Walter E Thirring. A soluble relativistic field theory. *Annals of Physics*, 3(1):91 – 112, 1958.

[Tho83] D. J. Thouless. Quantization of particle transport. *Phys. Rev. B*, 27:6083–6087, May 1983.

[TK10] Jeffrey C. Y. Teo and C. L. Kane. Topological defects and gapless modes in insulators and superconductors. *Phys. Rev. B*, 82:115120, Sep 2010.

[TKNdN82] D. J. Thouless, M. Kohmoto, M. P. Nightingale, and M. den Nijs. Quantized hall conductance in a two-dimensional periodic potential. *Phys. Rev. Lett.*, 49:405–408, Aug 1982.

[TKPS10] I. S. Tupitsyn, A. Kitaev, N. V. Prokof'ev, and P. C. E. Stamp. Topological multicritical point in the phase diagram of the toric code model and three-dimensional lattice gauge Higgs model. *Phys. Rev. B*, 82(8):085114, August 2010.

[TLLM80] Hajime Takayama, Y. R. Lin-Liu, and Kazumi Maki. Continuum model for solitons in polyacetylene. *Phys. Rev. B*, 21:2388–2393, Mar 1980.

[Tom50] Sin Tomonaga. Remarks on Bloch's Method of Sound Waves applied to Many-Fermion Problems. *Progress of Theoretical Physics*, 5(4):544–569, 07 1950.

[TPB11] Ari M. Turner, Frank Pollmann, and Erez Berg. Topological phases of one-dimensional fermions: An entanglement point of view. *Phys. Rev. B*, 83:075102, Feb 2011.

[TRS+19] E. Tirrito, M. Rizzi, G. Sierra, M. Lewenstein, and A. Bermudez. Renormalization group flows for wilson-hubbard matter and the topological hamiltonian. *Phys. Rev. B*, 99:125106, Mar 2019.

[TSG82] D. C. Tsui, H. L. Stormer, and A. C. Gossard. Two-dimensional magnetotransport in the extreme quantum limit. *Phys. Rev. Lett.*, 48:1559–1562, May 1982.

[TT83] R. Tao and D. J. Thouless. Fractional quantization of hall conductance. *Phys. Rev. B*, 28:1142, 1983.

[TU03] Michael Thies and Konrad Urlichs. Revised phase diagram of the gross-neveu model. *Phys. Rev. D*, 67:125015, Jun 2003.

[TV11] L. Tagliacozzo and G. Vidal. Entanglement renormalization and gauge symmetry. *Physical Review B*, 83:115127, March 2011.

[TWT+07] Simon Trebst, Philipp Werner, Matthias Troyer, Kirill Shtengel, and Chetan Nayak. Breakdown of a Topological Phase: Quantum Phase Transition in a Loop Gas Model with Tension. *Phys. Rev. Lett.*, 98(7):070602, February 2007.

[TZV10] Ari M. Turner, Yi Zhang, and Ashvin Vishwanath. Entanglement and inversion symmetry in topological insulators. *Phys. Rev. B*, 82:241102, Dec 2010.

[VDS09] J. Vidal, S. Dusuel, and K. P. Schmidt. Low-energy effective theory of the toric code model in a parallel field. *Phys. Rev. B*, 79(3):033109, January 2009.

[Vid04] Guifré Vidal. Efficient simulation of one-dimensional quantum many-body systems. *Phys. Rev. Lett.*, 93:040502, Jul 2004.

[Vid07] G. Vidal. Entanglement renormalization. *Phys. Rev. Lett.*, 99:220405, Nov 2007.

[VLRK03] G. Vidal, J. I. Latorre, E. Rico, and A. Kitaev. Entanglement in quantum critical phenomena. *Phys. Rev. Lett.*, 90:227902, Jun 2003.

[VMC08] F. Verstraete, V. Murg, and J.I. Cirac. Matrix product states, projected entangled pair states, and variational renormalization group methods for quantum spin systems. *Advances in Physics*, 57(2):143–224, 2008.

[vOM96] Alexander van Oudenaarden and JE Mooij. One-dimensional mott insulator formed by quantum vortices in josephson junction arrays. *Physical review letters*, 76(26):4947, 1996.

[VPC04] F. Verstraete, D. Porras, and J. I. Cirac. Density matrix renormalization group and periodic boundary conditions: A quantum information perspective. *Phys. Rev. Lett.*, 93:227205, Nov 2004.

[VTSD09] J. Vidal, R. Thomale, K. P Schmidt, and S. Dusuel. Self-duality and bound states of the toric code model in a transverse field. *0902.3547*, February 2009. Phys. Rev. B 80, 081104 (2009).

[VZNS82] A.I. Vainshtein, Valentin I. Zakharov, V.A. Novikov, and Mikhail A. Shifman. ABC's of Instantons. *Sov. Phys. Usp.*, 25:195, 1982.

[WAH15] Manuel Weber, Fakher F. Assaad, and Martin Hohenadler. Excitation spectra and correlation functions of quantum su-schrieffer-heeger models. *Phys. Rev. B*, 91:245147, Jun 2015.

[WBÜ+20] Karen Wintersperger, Christoph Braun, F. Nur Ünal, André Eckardt, Marco Di Liberto, Nathan Goldman, Immanuel Bloch, and Monika Aidelsburger. Realization of an anomalous floquet topological system with ultracold atoms. *Nature Physics*, Jun 2020.

[Weg71] Franz J. Wegner. Duality in generalized ising models and phase transitions without local order parameters. *J. Math. Phys.*, 12(10):2259–2272, 1971.

[Wei67] Steven Weinberg. A model of leptons. *Phys. Rev. Lett.*, 19:1264–1266, Nov 1967.

[Wen89] X. G. Wen. Vacuum degeneracy of chiral spin states in compactified space. *Phys. Rev. B*, 40:7387–7390, Oct 1989.

[Wen90] X. G. Wen. Topological orders in rigid states. *International Journal of Modern Physics B*, 04(02):239–271, 1990.

[Wen07] X.-G. Wen. *Quantum field theory of many-body systems: from the origin of sound to an origin of light and electrons.* Oxford University Press, Oxford, 2007.

[Wen17] Xiao-Gang Wen. Colloquium: Zoo of quantum-topological phases of matter. *Rev. Mod. Phys.*, 89:041004, Dec 2017.

[Whi92] Steven R. White. Density matrix formulation for quantum renormalization groups. *Phys. Rev. Lett.*, 69:2863–2866, Nov 1992.

[Whi93] Steven R. White. Density-matrix algorithms for quantum renormalization groups. *Phys. Rev. B*, 48:10345–10356, Oct 1993.

[Wie13] U.-J. Wiese. Ultracold quantum gases and lattice systems: quantum simulation of lattice gauge theories. *Annalen der Physik*, 525(10-11):777–796, 2013.

[Wil74] Kenneth G. Wilson. Confinement of quarks. *Phys. Rev. D*, 10:2445–2459, Oct 1974.

[Wil75] Kenneth G. Wilson. The renormalization group: Critical phenomena and the kondo problem. *Rev. Mod. Phys.*, 47:773–840, Oct 1975.

[Wil77] Kenneth G. Wilson. Quarks and strings on a lattice, Jan 1977.

[Wil99] Frank Wilczek. Mass without mass i: Most of matter. *Physics Today*, 52(11):11–12, 1999.

[Wit89] Edward Witten. Quantum field theory and the jones polynomial. *Communications in Mathematical Physics*, 121(3):351–399, Sep 1989.

[WK74] Kenneth G. Wilson and J. Kogut. The renormalization group and the ϵ expansion. *Physics Reports*, 12(2):75 – 199, 1974.

[WML+10] Hendrik Weimer, Markus Müller, Igor Lesanovsky, Peter Zoller, and Hans Peter Büchler. A rydberg quantum simulator. *Nature Physics*, 6(5):382–388, 2010.

[WTD13] Lei Wang, Matthias Troyer, and Xi Dai. Topological charge pumping in a one-dimensional optical lattice. *Phys. Rev. Lett.*, 111:026802, Jul 2013.

[WWZ89] X. G. Wen, Frank Wilczek, and A. Zee. Chiral spin states and superconductivity. *Phys. Rev. B*, 39:11413–11423, Jun 1989.

[WY75] Tai Tsun Wu and Chen Ning Yang. Concept of nonintegrable phase factors and global formulation of gauge fields. *Phys. Rev. D*, 12:3845–3857, Dec 1975.

[WYL+19] Jinsheng Wen, Shun-Li Yu, Shiyan Li, Weiqiang Yu, and Jian-Xin Li. Experimental identification of quantum spin liquids. *npj Quantum Mater.*, 4(1):1–9, April 2019.

[WZ89] X.G. Wen and A. Zee. Winding number, family index theorem, and electron hopping in a magnetic field. *Nuclear Physics B*, 316(3):641 – 662, 1989.

[XCN10] Di Xiao, Ming-Che Chang, and Qian Niu. Berry phase effects on electronic properties. *Rev. Mod. Phys.*, 82:1959–2007, Jul 2010.

[YM54] C. N. Yang and R. L. Mills. Conservation of isotopic spin and isotopic gauge invariance. *Phys. Rev.*, 96:191–195, Oct 1954.

[YN03] J. Q. You and Franco Nori. Quantum information processing with superconducting qubits in a microwave field. *Phys. Rev. B*, 68:064509, Aug 2003.

[YSH+20] Bing Yang, Hui Sun, Chun-Jiong Huang, Han-Yi Wang, Youjin Deng, Han-Ning Dai, Zhen-Sheng Yuan, and Jian-Wei Pan. Cooling and entangling ultracold atoms in optical lattices. *Science*, June 2020.

[YSO+20] Bing Yang, Hui Sun, Robert Ott, Han-Yi Wang, Torsten V. Zache, Jad C. Halimeh, Zhen-Sheng Yuan, Philipp Hauke, and Jian-Wei Pan. Observation of gauge invariance in a 71-site quantum simulator, 2020.

[Zak89] J. Zak. Berry's phase for energy bands in solids. *Phys. Rev. Lett.*, 62:2747–2750, Jun 1989.

[ZCR12] Erez Zohar, J. Ignacio Cirac, and Benni Reznik. Simulating compact quantum electrodynamics with ultracold atoms: Probing confinement and nonperturbative effects. *Phys. Rev. Lett.*, 109:125302, Sep 2012.

[ZCR13a] Erez Zohar, J. Ignacio Cirac, and Benni Reznik. Cold-atom quantum simulator for su(2) yang-mills lattice gauge theory. *Phys. Rev. Lett.*, 110:125304, Mar 2013.

[ZCR13b] Erez Zohar, J. Ignacio Cirac, and Benni Reznik. Quantum simulations of gauge theories with ultracold atoms: Local gauge invariance from angular-momentum conservation. *Phys. Rev. A*, 88:023617, Aug 2013.

[ZCR15] Erez Zohar, J Ignacio Cirac, and Benni Reznik. Quantum simulations of lattice gauge theories using ultracold atoms in optical lattices. *Reports on Progress in Physics*, 79(1):014401, dec 2015.

[ZCZW19] Bei Zeng, Xie Chen, Duan-Lu Zhou, and Xiao-Gang Wen. *Quantum information meets quantum matter*. Springer, 2019.

[ZFRC17] Erez Zohar, Alessandro Farace, Benni Reznik, and J. Ignacio Cirac. Digital quantum simulation of $\mathbb{Z}_2$ lattice gauge theories with dynamical fermionic matter. *Phys. Rev. Lett.*, 118:070501, Feb 2017.

[ZGT+12] Yi Zhang, Tarun Grover, Ari Turner, Masaki Oshikawa, and Ashvin Vishwanath. Quasiparticle statistics and braiding from ground-state entanglement. *Phys. Rev. B*, 85(23):235151, June 2012.

[ZK65] N. J. Zabusky and M. D. Kruskal. Interaction of "solitons" in a collisionless plasma and the recurrence of initial states. *Phys. Rev. Lett.*, 15:240–243, Aug 1965.

[ZMP14] Michael P Zaletel, Roger S K Mong, and Frank Pollmann. Flux insertion, entanglement, and quantized responses. *Journal of Statistical Mechanics: Theory and Experiment*, 2014(10):P10007, oct 2014.

[ZPSK10] Christoph Zipkes, Stefan Palzer, Carlo Sias, and Michael Köhl. A trapped single ion inside a bose–einstein condensate. *Nature*, 464(7287):388, 2010.

[ZR88] F. C. Zhang and T. M. Rice. Effective hamiltonian for the superconducting cu oxides. *Phys. Rev. B*, 37:3759–3761, Mar 1988.

[ZR11] Erez Zohar and Benni Reznik. Confinement and lattice quantum-electrodynamic electric flux tubes simulated with ultracold atoms. *Phys. Rev. Lett.*, 107:275301, Dec 2011.

[Zur85] W. H. Zurek. Cosmological experiments in superfluid helium? *Nature*, 317(6037):505–508, oct 1985.

[ZWZ15] Tian-Sheng Zeng, Ce Wang, and Hui Zhai. Charge pumping of interacting fermion atoms in the synthetic dimension. *Phys. Rev. Lett.*, 115:095302, 2015.

[ZZS16] Tian-Sheng Zeng, W. Zhu, and D. N. Sheng. Fractional charge pumping of interacting bosons in one-dimensional superlattice. *Phys. Rev. B*, 94:235139, 2016.